PP/Clay Nanocomposites:

Compounding and Thin-Wall Injection Moulding

By

Tingrui Fu

A doctoral thesis submitted in partial fulfilment of the requirements for the award of Doctor of Philosophy of Loughborough University

Supervisor: Mr Barry Haworth

Loughborough University, Department of Materials

December 2016

ACKNOWLEDGEMENTS

This study would not have been possible without the support and encouragement that I have received from many people.

I would first likely to express my special appreciation and thanks to my academic supervisor Mr Barry Haworth for his enthusiasm, support and guidance throughout my time at Loughborough University. His help and knowledge has been invaluable.

I am so grateful to my parents and I would like to say a big thank you to them. My family has been encouraging, supportive and shown belief in me and my research all the time. Without their continuing support, I could never have done this PhD.

My sincere thanks must go to the technicians in Materials Department, especially Mr Andy Woolley, Mr Ray Owens, Mr David Insley and Dr Zhaoxia Zhou. They have been so helpful throughout my research project.

I would like to thank all my friends at Loughborough, because they make my life so colourful. Their names include, but not limited to, Xu Xu, Amy Tan, Elvis Wu, Eason Deng, Juntao Guo, Lucy Chen, Pengxiang Zheng, Chao Huang.

And finally great thanks go to, my beloved one, Linzi Wu who has been an important part of my life. She gives me infinite courage to face the challenges and difficulties in my life.

Abstract

This research investigates formulation, compounding and thin-wall injection moulding of Polypropylene/clay nanocomposites (PPCNs) prepared using conventional melt-state processes. An independent study on single screw extrusion dynamics using Design of Experiments (DoE) was performed first.[1] Then the optimum formulation of PPCNs and compounding conditions were determined using this strategy. The outcomes from the DoE study were then applied to produce PPCN compounds for the subsequent study of thin-wall injection moulding, for which a novel four-cavity injection moulding system was designed using CAD software and a new moulding tool was constructed based upon this design. Subsequently, the effects of moulding conditions, nanoclay concentration and wall thickness on the injection moulded PPCN parts were investigated. Moreover, simulation of the injection moulding process was carried out to compare the predicted performance with that obtained in practice by measurement of real-time data using an in-cavity pressure sensor.

For the selected materials, the optimum formulation is 4 wt% organoclay (DK4), 4 wt% compatibiliser (Polybond 3200, PPgMA) and 1.5 wt% co-intercalant (erucamide), as the maximum interlayer spacing of clay, d_{001} (from XRD data), can be achieved in the selected experimental range. Furthermore, DoE investigations determined that a screw speed of 159 rpm and a feed rate of 5.4 kg h^{-1} are the optimum compounding conditions for the twin screw extruder used to obtain the highest tensile modulus and yield strength from the PPCN compounds.

The optimised formulation of PPCNs and compounding conditions were adopted to manufacture PPCN materials for the study of thin-wall injection moulding. In the selected processing window, tensile modulus and yield strength increase significantly with decreasing injection speed, due to shear-induced orientation effects, exemplified by a significantly increased frozen layer thickness observed by optical microscopy (OM) and Moldflow® simulation. Furthermore, the TEM images indicate a strong orientation of clay particles in the flow direction, so the PPCN test pieces cut parallel to the flow direction have 36.4% higher tensile modulus and 13.6 % higher yield strength than those cut perpendicular to the flow direction, demonstrating the effects of shear induced orientation on the tensile properties of thin-wall injection moulded PPCN parts. In comparison to injection speed, mould temperature has very

limited effects in the selected range investigated (25-55 °C), in this study. The changes in moulding conditions show no distinctive effects on PP crystallinity and intercalation behaviour of clay.

Impact toughness of thin wall injection moulded PPCN parts is not significantly affected by either the changes in moulding conditions or clay concentration (1-5 %). The SEM images show no clear difference between the fracture surfaces of PPCN samples with different clay concentrations. TEM and XRD results suggest that higher intercalation but lower exfoliation is achieved in PPCN parts with higher clay content. The composites in the thin sections (at the end of flow) have 34 % higher tensile modulus and 11 % higher yield strength than in the thicker sections, although the thin sections show reduced d_{001} values. This is attributed to the significantly enhanced shear-induced particle/molecular orientation and more highly oriented frozen layer, according to TEM, OM and process simulation results. In terms of the reduced d_{001} values in the thin sections, it is proposed that the extreme shear conditions in the thin sections stretch the PP chains in the clay galleries to a much higher level, compaction of clay stacks occurs as less interspacing is needed to accommodate the stretched chains, but rapid cooling allows no time for the chains to relax and expand the galleries back.

Overall, data obtained from both actual moulding and simulation indicate that injection speed is of utmost importance to the thin-wall injection moulding process, development of microstructure, and thus the resulting properties of the moulded PPCN parts, in the selected experimental ranges of this research.

Contents

List of figures

List of tables

List of symbols

A	Projected area of cavity and feed system
A_{cavity}	Projected area of cavity
C	Freeze-off constant
d_{001}	Interlayer spacing
Df	Degree of freedom
E	Tensile modulus
F	Clamp force
F_0	Dimensionless time
H	Channel depth
ΔH	Enthalpy of fusion
ΔH_{100}	Enthalpy of fusion for 100% crystalline polymer
H_{EFF}	Effective channel depth
K	Flow consistency index in power law
L	Channel length
$\dot{m}$	Extruder mass output
M	Screw torque
n	Power law index
ΔP	Melt pressure
Q	Volumetric output
t	Mould filling time
t_r	Time allowed for relaxation of the flow induced orientation
T_m	Melting point
T_g	Glass transition temperature
T_c	Crystallisation Temperature
Tf	Freeze off temperature
T_M	Mould temperature
T	Temperature increase at the die for single screw extrusion
U	Failure energy
U*	Normalised failure energy
W	Channel depth
α	Thermal diffusivity
$\dot{\gamma}$	Shear rate
η	Shear viscosity
η_0	Zero shear viscosity
θ	Dimensionless temperature
λ	Relaxation time of the material
σ^*	Yield strength
φ_S	Heat dissipation per unit volume

Abbreviations

AM	Short chain amide molecules
ANOVA	Analysis of variance
DMA	Dynamic mechanical analysis
DSC	Differential scanning calorimetry
OM	Optical microscopy
OMLS	Organic modified layered silicate
PE	Polyethylene
PEO	Poly (ethylene oxide)
PP	Polypropylene
PP-C	PP copolymer
PP-H	PP homopolymer
PPCNs	Polypropylene/clay nanocomposites
PPgMA	Maleic anhydride grafted polypropylene
PS	Polystyrene
PVE	Poly (vinyl ethylene)
PVP	Poly (vinyl pyrrilidone)
SEM	Scanning electron microscopy
TEM	Transmission electron microscopy
TME	Thermomechanical environment
XRD	X-ray diffraction

CHAPTER 1: INTRODUCTION

Nowadays, the uses and importance of plastics in our daily life is all encompassing. According to Plastics Europe[2], in 2015, the Europe and world plastics production reached 58 and 322 million tonnes respectively, and a turnover of more than 340 billion euros was achieved by the European plastics industry. Among the great number of plastics, polypropylene (PP) is the second most important commercial thermoplastic, which is used in a wide variety of applications including textiles, stationery, reusable containers, plastic parts and many others.[3] As one of the five major commodity plastics, it has a great global market. It is reported that the global production of PP hit 61.7 million tonnes in 2015.[4]

In recent years, PP nanocomposites are of great interest to many researchers for their significantly enhanced properties. In the family of PP nanocomposites, PP/clay nanocomposites (PPCNs) have become the most common type and they are of great potential importance in a number of applications, if the ongoing research activity can be translated into commercial product.

1.1 PP/Clay Nanocomposites and Processing Methods

PP/clay nanocomposites (PPCNs) have enormous potential for use in many industrial sectors such as the automotive and packaging industries, for their excellent processibility, low cost and potential enhance to physical and chemical properties relative to the conventional unfilled PP materials. The addition of clay can dramatically improve the mechanical properties of pristine PP by forming nanostructures, which is the essential difference between a nanocomposite and a conventional composite. The enhancing effects of clay in PP are completely determined by the nano-scale structures formed, i.e., intercalated or exfoliated structures. Intercalated structures are formed when PP chains diffuse into the clay interlayer galleries and expand the interlayer spacing, resulting in a well ordered multilayer structure of alternating polymeric and inorganic layers. Exfoliated structures are achieved when the layered silicates are completely fragmented into smaller individual sheets and homogeneously dispersed in the continuous PP matrix.

Therefore, the study on the dispersion of clay in the continuous PP matrix is of great importance to optimise the performance of PPCNs.

There are several factors that can influence whether intercalation or exfoliation of clay in PP matrix occurs, such as the chemical modification on the nanoclay surface, the use of compatibilisers and the incorporation of co-intercalants.[5–12] For a selected system, such as PP/nanoclay/compatibiliser/co-intercalant, the concentration of each ingredient plays an important role in clay dispersion and thus the mechanical properties of PPCNs fabricated, which highlights the importance of optimising the formulation. Although extensive studies have been done on the preparation and properties of PPCNs, less attention has been focused on the optimisation of PPCN formulation.[13,14] As the very first step to formulate PPCNs, compounding or mixing is a critical stage to determine the dispersion behaviour of clay in the PP matrix. Several studies have reported the effects of compounding conditions on the clay dispersion in PP matrix[15–18], but very few of them tried to optimise the operative processing parameters for any compounding equipment to achieve the optimum dispersion of clay. Thus, it seems that there have not been any important studies focused on the optimisation of formulation and compounding conditions for PPCNs.

The compounded PPCNs are normally processed into final PPCN products by other plastic moulding techniques, such as injection moulding which is one of the most common processing methods for commercial thermoplastics. As the polymer melt is injected into the designed cavity very rapidly, high shear rate and shear stress are generated during the injection moulding process. This leads to molecular and particle orientation, by which the mechanical properties of injection moulded parts are highly affected. For that reason, injection moulding process conditions have certain effects on the injection moulded parts.[19–21] In addition to the choice of polymer and processing conditions, cavity wall thickness is also a key factor determining the orientation of polymer chains and clay platelets, because a thin-wall structure generates extremely high shear rate and shear stress during the unsteady and non-isothermal moulding filling stage, followed by a rapid but inhomogeneous cooling.[22–24] High shear stress and inhomogeneous, rapid cooling strongly promote the orientation effects and residual stress, and thus affect the mechanical properties of the final PP/clay nanocomposite products.[24,25] Flow and cooling processes are highly complex and the resulting microstructures are difficult to predict. Additionally, the

incorporation of clay into PP and its concentration have significant effects on the developed morphology of injection moulded PPCN parts.[26] Although in the recent past, some work has been done on the effects of injection moulding conditions, cavity geometries and clay concentration[26–29], very limited data are available for thin-wall injection moulding of PPCNs.

Based on the discussion above, it is clear that the compound formulation, compounding conditions, injection moulding conditions, wall thickness of an injection mould and clay concentration in injection moulded components can have significant effect on the mechanical properties of PPCNs manufactured. However relatively little work has been published that considers all these aspects for the same set of formulations. In this project, those factors mentioned above will be investigated thoroughly, since the existing literature focused on the translation of nanocomposite formulation/synthesis into bulk commercial compounds/products is relatively sparse.[29–31]

1.2 Novelty of This Research Project

When conducting studies on multi-factor systems such as optimising PPCN formulations or processing conditions, there are quite a few independent and response variables to study and consider. Therefore, it is critical to link and subsequently to predict the quantitative relationships between them. Design of Experiments (DoE), a powerful statistical technique, is particularly useful when dealing such multi-factor systems. It is defined as a test or series of tests in which purposeful changes are made to selected input variables of a process so that corresponding changes in the output responses may be observed and identified.[32] By using the DoE approach, the output information can be maximised with minimum number of experiments, and quantitative predictive models as well as 3D ‘visual’ trends can be obtained.

Although some studies have been reported on PPCN formulations and compounding conditions, it is still very rare to see the DoE statistical approaches employed in published studies. In this study, the DoE statistical approach was employed to analyse and optimise the formulation of PPCNs. Additionally, by using this strategy,

the large-scale compounding (twin-screw extrusion) and small-scale compounding (batch mixing) processes were investigated and compared, and the processing conditions for each technique were optimised. This experimental strategy contributes to the novelty of this research project, especially in the early, pre-moulding stages to determine optimum formulations and mixing conditions.

Another highlight of this research project is to apply the outcomes from the powerful statistical technique, DoE, to study thin-wall injection moulding. A four-cavity injection moulding system was designed using CAD software and a new moulding tool was constructed based upon the design, accommodating cooling channels, ejection systems and facilities for in-cavity pressure measurement. Also, injection moulding process simulation was carried out using Autodesk Moldflow software package, in order to compare predicted performance with that obtained in practice by the in-cavity pressure sensor. Emphasis is therefore being placed on the mechanical properties obtained from these components, investigating the effects associated with localised effects in thin-wall sections.

1.3 Aims, Objectives and Work Plan

The overarching aim of this research programme is to gain a comprehensive understanding of clay dispersion state and polypropylene structure development in polypropylene/clay nanocomposites (PPCNs), from melt compounding of modified clays with co-agents and polypropylene through to mechanical property of thin wall injection moulded PPCN parts.

On the basis of the overarching aim, a set of general aims have been defined for this research as below:

1. Optimise PPCN formulation with the aid of DoE to achieve optimum clay dispersion in the continuous PP matrix.

2. Investigate and compare twin-screw extrusion and batch mixing processes using a DoE approach and then optimise processing conditions for each technique.

3. Perform injection mould design with the aid of CAD software, and construct a new mould tool upon this design.
4. Apply the outcomes from the DoE studies above to thin-wall injection moulding and then investigate the effects of processing conditions, wall thickness and clay concentration on moulded PPCN components.

5. Perform real-time injection moulding simulations using Moldflow® Synergy, in order to compare predicted performance with that obtained in actual moulding.

This research has been divided into six work packages, to make sure it is carried out clearly and orderly. The work packages are shown in a flow chart below.

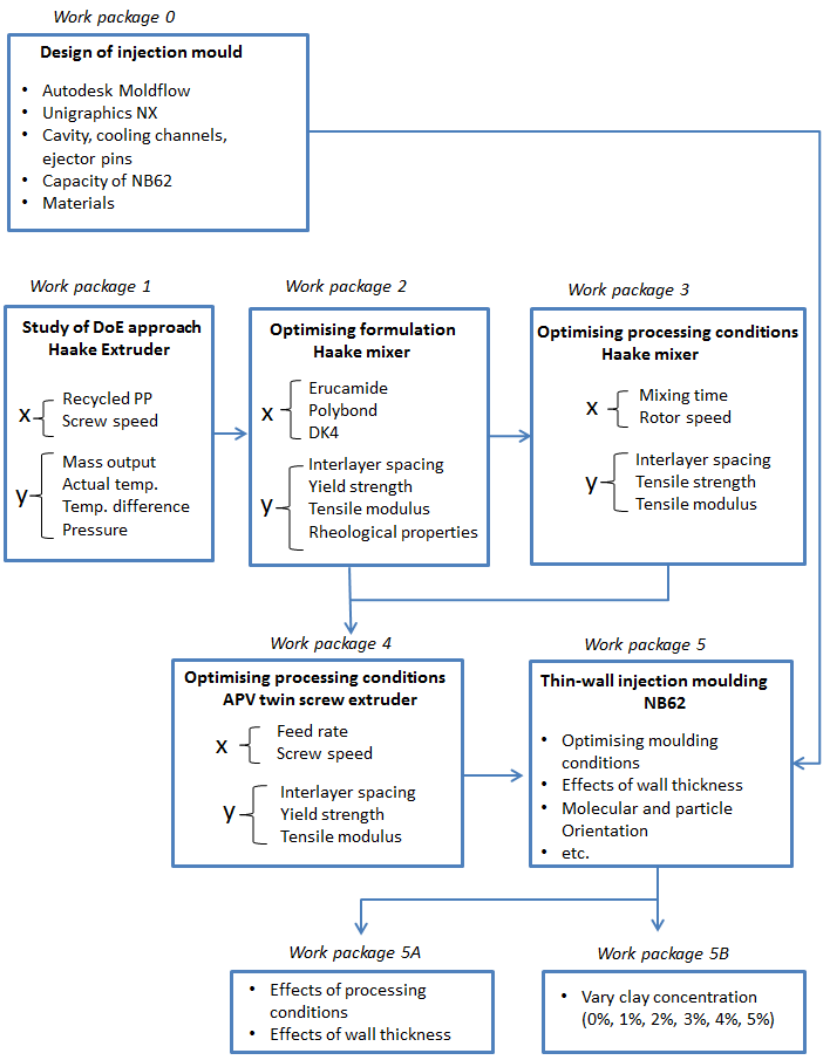

Figure 1.3-1 Proposed work packages

The work packages can be further subdivided into a number of more specific research tasks (objectives), which are formed into a project Gantt chart as shown in Figure 1.3-2:

Task List:

1. Design test products and an appropriate new mould cavity design for thin wall injection moulding, using computer-aided design (CAD) software techniques.
2. Use dynamic flow analysis (Autodesk Moldflow Synergy) to analyse flow of PP and nanocomposites into the test mould, to optimise its design, processing conditions and materials selection.
3. Construct a new moulding tool based upon the chosen design, accommodating cooling channels, ejection systems and facilities for in-cavity, real-time pressure measurement.
4. Investigate single screw extrusion with Thermo Fisher single-screw extruder using a DoE approach, to learn and understand DoE and its underlying statistical principles.
5. Characterise the selected raw materials and also produce shear flow curves of PP over a wide range of shear rate, in order to investigate the flow of PP during injection moulding process.
6. Optimise the compound formulations with Thermo Fisher Haake twin rotor mixer (batch mixing) using a DoE approach
7. Study the properties of PPCN samples prepared by the different compounding techniques (twin screw mixing vs. batch mixing) using a DoE approach, to compare the different mixing techniques and find out optimum processing conditions for each.
8. Produce PPCN compounds using the optimised formulation and compounding conditions and set up the injection moulding machine (injection stroke, shot size, packing pressure, packing time etc.) for the subsequent study.
9. Perform thin-wall injection moulding with the designed mould tool under the selected different moulding conditions, and collect in-cavity pressure data measured by the Kistler pressure sensor installed.
10. Investigate the properties of PPCN parts moulded under different conditions, to explore the effects of moulding conditions

11. Investigate the properties of the thin and thick sections of injection moulded PPCN parts, to understand the effects of cavity wall thickness
12. Compound PPCNs with difference clay concentrations under the optimised conditions and then perform thin-wall injection moulding and investigate the properties of moulded parts to reveal the effects of clay concentration
13. Compare the predicted data from real-time simulation with that obtained in actual moulding process, to investigate the discrepancy and possible reason.
14. Write up PhD thesis

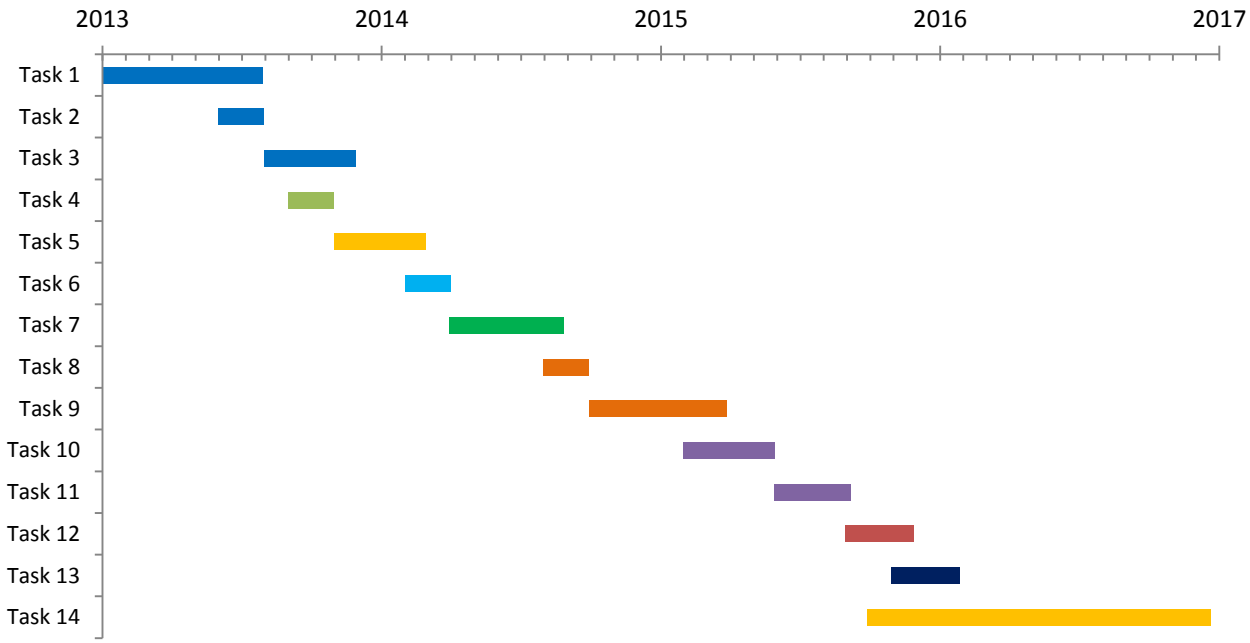

Figure 1.3-2 Research project timeline

CHAPTER 2: LITERATURE REVIEW

Firstly, this literature review presents an overview of PP/clay nanocomposites, and the emphasis is placed on the factors that determine the intercalation/exfoliation of clay particles in PP matrix and the effects of additives on the properties of PP/clay nanocomposites.

The second section addresses polymer processing technology. Two processing techniques, extrusion and injection moulding, are covered in this review. Real-time injection moulding simulation software, Moldflow® Insight, is also introduced, as it will be employed to perform simulation experiments in this research programme. Due the fact that polymers are processed in the melt-state in most polymer processing techniques, polymer melt rheology is presented first in this section.

The last section focuses on the statistical approach to experimental design, specifically Design of Experiments (DoE), as it will be widely used throughout this research programme. In this section, the underlying statistical principles behind the DoE approach are presented in detail. The DoE software package, Design Expert®, is also briefly introduced.

2.1 Polypropylene/Clay Nanocomposites (PPCNs)

2.1.1 General

Nowadays polymer nanocomposites have gained enormous academic and industrial research interest, because the mechanical properties of polymers can be dramatically improved via the addition of nanofillers at very low additive levels.[33–41] Since the pioneering work on nylon 6/clay nanocomposites was first reported in the 1990s [42,43], polymer/clay nanocomposites have always been an important class within the nanocomposite family and have attracted wide interest in academia.[44–49]

During the past two decades, polyamide (nylon)/clay type nanocomposites have been thoroughly investigated and an important progress is reported.[50–54] In addition to PA/clay nanocomposites, polypropylene (PP)/clay nanocomposites today also play an important role in the domain of these advanced materials. PP, as one of the

most successful and prolifically used commercial plastics, possesses many major advantages such as excellent processability, low cost, low density, high thermal stability, and a good balance of chemical and physical properties. The incorporation of nanoclay into PP to form nanocomposites can further expand its performance envelope.[7,11–14,55–57] Therefore, PP/clay nanocomposites (PPCNs) have enormous potential for use in many industrial sectors such as the automotive and packaging industries.

It was recently reported that the global PP industry experienced growth over the last five years and is expected to continue its growth momentum, reaching approximately 92 billion US dollars in 2017. The Compound Annual Growth Rate (CAGR) is predicted to be 3.7 % over the next five years. Rising demand in end-user markets such as packaging, automotive and construction are expected to drive the industry.[58]

In nanocomposites, the clay is often in the form of agglomerated tactoids, and dispersion of the clay into individual tactoids and individual platelets is difficult in most polymers. Intercalation and exfoliation of the clay particles into individual platelets is further hindered by the intrinsic incompatibility of hydrophilic clay and hydrophobic polymers. There are several ways to improve the dispersion of clay in PP matrix, such as modification of clay and incorporation of compatibiliser. These are presented and discussed in the later sections, where the characterisation of polymer/clay nanocomposites is also covered.

Compounding is the very first step to formulate PPCNs by large scale melt-state processing with the chosen additives including compatibiliser and co-intercalant, and will determine the dispersion, intercalation and exfoliation behaviour of clay in the PP matrix. Injection moulding is potentially the most important processing method for PPCN components. Mould cavity wall thickness is a key factor determining the thermo-mechanical environment during non-isothermal shear flow, and therefore the orientation of polymer chains and clay nano-particles is potentially very important. Therefore, polymer rheology, extrusion, injection moulding are covered in this literature review.

Design of experiments (DoE) is a powerful statistical tool for ‘quality control and improvement’, which is widely used in many scientific disciplines to investigate multi-factor systems or processes. A DoE approach can maximise information gained with

minimum resources or experimental time. As DoE approach is highly involved in this research project, it is thus presented in the later sections.

2.1.2 Polypropylene (PP)

A polymer is known as a large molecule composed of many repeated subunits. The arrangements of these units, the types of chains that can be synthesised, and the shapes that the chains can form themselves into, allow polymers to possess an enormous and intriguing range of properties, and play an essential and ubiquitous role in our daily life. The large number of natural and synthetic polymers can be classified in several ways, such as by origin, thermal behaviour, chain structure, polymerisation mechanism, *etc*.[59]

Among the great number of different polymers, polypropylene (PP) is one of the most successful commercial thermoplastics. It has a vast variety of applications such as packaging, automotive components, stationery, reusable containers, laboratory equipment, construction *etc.* PP is the second most important plastic and has a great global market and rising demand.[58]

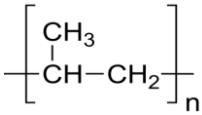

Figure 2.1-1 The repeating unit of PP

Figure 2.1-1 shows the repeating of PP. Clearly, the propylene monomer is asymmetrical in shape as a methyl group is attached to one of the backbone carbon. This asymmetric nature of propylene monomers, due to the presence of methyl groups, creates several possibilities to link them together into polymer chains and give rises to regio-isomers and stereo-isomers in the PP chains.

The type of propylene insertion determines the formation of regio-isomers. The tertiary carbon with methyl group on it is referred to as the ‘head’, while the other olefinic carbon as the ‘tail’ of the monomer. ‘Head-to-tail’ sequence, which gives a high chemical regularity of the PP chain, is the most common insertion type, due to the steric effect of the methyl group.[60]

Considering the chain to be stretched out in its fully extended zigzag planar conformation, different configurations are possible, as the methyl group may be situated on either side of the plane. Isotactic PP, in which all the pedant methyl groups are on the same side of the zigzag plane, results from polymerisation of only one isomeric configuration from propylene monomer. Syndiotactic PP is defined by methyl groups arranged alternatively on either side of the zigzag chain, which is obtained by alternative addition of the two stereo-isomeric configurations from propylene monomer. A random sequence of pedant methyl groups along the chain provides little or no symmetry, leading to atactic PP. Figure 2.1-2 shows the three types of stereo-isomers of PP.

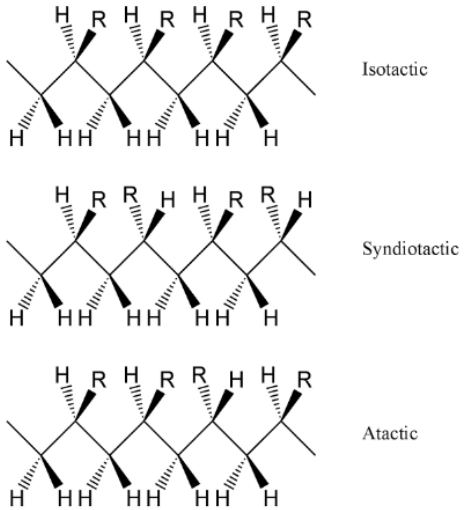

Figure 2.1-2 Isotactic, syndiotactic and atactic PP chains[61]

Rotation around the backbone bonds is direction-dependent, due to the presence of the asymmetrically substituted methyl groups. Stable and specific confirmations are induced by the stereo-isometric configurations: 3_1 helix for isotactic PP, 2_1 helix for syndiotactic and a random conformation for atactic PP.[60] The structural regularity of isotactic and syndiotactic chains promotes crystallisation by a parallel organisation of chain segments issued from the same chain or the chains in the vicinity. The random isotactic/syndiotactic placements in atactic PP lead to an irregular knobbly helical chain that cannot pack into a crystal lattice, causing atactic PP to be amorphous.

Most commercial polypropylene is isotactic and has an intermediate level of crystallinity about 70 %, which is between that of low-density polyethylene (LDPE) and high-density polyethylene (HDPE).[60] Generally, perfectly isotactic PP has a melting point of 171 °C and commercial isotactic PP usually has a melting point

around 160 °C, depending on crystallinity. Syndiotactic PP has a crystallinity of 30 % and a melting point of 130 °C.[60]

In terms of polymer composition, there are three general types of PP: homopolymer, block copolymer and random copolymer. PP homopolymers, which are more rigid and have better resistance to high temperature than PP copolymers, are made by polymerising propylene monomers in the presence of a stereospecific catalyst. The typical applications of PP homopolymers include housings for domestic appliances, windshield washer tanks, automotive interior fabrics, etc.[62]

Random PP copolymers contain 1.5% to 6% by weight of ethylene or higher olefin units that are randomly distributed among the propylene units. The ability to crystallise is reduced by the presence of ethylene, resulting in improved impact strength and clarity, and a wider range of sealability. Random PP copolymers have a lower melting point and specific gravity than the PP homopolymers, due to the reduced crystallinity. Therefore, random PP copolymers are attractive for injection moulded houseware, thermoforming and films, and can be used to replace PVC, PS and PET in food packing and stationary applications.[62]

PP block copolymers are obtained by copolymerising PP homopolymer with ethylene. The ethylene content in block copolymers is much higher than the random copolymers. The essential difference between a random and a block copolymer is that the block copolymer contains a separate dispersed rubber phase (core-shell structure) within the PP matrix (see Figure 2.1-3). A copolymerised PP block copolymer consists of a PP matrix, a series of crystallisable ethylene-propylene copolymers, amorphous ethylene-propylene random copolymer (EPR) and a small amount of pure PE.[63] Tong *et al.*[64] point out that the crystallisable ethylene-propylene copolymers can be further divided into ethylene-propylene segmented copolymer with a short sequence length of PE and PP segments (PE-s-PP), and ethylene-propylene block copolymer with a long sequence length of PE and PP blocks (PE-b-PP), and they participate differently in the formation of multi-layered core-shell structure of the dispersed phase. PE-s-PP (like PE) constructs inner core, ethylene- PE-b-PP forms outer shell, and intermediate layer is resulted from EPR.

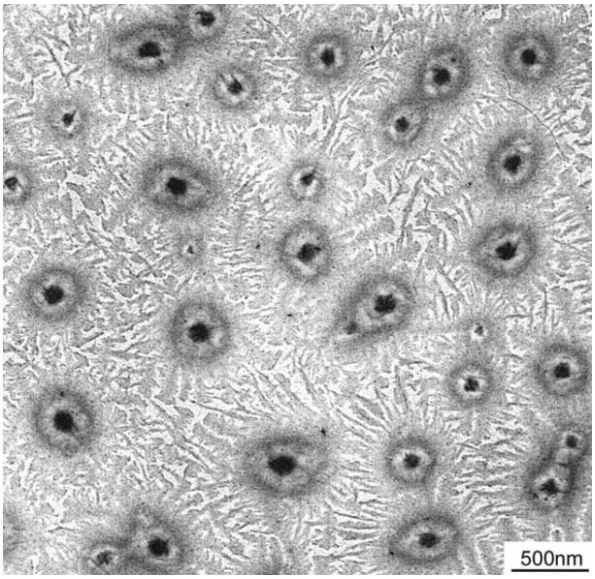

Figure 2.1-3 TEM Bright field image of a solution-cast film of PP block copolymer[64]

Due to the presence of dispersed rubber phase, PP block copolymers can withstand higher impact even at low temperatures in comparison to PP homopolymers but at the expense of transparency and softening point. This makes PP block copolymers suitable for containers for refrigerated or frozen products, and they are also widely used to make suitcase shells, crates, boxes and automotive parts. In this research project, both PP-H and PP-C are used to make PPCNs.

PP is vulnerable to chain degradation from exposure to heat and UV radiation such as that present in sunlight. Oxidation usually occurs at the tertiary carbon atom present in every repeat unit, where a free radical is formed and then reacts further with oxygen, resulting in chain scission to yield aldehydes and carboxylic acids. Therefore, for external applications, UV-absorbers must be added. Oxidation of PP also occurs at high temperatures, which is a common problem during moulding operations. Thus, anti-oxidants are normally added to prevent the material from degrading.[60] The incorporation of clay into pristine PP has some effects on PP stability, and this will be discussed later. Clay and its dispersion in polymers are to be presented next, in the review.

2.1.3 Clay and Its Dispersion in Polymers

The clay used in polymer nanocomposites is actually a layered silicate, which are natural or synthetic minerals. The pristine layered silicates have a dioctahedral or

trioctahedral structure, and the basic building blocks are tetrahedral sheets. Negative charges on the layers are generated due to the substitution of Si^{4+} by Al^{3+} in tetrahedral positions and Al^{3+}, or Fe^{3+} by Mg^{2+} or Fe^{2+} in octahedral positions, and the excessive negative charges generated are balanced by alkali or alkali earth cations in the interlayer space, which are usually hydrated Na^{+}, K^{+}, Ca^{2+} and Mg^{2+}.[65] Obviously, the thin sheets of layered silicates are bound together with counter-ions by electrostatic forces. In actual fact, a wide variety of organic cations, such as alkylammonium ions, can be introduced by exchange reaction, which can increase the compatibility between the clay and the hydrophobic polymer matrix such as the Cloisite series from Southern Clay.[66]

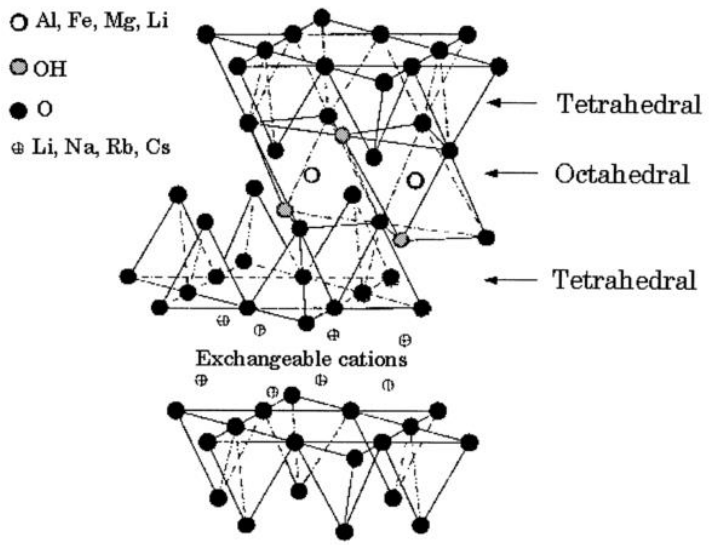

Figure 2.1-4 The structure of layered silicates[67]

There are different types of clay, as the structure/composition of layered silicates varies slightly, montmorillonite and bentonite are the most widely used clay minerals. Montmorillonite, named after Montmorillon in France, is a very soft phyllosilicate mineral and typically forms in microscopic crystals. Bentonite is named by Wilbur C. Knight and is essentially a impure clay consisting mainly of montmorillonite.[68]

According to the dispersion of clay in polymer matrix, polymer composites can be classified into three main types. They are (conventional) micro-composites, intercalated nanocomposites and exfoliated nanocomposites.

(A) In micro-composites, phase separation occurs due to the poor compatibility between the clay and the polymer matrix. In this case, the addition of clay is unlikely to improve any mechanical properties of the polymer, because the weak

interface cannot transfer the load from the matrix to the filler effectively. Furthermore, the existence of weak interface may function as defects in the continuous polymer matrix, which weakens the mechanical properties of the composites. Conventional polymer/clay composites are typical micro-composites.

(B) Intercalated structures are formed when the polymer chains diffuse into the clay interlayer galleries. In this case, the d-spacing of the clay can be increased by around 2-3 nm or more due to the intercalation of polymer chains, and a well ordered multilayer structure of alternating polymeric and inorganic layers is formed. [67,69–72]

(C) Exfoliated structures are obtained when the layered silicates are completely broken down into individual platelets and homogeneously dispersed in the continuous polymer matrix.[67,69,71,72] In this case, the interspacing of clay platelets are separated by 8-10 nm or more.[70]

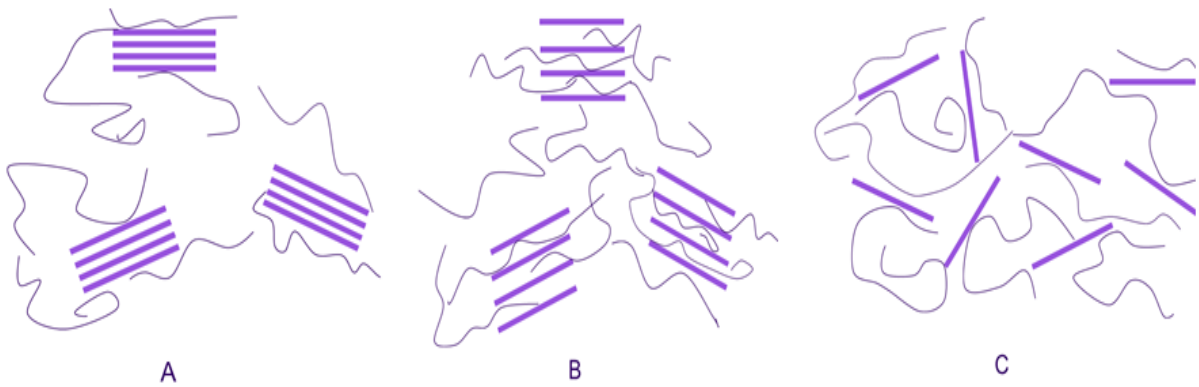

Figure 2.1-5 Clay dispersion in polymer matrix: A) Immiscible, B) Intercalated and C) Exfoliated structures

The exfoliated or intercalated structures are of particular interest, because they bring polymer/clay composites into the nano-scale category, hence the term polymer/clay nanocomposites. It makes the entire clay surface available for attraction to the polymer and, also, maximises the polymer-clay interactions, resulting in the most significant improvement in mechanical and physical properties.[65,73] Normally, it is believed that exfoliated structures can provide further enhancement in properties relative to intercalated structures, due to increased polymer-clay interaction hence increased interfacial area.[72,74,75]

There are six characteristics distinguishing polymer/clay nanocomposites from conventional ones, and they are attributed to the nanoscopic dimensions and the extreme aspect ratios of layered silicates. These characteristics are:[76]

- Low percolation threshold (ca. 0.1-2 vol.%)
- Particle-particle correlation (orientation and position) arising at low volume fractions.
- Large number of particles per particle volume (10^6-10^8 particles/μm^3).
- Extensive interfacial area per volume of particles (10^3-10^4 m^2/ml).
- Short distances between particles (10-50 nm at ~ 1-8 vol.%).
- Comparable size scales among the rigid nanoparticle inclusions, distance between particles, and the relaxation volume of polymer chains.

To obtain effective polymer/clay nanocomposites, at least two significant issues need to be solved first. The first issue is to separate the clay platelets within tactoids by polymer migration and to broaden their interlayer spacing, and eventually separate individual clay sheets apart. The second one is to enhance the interfacial interactions and improve the compatibility between the clay sheets and the polymer matrix, because intercalation/exfoliation of clay is significantly affected by the compatibility between clay particles and the polymer matrix. Pristine clay platelets have hydrophilic surfaces while many of polymers are hydrophobic e.g. PP, thus, their compatibility is very poor, leading to unsatisfactory clay dispersion. To improve the compatibility, clay surface can be chemically modified with organic cations, alkylammonium ions are most commonly used. [67,77] As a result of chemical modification, the dispersion of clay in polymer matrix such as PP, is significantly improved.[55,78–80]

In actual fact, for non-polar polymers like PP, the modification of clay is far from sufficient to a high level of dispersion, because the difference in polarity of molecules restricts the compatibility. In order to further improve the compatibility and the dispersion of clay in polymers, compatibilisers and co-intercalants can be used.[11,12,56,81,82] For PP/clay nanocomposites, clay modification, incorporation of compatibilisers and co-intercalants, and mixing effects are thought to be the most significant factors that determine the dispersion of clay,[65] and they are thoroughly discussed in the a later section (2.1.6). As a matter of fact, it is difficult to achieve

complete exfoliation for polymer/clay nanocomposites especially when the polymer matrices are non-polar. The majority of the polymer nanocomposites reported in the literature were found to be partially exfoliated, which indicates that the clay particles are in a state that is between intercalation and complete exfoliation.[72]

2.1.4 Characterisation of Polymer/Clay Nanocomposites

(A) X-ray diffraction (XRD)

Due to its ease of use and availability, X-ray diffraction (XRD) is widely used to characterise the nano-structures in polymer nanocomposites. It is widely used for determination of basal spacing (d_{001}) and thus the space between structural layers, which is known as the interlayer spacing (d_{IL}). It is also occasionally used to study the kinetics of polymer melt intercalation. [65,83] Figure 2.1-6 illustrates the importance spacings in layered silicate.

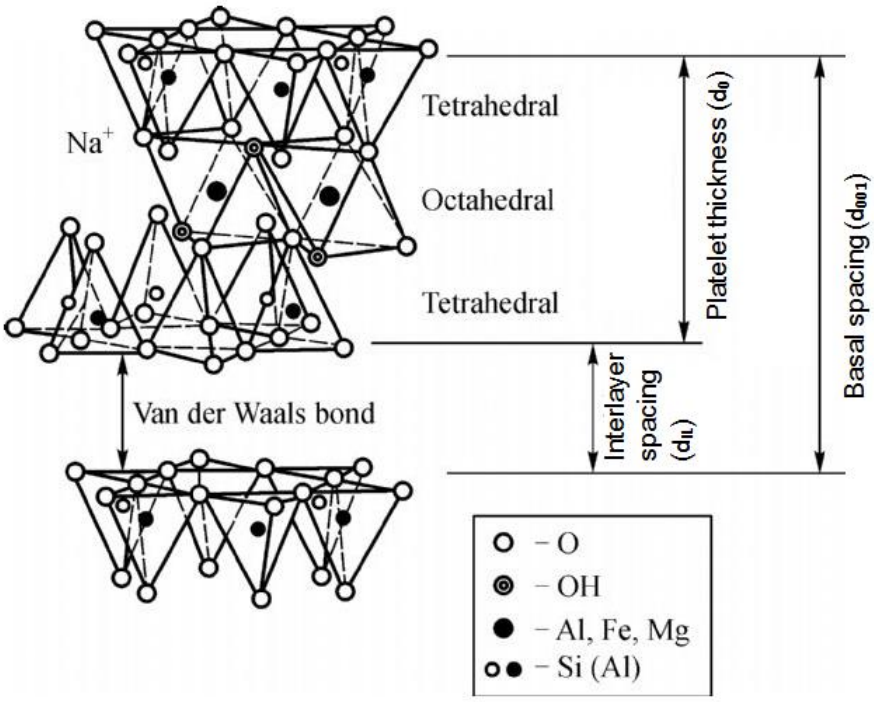

Figure 2.1-6 Important spacings in layered silicate[84]

The basal spacing (d_{001}) can be calculated according to the XRD patterns obtained, utilising Bragg's law:

$$2d \sin\theta = n\lambda, \tag{2.1-1}$$

where d is the distance between diffractional lattice planes, θ refers to the measured diffraction angle and λ is the wavelength of the X-ray used. A montmorillonite platelet is typically 0.95 nm thick, the interlayer spacing (d_{IL}) can thus be roughly estimated by the equation below.

$$d_{IL} = d_{001} - 0.95 \tag{2.1-2}$$

By monitoring the characteristic features of XRD patterns, such as peak position, intensity, shape and the presence of higher order reflections, the composite structure may be identified.[83]

Figure 2.1-7 shows some typical XRD patterns. For immiscible composites, the layered structure of clay is not affected when it is incorporated into the polymers. Therefore, the characteristics of the clay in the immiscible composites do not change compared to those of the original clay. On the other hand, in intercalated nanocomposites the polymer chains diffuse into the interlayer galleries and the interlayer spacing is expanded. As a result of that, the characteristic peak shifts towards a smaller angle, indicating an increase in d-spacing according to Bragg's law. Although the interlayer spacing is increased in intercalated nanocomposites, the repetitive multilayer structure is preserved, which allows the interlayer spacing to be determined by XRD. However, for the third type of polymer nanocomposites, no diffraction peaks can be seen in the XRD diffractograms. This is because multi-layered clay stacks break down into individual clay sheets in the nanocomposites, leading to a large interlayer spacing over 8 nm, and there is no ordering in the nanocomposites at all. [65,67,73,85] However, completely exfoliated structure shown as (c) is Figure 2.1-7 is 'theoretical', and is rarely achieved in practice.

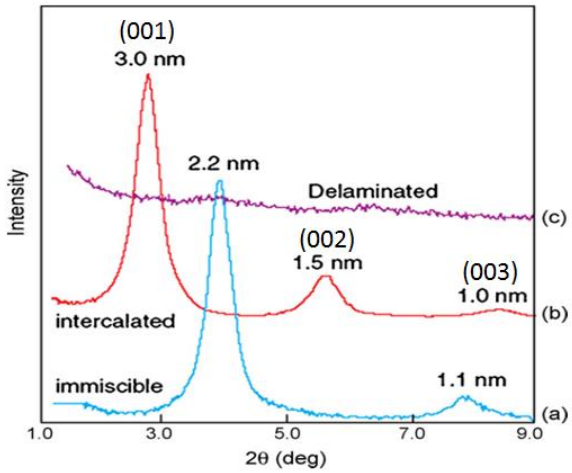

Figure 2.1-7 Typical XRD patterns from polymer/clay nanocomposites: (a) immiscible structure, (b) intercalated structure, (c) exfoliated or delaminated structure.[65]

A 'full-width-at half-maximum' (fwhm) parameter and intensity of the diffraction peaks can be used to monitor the influence of intercalation on the layered structure of clay. Peak broadening and intensity loss indicates that a system becomes more disordered, that is to say, a decrease in the degree of coherent layer stacking. On the other hand, peak sharpening and increased intensity suggest a better ordered multilayer structure.[85]

Vaia and Liu[86] point out that XRD data of polymer/layered silicate nanocomposites contain a wealth of information, not only on interlayer spacing but also on the extent of layer correlation, such as stack size and stacking disorder of the layers. The decreased size of the coherent stacks reduces the magnitude of the observed basal reflections, and also broadens the basal reflections at high 2θ, such as (002) and (003) reflections. In contrast to stack size, which uniformly reduces the intensity of all interference, the increased internal disorder of the stack reduces and broadens the higher order basal reflections significantly more than (001).

(B) Transmission Electron microscopy (TEM)

Although XRD is very helpful to characterise the nano-structures of clay formed in polymer matrices, it provides only limited information. Neither spatial distribution nor structural inhomogeneity can be detected by XRD, also, peak broadening and intensity loss can be very difficult to study systematically if the diffraction pattern is

not well defined initially. Moreover, XRD traces usually show large background scattering at low 2θ, due to parasitic scatter from the sample holder and direct exposure of the detector to the incident beam. This may mask some characteristic peak in this range. Therefore, the analysis is unreliable if it is based solely on the information from XRD patterns. As a complementary technique in a localised area, transmission electron microscopy (TEM) can provide qualitative information on the internal structure, morphology and defect structures, and it can also be quantitative for measuring larger spacings and for image analysis. [87–90]

Heavier elements appear darker in bright-field images compared to lighter elements. Silicate sheets are composed of Al, Si and O, which are much heavier than C, H and N from which the interlayer and polymer matrix are composed. Therefore, in nanocomposites, the cross sections of silicate sheets are seen as dark lines on TEM, which are around 1 nm thick.

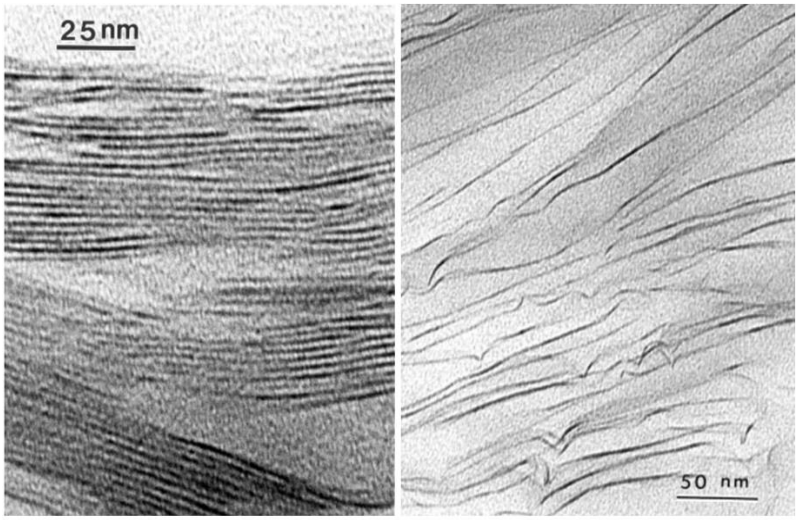

(a) (b)

Figure 2.1-8 TEM micrographs for polystyrene/clay nanocomposites: (a) intercalated structure, (b) exfoliated structure.[88]

The figure above shows typical TEM micrographs for nanocomposites with an intercalated structure and exfoliated structure, respectively. As mentioned previously, it is difficult for clay to achieve complete exfoliation in polymer matrices, and in many cases, semi-exfoliation is obtained, which means the clay is partially intercalated and partially exfoliated. The figure below shows a typical partially-exfoliated structure.

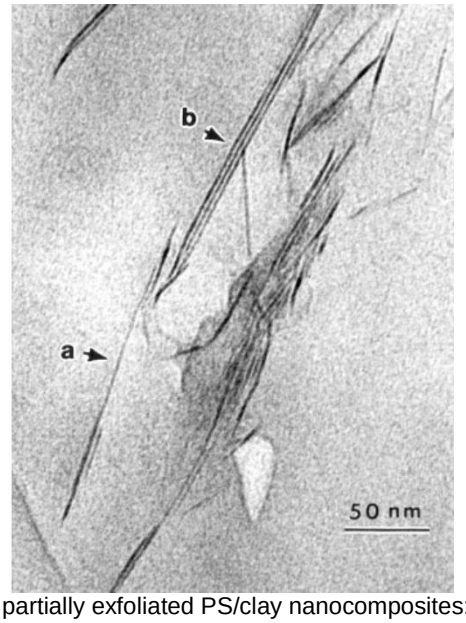

Figure 2.1-9 TEM micrographs for partially exfoliated PS/clay nanocomposites: (a) exfoliated single layers, (b) intercalated clay layers.[88]

XRD and TEM are extensively used in combination to characterise the nano-structures existing in polymer/clay nanocomposites. Additionally, there are also some other techniques that are often employed for the characterisation of polymer/clay nanocomposites, to provide complementary information. These techniques will be briefly presented next.

(C) Differential scanning calorimetry (DSC)

Differential scanning calorimetry (DSC) is also useful in providing further information on intercalation. As the intercalated polymer chains have strong interactions with the surface of clay sheets, their mobility is thus significantly reduced. As a result, the energy threshold required for glass transition is elevated, leading to an increase in glass transition temperature (T_g), which is readily detected by DSC. PP is a semi-crystalline polymer and has a low Tg. Therefore, this technique may provide complementary information on the clay dispersion in PP matrices.

The figure below illustrates DSC traces of PS, a physical mixture of PS and organic modified layered silicates (OMLS), and an intercalated nanocomposite.

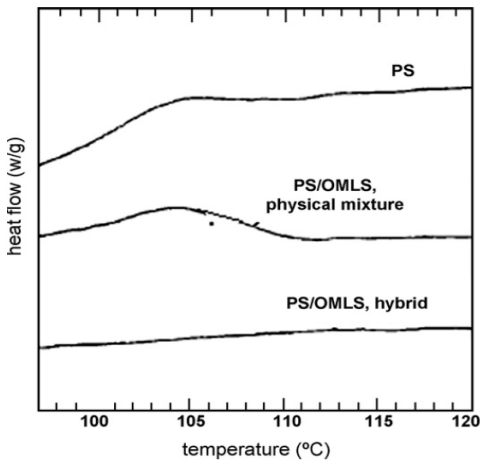

Figure 2.1-10 DSC traces for pure PS, a physical mixture of PS/OMLS, and an intercalated PS/OMLS nanocomposite. [77]

According the DSC traces above, it is clear that both the pure PS and the mixture of PS/OMSL display the characteristic peak due to glass transition of PS, while the intercalated PS/OMSL shows no characteristic peak in this temperature range. The peak in the mixture indicates that the interactions between the PS and the OMLS are absent or negligible. On the other hand, the peak for the nanocomposite is absent within this temperature range, but actually occurs at a higher temperature. This reveals the strong interactions between the matrix and the OMLS. Furthermore, the large increase in glass transition temperature (T_g) is of great importance, because it allows the nanocomposite to maintain its rigidity at even higher temperatures compared to the original polymer. This certainly extends the range of potential applications greatly.[77]

(D) Scanning electron microscopy (SEM)

Scanning electron microscopy (SEM) is often used to examine morphology of the fracture surface of polymer/clay nanocomposites. The information provided by SEM is typically at the micro-scale, but a modern SEM can resolve at the 10-100 nm scale with relative ease. Figure 2.1-11 shows a typical SEM observation of the fracture surface of polymer/clay nanocomposites. In the figure, the clay aggregates are pointed out. This kind of information obtained from SEM images is of great importance when analysing the impact properties of polymer/clay nanocomposites, post-failure.

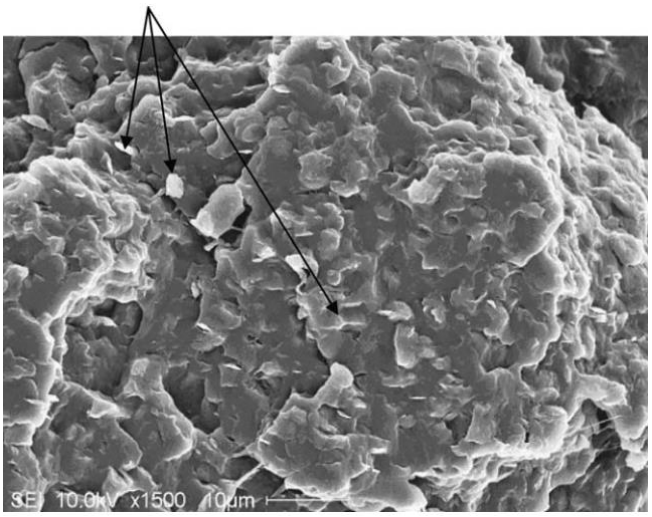

Figure 2.1-11 SEM observation of PP/clay nanocomposites[91]

(E) Fourier transform infrared (FTIR) spectroscopy and ^{13}C solid-state nuclear magnetic resonance (^{13}C NMR)

Fourier transform infrared spectroscopy (FTIR) is also helpful when investigating nanocomposite structures.[92,93] The bonding in a mixture and that in a nanocomposite are different, and this difference may be identified by FTIR. However, at the moment, FTIR is not completely reliable in most cases, because the vibrations involved due to the formation of intercalation are difficult to detect.[94] FTIR is thus more useful for characterisation of organically modified clay than the nanocomposites themselves. For instance, valuable insight into the state of order organic modifier alkyl tails can be obtained with the aid of FTIR in the work reported by Liauw *et al.*[95]

Additionally, ^{13}C solid-state nuclear magnetic resonance (^{13}C NMR) was first employed by Van der Hart *et al*. to investigate the level of clay exfoliation in nanocomposites, which is one of the most important parts of nanocomposite characterisation. [96] Measuring longitudinal relaxation, T^1s of proton (and ^{13}C nuclei) with the quality of clay dispersion is the main objective in solid-state NMR measurement. [83,97,98]

Overall, TEM and XRD are the primary techniques for polymer/clay nanocomposite characterisation, and the other techniques, (such as NMR, FTIR and DSC) may also provide very useful complementary information. Indeed, rheological, mechanical and thermal testing can also indicate the dispersion of clay in nanocomposites to some

extent, because better clay dispersion normally results in improved mechanical properties. However, these tests focus on the properties of nanocomposites and can only provide very limited information on the microstructures of nanocomposites, and thus they are not reviewed in detail here.

2.1.5 Preparation of Polymer/Clay Nanocomposites

Basically, there are four major methods for fabricating polymer/clay nanocomposites: (1) in-situ template synthesis, (2) solvent methods, (3) in-situ intercalative polymerisation and (4) melt compounding. [65,67,70,71,73,99,100] A brief description is given to the four fabrication methods.

(A) In-situ template synthesis

Briefly, with this method, an aqueous solution or gel containing the polymer and the silicate building blocks is used to synthesise the clay within the polymer matrix. During the synthesis, the polymer helps the nucleation and growth of the inorganic host crystals and, in the meantime, the polymer chains are trapped within the clay platelets. This method, as a one-step process, seems to be a good way to promote the clay dispersion but in actual fact, it holds serious undesirable drawbacks. In the first place, the synthesis of clay is a process that requires high temperatures, which cause degradation of the polymers. In addition, the growing silicate layers always tend to form aggregates. Thirdly, the cost of this method is relatively too high compared to the other methods. Therefore, in situ template synthesis is not widely used to fabricate polymer/clay nanocomposites.[65,67,77,101]

(B) Solvent method

Figure 2.1-12 illustrates the solvent method. In this technique, a solvent, in which the soluble polymer (or prepolymer for insoluble polymers), is used to exfoliate the clay stacks into individual layers. Layered silicates can be easily dispersed in an adequate solvent because the weak forces that stack the layers together can be overcome easily. The polymer is added into the solution once the clay has swollen in

the solvent, and the polymer molecules diffuse into the clay layers. The important step is to remove the solvent either by vaporisation under vacuum or by precipitation. The dispersed clay sheets reassemble after the removal of the solvent, sandwiching the polymer molecules. The major advantage of this method is that intercalated structures can be obtained even when the polymer matrices used are with low or no polarity. On the other hand, the most serious drawback of this method is the use of large amount of solvents which causes a series of problems such as solvent disposal and pollution prevention. As a result, this technique is not widely applied in industry, but this technique has been reported to be used with PEO, PVE, PVP and PA *etc.*, as they are soluble in water and cause less environmental problems.[65,67,73]

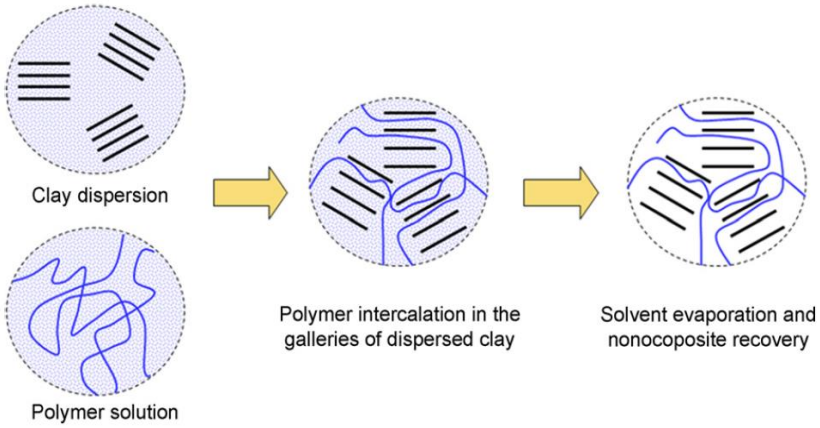

Figure 2.1-12 Intercalated structure obtained by solvent method.[65]

(C) In-situ intercalative polymerisation

This technique was first reported to fabricate PA6/clay nanocomposites.[43] A liquid monomer or a monomer solution, in which the modified clay is swollen, is employed in this method. The polymerisation reaction is initiated after the monomers have diffused into the clay galleries, which allows the polymer chains to grow inside the interlayer spacing. There are many ways to initiate the reaction such as: heat, radiation, the diffusion of a suitable initiator, or catalyst fixed through cationic exchange inside the interlayer initially. Under the condition that the polymerisation rates are properly balanced inside and outside the clay galleries, delamination of the clay stacks occurs and an exfoliated structure is obtained. However, it is difficult for this technique to be widely used in industry due to its low production rate and the use

of monomers which restricts the choices of polymers, and some monomers can be toxic.[65,67,73,102]

(D) Melt compounding

In this technique, the polymer in molten state is mixed with the modified clay, and the polymer chains diffuse into the clay galleries if the modified clay and the polymer melt are sufficiently compatible. As a result, an intercalated or an exfoliated nanocomposite can be obtained. Very often, such composites contain a mix of intercalated and exfoliated structures.

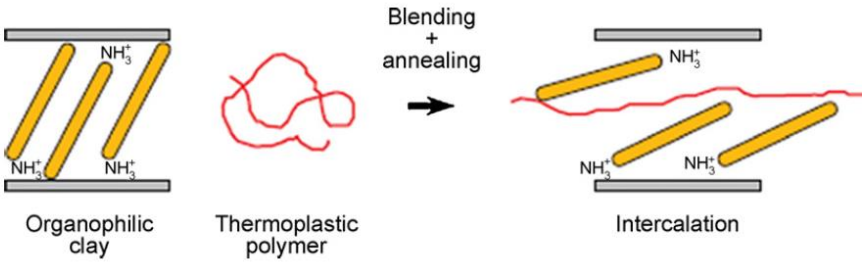

Figure 2.1-13 The melt compounding process.[73]

During melt compounding, the polymer is in its molten state and under shear stress, at a temperature that is above the softening point of the polymer. This approach minimises capital costs, because it allows polymer/clay nanocomposites to be formulated directly using ordinary compounding devices such extruder or mixers. It is thus more economical and simpler than the other techniques. Therefore, melt compounding is the most versatile and environmentally benign, and it is commercially attractive among the four techniques. Thus it is of particular interest since melt compounding has these significant advantages over the other three approaches. This makes it the mostly used approach for the preparation of polymer/clay nanocomposite products, very typically, PP/clay nanocomposites.[65,67,73]

The PP/clay nanocomposites to be fabricated in this research project are prepared using melt compounding method, specifically, with a twin screw extruder, and a twin rotor mixer. This is likely to be the technique most widely used in future industrial applications.

2.1.6 Factors Determining Clay Dispersion in PP Matrix

Generally, several factors have been reported to have significant effects on the intercalation/exfoliation of clay particles in PP matrix. These factors include modification of clay, addition of compatibiliser, incorporation of co-intercalants and melt-compounding conditions. This section gives some insight into the four main factors determining clay dispersion in PP.

(A) Clay modification

Modification of clay is the key to the preparation of PP/clay nanocomposites. However, it should be noted that clay modification alone is far from enough to achieve a high level of intercalation/exfoliation. Although clay is chemically modified, the compatibility between non-polar PP matrix and polar functional groups on the clay surface is still not sufficient. Modified organoclay and compatibiliser are always used together to make PP/clay nanocomposites. The most commonly used compatibiliser in PP/clay system is known as maleic anhydride grafted PP (PP-g-MA), first reported in 1996.[103] In PP-g-MA, the maleic anhydride derived grafts are compatible with the polar modifiers on the clay surface while the PP segments of PP-g-MA are obviously physically and chemically compatible with the PP matrix. Therefore, links are formed between the clay platelets and the matrix, significantly improving the compatibility between clay and the PP matrix and resulting in greatly enhanced properties. Studies regarding clay modification have been continuously reported over the past few years. [5,6,9,10,91,104–111]

Incorporation of alkyl amine modified clays and PP-g-MA into PP, can improve intercalation/exfoliation of clay particles in PP and thus enhance performance of the nanocomposites[5,108,111] Amidation reaction between amine on clay surface and maleic anhydride groups in PP-g-MA has also been confirmed, in other words, amine modified clay is connected to PP matrix by PP-g-MA because of the bonding formed between the amine and maleic anhydride groups.[108] The alkyl chain length of alkyl amine must exceed 8 C-atoms in order to achieve nanocomposite formation, which is also promoted by increasing anhydride functionality of the PP-g-MA compatibiliser.[5] Alkyl ammonium is also widely used to modify the surface of clay, and improved exfoliated/intercalated structures have been reported.[104] Normally, the

more hydrophobic the clay is, the better the dispersion improvement that can be obtained.[106]

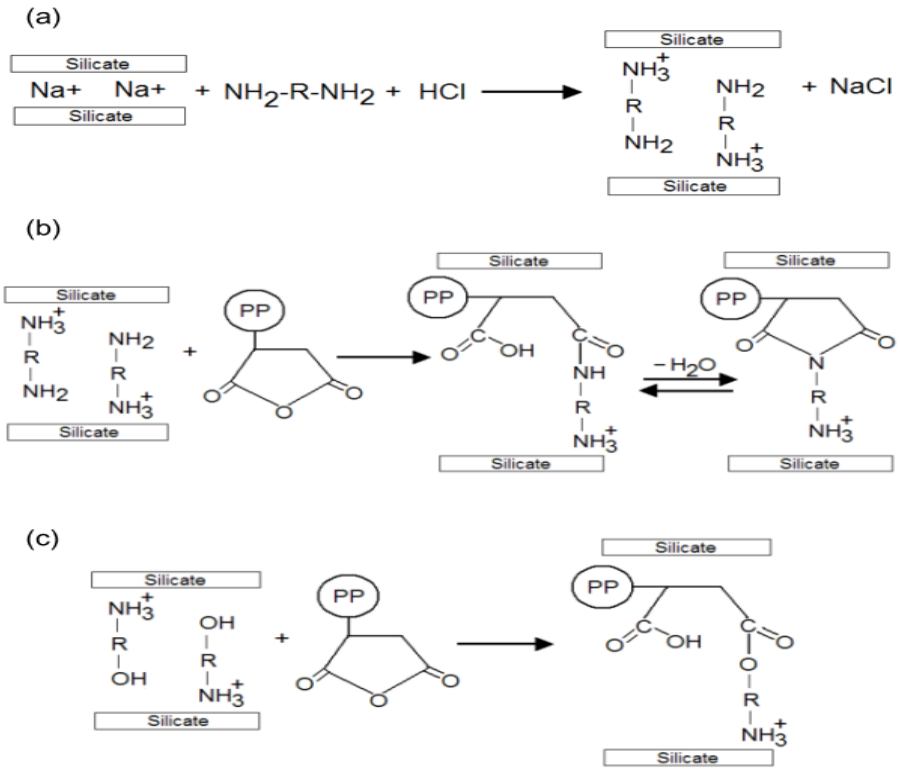

Figure 2.1-14 Scheme of (a) ion exchange reaction and reaction of PP-g-MA with (b) diamine or (c) ethanol amine.[108]

After comparing the dispersion of pristine clay and the clays modified by alkyl ammoniums and alkyl amines in PP matrix, Lei *et al*. concluded that the clay dispersion in PP matrix is significantly improved by the surface treatment of clay, while alkyl ammonium treated clays have better thermal stability than ones treated by alkyl amines.[91]

It was reported later that clays with high cation exchange capacity (CEC) and organically modified with quaternary ammonium salts were found to give better dispersion and intercalation compared to clays with low CEC value and modified with octadecylamine (ODA).[105] According to the study based on clays modified with quaternary ammonium and phosphonium salts, it was found that organic modifiers with a very long backbone may possibly hinder entry of PP segments through the clay layer and excess surfactant during modification process is unnecessary.[9,109]

The modification of clay discussed above is very common and general, but when it comes to the nanocomposites prepared by in-situ polymerisation, the modification of

clay can be very different.[6,112–117] In-situ polymerisation is one of the best methods to achieve homogeneous distribution and dispersion of clay, because the clay stacks are broken down into individual sheets easily for the polymer chains to grow inside the interlayer galleries during the polymerisation process (see section 2.1.5 D). $TiCl_4$ based Ziegler-Natta catalysts were reported to be used to obtain PP/clay nanocomposites.[6] In this work, the $TiCl_4/MgCl_2$/ clay –supported Ziegler-Natta catalysts were synthesised first, and then introduced into the reactor initiating the polymerisation.[6]

However, in-situ polymerisation is not widely used to manufacture PP/clay nanocomposite products in industry. This thesis is therefore entirely focused on PP nanocomposite formation by melt compounding.

(B) Compatibilisers

In addition to clay modification, the use of a chemical compatibiliser is another key factor affecting exfoliation/intercalation of clay in PP matrix, which also determines the final mechanical properties of PPCNs obtained.[118] As mentioned previously, PP-g-MA has been widely used in PP/clay nanocomposites**,** since it was reported that in the presence of PP-g-MA the particles of silicate layers were dispersed at the nanometre level and became smaller and were dispersed more uniformly as the ratio of PP-g-MA to the clay increased.[103] It has been reported that PP-g-MA of low average molecular weight and high maleic anhydride content is a more effective compatibiliser for PP/clay nanocomposites.[119]

In recent years, compatibilisers, not only PP-g-MA, have been investigated and reported when researchers made efforts to improve the dispersion of organically modified clay in PP matrix.[7,8,13,14,105,107,120–123] López-Quintanilla *et al*. [121] compared the effects of three different compatibilisers on the dispersion of clay in PP, and the three compatibilisers were glycidyl methacrylate grafted PP (PP-g-GMA), acrylic acid grafted PP (PP-g-AA) and PP-g-MA. Based on the study, it was concluded that PP-g-GMA and PP-g-MA were better compatibilising agents than PP-g-AA, as GMA and MA groups are more polar than AA. As a result, better clay dispersion and interfacial adhesion thus highly improved mechanical properties were achieved.

Shroff Rama *et al*.[8] compared PP-g-MA with potassium succinate grafted PP (KPPSA). In this study, exfoliated nanocomposites were achieved with KPPSA at concentrations of 20 wt% and 25 wt%, but only intercalated structures were obtained with PP-g-MA. Consequently, greater improvements in mechanical properties were found in the exfoliated nanocomposites prepared with KPPSA, in comparison to the intercalated nanocomposites prepared using PP-g-MA. Maleic anhydride grafted poly(ethylene-co-octene) (MAH-g-POE) was also used as a compatibiliser to improve clay dispersion in PP matrix, and the dispersion of clay was considerably increased by the incorporation of MAH-g-POE.[122]

A new compound coupling compatibiliser was studied by Liaw *et al*.[123] aiming to further improve clay dispersion. This new compatibiliser coupled γ-(aminopropyl) triethoxy silane (APTS) and PP-g-MA, and was synthesized through simple condensation reaction. The amide bond formed between PP-g-MA and ATPS together with the stable C-Si bonds formed at the organic-inorganic interface providing a strong bridge that convalently linked the clay and the PP matrices. Consequently, the boundary between the organic and inorganic domains was blurred to some extent, resulting in an intercalated-exfoliated structure at 5 wt% clay content and significant improvements in tensile strength and modulus.

Recently, Dong *et al*. [13,14] carried out a systematic study on PP-g-MA to investigate the competing effects of the compatibiliser on clay dispersion and matrix plasticisation for PP/clay nanocomposites, which will be discussed in the later section regarding the effects of clay and compatibiliser.

(C) Co-intercalants

It is also known that due to the difference in polarity, high maleic anhydride (MA) concentration causes phase separation which weakens the achievable mechanical properties of PP/clay nanocomposites.[124] To reduce the MA concentration and improve the dispersion of clay in bulk PP, the incorporation of co-intercalants has been reported in some studies.[11,12,107,120,125,126]

Ratnayake *et al.* used short chain amide molecules (AM) as the co-intercalant for PP/clay/PP-g-MA system and this study is of special interest, because AM is widely

used as a slip agent for the processing of commercial PP products.[11,12] XRD analysis was performed for pristine unmodified montmorillonite (MMT), organically modified montmorillonite (OMMT) and a mixture of AM with OMMT (AM-OMMT) made at 100 °C. The characteristic (001) diffraction peaks of MMT, OMMT and the mixture appear at 7.22°, 2.96° and 2.58°, which refer to the interlayer spacing of 1.22 nm, 3.02 nm and 3.42 nm respectively. It is highly likely that the AM molecules diffused into the clay galleries and extended the spacing. Contact angle measurements show that the AM molecules did not migrate to the composite surface especially at low concentrations, which is completely different from what AM molecules usually do when used as a slip additive in commercial PP products. The diffusion of AM into OMMT and the interactions among the AM molecules, PP-g-MA and OMMT were confirmed by FTIR and MFI.[11]

As reported in this study, the driving force of the migration of AM into the clay galleries was likely to be the attraction of the polar groups ($CONH_2$) in the AM molecules to the polar sites on the modified clay surface. Eventually, the hydrogen bonding formed bonded the AM molecules to the clay surface. However, in such a system consisting of modified clay, AM molecules and PP-g-MA, the interactions among them are very difficult to understand in detail because many potential reactions might occur.[11]

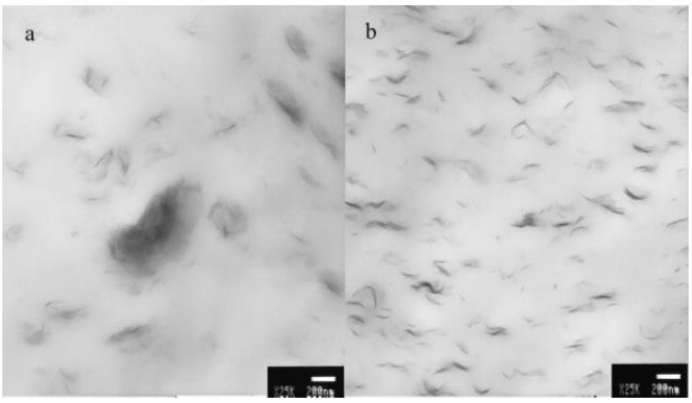

Figure 2.1-15 TEM micrographs of (a) a conventional PP/clay nanocomposite (2 wt% PP-g-MA, 2 wt% clay) and (b) a co-intercalated PP/clay nanocomposite (0.5 wt% AM, 2 wt% PP-g-MA, 2 wt% clay)[11]

In addition to AM, other co-intercalants have also been reported, such as, dibenzoyl peroxide (BPO) and N-imidazol-O-(bicyclo pentaerythritol phosphate)-O-(ethyl methacrylate) phosphate (PEBI).[107,125]

It can generally be concluded that addition of co-intercalants facilitate dispersion of clay platelets in a PP matrix and promotes the formation of intercalated/exfoliated structures. PP-g-MA and AM are used in this research programme to make PP/clay nanocomposites. The optimum formulation of PP/clay nanocomposites will be investigated first with the help of a DoE approach.

(D) Compounding conditions

As mentioned previously, melt compounding is the main method used to fabricate PP/clay nanocomposites in industry. Twin screw extrusion is the most widely used melt-compounding method. Thus, published studies on the effects of processing conditions on clay dispersion mainly relate to twin-screw extrusion.

Effects of processing conditions on the dispersion of clay in PP matrix are receiving more and more attention. Suitable processing conditions could facilitate the intercalation/exfoliation of layered silicates and help further improve the properties of PP/clay nanocomposites. Some studies focusing on the effects of processing conditions have been reported in recent years.[15,16,106,109,121,127–130]

Due to Hoffman elimination mechanism, the organic modifiers, such as ammonium salts, on organoclay surface start to degrade at 180 °C which is lower than the normal processing temperatures of PP.[131] So extra care needs to be taken when choosing processing conditions, because the interlayer spacing of layered silicates decreases when the organic modifiers are degraded, which causes a difficulty in clay dispersion.

It was reported that when compounding PP/clay nanocomposites, sufficient residence time and shear stress are of great importance in dispersing the clay sheets.[127] Whilst high shear stress helps to separate clay platelets from tactoids, excessively high shear rates may lead to fracture of the platelets and thus compromise the aspect ratio of the clay platelets. Sufficient residence time is required for the polymer to diffuse into the clay galleries but excessively long residence time may cause the polymer to degrade. Therefore, it is essential to find the proper balance of the two variables when making PP/clay nanocomposites.

Lertwimolnun *et al.* [128] studied the effects of processing conditions of a twin screw extruder on the morphology of PPCNs and on the evolution of platelet dispersion along the screws. The level of exfoliation was estimated using rheological measurements including determination of melt yield stress. It is concluded from this study that the increase in the ratio of feed rate Q to screw speed N (i.e. Q/N) promotes exfoliation. The effect of screw profile on the platelet dispersion along the screw was determined by the operating condition, and it is more significant at low Q/N. A similar conclusion was drawn by the recent work reported by Jiang *et al*. after studying the relationship between the microstructure of PP/clay nanocomposite and shear strain in the flow field.[16]

Modesti *et al.*[129] pointed out that the effect of processing conditions was not very evident, but low barrel temperature and high screw speed give better clay dispersion because they transmit higher shear stress to the molten polymer. Lately, reversion of clay dispersion in a twin screw extruder with increasing feed rate and screw speed was reported by Barbas *et al.*[17] They indicated that increasing screw speed led to parallel growth of viscous dissipation and degradation of the clay surfactant, reducing clay-polymer affinity and enabling diffusion of the polymer chains out of the clay galleries. The reversion of dispersion with increasing feed rate was related to relaxation phenomena.

Recently, a twin-screw extruder, single screw extruder and single screw extruder with an extensional flow mixer were studied and compared by Li *et al.*[130] Two different processing methods, masterbatch and single pass, were also studied and compared in their work. According to this study, the quality of clay dispersion is mainly determined by mixing intensity and residence time, and the degradation of the organoclay is also sensitive to these parameters. Furlan *et al.*[15] reported the importance of screw design and pointed out that aggressive screw shear profile is not the best for the development of optimal nanocomposites properties. By adding 4 wt% of sodium acetate trihydrate and by using a water-assisted extrusion process, novel PPCNs showing a very good clay dispersion have been obtained in the study reported by *Rousseaux et al*.[18]

Overall, according to the literature for twin-screw extrusion, it seems that screw speed and feed rate, which determine shear rate/stress and residence time, play an

important role in clay dispersion in PP.[17] Reasonably high shear stress/rate and sufficient residence time promote the intercalation/exfoliation of clay particles.

In this research programme, a twin rotor chamber mixer and a twin screw extruder will be employed to investigate the effects of compounding conditions using DoE approach. The two compounding methods will be compared and the optimum compounding conditions of twin screw extruder will be determined and used to manufacture PP/clay composites.

2.1.7 Effects of Clay & Compatibiliser

To fabricate PPCNs, modified clay and compatibiliser are incorporated into the PP matrix. The addition of clay and compatibiliser may not only enhance the mechanical properties, but also affects the other properties. In this section, the effects of clay and compatibiliser on melt rheology, mechanical (including dynamic) properties, matrix morphology, and thermal and photo oxidation are reviewed.

(A) Mechanical properties

Improving the mechanical properties of PP, mainly tensile modulus, is the main reason to make a PP/clay nanocomposite. It is common sense that clay, as an inorganic ceramic material, is generally much stiffer and stronger than polymers. Therefore, the incorporation of the clay into the PP matrix can greatly enhance the stiffness and strength of the neat PP, assuming that there is strong bonding between the clay and PP.

It seems that increased clay concentration in the PPCNs would lead to higher stiffness, because the percentage of the rigid phase is increased. This is true when clay concentration is still at low level.[132] However, clay particles always tend to aggregate forming tactoids, especially at a relatively high clay content (above 5 wt%). Due to the reduced compatibility at high clay content, the dispersion of clay becomes very difficult resulting in a great number of visible clay tactoids and cavity-like voids, which can be observed clearly in the SEM images shown in Figure 2.1-16. This, in turn, can weaken the enhanced mechanical properties.[56]

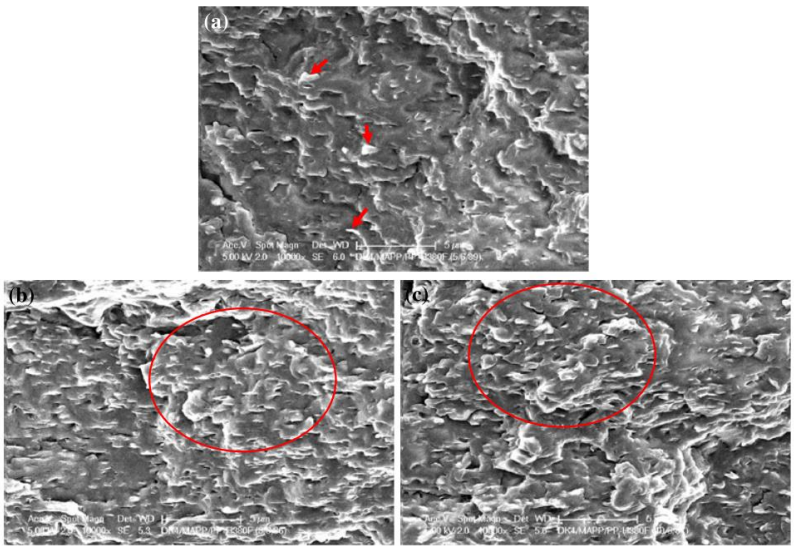

Figure 2.1-16 SEM micrographs: (a) 5 wt% clay, 6 wt% PP-g-MA, (b) 8 wt% clay, 6 wt% PP-g-MA and (c) 10 wt% clay, 6 wt% PP-g-MA. The scale bar is 5um and the arrow/circles indicate the clay tactoids.[14]

To improve the dispersion at high clay content, more compatibiliser, such as PP-g-MA, is required to further increase the compatibility between the clay and the PP matrix. However, the compatibiliser (such as PP-g-MA) is actually a low molecular weight species compared to the PP matrix, and has relatively inferior mechanical properties. Therefore, excessive PP-g-MA may be detrimental to the mechanical properties of the nanocomposites to some extent.[14,121,133–136]

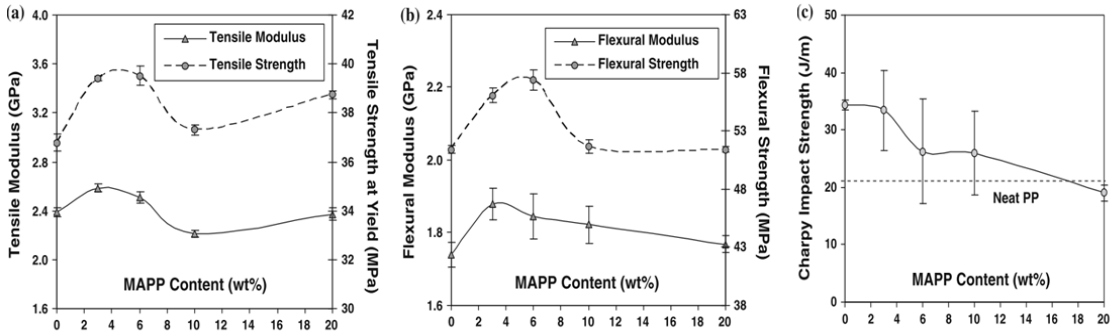

Figure 2.1-17 Mechanical properties of PP/clay nanocomposites (5 wt% clay): (a) tensile properties, (b) flexural properties and (c) Charpy impact strength.[14]

Figure 2.1-18 displays clearly the relationship between the mechanical properties of PPCNs and the concentration of PP-g-MA, while the TEM images in Figure 2.1-19 show the improved clay dispersion with increasing PP-g-MA concentration.[14] According to the two figures, it is quite clear that the addition of a small and suitable amount of PP-g-MA improves the dispersion of the clay leading to enhanced tensile modulus and flexural modulus. When the concentration of PP-g-MA is above a certain level (5 wt%), the mechanical properties of PPCNs reduce with PP-g-MA. It

was reported that up to the saturation level, short chains of the compatibiliser mainly exist in the interfacial area, but above this level, the excessive compatibiliser is dispersed in the PP matrix which adversely affects the homogeneity of the matrix reducing the tensile and flexural properties as well as impact strength.[14]

As suggested by the comprehensive study reported recently, a relatively small amount of PP-g-MA is more desirable if both the plasticising effects and clay agglomeration can be controlled to an acceptable level, and the optimum amount of PP-g-MA is about 3 to 5 wt%.[14]

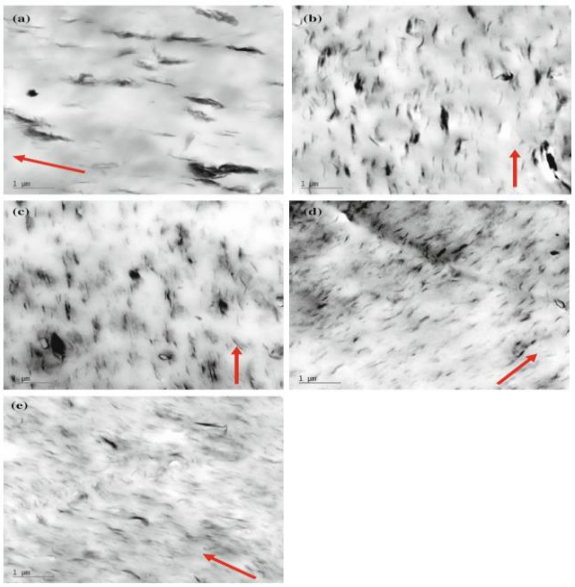

Figure 2.1-18 TEM micrographs of PP/clay nanocomposites (5 wt% clay): (a) 0 wt% PP-g-MA, (b)3 wt% PP-g-MA, (c)6 wt% PP-g-MA, (d)10 wt% PP-g-MA and (e)20 wt% PP-g-MA.[14]

In addition to the dosage of PP-g-MA, the MA content and molecular weight also exert a great influence on clay intercalation/exfoliation and thus the mechanical properties of PP nanocomposites.

Low MA content will result in relatively high average molecular weight, and also relatively high crystalline content, as the crystalline content of PP-g-MA is dependent on the MA level. The crystallisable sequences of PP in PP-g-MA are compatible with the PP matrix crystalline regions enabling transcrystallinity and effective filler-matrix coupling. Moreover, MA is polar whilst PP is a typical nonpolar polymer. Therefore, it is very likely that a too high MA content may considerably reduce the miscibility between the PP-g-MA and PP matrix, and harm the mechanical properties of the composites. Kawasumi *et al.*[66] reported that macrophase separation texture was

observed for the PP/PP-g-MA blend when the MA level in the PP-g-MA was too high, and it is thus suggested that miscibility is also an important factor to achieve the intercalated/exfoliated homogeneous dispersion of the clay. On the other hand, the intercalation capability of PP-g-MA increases with increasing MA level. Therefore, high MA level enhances the melt intercalation of PP-g-MA into clay layers, improving mechanical properties of the composites.[137]

Wang *et al*.[119] indicate that the molecular weight, which determines the shear viscosity of PP-g-MA, also play a vital role in the effective breakup of clay agglomerates, thus the relationship between the chemistry of compatibilisers and the processing conditions should be coupled. According to their study, PP-g-MA with about 1 wt% MA content would be a suitable compatibiliser and the weight ratio of PP-g-MA to organoclay should be around 3 to achieve maximum improvement in mechanical properties.

The effects of fillers or compatibilisers on PP nanocomposites or PP blends have also been reported elsewhere.[138–142]

(B) Crystalline structure of PP matrix

PP is a very typical semi-crystalline material, whose mechanical properties are significantly affected by the crystalline regions within it. The bulk PP in PPCNs still possesses crystalline regions, which can affect the physical and mechanical properties of nanocomposites. PP crystal structures and morphology are briefly reviewed here.

Due to the presence of pedant methyl group, the PP chain will form a helical structure to pack atoms closely together in an energy minimum state. During crystallisation, the helical PP chains fold back and forth on themselves to form thin-plate structures called lamellae. The lamellae, which are typical 10 nm in lateral dimensions, are slight curved and their surfaces are covered with a disordered amorphous layer with certain amount of loose loops, chain ends *etc.*[143] Lamellae can grow in either radical or tangential direction within one structure unit.

The lamellae aggregate together to form a superstructure called a spherulite, and its typical dimensions is of the order of microns and sometimes, even millimetres. Spherulites may be viewed as spherical aggregates of lamellae originate from a common centre and radiate outwards, and the spherical shape is formed as a result of branching and splaying of lamellae at dislocation points. The amorphous regions between lamellae, which are called 'tie chains', provide not only complete space filling but also flexibility and impact resistance to the crystalline regions.

The spherulites continue to grow radially until they impinge upon one another, thus polygonal boundary lines may be developed between two adjacent spherulites. The average size of spherulites may be markedly influenced by crystallisation temperature or the presence of nucleation agent, which determines the nuclei density. Figure 2.1-19 shows isotactic PP and its crystal morphologies.

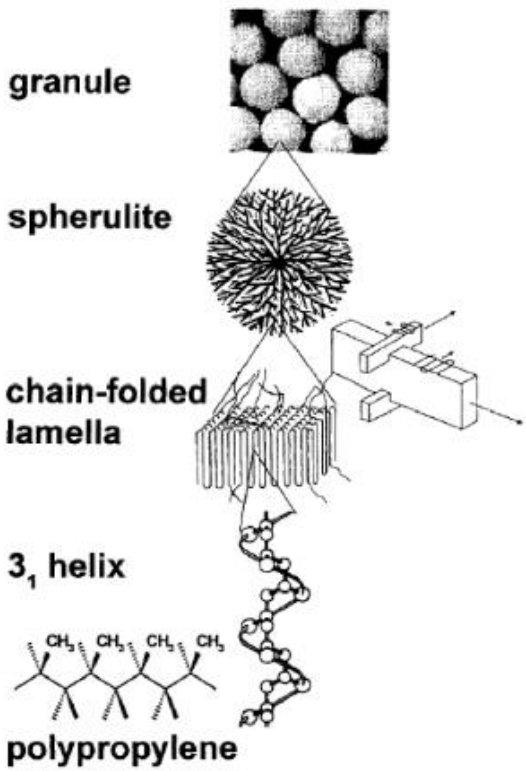

Figure 2.1-19 Isotactic PP and supramolecular strucutres.[61]

The two types of morphologies mentioned above are usually developed during the crystallisation of PP under quiescent conditions. However, crystallisation under flow could result in flow-induced oriented morphologies such as a shish-kebab structure,

which is highly relevant to polymer processing, such as injection moulding. Figure 2.1-20 shows a schematic model of shish-kebab structure.

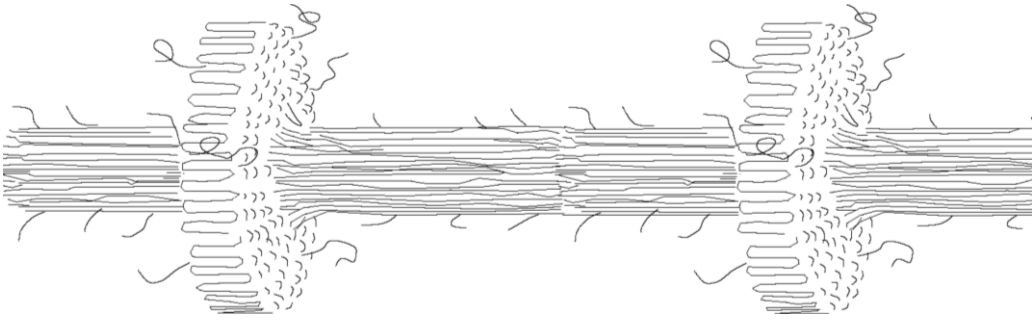

Figure 2.1-20 A schematic model of shish-kebab structure[144]

According to the conventional view, a long and macroscopically smooth extended-chain crystalline assembly, which originates from the oriented and/or extended chains under flow, forms the innermost portion of the shish-kebab structure. The shish provides nucleating sites or primary nuclei for lateral growth of folded-chain crystals or kebabs.[145]

Crystal structures and morphologies of PP are determined by crystallisation conditions.[146,147] High shear rate/stress and a rapid but inhomogeneous cooling are involved in injection moulding process, therefore different crystal morphologies, such as spherulites and shish-kebab structures, may exist simultaneously in an injection moulded PP part. This will be presented later in section 2.2.3.

For isotactic PP, the most common form is α-form (a=0.665 nm, b=2.096 nm, c=0.650 nm, and β=99.33°). On the other hand, isothermal crystallisation in an intermediate temperature range (105-140 °C) or on slow cooling through this range gives β-phase (a=b=1.101 nm, c=0.650 nm, and γ=120°).[148] γ-from with the orthorhombic unit cell (a=0.851 nm, b=0.995 nm, and c=4.168 nm), which is least observed, is formed when melt crystallises at high pressure or under restriction.[146]

The addition of clay and compatibiliser is very likely to affect the crystallisation mechanism in the bulk PP. Therefore, many studies have been done to study the effects of clay or compatibiliser on the crystal structures and crystallinity in PP/clay nanocomposites. [148–152]

It has been reported that nanoclay at low concentrations suppresses the formation of the β-form.[148] Yuan *et al.*[149] reported the epitaxial growth of γ-from in the presence of nanoclay additives. Nam *et al*.[150] confirmed the existence of γ-form in PPCNs, and the γ-form was due to the intercalated PP chains restricted between the narrow interlayer spacing. Perrin-Sarazin *et al.* [151] pointed out that the presence of PP-g-MA could cause better clay dispersion and lead to crystallisation at low temperature and lower rate while the level of crystallinity was not affected evidently.

Recently, Hegde *et al.*[152] investigated the crystallisation mechanisms in PP/clay nanocomposites with varied nanoclay concentrations. As shown in Figure 2.1-21, different crystallisation mechanisms were found in the bulk PP at low clay contents (1-5 wt%) compared to the bulk PP at high clay contents (10-15 wt%). Due to the hindrance to crystallisation caused by a large number of dispersed clay sheets, low clay content (1-5 wt%) shows lower nucleation rate and less impingement. On the contrary, the high nucleation rate overrides the slow chain diffusion at high clay contents, which makes it difficult to achieve complete exfoliation of the clay. It is also pointed out that clay platelets that are unenclosed by PP chains and crystals, tend to be excluded out of spherulites and gather at interspherulite regions during crystallisation of the molten PP.[152]

Dong *et al*. [13] investigated the effects of PP-g-MA on the crystalline structure of bulk PP. They found that the incorporation of PP-g-MA did not change the crystalline structures of the bulk PP significantly, but the α-form and preferred orientation of PP crystals were enhanced considerably. Additionally, an excessive amount of PP-g-MA was found to hinder the growth of α-PP. It is known that α-form PP contributes to high tensile modulus, while β-PP is stated to have better impact strength and greater elongation at break.[153] Thus, excessive amount of PP-g-MA weakens the tensile properties of the nanocomposites by hindering the formation of α-PP. Overall, the amounts of clay and PP-g-MA need to be balanced well to facilitate the crystallisation of the bulk PP in the nanocomposites, in order to obtain desirable mechanical properties.

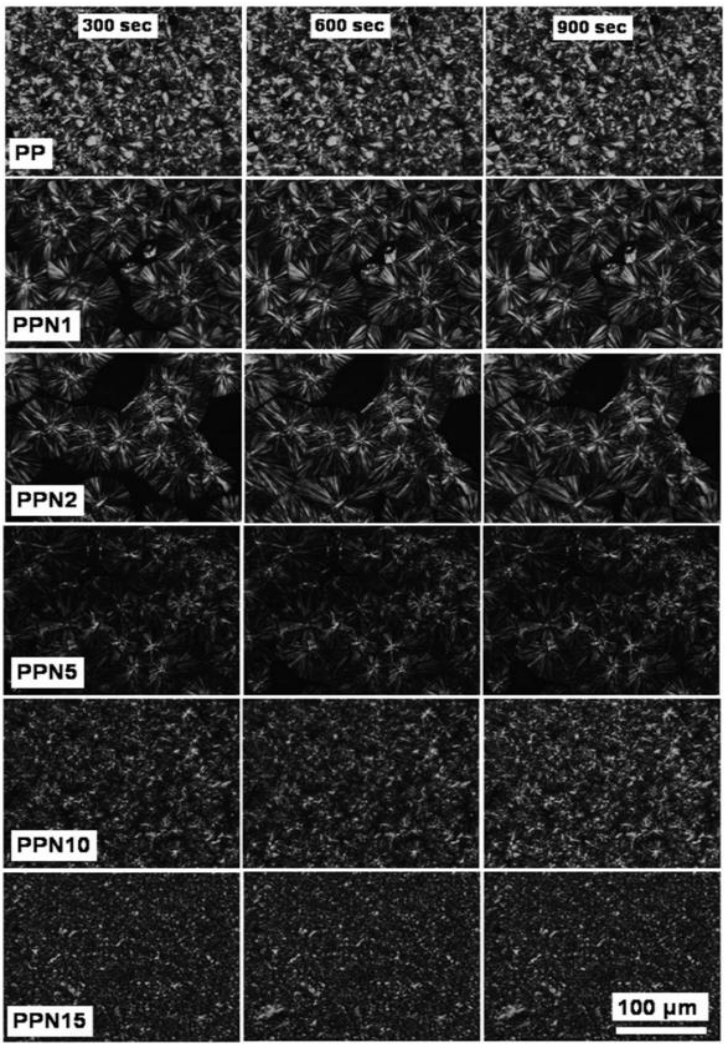

Figure 2.1-21 Sequence of photographs of different clay contents at 125°C (PP: 0 wt% clay, PPN1: 1 wt% clay, PPN2: 2 wt% clay, PPN5: 5 wt% clay, PPN10: 10 wt% clay and PPN15: 15 wt% clay)[152]

(C) Dynamic mechanical properties

Dynamic mechanical testing determines the viscoelastic behaviour of polymers by describing the response of the polymer to dynamic stresses as a function of the frequency of oscillations applied, over a wide range of temperatures. An oscillating strain, which varies sinusoidally with time, is applied to a specimen, resulting in a stress that varies in a similar way but out of phase by an angle δ. The modulus of the specimen is expressed in complex number notation, E*:

$$E^* = E' + iE'' \tag{2.1-3}$$

where E' is in-phase (elastic) storage component and E'' is the (viscous) loss modulus. The ratio of the loss modulus to the elastic modulus is related by:

$$\tan\delta = \frac{E'}{E''} \tag{2.1-4}$$

With tan δ, the primary transition, glass transition, and secondary (sub Tg) transitions of a polymeric material can be determined. The dynamic mechanical properties determine the performance of polymer under stress and temperature.

Dynamic mechanical thermal analysis (DMTA) is widely used to determine the dynamic mechanical properties of polymers over a temperature range, and Tg can be conveniently determined by tan δ. Dynamic mechanical analysis on PPCNs has been reported in many studies when investigating the effects of clay or compatibiliser.

It has been reported that the addition of clay and PP-g-MA into PP leads to significant increase in E' within the glassy regions and rubbery plateau, as shown in Figure 2.1-22. Also, PPCNs demonstrate slightly higher Tg compared to the pristine PP, due to the interactions between the PP chains and the clay platelets. However, it should be noted that a polymer chain sandwiched between platelets that are coated with a carpet of writhing alky tails may well be less rotationally restricted than one surrounded and entangled with other polymer chains in bulk matrix. This effect may lead to no change or reduction in Tg in some polypropylene layered silicate nanocomposites.[107,111,129] Higher clay concentration results in more restriction for PP chains, and thus a higher Tg and elastic modulus. [13,14]

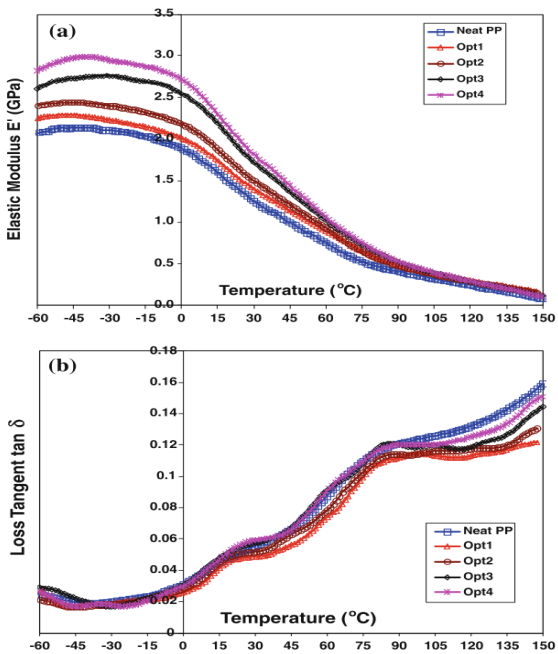

Figure 2.1-22 Enhanced dynamic mechanical properties: Opt1: 3 % clay, 6 % PP-g-MA; Opt2: 5 % clay, 10 % PP-g-MA ; Opt3: 8 % clay, 16 % PP-g-MA; Opt4: 10 % clay, 20 % PP-g-MA.[13]

The factors that affect the dynamic mechanical properties of PPCNs have also been investigated in many other studies. Zhang *et al*. pointed out that with a swelling agent in PPCNs, the heat resistance and storage modulus could be enhanced considerably, and the Tg was shifted to a higher temperature.[120] Different modification on clay surface can also affect the dynamic mechanical properties of PPCNs.[91] Modesti *et al.*[129] indicated that the enhancement of storage modulus of PP/clay nanocomposites was also affected by the compounding conditions. Low barrel temperature profile and high screw speed shows better enhancing effect, but no sensible variation in Tg was found. The enhancing effects of modified clay and the compatibiliser, MAH-g-POE, on dynamic mechanical properties were reported by Zhong *et al*.[122] However, compared to PP-g-MA, a higher content is required to obtain a good dispersion of clay for MAH-g-POE.

(D) Thermal and photo-oxidative stability

For outdoor applications, such as interior and exterior automotive parts, the thermal and photo-oxidative stability of PPCNs is of great importance.

Photo-oxidative stability

Aldehydes, ketones and carboxylic acids along or at the end of polymer chains are generated by oxygenated species in photolysis of photo-oxidation, and the existence of chromophoric groups in the macromolecules initiates the photo-oxidation reactions. Photo-oxidation can occur simultaneously with thermal degradation and each of these effects can accelerate the other.[154] The photo-oxidation reactions include chain scission, crosslinking and secondary oxidative reactions. The following process steps can be considered (Figure 2.1-23): [154]

1. Initial step: Free radicals are formed by photon absorption.
2. Chain propagation step: A free radical reacts with oxygen to produce a polymer peroxy radical (POO▪). This reacts with a polymer molecule to generate polymer hydroperoxide (POOH) and a new polymer alkyl radical (P▪).

3. Chain branching: Polymer oxy radicals (PO•) and hydroxyl radicals (HO•) are formed by photolysis.

4. Termination step: Crosslinking is a result of the reaction of different free radicals with each other.

Compared to the pristine polymer matrix, polymer/clay nanocomposites show high photo-oxidation rates, which may reduce the enhanced mechanical properties of the nanocomposites. Photo-oxidation of polymer/clay nanocomposites has been reported in many research papers, mainly attributed to a reduction of the photo-oxidation induction time. The photo-oxidation is attributed to factors such as the presence of iron ions, the formation of catalytic acidic sites or radicals following the decomposition of the organo-modifier.[155–162]

$$Polymer \longrightarrow P\bullet + P\bullet$$ Initial step

$$P\bullet + O_2 \longrightarrow POO\bullet$$
$$POO\bullet + PH \longrightarrow POOH + P\bullet$$ Chain Propagation

$$POOH \longrightarrow PO\bullet + \bullet OH$$
$$PH + \bullet OH \longrightarrow P\bullet + H_2O$$
$$PO\bullet \longrightarrow \text{Chain scisson reactions}$$ Chain branching

$$\left.\begin{array}{l} POO\bullet + POO\bullet \\ POO\bullet + P\bullet \\ P\bullet + P\bullet \end{array}\right\} \longrightarrow \begin{array}{l}\text{Cross linking} \\ \text{reactions to non-} \\ \text{radical products}\end{array}$$ Termination

Figure 2.1-23 Process steps of photo-oxidation (PH = Polymer, P• = Polymer alkyl radical, PO• = Polymer oxy radical, POO• = Polymer peroxy radical, POOH = Polymer hydroperoxide, HO• = hydroxyl radical)[154]

Morreale *et al.*[163] pointed out that both organoclay and nanometric calcium carbonate addition to PP can increase the photo-oxidation rates, by comparing the photo-oxidation behaviour of clay-filled and calcium carbonate filled PP nanocomposites. It seems that the photo-oxidation in calcium carbonate nanocomposites is due to the nucleation phenomena and thus the changes in morphology and structure. Also, the distribution of the photo-oxidation products in

PP/calcium carbonate nanocomposites is significantly different, compared to that in PP/clay nanocomposites. Singala *et al.*[164] reported that the photo-oxidation starts around the residual impurity, and the residual impurity was increased by the incorporation of nanoclay, leading to faster degradation of PPCNs compared to its virgin counterpart.

The modification of clay also shows some effects on photo-oxidation. The thermal decomposition of alkyl ammonium salts on the clay surface takes place following Hoffman elimination mechanism, the result of which is ammonia, the corresponding olefin and an acidic site on the layered silicate. These decay products, such as the acidic sites and the corresponding olefin, lead to the formation of free radicals and thus accelerate the photo-oxidative degradation of polymer matrix.[161] The source of the tallow alkyl chains in the organic modifier may also have an influence on stability, as Hoang and Liauw *et al.*[165] reported that animal based tallow may be less unsaturated and less prone to oxidation/peroxidation than vegetable based tallow.

Mailhot *et al.*[159,166] reported that the presence of montmorillonite reduces the efficiency of light stabiliser and this effect is enhanced by the combination of nanoclay with PP-g-MA. They suggested that the adsorption of stabiliser onto the clay in polymer/clay nanocomposites could be a possible factor in favour of reduced thermal oxidative and photo oxidative stability, in addition to the decomposition of alkyl ammonium salts.

The effect of compatibiliser on the photo-oxidation of PPCNs has also been reported. Qin *et al.*[161] indicated that addition of maleic anhydride grafted polypropylene (PP-g-MA) did not significantly affect the photo-oxidation rate. On the contrary, Mailhot *et al*.[159] pointed out that some photo-responsive groups was introduced by PP-g-MA, which caused an acceleration of the photo-oxidation in PPCNs.

Recently, Morreale *et al.*[163,167] reported their comprehensive study regarding the effect of PP-g-MA on photo-oxidation behaviour of PPCNs. The formation of photo-oxidation products in the nanocomposites was significantly reduced by the addition of PP-g-MA, and a reduced formation of photo-oxidation products in the carbonyl region was found clearly, as shown in Figure 2.1-24. It is pointed out in this study that the presence of PP-g-MA had positive effects on the photo-oxidation behaviour

of PPCNs, but nanoclay alone led to higher sensitivity to photo-oxidation. This result is in contradiction to that reported by Qin *et al.* [161] mentioned above.

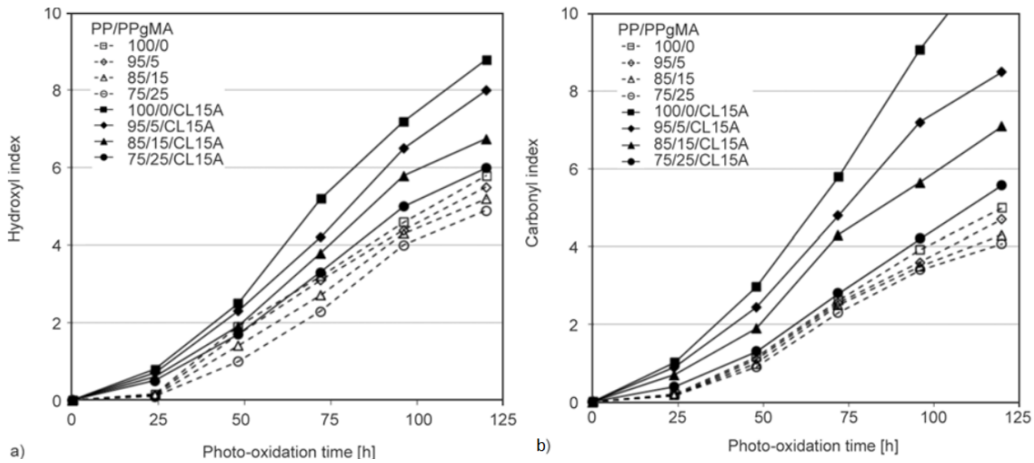

Figure 2.1-24 (a) Hydroxyl index and (b) Carbonyl index for PP/Cloisite 15A nanocomposites at different PP/PP-g-MA ratios as a function of the photo-oxidation times[167]

The UV degradation of PPCNs has been investigated recently by Ben *et al*.[168] and it was found that the UV degradation process for PPCNs is much more intense than that observed for the neat PP.

Thermal stability

Thermal stability is an important property for PPCNs. Valle *et al.*[108] reported that PPCNs showed higher initial degradation temperature than pure PP and the organic modification on clay surface could further increase the initial degradation temperature in comparison to the unmodified clay, which is attributed to a better clay intercalation-exfoliation due to the higher compatibility between the modified clay and polymer. The study reported by Modesti *et al.*[129] confirmed that PPCNs had higher initial degradation temperature than neat PP. Ratnayake *et al*. [11] explained that the enhanced thermal stability of the PPCNs was due to the exfoliated and well-dispersed clay particles acting to reduce the oxygen permeability rate, and also, to slow down the diffusion of volatile degradation products from the bulk PP matrix to the gaseous phase. A recent study points out that the presence of clay alters the decomposition mechanism of the polymeric matrix and the presence of quaternary ammonium salts on the clay surface dramatically accelerates the decomposition of PPCNs.[169] Recently, by using thermogravimetric analysis (TGA) and oxidation

induction time (OIT) in a complementary manner, Fitaroni *et al.*[170] points out that organoclay acts as a degrading influence below 210 °C and as a stabiliser agent after this temperature.

Song *et al.*[107] reported that the thermal stability of PP was significantly improved by the addition of PP-g-MA and modified clay, and further improvement could be obtained by the incorporation of the co-intercalant, N-imidazol-O-(bicyclo pentaerythritol phosphate)-O-(ethyl methacrylate) phosphate (PEBI). A considerable increase in the initial degradation temperature was reported by Zhang *et al.* [120] who used a swelling agent, maleic anhydride, to prepare PP/clay nanocomposites. The initial degradation temperature was 130 °C higher than that of the pure PP. Liaw *et al.*[123] found that the PP-g-MA/APTS compound coupling compatibiliser facilitated the dispersion of clay and thus improved the thermal stability showing a marked shift of the mass loss curve towards a higher temperature.

López-Quintanilla *et al.*[121] reported the effect of processing conditions on the thermal stability of PPCNs obtained. It was found that TGA curve for two-step mixing was shifted towards a higher temperature than that for one step mixing, and also indicated an improved dispersion of clay.

It can generally be concluded that the incorporation of nanoclay and compatibilisers into neat PP to form nanocomposites can significantly enhance the thermal stability. However, due to the fact that the alkyl ammonium salts on clay surface degrades around 180 °C,[131] it is thus suggested that the maximum process temperature for PPCNs should not be significantly higher than 180 °C and the PPCNs should not be kept at a temperature higher than 180 °C for too long.

(E) Rheological properties

Rheological properties of polymers are of great importance for processing, and rheological behaviour can provide further insight into the structure-property relationship of PPCNs. This section focuses only on the effects of clay and PP-g-MA on the rheological properties. Basic polymer flow theory and rheology will be presented in detail later (section 2.2.1).

Valle *et al*.[108] studied the effects of different clay modification on the rheological behaviour of PPCNs. It was reported that the viscosity of the PP/clay nanocomposites could either increase or decrease depending on the modification of the clay. The decrease in the viscosity was attributed to the adsorption of high molecular weight fractions on the clay surface and the lubrication flow effects along the polymer-clay interface. The decreased viscosity may also be related to the poor interactions between the bulk PP and the modified clays. On the other hand, the increased viscosity could be attributed to the strong interactions between the bulk PP and the modified clay surface through formation of chemical bonds.

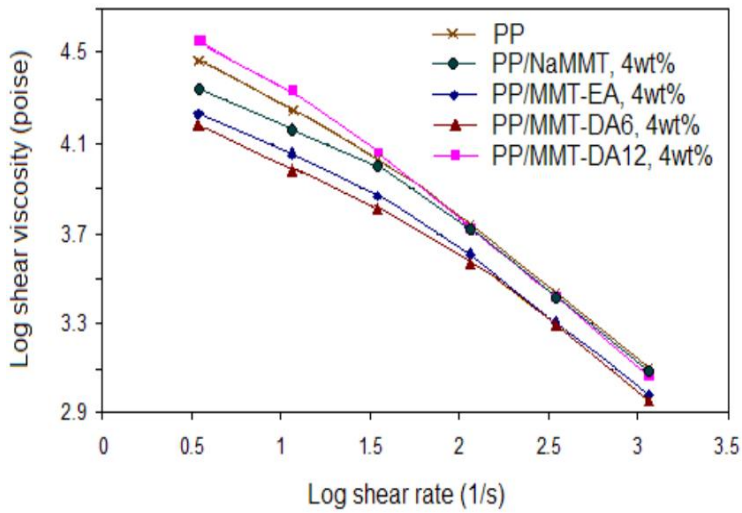

Figure 2.1-25 Shear viscosity versus shear rate of PP/PP-g-MA/amine modified clay nanocomposites with 4 wt% clay at 195 °C. (EA-ethanolamine, DA6-hexamethylenediamine, DA12 -1,12-diaminododecane) [108]

It was also pointed out in the same study that the observed changes in viscosity might also be attributed to the different levels of intercalation/exfoliation.[108] With similar clay content, the nanocomposite viscosity is increased when the size and number of clay aggregates is reduced or the clay sheets are more exfoliated. Valle *et al.*[108] also indicated that increasing clay content might lower the viscosity, because the attractive interaction between clay platelets might be increased with increasing clay content, and becomes more significant than the interactions between the clay and the bulk PP. This was also reported in some other studies.[171,172]

Melt flow index (MFI) was successfully used by Zhu *et al.*[173] to study the relationship between rheology and morphology of clay in PPCNs. Their study showed that MFI is able to provide an indication of exfoliation and dispersion of clay in the PP matrix. Ratnayake *et al.* [12] used a normalised MFI (n-MFI) to investigate the effects of PP-g-

MA and the co-intercalant, short-chain amide molecules (AM), on clay structure in PP the interaction between them. The control PP matrix effect can be excluded by using n-MFI, which is calculated as below:[12]

$$Nomalised\ MFI = \frac{MFI\ of\ composite}{MFI\ of\ corresponding\ control} \quad (2.1\text{-}4)$$

It was found that the n-MFI of PP composite, in which PP was melt blended with clay with neither PP-g-MA nor AM, did not change with clay content, due to the fact that the clay particles remained in their original state with no significant intercalation and thus had little effect on rheological properties. On the other hand, in the presence of PP-g-MA and AM, a steady decrease in n-MFI was obtained, which implies that the PP molecules diffused into clay galleries with PP-g-MA and AM, leading to an intercalated nanocomposite structure and higher viscosity, thus reduced MFI value.[12]

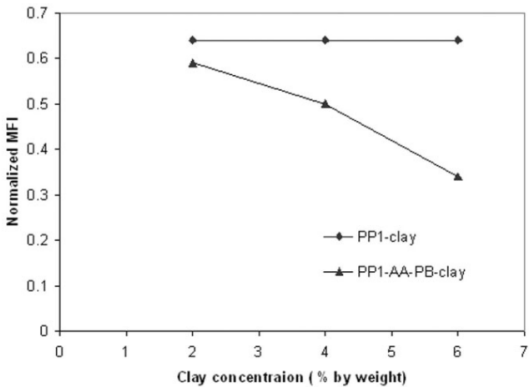

Figure 2.1-26 Normalised MFI of PP/clay nanocomposite and PP/clay composite with increasing clay content [12]

Dolgovskij *et al.*[127] used melt-state and solid-state data from dynamic frequency sweep experiments to investigate the effects of clay content on its dispersion. It was found that the nanocomposites behaved as viscoelastic liquids with 5 wt% or less clay, but a transition to solid-like behaviour occurred at 5 % (Figure 2.1-27). The solid-like rheology was due to a network formed by the clay stacks dispersed in the bulk PP, and the transition from viscoelastic to solid-like behaviour corresponded to a percolation of the clay network in the PP matrix. Thus, it seems that at high clay concentrations, conventional melt-state rheology is no longer an effective method to indicate effective the dispersion of clay.

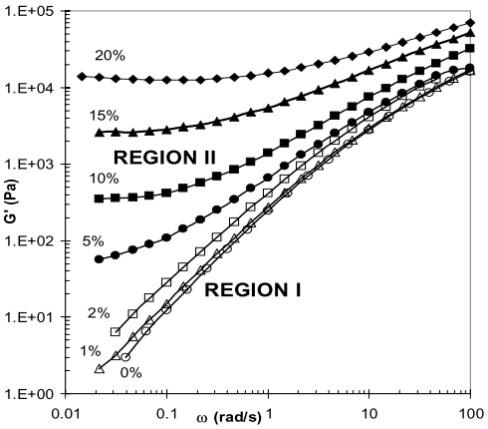

Figure 2.1-27 Elastic modulus G' as a function of clay concentrations at T=180 °C for PP/clay nanocomposites. Region I: viscoelastic liquids; Region II: solid-like behaviour.[127]

Zhong *et al.*[122] used strain sweep test to investigate the effect of compatibiliser, MAH-g-POE, on rheological properties and found that the modulus of different PP/clay nanocomposites was sensitive to the concentration of MAH-g-POE.

2.2 Polymer Processing

The processing of plastics is primarily concerned with forcing the raw material into the designed shape and then fixing the shape by cooling or by chemical reaction. The shaping process mainly involves the flow of the polymeric material in molten state at some time during the process. Therefore, a complete understanding of the flow behaviour of the material is essential to improve the efficiency and accuracy of product manufacture.

2.2.1 Polymer Rheology

Rheology is the study of the flow and deformation of materials, primarily in the liquid state. However, the flow of polymers in actual processes is very complex, because the three dimensional flow is often under non-isothermal and non-steady state conditions. Thus, in many cases, the flow is modelled as a series of simplified idealised viscometric flows, which usually give reasonable approximations.

Viscosity of a liquid material is defined by the equation below:

$$Viscosity(\eta) = \frac{shear\ stress}{shear\ rate} = \frac{\tau}{\dot{\gamma}} \quad (2.2\text{-}1)$$

Viscosity can be regarded as the resistance of a material to flow, and is a fundamental rheological parameter with SI units of Ns m^{-2}, which is often expressed as Pa.s.

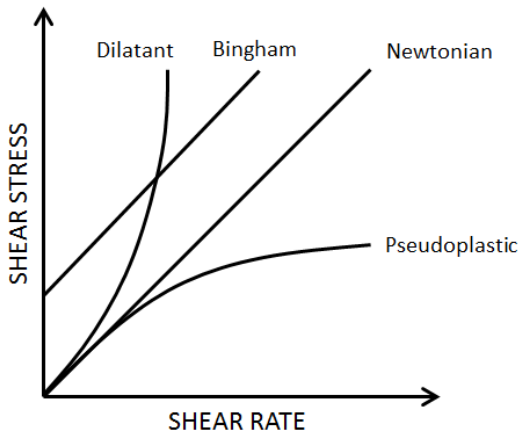

Figure 2.2-1 Flow curves of idealized fluids

Newtonian is the simplest model and Newtonian fluids have a constant viscosity, which means it is independent of shear rate. For low molecular weight fluids such as water, this model describes their behaviour accurately. Bingham fluids behave as a simple Newtonian fluid above the yield stress, below which the fluids do not flow; clay slurries and some highly filled polymers can sometimes exhibit a yield stress before flow occurs. Dilatant fluids show an increase in viscosity with increasing shear rate. On the contrary, pseudoplastic fluids have a decreasing viscosity when shear rate increases, which is the most common response for the large majority of polymer melts.

Plastic melts have a number of typical characteristics although there are a few exceptions:[174]

a. The typical value for the viscosity of a polymer melt is 10^2 to 10^7 Pa.s

b. Viscosity decreases with increasing shear rate. In a few cases, some polymer systems exhibit dilatant behaviours, e.g. PVC dispersions or other highly filled dispersions.

c. The viscosity tends to a constant value when the shear rate tends to zero and the constant value is often referred to 'Newtonian or 'zero shear' viscosity', η_0. i.e. $\eta \rightarrow \eta_0 \;\; as\, \dot{\gamma} \rightarrow 0$

d. Some evidence shows that at very high shear rates the viscosity also tends to a constant, limiting value η_∞. i.e. $\eta \rightarrow \eta_\infty \; as\, \dot{\gamma} \rightarrow \infty$.

There are some mathematical models describing the viscosity data of plastics, and the purpose of these models is to simplify the analysis of real flow problems making the comparison of materials easier and to allow prediction of behaviour in real, scaled-up processes. In terms of polymer melts, Equation (2.2-1) is not usually valid except at a specific point on a flow curve. Polymer melts exhibit non-Newtonian behaviour; therefore, some other non-Newtonian solutions are needed to describe more accurately the behaviour of polymer melts. A plot of $log\tau$ versus $log\dot{\gamma}$ often shows a linear feature over a limited range of shear rates, which suggests a simple model, known as power law model:

$$\tau = k \cdot (\dot{\gamma})^n \tag{2.2-2}$$

where k is the consistency index (a measure of the flow resistance of the material), and n is the power law index which is a measure of the non-Newtonian behaviour of the fluid. For a Newtonian fluid, n is 1 and k is thus actually the viscosity.

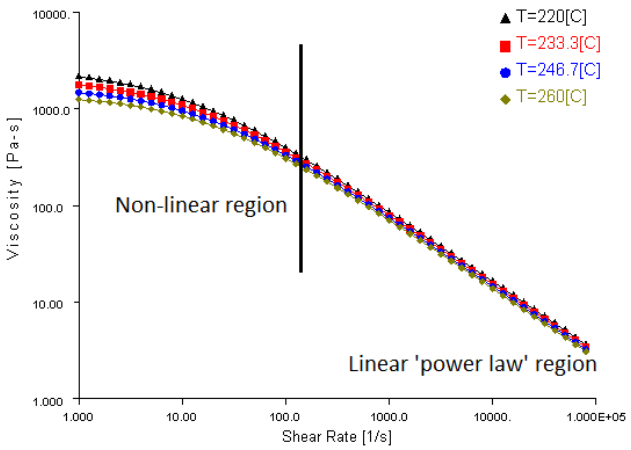

Figure 2.2-2 The flow curves of 'Generic PP'. (Data taken from Moldflow® database)

The power law model is simple, and only two parameters are needed to fit the model. The two parameters can be readily determined by experiments. Power law model is often acceptable for approximate solutions to extrusion or injection moulding

problems, within the linear part of the flow curve (Figure 2.2-2). The power law can be rewritten as:

$$\eta = k(\dot{\gamma})^{n-1} \tag{2.2-3}$$

or in logarithmic form:

$$\log \eta = \log k + (\mathrm{n} - 1)\log \dot{\gamma} \tag{2.2-3*}$$

The power law has good balance between accuracy and simplicity. However, this model is only valid over a limited range of shear rates, namely, the linear region. An infinite viscosity is predicted by this model at very low shear rates. Therefore, the real 'zero-shear viscosity' cannot be correctly predicted by this model. Some other more advanced models described by Osswald *et al*[175] in their book are briefly presented here.

Polynomial model, which is valid over a wide range of shear rates, is obtained by modifying the power law.

$$\log \tau = A_0 + A_1 \cdot \log \dot{\gamma} + A_2 \cdot (\log \dot{\gamma})^2 \tag{2.2-4}$$

There are three coefficients: A_0, A_1 and A_2, which can be evaluated from experimental data by regression analysis. To allow for constant viscosity region at low shear rate, Ellis model has been developed, which is shown as follows:

$$\frac{\eta_0}{\eta} = 1 + \left(\frac{\tau}{\tau_*}\right)^{\alpha-1} \tag{2.2-5}$$

There are three constants in this equation: η_0, τ_* and α, which is related to the power law index n. At high shear rates, $\log \tau$ versus $\log \dot{\gamma}$ is linear, which is similar to power law. At low shear rates, constant viscosity η_0 is obtained, thus the zero shear viscosity can be predicted by this model. However, this model is not favoured, because it is difficult in obtaining real data hence model coefficients and in analysing practical flow problems.

Carreau model is a development of the various integral rheological equations. It has the form:

$$\frac{\eta - \eta_\infty}{\eta_0 - \eta_\infty} = [1 + (\lambda \dot{\gamma})^2]^{\frac{n-1}{2}} \tag{2.2-6}$$

where η_0, η_∞, λ and n are constants. At high shear rates, this equation reduces to the power law, but for even higher shear rates, the model also tends to give limiting viscosity. At low shear rates, the viscosity tends to limiting, therefore, zero shear viscosity, η_0, is predicted.

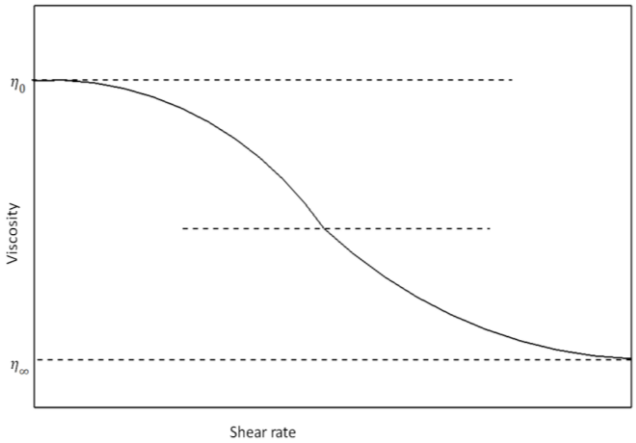

Figure 2.2-3 A brief sketch of Carreau model

Cross model is expressed by the equation below:

$$\eta = \frac{\eta_0}{1+\left(\frac{\eta_0\dot{\gamma}}{\tau^*}\right)^{1-n}} \tag{2.2-7}$$

in which n, η_0 and τ^* are constants. η_0 is zero shear viscosity, n is power law index and $\tau^*$is the stress at the transition to shear thinning. Based on the Cross model and Williams-Landel-Ferry (WLF) equation, a complex model, in which both temperature sensitivity and pressure sensitivity are considered, has been developed. It is known as the Cross/WLF model:

$$\eta = \frac{\eta_0}{1+\left(\frac{\eta_0\dot{\gamma}}{\tau^*}\right)^{1-n}} \tag{2.2-8}$$

where:

$$\eta_0 = D_1 exp\left[\frac{A_1(T-T^*)}{A_2+(T-T^*)}\right] \tag{2.2-9}$$

In this model, T is temperature, A_i and D_i are constants; A_2 and T^* are functions of pressure: $T^* = D_2 + D_3.P$; $\tau^*$is the stress at the transition to shear thinning; D_2 is related to Tg as in the WLF equation. Cross/WLF model is the one used in Moldflow® simulation, the real-time injection moulding simulation software package.

All the above models presented above, are purely viscous models, not viscoelastic. In practice, viscoelastic models are available and thought to be more accurate, but

are much more complex than those presented above, and are outside the scope of this literature review.

2.2.2 Extrusion

The extrusion process is in frequent use in today's plastics industry, for it can transform any number of raw materials into intermediate or finished products in a short time. It has high consumer appeal because it is readily available and easy to work with. Briefly speaking, the extrusion process involves melting plastic material, pumping it through a die to shape it into a product whose cross-sectional dimensions are fixed by the die. Overall, the extruders used today to process polymers generally fall into two categories: single screw extruders and twin-screw extruders. The basic principles of both types of extruders are briefly presented in this section, as both single screw extrusion and twin-screw extrusion are performed in this research project.

(A) Single screw extrusion

Figure 2.2-4 shows a schematic cross-sectional view of a single screw extruder. The extrusion process begins with the placement of plastic resin into the hopper, and the resin goes down into the barrel through the feed throat of the hopper. The rotating screw in the barrel conveys the material towards the die. The heaters installed on the barrel heat the polymer that then starts to melt/soften as it moves along the barrel. To remove possible contaminants, when the molten plastic reaches the end of the barrel, it is forced through a screen pack that is supported by a breaker plate due to the high pressure. Then the molten plastic is fed into the feed pipe that leads to the die. Water bath or cooling rolls are usually applied to expedite the cooling process of the extrudate.

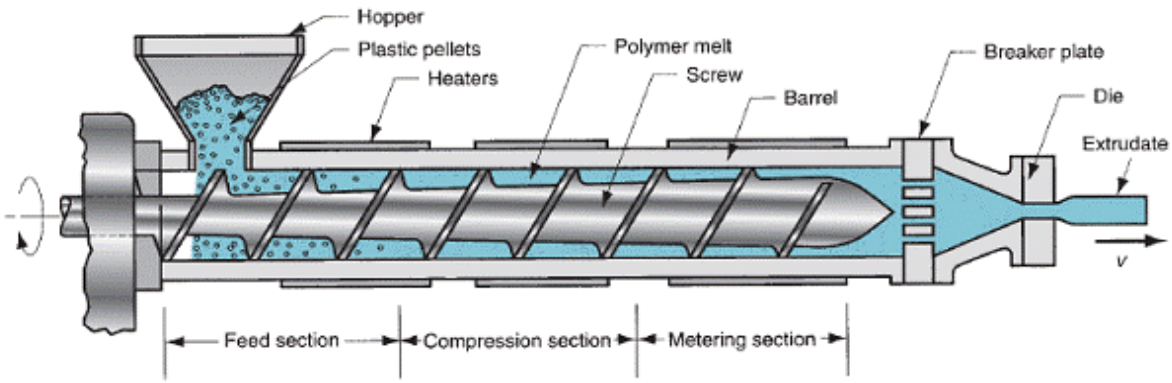

Figure 2.2-4 Components and features of a single screw extruder [176]

According to the basic flow analysis and extrusion principles,[177,178] the simplified extruder and die characteristics are shown as flow:

$$Q = \alpha N - \beta \frac{\Delta P}{\mu} \tag{2.2-10}$$

$$Q = \gamma \frac{\Delta P}{\mu} \tag{2.2-11}$$

where Q is the overall volumetric output, N is screw speed, ΔP is pressure drop, μ is melt viscosity, α and β are screw constants for a given screw design, while γ is die constant. The dotted lines in Figure 2.2-5 represent the extruder and die characteristics expressed by the basic equations above. Their intersections, A and B, are the operating conditions at different screw speed (N).However, molten plastics are typical pseudoplastic flows, and shear thinning happens. The solid lines in Figure 2.2-5 represent the solution of the basic equations for pseudoplastic rheological behaviour. A' and B', instead of A and B, are the actual operating points.

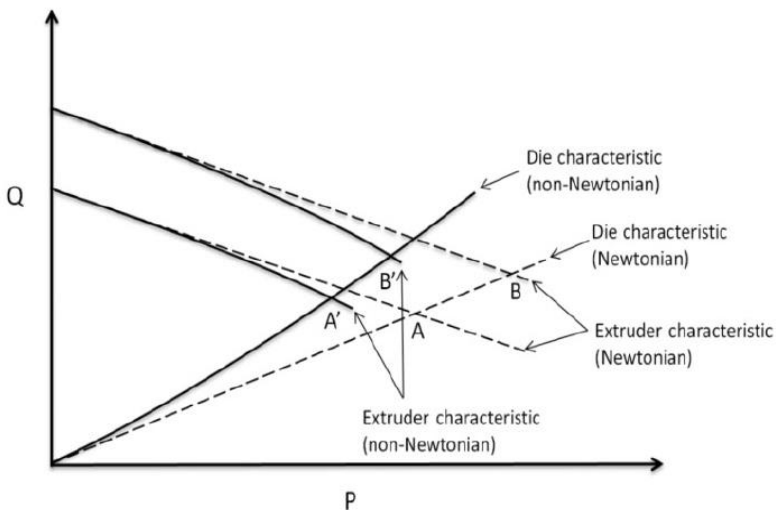

Figure 2.2-5 Schematic depiction of the output of a single-screw extruder (Q) as a function of head pressure (P)

Usually, single-screw extruders operate with flood feeding, while twin-screw extruders are starve fed. Substantial improvements in mixing and melting actions are found in the starve-fed twin-screw extruders, and this leads to the concept of starve feeding for single-screw extruders. Global models for flood-fed single screw extruders have been studied and developed many years ago.[179] In recent years, Wilczynski *et al*.[180] proposed a model for melting in starve-fed single screw extruder, and this later developed into a global model for conventional and nonconventional starve-fed single screw extrusion process.[181,182] Lately, they have proposed a composite model for starve/flood fed mixing single screw extruders.[183]

Langauer *et al*[184] pointed out that the shape and the dimensions of the pellets significantly affected the output of a small scale single screw extruder when processing PP. It was found that the dimensions and higher external coefficient of friction of cylindrical pellets led to higher extruder output in comparison to the virgin pellets. Process energy behaviour and melt thermal fluctuations in single screw extrusion were investigated by Abeykoon *et al*.[185] It was reported in their work that extruder specific energy consumption decreased with screw speed, while melt thermal fluctuations increased with screw speed. Moreover, the polymer type showed a great influence on the level and fluctuations of the extruder's power factor. Also, a possible relation between the level of energy demand of the heaters and the level of melt temperature fluctuations was pointed out.

Overall, single screw extrusion is simple and can achieve a consistent product in a short time. Solid conveying, melting, pumping and mixing occur simultaneously and are interdependent. In this research programme, process parameters related to the single screw extrusion of recycled PP blends will be analysed using a DoE approach.

(B) Twin screw extrusion

Process control of single screw extrusion is difficult and mixing is insufficient. The transport method is pressure sensitive, and the pressure induced by the die causes backflow along the metering zone, which significantly limits the conveying capacity and production of single screw extrusion. To achieve greater operating flexibility and

greater process control, twin-screw extruders were developed. Figure 2.2-6 is a schematic diagram of a typical twin-screw extruder.

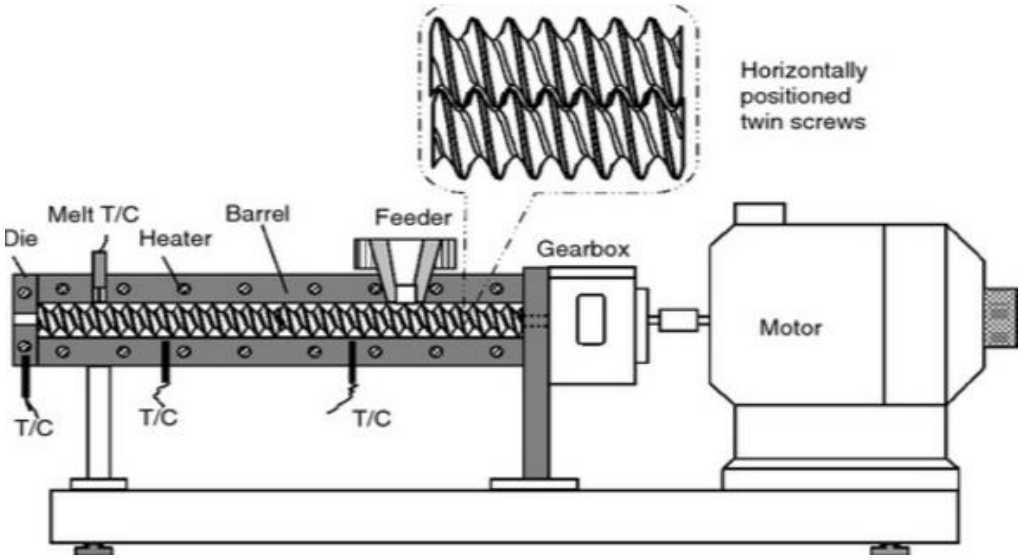

Figure 2.2-6 Components and features of a twin-screw extruder[186]

In terms of basic designs,[177,178] twin screw extruders can be co-rotating, counter-rotating, intermeshing or non-inter meshing. The APV MP30TC extruder to be used in this research project is a co-rotating intermeshing twin screw extruder.

Single screw extruders act as a 'screw viscosity pump' while twin-screw extruders are 'closed cell pump', in terms of melt transport pumping mechanism. Due to the difference in pumping mechanism, the transfer method of twin-screw extruder is not particularly sensitive to pressure, as shown in Figure 2.2-7.

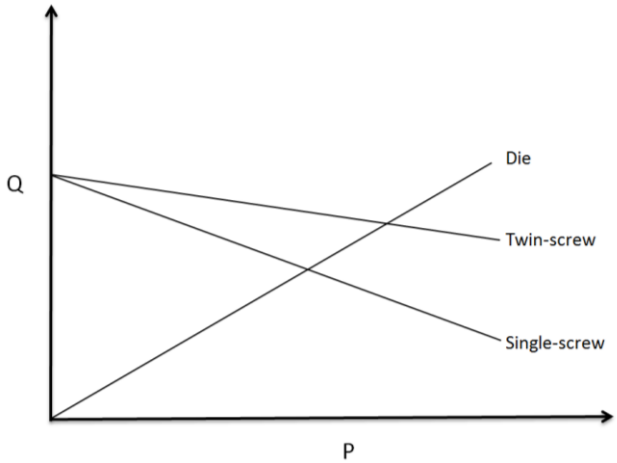

Figure 2.2-7 Die/extruder characteristics for sing/twin screw extruders

Normally, twin-screw extruders operate by starve-feeding. Thus, under steady state, the output of a twin-screw extruder is simply determined by the feed rate. In a co-rotating twin screw extruder, the average residence time can be estimated by[187]:

$$\bar{t} = \frac{A}{Q} + \frac{B}{N} \tag{2.2-12}$$

where A and B are constant for specific screw configurations, Q is volumetric throughput and N is screw speed. As mentioned previously in section 2.1.6, for twin screw extrusion, the residence time and shear rate/stress have significant effects on the dispersion of clay in PP matrix. The effects of processing parameters of twin-screw extrusion are not repeated here.

Increasing screw speed leads to increased localised shear rates in co-rotating twin-screw extruders, increasing shear non-uniformity. Shear rates induced by kneading paddles with different geometries were investigated by Padmanabhan *et al*.,[188] and they pointed out that kneading elements with fractional lobed geometry having unequal tip angles showed greater shear uniformity, minimising excessive shear in small regions. Although the evolution of pressure, temperature, shear rate, degree of fill *etc.* are complex in a twin-screw extruder, the modelling and simulation of twin-screw extrusion processes have been reported in some studies.[189–191]

In this research project, the processing parameters of twin-screw extrusion for the melt-compounding of PPCNs will be optimised using DoE approach. Then, the PPCNs compounded with twin screw extrusion under optimised conditions would be used for the injection moulding and other subsequent studies.

2.2.3 Injection Moulding

(A) General

Injection moulding is potentially the most important processing method for PPCN components. A schematic diagram of an injection moulding machine is shown in Figure 2.2-8. To some extent, the first step of injection moulding is very similar to a single screw extrusion process. Plastic resin is fed into a feed hopper through which it enters the barrel. The material is then heated up to molten state as it is conveyed

towards the nozzle by the rotating screw. A reservoir of plastic melt is formed at the front of the screw. When a certain volume of melt is achieved, the molten plastic is forced through a nozzle into a mould which is tightly clamped. After sufficient cooling, the material solidifies and the mould opens, the shaped article is then ejected. Then the moulding cycle is repeated.

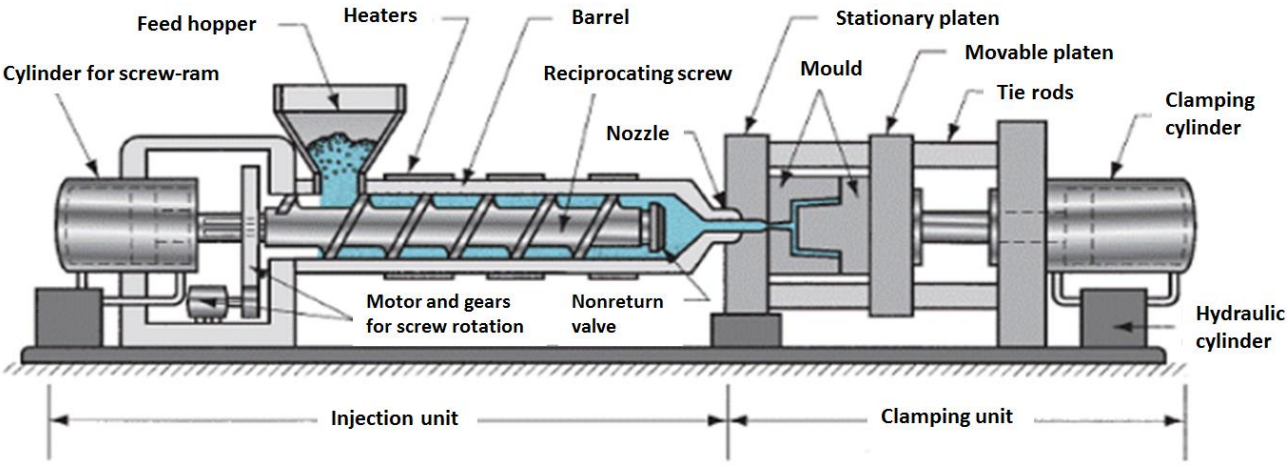

Figure 2.2-8 Components and features of an injection moulding machine[192]

In comparison to the other processing methods, the major advantages of injection moulding are:[193]

- The versatility in moulding a wide range of products
- The ease with which automation can be introduced
- The possibility of high production rates
- The manufacture of articles with close tolerances
- The concept can also be adapted for use with thermosetting materials and elastomers.

Maximum shot weight/volume and maximum clamp force are the most important specification parameters for injection moulding machines. For example, the injection moulding machine to be used in the project is Negri-Bossi NB62 machine, which has a screw diameter of 28 mm, a maximum shot volume of 84 cm^3 and a maximum clamp force of 62 tonnes. When designing the mould tool in this project, those parameters would be of great importance.

Injection moulding cycle time is shown below, and the cycle can be divided into several phases. An optimised cycle time is important for industrial manufacturing,

which always focuses on optimised productivity and quality. Generally, the cycle consists of:

- Injection phase
- Cooling (packing, screwback, suckback/decompression)
- Mould opening
- Ejection
- Mould closing

The injection phase is velocity/displacement controlled, and the packing phase is pressure controlled. Hence, there is a V/P switch-over during an injection moulding cycle. Correctly controlled in-cavity pressure during injection moulding cycle guarantees a sustainable quality improvement and a reduction in scrap. Therefore, the monitoring of cavity melt pressure data is very important. Figure 2.2-9 shows a typical measured in-cavity pressure profile.

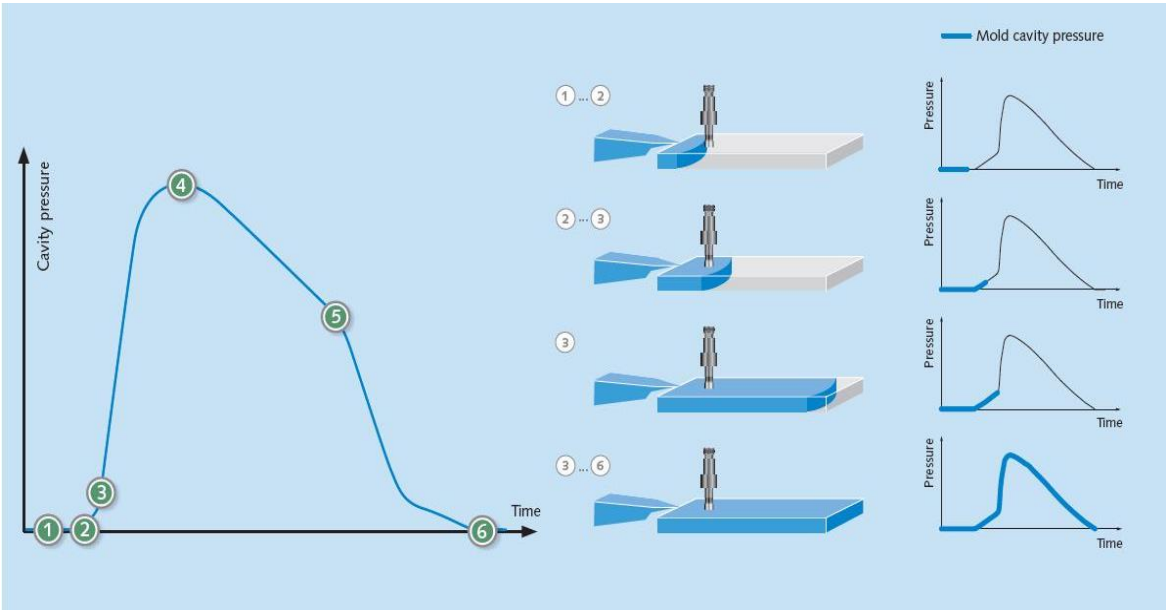

Figure 2.2-9 A typical measured in-cavity pressure profile[194]

It is very clear that the plastic melt enters the cavity at the start of injection phase at a pre-set rate (1), but it does not reach the pressure sensor yet. As soon as the flow front reaches the sensor (2), the pressure can be measured. The pressure will increase linearly with filling time, until the end of the injection phase (3) has been reached after the volumetric filling of the cavity. The melt will be compacted during the packing phase to guarantee the moulding of the part contours, and the packing

phase starts after the maximum cavity pressure has been reached (4). The high volume shrinkage of the plastic material due to cooling is compensated during this phase by pressing additional material into the cavity until the gate freezes (5). Due to the continued thermal contraction, the in-cavity pressure drops to ambient pressure (6).[194]

In this research programme, a pressure sensor will be installed in the mould to measure the real-time in-cavity pressure, in order to investigate the effects of processing conditions on cavity pressure as well as the properties of moulded parts.

Some useful calculations for injection moulding process are briefly presented here, according to the calculation methodology cited by Lenk.[195] The clamp force (F) required for an injection moulding process can be calculated using the following equation:

$$F = \frac{\Delta P}{A} \tag{2.2-13}$$

where ΔP is the pressure developed during mould filling/ packing, and A is the overall projected area of parts.

As mould filling stage is a non-isothermal process, there is a highly oriented layer frozen immediately below the part surface, due to a combination of high shear stress and high cooling rate adjacent to the mould wall. This frozen layer formed during mould filling results in reduced channel depth.

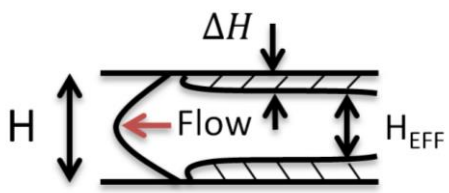

Figure 2.2-10 Decreased channel depth due to the formation of frozen layer

Therefore, the effective (H_{EFF}) channel depth is:

$$H_{EFF} = (H - 2\Delta H) \tag{2.2-14}$$

where H is the channel depth, ΔH is the thickness of frozen layer.

It is known that $$\Delta H = Ct^{1/3} \tag{2.2-15}$$

where C is freeze-off constant, t is filling time. Therefore, the pressure drop for mould filling can be calculated by the following equation:

$$\Delta P = \frac{2LK(\frac{6Q}{W})^n}{H^{2n+1}\left[1-\frac{2C}{H^{\frac{2}{3}}}(\frac{WHL}{Q})^{1/3}\right]^{2n+1}} \tag{2.2-16}$$

where W, H and L are the channel width, depth and length respectively, K is the power law consistency index, n is the power law index, Q is the volumetric flow rate. Furthermore, cross-WLF equation which has been presented previously as Equation (2.2-8), can be integrated into Equation (2.2-16) above to obtain a new equation for ΔP. The relationship between pressure drop and volumetric flow rate under non-isothermal condition is described clearly by Equation (2.2-16), which is shown as the solid line in Figure 2.2-11.

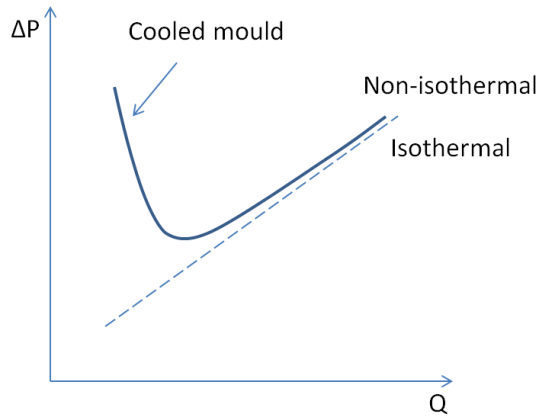

Figure 2.2-11 Filling pressure vs. volumetric flow rate

Clearly, Figure 2.2-11 shows that at very low volumetric flow rate, the filling pressure is extremely high. This is because the frozen layer is so thick resulting in very narrow effective channel depth, and thus massive pressure is required to force the melt through the channel. With increasing volumetric flow rate, the filling pressure of non-isothermal process is increasingly close to that of isothermal process, because the frozen layer becomes thinner and thinner leading to less difference between the non-isothermal and thermal conditions. Also, higher volumetric rate generates more shear heating, leads to local increase in temperature reducing frozen layer thickness.

For injection moulded PP parts, at least two regions are noticeable across a specimen thickness.[196–198] As shown in Figure 2.2-12, the first frozen surface layer (A) is called ‘the skin’, while the zone in the middle of the cavity (C) is called ‘the

core'. The region between them is called 'the shear zone' due to the foundation flow.[196] The skin layer possesses a highly oriented shish-kebab like structure and has a homogenous appearance with no discernible morphological features.[199]

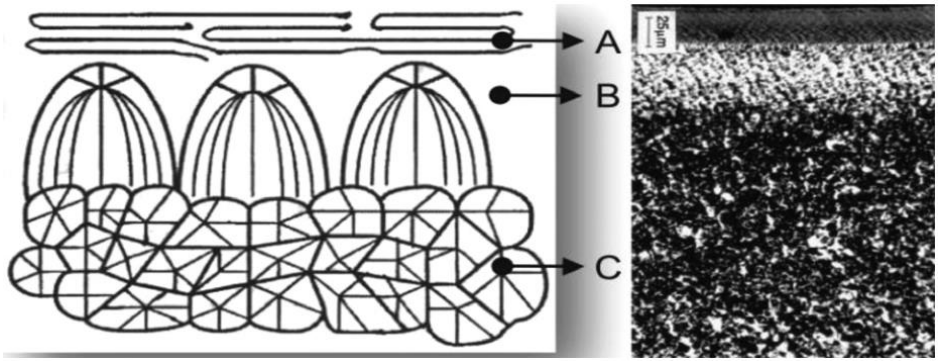

Figure 2.2-12 Morphological structure of moulded PP part: A – non-spherulitic skin, B – intermediate zone, C – inner spherulitic core [198]

The development of the oriented skin layer in injection moulding has been widely studied in the past decades, as the thickness of skin layer has been evidenced as a highly significant microstructural parameter.[200–203] It has been reported that skin layer thickness is controlled by the combined effect of the thermal and stress field imposed during processing, both of which determine the cooling and crystallisation conditions.[202,204,205] The development of skin can also be interpreted in the light of two main factors: the time allowed for relaxation until the crystallisation temperature is reached and the material relaxation time.[202] The skin thickness increases with reduced (melt and mould) temperatures and flow rates,[201,202,205] whilst skin thickness decreases with the reduction of the average molecular weight of the material,[204] and narrowing of its molecular weight distribution.[206] The presence of nucleating agents also has a significant effect on the skin thickness.[207] The skin-core morphology has been reported to have great effects on the mechanical properties of injection moulded PP parts, and large skin-core effect lead to a higher tensile strength and Young's modulus, but lower ductility.[196]

According to Viana *et al.,*[208] the thermomechanical environment (TME) in injection moulding is defined by the part mould geometry, the intrinsic material properties and the injection parameter whose combinations lead to specific profiles of pressure, temperature, shear rate and stress. They related the imposed TME to the skin layer thickness and interpreted the relationship in the light of a phenomenological

model.[205] In their later work,[27,28] the relationship between the injection moulding processing conditions, the applied TME and the tensile properties and impact properties of talc-filled polypropylene was established. The effects of injection moulding conditions on the mechanical properties of moulded PP parts have been reported in many other studies.[29,196,209,210] However, there is very little work that has been reported for the injection moulding of PP/clay nanocomposites (PPCNs) so far.

(B) Thin-wall injection moulding

Multifunctional mobile products such as smartphones, laptop computers and personal media players have become smaller and lighter. Thus, the technology of thin-wall injection moulding has been highlighted for making lightweight and portable electronic products in the fields of automotive, communication, medical and packing *etc*. A product that has a thickness less than 1 mm with an aspect ratio of more than 100 should be considered as thin wall moulding. However, the fast solidification of molten material during the thin-wall injection moulding can be an important issue, thus, high speed and high pressure injection conditions are required to decrease the time for filling molten resin in the cavity. High shear stress and shear rate are generated as a result of the extreme injection conditions, and this promotes the flow-induced molecular and particle orientation in the thin-wall injection moulded parts. In addition, residual stress generates due to the rapid but inhomogeneous cooling of the parts. To date, many studies focusing on thin wall injection moulding have been reported.[23–25,211–215]

Moon *et al*.[24] studied the effect of processing conditions on the dart impact properties of thin-wall injection moulded polycarbonate plates. Specifically, the effects of injection speed, gate size and melt temperature were investigated. It was found that the mass of thin wall injection moulded parts increased as the gate size increased, due to uniform transmission of the pressure to the molten material. Also, increasing melt temperature slightly increased the mass of injection moulded parts. The effect of injection speed was not clearly resolved. In terms of dart impact properties, the major determining factor was the gate size and the gate location rather than melt temperature and injection speed.

Chen *et al*.[211] investigated the tensile properties of polycarbonate thin-wall injection moulded parts. Combining the resulting mechanical properties with the residual stress measured, they pointed out that for the thin-wall injection moulding of PC, residual stress played a more significant role in influencing mechanical properties. Part thickness and injection speed were the most significant factors affecting residual stress. As part thickness decreased, residual stress increased resulting in greater reduction of part tensile strength, yield stress and Young's modulus. In addition, lower melt temperature, lower mould temperature, higher packing pressure and longer injection time led to greater residual stress and thus decreased mechanical properties. Liao *et al*.[213] investigated optimal process conditions and shrinkage and warpage of cellular thin-wall parts using Taguchi's method. It was found that increasing packing pressure could reduce the shrinkage and warpage of the thin wall injection moulded parts. However, optimal processing conditions were different in terms of minimising shrinkage and warpage, because the mechanisms affecting shrinkage and warpage were different. The shrinkage is due to the increase in density when the thermoplastic inside the cavity solidifies, while warpage is caused by uneven thickness and shrinkage in various directions. It is found that the geometry of a real commercial part does affect the optimal conditions and the order of influence of process parameters.

Wang *et al*.[215] thoroughly investigated the effects of the processing conditions on the residual stress in thin-wall injection moulded ABS parts by comparing the numerical simulation and the measured deformations and curvatures obtained by the layer-removal method, which is briefly presented here. Figure 2.2-13 shows the layer to be removed from the thin-wall injection moulded part clearly indicated.

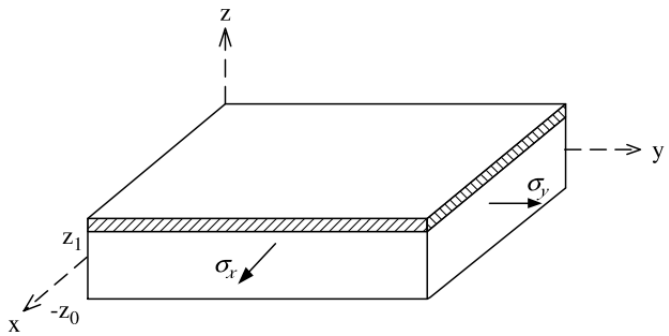

Figure 2.2-13 A flat moulding part and the layer to be removed in layer removal method.[215]

The final equation for calculating the residual stress in x-direction is obtained as: [215]

$$\sigma_x(z_1) = -\frac{E}{6(1-\nu^2)}\left\{(z_0+z_1)^2\left[\frac{dk_x(z_1)}{dz_1}+\nu\frac{dk_x(z_1)}{dz_1}\right]+4(z_0+z_1)\left[k_x(z_1)+\nu k_y(z_1)\right]-2\int_{-z_0}^{z_0}\left[k_x(z_1)+\nu k_y(z_1)\right]dz\right\} \quad (2.2\text{-}17)$$

where, z_0 and z_1 are the half thickness and the left thickness above the original middle plane of the part respectively, E is Young's modulus, ν is Poisson's ratio, k_x and k_y are the curvatures in the x- and y-directions. The curvature can be estimated by the following equation:[215]

$$k_x = \frac{1}{\rho} \quad (2.2\text{-}18)$$

$$\rho = \frac{L^2+4\phi^2}{8\phi} \quad (2.2\text{-}19)$$

The definitions of ϕ, L and ρ are shown illustrated in the figure below.

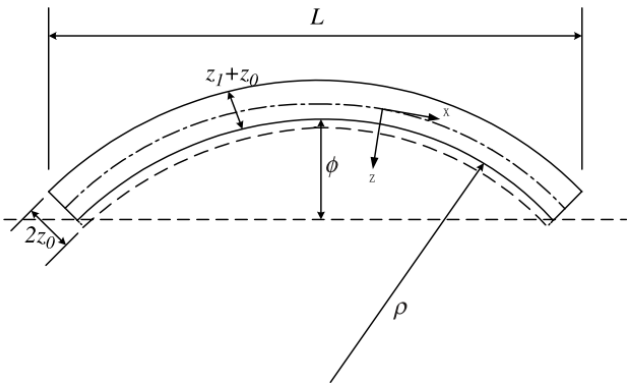

Figure 2.2-14 Determination of the curvature of a deformed bar [215]

Assuming the part has equal residual stress and curvatures in x- and y- direction, which is a common case, the equation for residual stress can be further simplified as:[215]

$$\sigma_x(z_1) = -\frac{E}{6(1-\nu)}\left\{(z_0+z_1)^2\frac{dk_x(z_1)}{dz_1}+4(z_0+z_1)k_x(z_1)-2\int_{-z_0}^{z_0}k_x(z_1)dz\right\} \quad (2.2\text{-}20)$$

So far, many studies focusing on thin wall injection moulding have been reported, but very few of them focused on the thin-wall injection moulding of PP/clay nanocomposites. In this research project, the thin-wall injection moulding for PP/clay nanocomposite will be performed, the effects of processing conditions and wall-thickness will be investigated.

2.2.4 Real-time simulation: Moldflow® Insight

Autodesk Moldflow Insight is a software package designed to simulate the plastic injection moulding process. The software package has a single common user interface called Autodesk Moldflow Synergy and a range of analysis products. They work together to provide an insight into many aspects of injection moulding of plastics by advanced simulation techniques. The software package is simply presented in this section according to the documentation of Moldflow®.[216]

Synergy provides a quick simple method for preparing, running and post-processing an analysis for a model. Multiple cavities, runner systems, cooling circuits, mould boundaries and inserts can be easily created with the wizards in Synergy. Also, a material searching capability for the extensive material database is included in Synergy. Once a 3D model designed for injection moulding is created by other CAD software, it can be readily imported into Moldflow® Synergy in a suitable format that can be read by Synergy, then the analysis of the model can start. One of the most important steps before starting the analysis in Synergy is known as meshing, which directly determines the accuracy of the analysis and thus the whole simulation results, and also influences computing time to solve complex problems.

Mesh entities are known as elements. In other words, the model to be analysed by Synergy needs to be meshed into small elements first. Each element is the smallest unit that is analysed by the software when simulating dynamic flow and heat transfer in the injection moulding process. The simulation of the whole injection moulding process is carried out by analysing these numerous mesh entities one by one. Different element types are used to model different mesh types. There are three element types, and they are shown as follows:

- *Beam elements*: They are 2-noded elements, and they are used for modelling cold runners or cooling channels.
- *Triangle elements*: They are 3-noded elements and used for modelling Midplane or Dual Domain mesh types.
- *Tetrahedral elements*: They are 4-noded elements used to model the 3D mesh type.

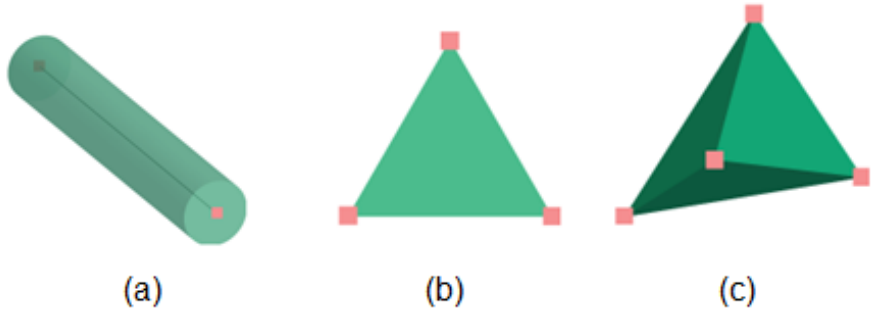

Figure 2.2-15 Images for (a) beam elements; (b) triangle elements and (c) Tetrahedral elements

Dual Domain is usually used for thin structures and 3D mesh type is widely used for thick structures. Considering the objective of this research programme, Dual Domain mesh type would be the most suitable analytical method. The figure below shows an original model designed by the CAD software NX, and the meshed model after imported into Synergy.

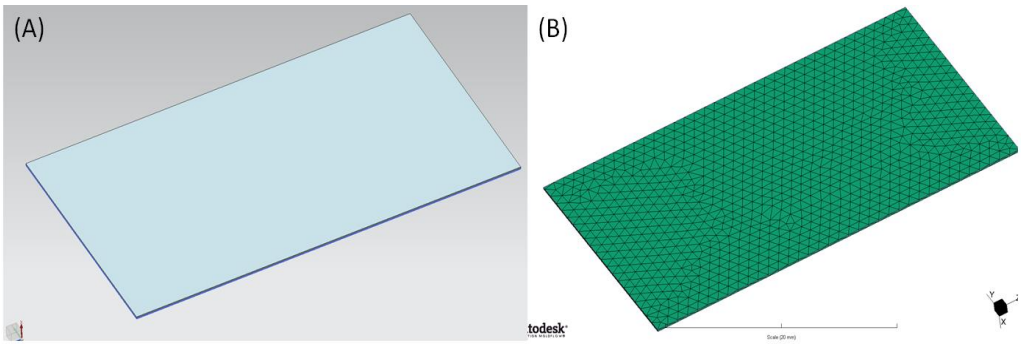

Figure 2.2-16 A simple thin-walled model designed by NX (A) and meshed in Moldflow Synergy (B)

The model above has a thickness of 0.2 mm and a surface dimension of 36x20 mm. After meshing, 3786 elements have been generated.

Mesh density can be altered by changing the size of the elements. It is apparent that for a fixed model, the finer the elements, the more accurate the analysis will be. However, a finer size gives much more mesh entities, which means much more processing/computing time is required for the analysis. An analysis run in Synergy takes from a few minutes to a couple of hours, or even longer; this is dependent on the number of elements in the model and the computing power available. Therefore, it is necessary to achieve a good balance between accuracy and simulation time.

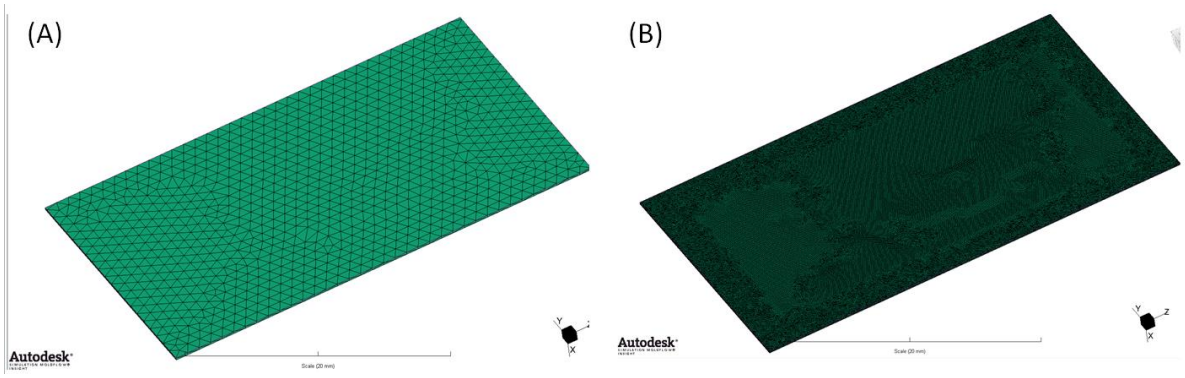

Figure 2.2-17 A comparison between (A) coarse mesh (3786 elements) and (B) fine mesh (246072 elements)

As mentioned previously in section 2.2.1, analysis of the polymer melt flow in Moldflow Synergy is based on the Cross/WLF equation:

$$\eta = \frac{\eta_0}{1+\left(\frac{\eta_0 \dot{\gamma}}{\tau^*}\right)^{1-n}} \tag{2.2-8}$$

where:

$$\eta_0 = D_1 exp\left[\frac{A_1(T-T^*)}{A_2+(T-T^*)}\right] \tag{2.2-9}$$

The database of Synergy offers Cross/WLF model coefficients for different materials. For example, the 'generic PP' which is used as a default material in Moldflow Synergy has the following coefficients:

$$n = 0.2916$$

$$\tau^* = 28233 \quad Pa$$

$$D_1 = 8.94e + 014 \quad Pa.s$$

$$D_2 = 263.15 \quad K$$

$$D_3 = 0$$

$$A_1 = 32.563$$

$$A_2 = 51.6$$

After taking these coefficients into Cross/WLF equation, idealised flow curves can be obtained at different temperatures. The flow curves of 'generic PP' are shown below:

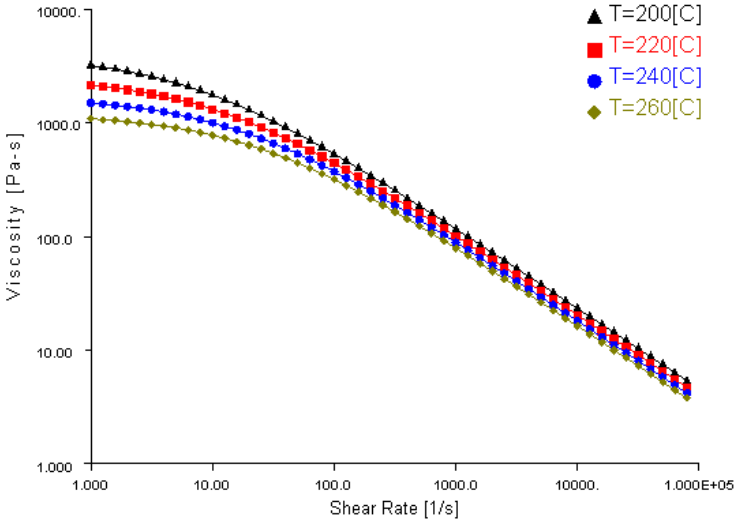

Figure 2.2-18 Flow curves of 'generic PP' produced by Moldflow Synergy

The figure below shows a picture of the simulated injection moulding process in Synergy with 'generic PP', which is on the basis of Cross/WLF equation shown above.

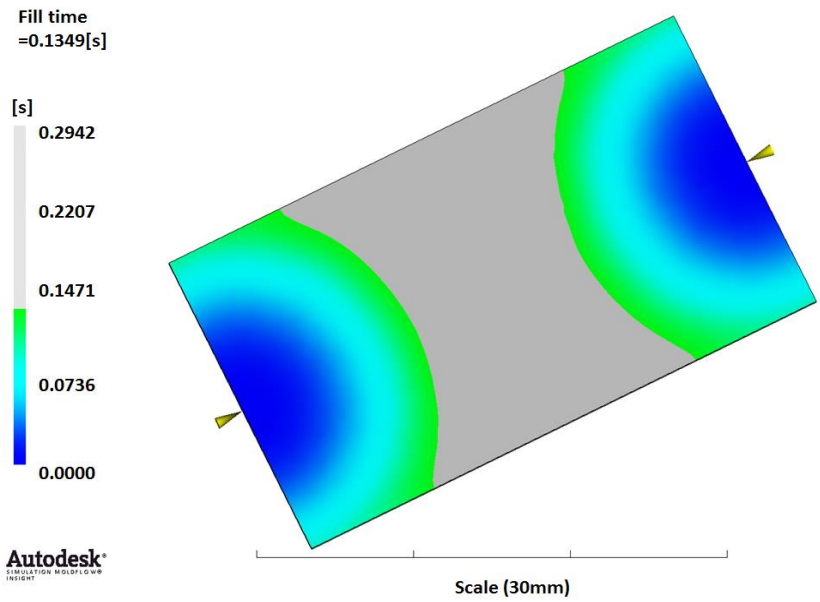

Figure 2.2-19 Simulation of injection moulding in Synergy

The PP materials to be used in this research programme are Sabic 571P and PHC 26, provided by Sabic UK Ltd. The coefficients of the two grades of PP provided by Moldflow database are list in Table 2.2-1.

Table 2.2-1 Coefficients for Sabic 571P and PHC26

Coefficient	571P	PHC 26
n	0.2916	0.2709
τ^* (Pa)	28233	55483.2
D_1 (Pa.s)	8.94E+14	1.25E+12
D_2 (K)	263.15	263.15
D_3 (K/Pa)	0	0
A_1	32.563	25.112
A_2 (K)	51.6	51.6

2.3 Statistical Approach: Design of Experiments (DoE)

2.3.1 Concept of DoE

The terminology, Design of Experiments (DoE), is a statistical concept that is widely used in research quality control and product or process improvement. To gain a good understanding of DoE, some basic statistical background of quality control and assurance needs to be introduced first.

Today, the modern definition of quality is more preferable: quality is inversely proportional to variability. Variability particularly refers to unwanted or harmful variability, but there are situations in which variability is actually good. Based on the modern definition of quality, quality improvement is defined as the reduction of variability in processes and products or the reduction of waste.[217]

Every product possesses a number of elements that jointly describe what the user or consumer thinks of as quality. These parameters are often called quality characteristics, and they may be of several types:[217]

1. Physical: length, weight, voltage, viscosity
2. Sensory: taste, appearance, colour
3. Time orientation: reliability, durability, serviceability

The different types of quality characteristics can relate directly or indirectly to the dimensions of quality discussed above. Data on quality characteristics is classified as either ‘attributes’ or ‘variables’. Variables data are usually continuous measurements, such as length, viscosity or voltage. On the other hand, attributes data usually describe discrete data, often taking the form of counts. A value of

measurement that corresponds to the desired value for that quality characteristic is called the nominal or target value for that characteristic. The largest allowable value for a quality characteristic is called the upper specification limit (USL), and the smallest allowable value for a quality characteristic is called the lower specification limit (LSL).[217]

There are three management aspects of quality improvement: quality planning, quality assurance, and quality control and improvement. Since variability is often a major source of poor quality, statistical techniques are the major tools of quality control and improvement. The major statistical techniques for quality control and improvement are: [217]

- Statistical process control (SPC): A control chart is one of the primary techniques.
- Design of experiments (DoE): This is extremely helpful in discovering the key variables influencing the quality characteristics of interest in the process. One major type of designed experiment is the factorial design, in which factors are varied together in such a way that all possible combinations of factor levels are tested.
- Acceptance sampling: This is defined as the inspection and classification of a sample of units selected at random from a larger batch or lot and the ultimate decision about disposition of the lot.

Obviously, the DoE method is the technique that will be focused upon, in this research. In statistics, the quality characteristic of interest is called a response, and the variables influencing the quality characteristic of interest are called factors. Before further review of DoE, the concepts of quality engineering and corresponding statistics must first of all be introduced to the area of materials science. Any properties of a material that we would like to study, such as tensile strength, modulus or toughness are actually quality characteristics, or known as responses in statistical terminology. Any variables influencing the properties of the material such as the concentration of fillers, the processing temperature or the crystallisation conditions etc. are the corresponding factors of the responses. Therefore, DoE approach can be a very powerful statistical tool when investigating materials science, to predict accurate responses from the input factors, whilst minimising experimental time.

A designed experiment or DoE is a test, or series of tests, in which purposeful changes are made to input variables of a process so that we may observe and identify corresponding changes in the output response. When there are several factors of interest in an experiment, a factorial design should be used, where designs factors are varied together. The effect of a factor is defined as the change in response produced by a change in the level of the factor. This is called a main effect because it refers to the primary factors in the study. In some experiments, the difference in response between the levels of one factor is not the same at all levels of the other factors. When this occurs, there is an interaction between the factors. When an interaction is large, the corresponding main effects have little meaning. Thus, knowledge of the interaction is often more useful than knowledge of the main effect, since a significant interaction can mask the significance of main effects. Therefore, interactions between the factors should be considered seriously.

A factorial design with k factors, each at two levels, is called a 2^k factorial design, because each complete replicate of the design has 2^k runs. The 2^2 Design is the simplest 2^k design, and the design can be represented geometrically as a square with the $2^2 = 4$ runs forming the corners of the square.

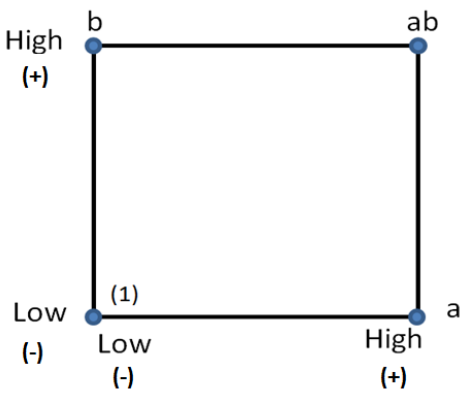

Figure 2.3-1 Test matrix of the 2^2 factorial design.[217]

The figure above shows the 4 runs in a tabular format often called the test matrix. Each run of the test matrix is on the corners of the square and the – and + signs in each row show the settings for the variables A and B for that run. The effect of factor A and B, and the interaction AB, can be calculated by the method called the analysis of variance (ANOVA), and the equations are shown below:[217]

Effect A: $A = \frac{1}{2n}[a + ab - b - (1)]$ (2.3-1)

Effect B: $B = \frac{1}{2n}[b + ab - a - (1)]$ (2.3-2)

Interaction AB: $AB = \frac{1}{2n}[ab + (1) - a - b]$ (2.3-3)

where a, b, ab and (1) are the totals of all n observations taken at these design points (Figure 2.3-1).

The 2^2 design is the simplest one, so for the 2^k design, regression model and residual analysis are used. The equation below is a typical regression model for the 2^2 design.

$$y = \beta_0 + \beta_1 x_1 + \beta_2 x_2 + \beta_{12} x_1 x_2 + \epsilon \quad (2.3\text{-}4)$$

where y is the response and the factors A and B are represented by coded variables $x_1$and x_2, and the AB interaction is expressed by the cross-product term in the model, $x_1 x_2$. The coefficients β_0, β_1, β_2 and β_{12} are named regression coefficients, and ϵ is a random error term.

If the response is well modelled by a linear function of the independent variables, then the function is known as the first-order model (Equation 2.3-4). On the other hand, if there is curvature in the system, a model with a higher order must be used, such as second-order model. The second-order is most widely used, because it is more accurate than the first-order model, but it is much simpler than the models with higher degree given that it can provide adequate accuracy. Equation 2.3-5 shows a full second-order regression model.

$$y = \beta + \beta_1 x_1 + \beta_2 x_2 + \beta_{12} x_1 x_2 + \beta_{11} x_1^2 + \beta_{22} x_2^2 + \varepsilon \quad (2.3\text{-}5)$$

The significance of the models can be examined by calculating and comparing F-ratios or p-values. The calculation methodology cited by Montgomery [32] is briefly introduced here. Assume a single factor with *a* different levels or treatments has *n* observations for each treatment. Total sum of squares (SS_T), treatment sum of squares ($SS_{Treatments}$) and error sum of squares (SS_E) can be calculated as follows:

$$SS_T = \sum_{i=1}^{a} \sum_{j=1}^{n} \left(y_{ij} - \bar{y}\right)^2 \quad (2.3\text{-}6)$$

$$= n \sum_{i=1}^{a} (\bar{y}_{i\cdot} - \bar{y})^2 + \sum_{i=1}^{a} \sum_{j=1}^{n} \left(y_{ij} - \bar{y}_{i\cdot}\right)^2$$

$$= SS_{Treatments} + SS_E$$

where y_{ij} represents the *j*th observation taken under treatment i, $\bar{y}_{i\cdot}$ stands for the average of the observations under the ith treatment and $\bar{y}$ presents the grand average. The mean square (MS) and F_0 can be calculated by the following equations:

$$MS = SS/D_f \tag{2.3-7}$$

$$F_0 = \frac{\frac{SS_{Treatments}}{a-1}}{\frac{SS_E}{[a(n-1)]}} = \frac{MS_{Treatments}}{MS_E} \tag{2.3-8}$$

where D_f is the number of degrees of freedom that corresponds to the sum of squares in Equation 2.3-6. The ratio F_0 has an F distribution with (a-1) and a(n-1) degrees of freedom. If the F_0 value computed is greater than the critical F value related to a certain significance level (α), that is $F_0 > F_{\alpha,\ a\text{-}1,\ a(n\text{-}1)}$, then the corresponding effect is considered as statistically significant. A p-value is an alternative approach, in which the p-value is equal to the probability above (F_0) in the $F_{\alpha,\ a\text{-}1,\ a(n\text{-}1)}$ distribution:

$$p - value = P[F_{a-1,a(n-1)} > F_0] \tag{2.3-9}$$

The significance level (α) is usually set as 0.05. With F_0 or p-value, it is possible to evaluate whether the variables are significant or the terms in Equation 2.3-5 are necessary.

Generally, the regression models can be simplified by removing the negligible terms with p-values greater than 0.10. On the other hand, the terms with p-values lower than 0.05 can be considered as important and kept in the models. Residual analysis needs to be carried out to confirm the adequacy of the model used. ANOVA assumes that the model errors (and as a result, the observations) are normally and independently distributed with the same variance in each factor, so the validity of the assumption needs to be checked. The normality assumption can be verified by constructing a normal probability plot of the residuals, while the independence assumption can be verified by using plots of residuals against run order.

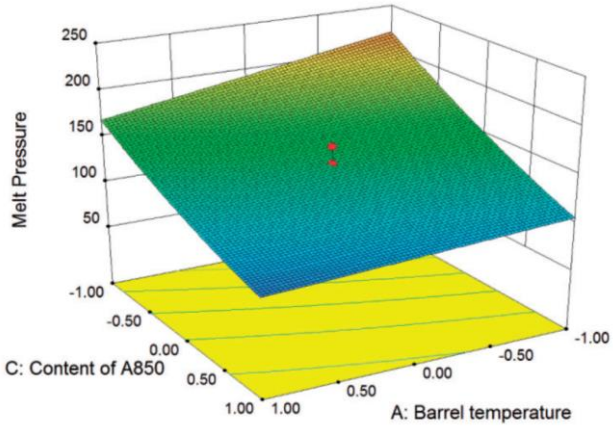

Figure 2.3-2 An example of 3D response surface generated by Design Expert®

Response surfaces can be plotted according to the regression model generated, which are 3D plots showing the plane of predicted response values generated by the regression model. A 3D response surface has many uses such as predicting the response value at a particular point. Figure 2.4-2 shows an example of 3D surface generated in a DoE experiment.

Within a typical design of experiments approach, a central composite design (CCD) is widely used to analyse a second order response surface. Generally, 2^k factorial runs, 2k axial runs, and at least one centre point are required by a CCD, for a set of investigations based upon k factors. In Figure 4.2 is shown the central composite design when k is equal to 2. These show that each numeric factor is varied over 5 levels: ± alpha (axial points), ± 1 (factorial points) and the centre point (0,0).

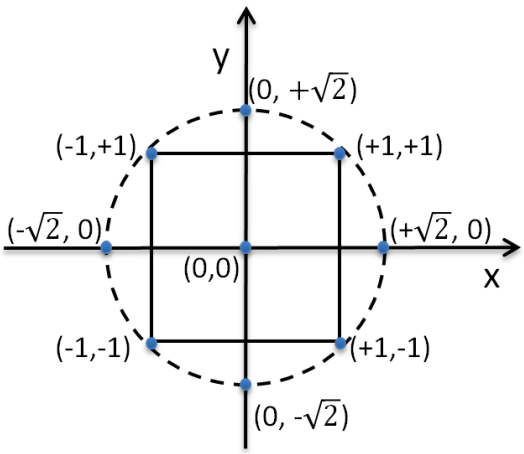

Figure 2.3-3 Central composite design for k = 2

The sparsity of effects principle states that the direct effects and two-factor interactions usually dominate in a system whilst the higher order interactions are

negligible. For this research programme, CCD would be employed for fitting second order surface response models.

DoE methodologies have been widely used in experimental research, and some studies of manufacturing process relating to polymer-based products have been reported in literature. In the field of polymers, DoE approach has been used to investigate blow moulding[218], electrospinning of nanofibers[219,220], mixing and blending processes for polyolefin compounds[221,222] and polymer-based composites[223–225].

Recently, as part of this research project, a study of single screw extrusion dynamics by the DoE approach has been published[1]. Other reported application of DoE in process research have included pharmaceutical products[226], UV-curable coatings[227] and sintered powder metal copper extrudates[228].

2.3.2 DoE Software Package: Design Expert®

The DoE software, Design Expert®, version 8.0.7.1 (Stat-Ease, Minneapolis, USA) is a software application designed to help with the design and interpretation of multi-factor experiments. As the underlying statistical principles of DoE software have been introduced already, this section briefly presents this software package.

A wide range of designs, including factorials, fractional factorials and composite designs such as CCD, are available with Design Expert®. It also offers computer generated D-optimal design for cases where standard designs are not applicable or where an existing design is debatable.

Generally, Factors can be divided into process variables and mixture variables. With a mixture variable, the effect depends on the proportion of a constituent in the mixture rather than on the absolute amount. Process variables have absolute values such as screw speed, barrel temperature or ram pressure, and process variables can be split into continuous and categorical. Continuous means the factor can be varied freely over a range, while a categorical factor is restricted to a few distinct values. In Design Expert®, continuous and categorical variables are described as ‘Numeric’ and ‘categoric’ respectively.

For continuous variables, Design Expert® offers different regression models from first order to higher order. Linear, factorial and quadratic models are the most common ones.

Linear model: $y = \beta_0 + \beta_1 x_1 + \beta_2 x_2 + \epsilon$ (2.3-10)

Factorial model: $y = \beta_0 + \beta_1 x_1 + \beta_2 x_2 + \beta_{12} x_1 x_2 + \epsilon$ (2.3-11)

Quadratic model: $y = \beta + \beta_1 x_1 + \beta_2 x_2 + \beta_{12} x_1 x_2 + \beta_{11} x_1^2 + \beta_{22} x_2^2 + \varepsilon$ (2.3-12)

In the equations above, linear terms of the form $\beta_i X_i$ are main effects, two-factor interactions are in the form of $\beta_i x_i x_j$, and quadratic terms of the form $\beta_{ii} x_i^2$ allow for curvature in the effect of a variable on the response. For categorical variables, the interpretation of the effects is more or less similar.

The first step of starting a DoE experiment is to decide the type of design according to the features of the factors to be studied. The selection is based on if they are process variables or mixtures variables, continuous or categorical and which model is more suitable. Once the type of design has been decided, it is time to run Design Expert®. There are three mains steps involved when running Design Expert®.

Step 1: Design Expert® offers a series of screens in which one can specify the information needed to construct the design, such as names and ranges of the variables. Design layout is given by the software at the end of this step.

Step 2: two types of information, alias pattern and precision of the fitted model, are offered to help check whether a design meets the requirements.

Step 3: Modelling and interpreting the experimental data. A wide range of analytical and graphical techniques for model fitting and interpretation are offered such as 3D response surface shown in Figure 2.3-2.

In this research programme, Design Expert® will be employed initially to investigate the process parameters related to single-screw extrusion of PP blends. In the main part of the PPCN research programme, the DoE approach will be used to:

(1) Optimise PPCN formulation (with clay, compatibiliser and co-intercalant)

(2) Optimise mixing/compounding conditions, for the ideal PPCN formulations.

CHAPTER 3: PROCESS SIMULATION AND DESIGN OF A NEW MOULD TOOL

To study thin-wall injection mouldings and achieve the objectives of this research programme, an injection mould has been carefully designed with the aid of process simulation and CAD modelling, and manufactured in the workshop of Materials Department. The design process of the injection mould required thorough and iterative work, based upon the development of a CAD model, choice of dimensions and within the constraints imposed by the maximum cavity size and moulding machine capacity. This section details the chronological order of research activity involved in its design and construction, to allow the influence of component thickness to be studied, for PP/clay nanocomposites.

3.1 Design of Mould Cavity

At the very beginning, a simple thin mould cavity with different thickness was proposed, in order to investigate the effects of wall thickness on molecular and particle orientation. In consideration of the testing techniques that might be performed on the thin-wall injection moulded parts, such as falling weight impact test, tensile testing, X-ray diffraction analysis *etc*., the simplest and most practical geometry of the cavity was thought to be a flat structure, i.e. machining into the plate only.

The CAD software package used to design the mould tool was Unigraphics NX 7.5. The whole design process is briefly presented in this chapter with graphs and drawings from NX 7.5.

3.1.1 Single-Cavity Design

When using NX 7.5, the sketch plane and orientation on which all of the subsequent drawings and designs were based, were selected first before sketching. The side profile of the single-cavity was plotted first as shown in Figure 3.1-1. A step-profile was proposed, to allow the injection moulded parts to have different wall thicknesses.

By comparing the properties of the thin and thick sections of moulded parts, the influence of component thickness could thus be studied.

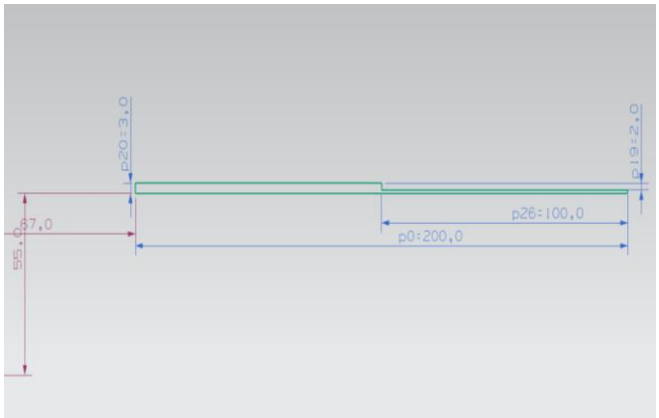

Figure 3.1-1 The side profile of single-cavity

The side profile of the single cavity was then ‘extruded’ by 100 mm to create a 3D model from the 2D sketch. Figure 3.1-2 shows the initial design of the simple single-cavity system.

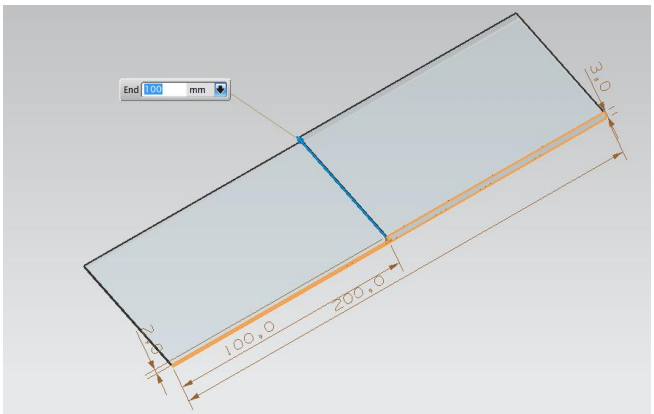

Figure 3.1-2 The initial design of a single-cavity system

For this design, the thinner part was designed to have a thickness of 1 mm, while the thicker part had a thickness of 3 mm. Both parts had a surface of 100x100 mm. Based upon this design, the total volume of the cavity was 35 cm^3, which was far below the maximum shot volume of 81 cm^3, given by the injection machine, Negri-Bossi NB62, in the laboratory. Technically, the design was feasible.

Although this single-cavity design could fully meet the research objective of investigating the effects of wall thickness, it was not really practical and feasible considering the required balance of polymer flow and pressure during injection moulding. The thin and thick parts would undergo very different pressures during

mould filling, resulting in very unbalanced pressure in the whole mould cavity. Such an imbalance in pressure is likely to cause a series of problems and inconsistency for the injection moulding process. Furthermore, having only one cavity would leave a large blank area over the cavity plate of the mould, resulting in a very inefficient and unreasonable use of the expensive injection mould tool. Therefore, the single-cavity design needed to be improved.

3.1.2 Four-Cavity Tool Design

In order to solve the problem of unbalanced pressure induced by single-cavity design and make more effective use of the expensive injection mould, a design for multi-cavity tool was proposed. The design process of multi-cavity system is briefly presented in this section.

The multi-cavity design was processed on the basis of the previous single-cavity design. In the first place, a gate was needed for the polymer melt to enter the cavity. Considering accepted practice that polymer melt should flow from 'thick' features into 'thin' features during injection moulding process, especially for packing phase.[229] A gate was then added on the geometric centre of the end of the thick section, with an initial size 1x1x4 mm (Figure 3.1-3 A).

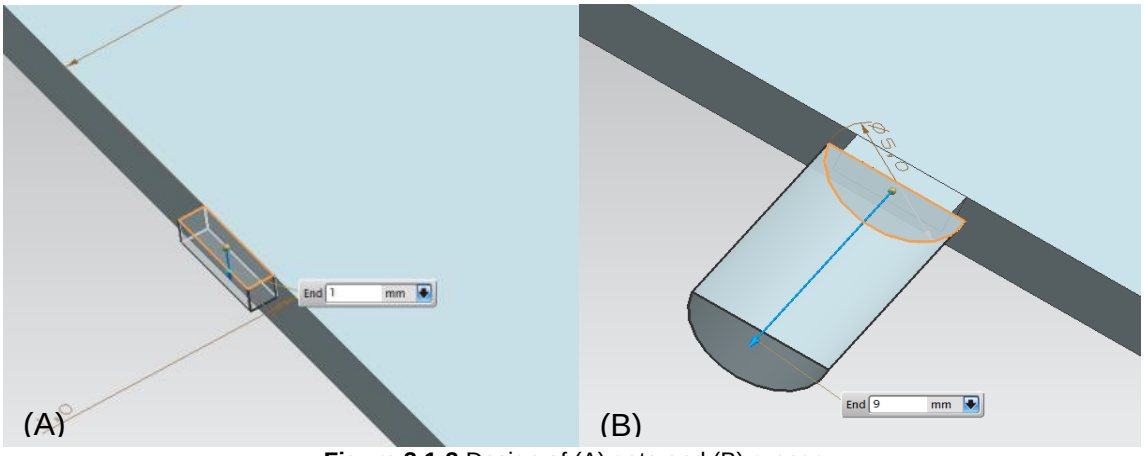

Figure 3.1-3 Design of (A) gate and (B) runner

After the gate was set, runner system was also needed to deliver polymer melt to the gate and thus cavity. The cross-section of the runner was designed as a semicircle with a radius of 5 mm, and then the semicircle was 'extruded' by 9 mm to form the runner (Figure 3.1-3 B).

Afterwards, the whole model including the cavity, gate and runner, were 'mirrored' about the mirror plane to create another half for the multi-cavity system (Figure 3.1-4).

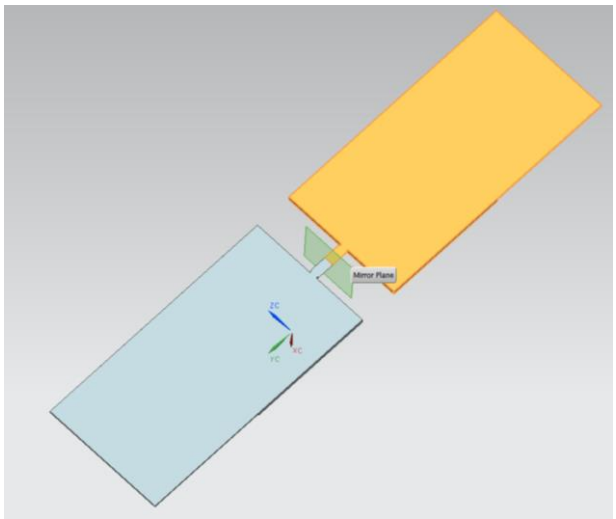

Figure 3.1-4 'Mirror' the body

A main runner was then designed from the geometric centre of the model above. The cross-section of the main runner was also semicircle with a radius of 5 mm. The main runner was formed by 'extruding' the semicircle by 53 mm.

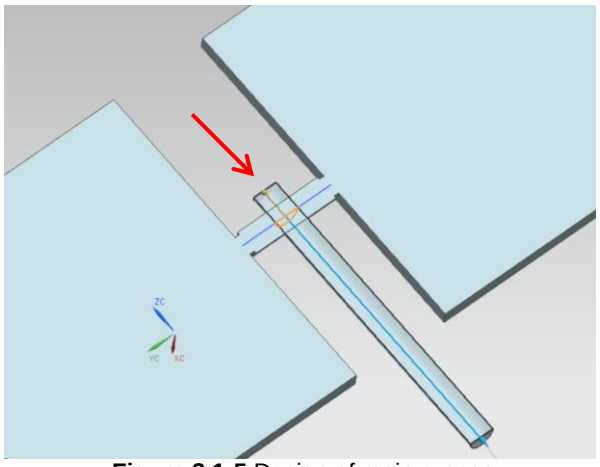

Figure 3.1-5 Design of main runner

A cold material trap, indicated by the red arrow in Figure 3.1-5, was also designed at this step. The function of this feature is to trap the cooler advancing front of the melt, permitting fresh and hotter melt to reach the gates and cavities.[230] The length of the cold slug trap was designed as 3.5 mm.

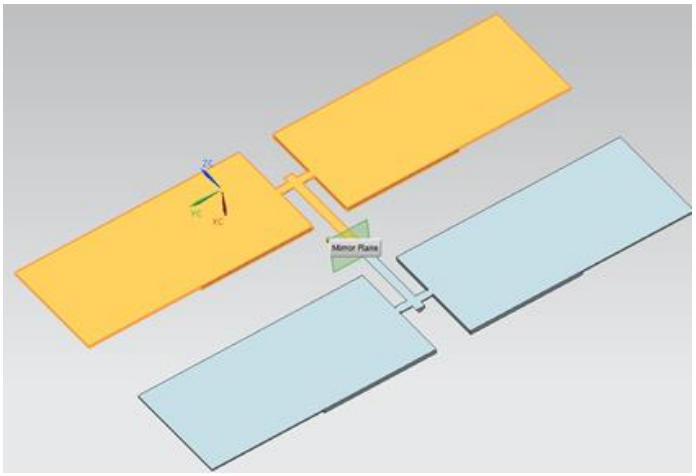

Figure 3.1-6 'Mirror' the body again to get multi-cavity system

The whole model was then 'mirrored' again, to get the multi-cavity, 4-impression system. Afterwards, the sprue and sprue well were added to the system to obtain the final completed four-cavity system. The function of spure well is to trap any cold material remaining in the nozzle tip on the next injection cycle.[230] Figure 3.1-7 shows the finished four-cavity design.

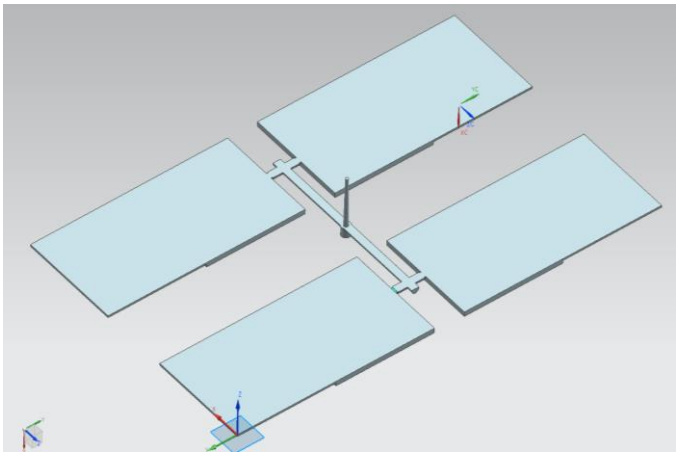

Figure 3.1-7 Finished four-cavity design

Initially, this design had four symmetric cavities, each of which was identical to the single cavity presented previously. As each of the cavities had a volume of 35 cm^3 and the feeding system had a certain volume, the total volume of the whole four-cavity system was far above the maximum shot volume of the injection machine, 81 cm^3. Thus, the size of each cavity needed to be reduced.

For each cavity, the thicknesses of the thin and thick parts were kept as 1 mm and 3 mm respectively, while the surface of each part was reduced to 70x70 mm. After the change was made to the cavity size, the total designed volume of the multi-cavity

system was reduced to 70 cm^3. Although total volume of 70 cm^3 was well below 81 cm^3, the maximum shot volume, it was still considered to be too much. In practice, the shot volume required during mould filling stage should be smaller than approximately three quarters of the maximum shot volume, to ensure complete heating of the material, and to allow sufficient material for packing phase. Thus, 70 cm^3 was still too much to be acceptable, also noticing that the packing phase must follow the injection phase.

3.1.1 Four-cavity design – next generation

In terms of the initial design, the total design volume still needed to be reduced further and some more details of the design needed to be amended. To this end, some further improvements and changes were made to the initial four-cavity design. The thickness of the thick section was further reduced to 2.5 mm, while that of the thin part remained the same. The surface of the thick section was slightly reduced to 66x66 mm, and that of the thin part was changed to 40x66 mm, to reduce the overall part volume.

The decision for the sizes of the thin and thick sections was made out of consideration for the tests of mechanical properties. As thin structures are not usually designed and used where impact strength is required, falling weight impact test would be carried out on the thick section only. The falling weight impact tester in the laboratory requires a disc sample with a minimum diameter of 65 mm. As falling weight impact test was considered as the primary test to be performed on the thick sections, the surface of thick section was thus designed as 66x66 mm, i.e. slightly bigger than the minimum size required.

Tensile test were to be performed with the samples cut from the thin parts. The smallest tensile specimen that can be cut in the laboratory is specimen type A15, BS ISO 20753:2008, which requires a minimum overall sample length of 30 mm. Therefore, the surface of the thin part was designed as 40x66 mm and tensile specimens could be cut in either flow direction or transverse direction.

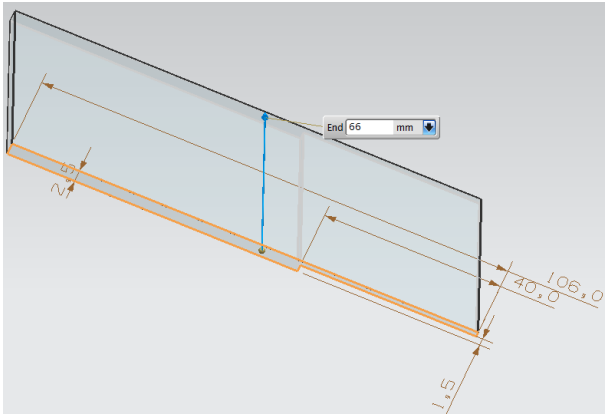

Figure 3.1-8 Improved cavity design

After altering the size of the sprue, the total designed volume of the cavity system was around 56 cm^3, more than sufficiently below the maximum shot volume of the injection moulding machine used. However, it should be noted that the actual dimensions of the spure were unknown at the time, as the spure was a separate item and purchased later. Therefore, the spure design was a best estimation, made for the purposes of flow analysis.

The dimensions of the parts in the designed model are briefly given Figure 3.1-9, but the spure is not shown in the 2D drawings here.

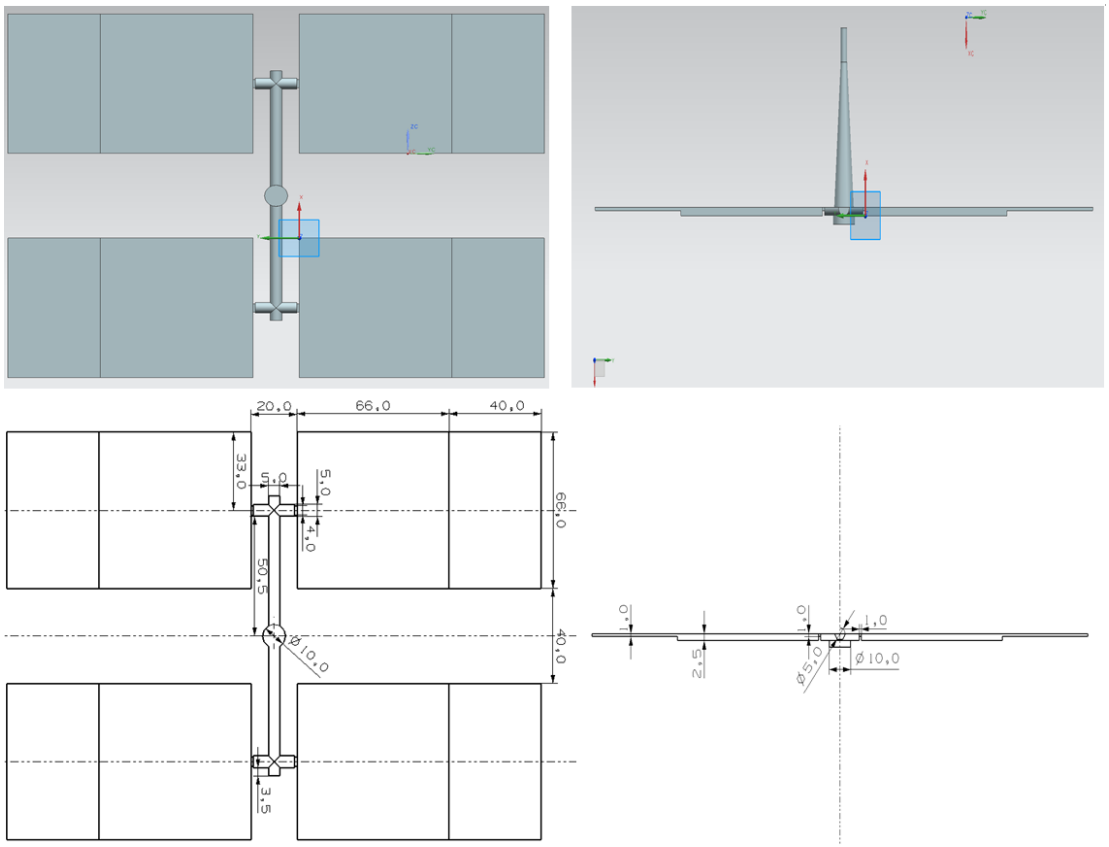

Figure 3.1-9 Dimensions of the designed four-cavity model

3.2 Flow Analysis

After finishing the preliminary design with the CAD software NX 7.5, the designed 3D model was the imported to the software package, Autodesk® Simulation Moldflow Synergy, to simulate injection moulding process and find out the defects existing in the design.

3.2.1 Influence of Mesh Density

As each single cavity designed was thin and flat, dual domain mesh type was selected. Initially, the 3D model was meshed both coarsely (including 11,328 elements) and finely (including 132,500 elements), and the difference caused by mesh density was investigated.

After comparing the simulation results, it was found that the difference in results caused by the different mesh densities was smaller than 1%. In other words, the effect of mesh density was negligible for this designed model. However, for the finely meshed model, the computing time of each simulation run was more than 2 hours, while that of the coarsely meshed model was only 2 minutes. Therefore, the coarsely meshed model was used for the flow analysis, since adequate accuracy was obtained.

Some graphs of simulation results are presented in Figure 3.2-1 and 3.2-2.

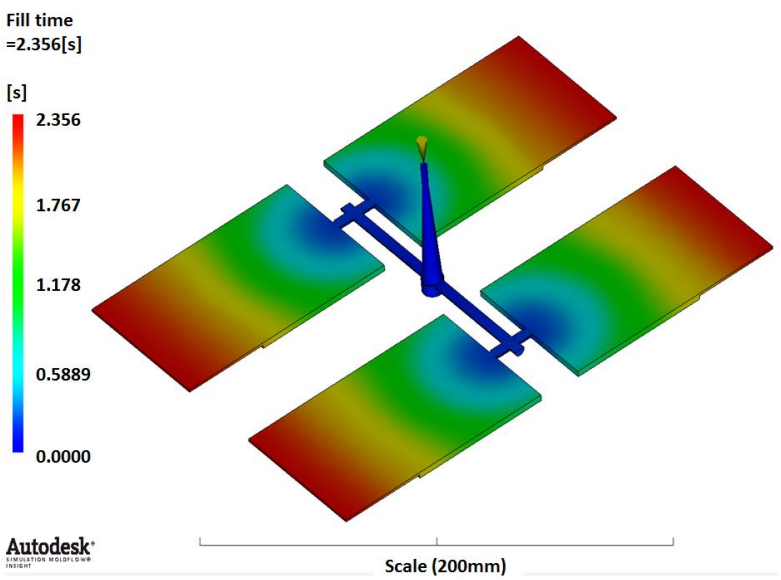

Figure 3.2-1 Fill time (T_{melt} = 240 °C, T_{mould} = 40 °C, injection time = 2 s)

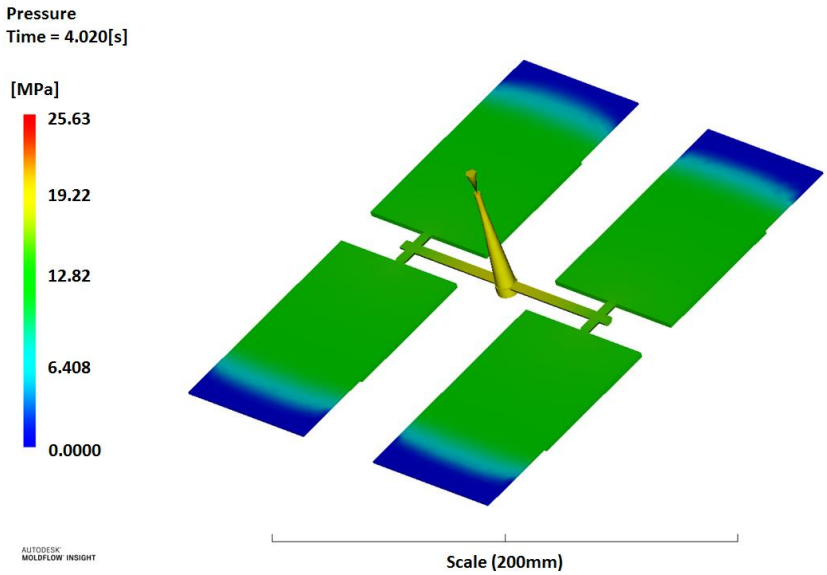

Figure 3.2-2 Pressure in cavities at 4.0 s (T_{melt} = 240 °C, T_{mould} = 40 °C, injection time = 2 s)

Clearly, the simulation results in Figure 3.2-1 and 3.2-2 strongly suggest that well balanced polymer flow and pressure have been achieved during injection moulding process with the four-cavity design.

3.2.2 Influence of Process Variables

The flow analysis of injection moulding with the designed 3D model was carried out under a wide variety of injection conditions using Moldflow, to ensure this four-cavity design was fully reliable and feasible.

The melt temperature varied from 200 °C to 240 °C, and mould temperature changed from 20 °C to 60 °C. The injection time varied from 1 s to 5 s, and different grades of PP were used. Table 3.2-1 summaries the changing ranges of processing settings of simulations.

Table 3.2-1 Changing ranges of injection moulding settings (simulation)

Melt temperature Tm (°C)	Cavity temperature Tc (°C)	Injection time (s)	PP grade
200 - 240	20 - 60	1 - 5	Generic, Sabic 571P, Sabic PHC26

The most important investigated predictions were: shot volume, total part weight, maximum injection pressure, temperature at flow front, shear rate, clamp force,

frozen layer fraction at end of fill, in-cavity residual stress, orientation at core and skin, shear stress at wall and pressure.

The numerous combinations of injection moulding conditions and resulting predictions of interest generated a large quantity of resulting data. Some of the most useful and representative feedback is presented in Table 3.2-2.

Table 3.2-2 Useful simulation data from Moldflow

Materials	Melt density ($g\ cm^{-3}$)	Tm (°C)	Tc (°C)	injection time (s)	Total weight (g)	Actual Shot Volume (cm^3)	Maximum injection pressure (MPa)
				1	53.04	68.42	35.99
				2	52.03	67.13	31.93
571P	0.7751	240	20	3	52.04	67.14	31.77
				4	52.11	67.23	32.02
				5	52.18	67.32	32.63

The actual shot volume and maximum injection pressure was used to confirm that the designed four-cavity system was completely within the capacity of the injection moulding machine provided. The other predictions were used to make sure there were no design flaws and the mould could be filled successfully in theory.

In summary, the data from the Moldflow® simulation helped to improve the four-cavity system designed and ensured feasibility. For example, under all the selected injection moulding conditions for the simulation, the multi-cavity system was filled successfully, and the actual shot volume was well below the maximum shot volume of injection moulding machine (81 cm^3) and the maximum injection pressure was still fairly low (much less than 100 MPa). Thus, the results of simulation suggest that the designed four-cavity system was within the capacity of the injection moulder provided.

The 3D model of the four-cavity system shuttled between NX7.5 and Moldflow for many iterations, and that is how the final next generation four-cavity design in section 3.1.3 was achieved. The design process involved iterative and rigorous work, because any errors in the mould design would be very expensive to rectify and could hamper the progress, and potentially the quality of the research programme.

3.3 Design of Other Mould Parts

The cavity design was the first step to design the mould tool, but the other parts of the mould also needed to be designed. This section briefly introduces the design process for the other parts of the mould.

3.3.1 Design of Ejection, Cooling Systems and In-Cavity Pressure Measurement

The ejection system and cooling system for the mould was also designed after the cavity design was completed fixed.

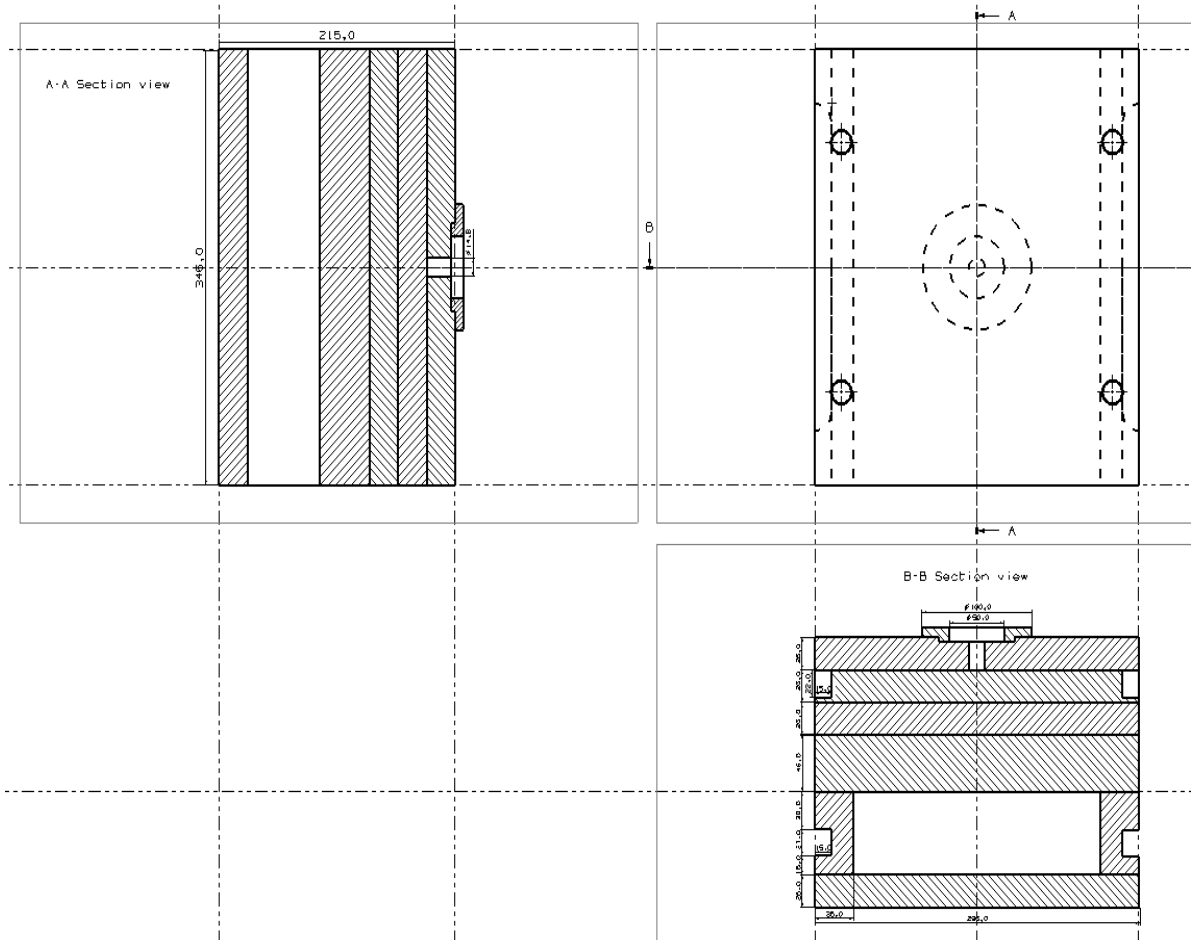

Figure 3.3-1 Engineering drawing of the mould

Figure 3.3-1 shows the 2D drawing of the mould plotted with NX7.5. The drawing reveals the all the basic features of the blank mould. The layout of cooling and ejection systems was initially designed as in Figure 3.2-2.

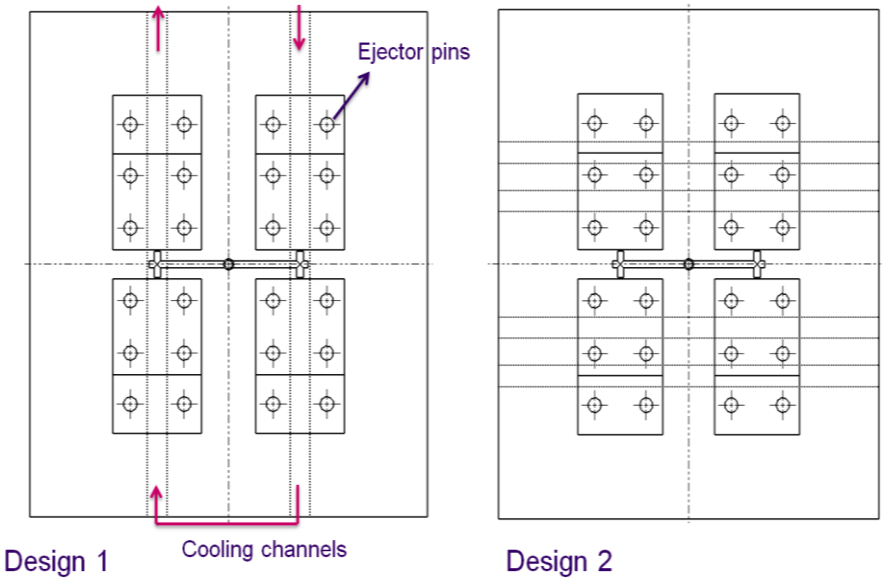

Figure 3.3-2 Designed layout for cooling and ejection systems in the cavity plate

The cooling channels were initially designed as vertical in Design 1 or horizontal in Design 2, and the distribution of ejector pins remained the same in both designs. However, the number of ejector pins seemed to be excessive and was to be reduced. After considering advice and suggestions provided by the experienced technicians in the workshop of the department, the design was further improved, and is shown in Figure 3.2-3.

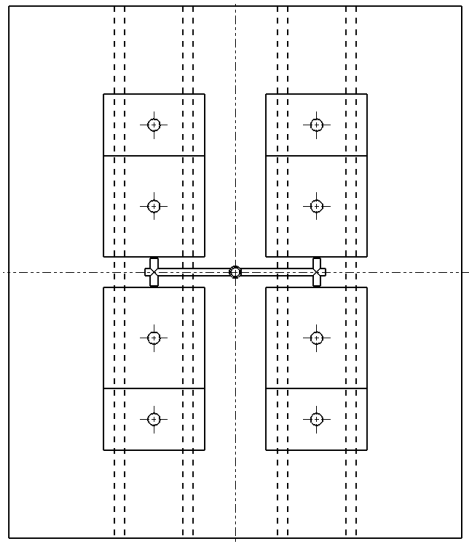
Figure 3.3-3 Improved design of cooling and ejection systems in the cavity plate

The designed position of the pressure sensor and the layout of cooling channels in the core plate are shown in Figure 3.2-4. The cavities are also displayed in the figure using dotted lines, because they would not be machined in the core plate, but would

be created in the cavity plate. They are shown in the figure to indicate the relative position of the pressure sensor, cavities and cooling channels.

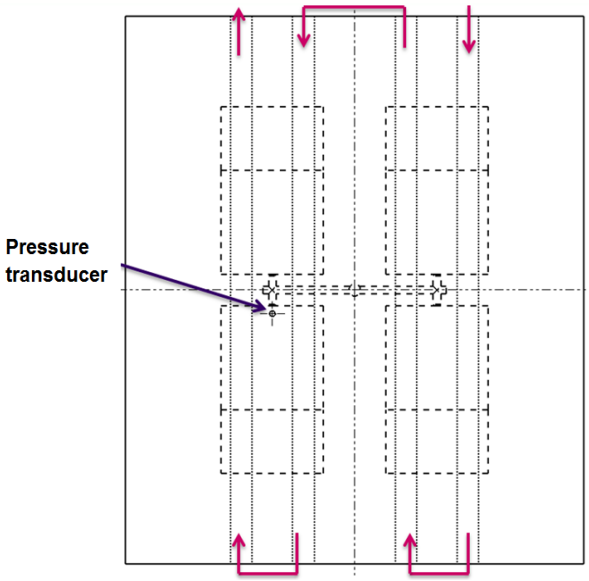

Figure 3.3-4 The designed position of pressure sensor and cooling channels in the core plate

During the injection phase, once the flow front of the melt reaches the sensor, the pressure progression will be acquired. A meaningful and longer lasting measuring result is achieved in most cases near the gate and in the area of the highest wall thickness because the thick-walled points solidify last.[194] Moreover, the highest pressure in the cavity appears near the gate. For these considerations, the sensor was thus positioned next to the gate, as shown in the figure above. Kistler mould cavity sensor, Type 6184A was selected. The front size of the sensor was only 1.2 mm, and the surface area of the sensor was to be flush with the mould. The dimensions of the sensor are clearly shown in Figure 3.3-5.

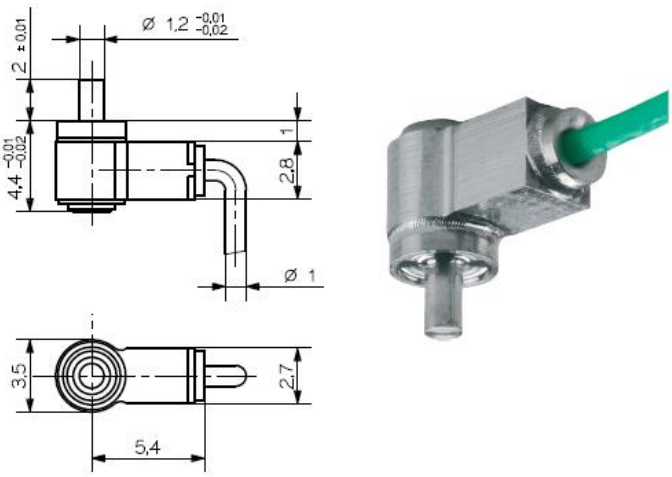

Figure 3.3-5 Dimensions of Kistler sensor, Type 6184A

3.3.2 Selection of Heated Sprue

A suitable heated sprue was needed for the mould to complete the design of the mould tool. The selection of a suitable hot spure is of great importance. The information of hot sprue products provided by DMS is shown in Figure 3.3-6 and 3.3-7.

Basically, the selection of the sprue was on the basis of the mould dimensions. For this mould tool, the total thickness of the clamping plate plus the core plate was 52 mm. In other words, the total length of the hot sprue, including head and body, should be around 52 mm. According to the product list in Figures 3.3-7, both products A1EN 1040 and A1EN2040 could meet the requirements.

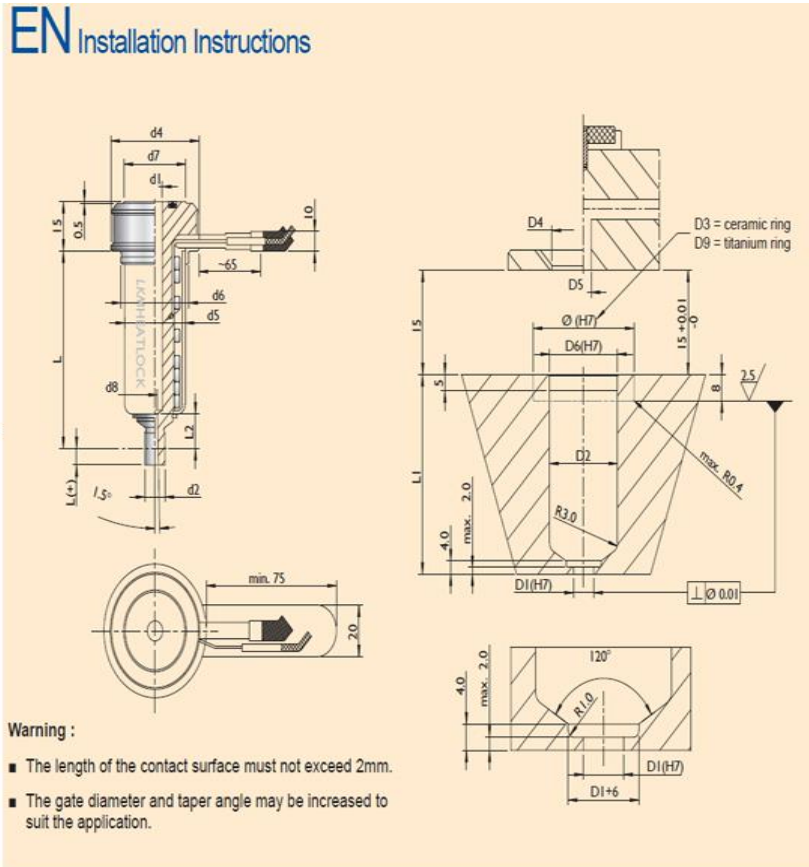

Figure 3.3-6 Information of hot sprue products provided by DMS

The existing through hole in the clamping plate to fit the sprue body, had a diameter of 30 mm, which reveals the diameter of the sprue head should larger than 30 mm. According to the information given, the diameter of spure head of A1EN2040 is 35 mm. After confirming all the other technical data of A1EN2040 could meet the requirements, it was selected as the hot sprue for this mould tool.

EN Installation Instructions

A1EN1 040 ← Order Example

A1 EN	Nozzle Dimensions												Fitting Dimensions								Options		
	Length	Length (including expansion at 200°C)	Machining Allowance	Feed Channel Ø		Ceramic Ring Ø (optional)	Head Ø				Gate Ø	Titanium Ring Ø (optional)									O - Ring	Ceramic Ring	Titanium Ring
Code	L	L1	L(+)	d1	d2	d3	d4	d5	d6	d7	d8	d9	L2	D1	D2	D3	D4	D5	D6	D9			
A1EN1040	40	40.08	5	4	6	30	29	20	23	18	1.5	30	6.7	6	23	30	21	6	23	30	ORING00608	KEM03002308	TIM03002308
A1EN1050	50	50.1																					
A1EN1060	60	60.11																					
A1EN1080	80	80.15																					
A1EN1100	100	100.19																					
A1EN1120	120	120.23																					
A1EN2040	40	40.08	5	6	8	40	35	24	27	24.5	2	36	8	8	27	40	28	6	27	36	ORING00620	KEM04002708	TIM03002708
A1EN2060	60	60.11																					
A1EN2080	80	80.15																					
A1EN2100	100	100.19																					
A1EN2120	120	120.23																					
A1EN2140	140	140.27																					
A1EN2160	160	160.3																					
A1EN3060	60	60.11	10	9	12	60	48	34	39	32	2	50	9	12	39	60	42	9	39	50	ORING00630	KEM06003908	TIM05003908
A1EN3080	80	80.15																					
A1EN3100	100	100.19																					
A1EN3120	120	120.23																					
A1EN3140	140	140.27																					
A1EN3160	160	160.3																					
A1EN3180	180	180.34																					
A1EN4080	80	80.15	20	14	16	56	52	38	44	34.5	3	56	9	16	44	56	46	14	44	54	ORING00640	KEM05004408	TIM05404408
A1EN4100	100	100.19																					
A1EN4120	120	120.23																					
A1EN4140	140	140.27																					
A1EN4160	160	160.3																					
A1EN4180	180	180.34																					
A1EN4200	200	200.38																					

Figure 3.3-7 Information of hot sprue products provided by DMS

After the hot sprue was selected, the design of the mould tool was finished. The blank mould was then sent to the workshop for processing. The processing of mould, in turn, affected the dimensions and features of the final finished mould.

3.4 Changes Made in Processing & Finished Mould Tool

For various reasons, some changes were made when the mould was being machined. Therefore, the finished mould was very slightly different to the designed one.

3.4.1 Change in The Cavity Wall Thickness

The surface quality of the processed cavities was not good enough at first. It is well known that polymer flows in the cavities are very sensitive to the cavity wall surface and surface quality of the injection moulded parts is also affected by the cavity wall surface.[231,232] Therefore, polishing was carried out to improve the surface quality.

The polishing resulted in a small increase in the wall thickness. The thicknesses of both the thin and thick cavity walls were increased by 0.2 mm. Therefore, the final cavity wall thicknesses of the mould after processing were 1.2 mm and 2.7 mm respectively. This, in turn, led to an increase of 5.6 cm^3 in total cavity volume.

3.4.2 Chamfering the Corners

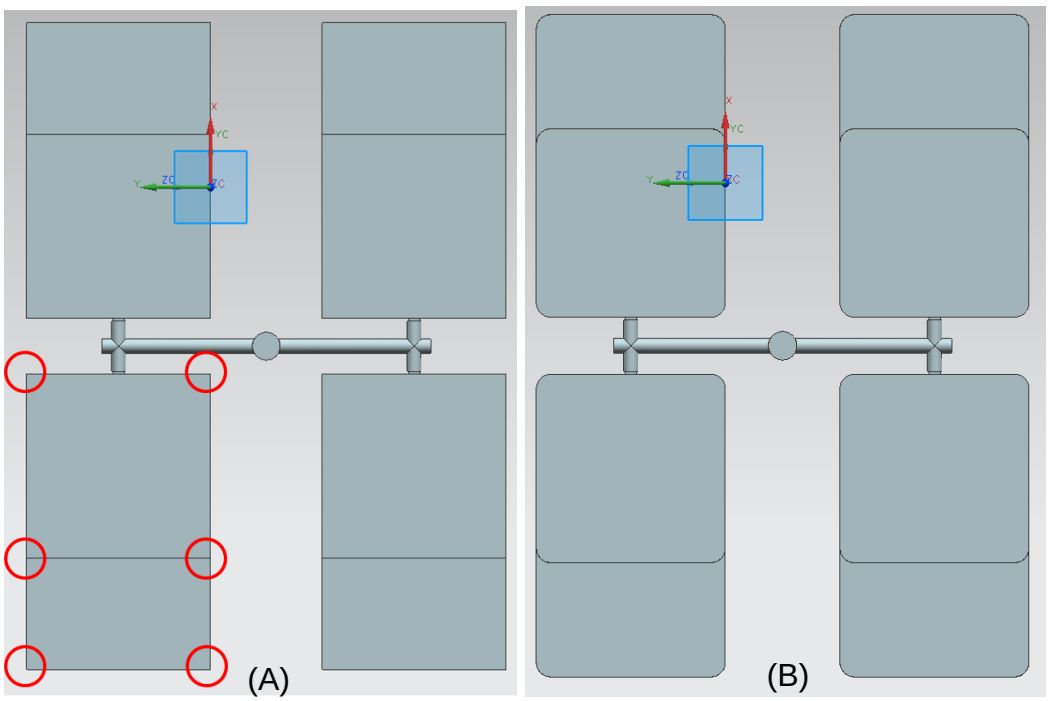

Figure 3.4-1 (A) Sharp corners in the initial design and (B) the model after chamfering

In the preliminary design, there were six sharp corners for each cavity, which are indicated in Figure 3.4-1A. These sharp corners were not practical design and would cause more difficulties when using the mould. After taking the advice from the workshop, these corners were chamfered and the radius of the chamfer was 5 mm for all corners. Figure 3.4-1B shows the 3D model after chamfering the corners. Also, the chamfering of the corners led to a slight decrease in total cavity volume.

3.4.3 Change in the Cooling System in the Cavity Plate

In the initial design, the presence of the support pillars in the cavity plate was not considered, and the problem was spotted during machining. The initially designed cooling system in cavity palate was not achievable, because the cooling channels would cross over the support pillars in the cavity plate. Therefore, the layout of cooling system in the cavity plate was thus changed as shown in Figure 3.4-2.

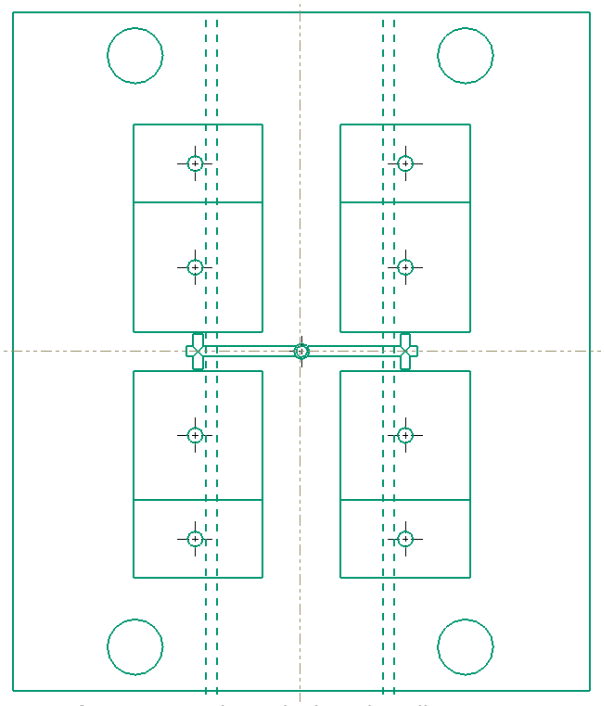

Figure 3.4-2 The redesigned cooling system

The four circles in Figure 3.4-2 indicate the positions of support pillars. The cooling channels which would cross over the support pillars in the initial design were removed (see Figure 3.3-3), and the left cooling channels were moved towards the centre of the cavities as much as possible to minimise the unbalance in cooling effect. It is inevitable that the change in cooling channel arrangements may cause

some potential asymmetry in cooling. However, the asymmetry in cooling is not likely to be significant, as there are symmetric cooling channels in the core plate (Figure 3.3-4). Also, testing pieces are always cut from the same position of the moulded parts, thus the effect of asymmetry in cooling can be cancelled out, when studying thin wall injection for PPCNs.

3.4.4 The Finished Mould

Some photos of the mould parts during processing and the finished mould are displayed in this section.

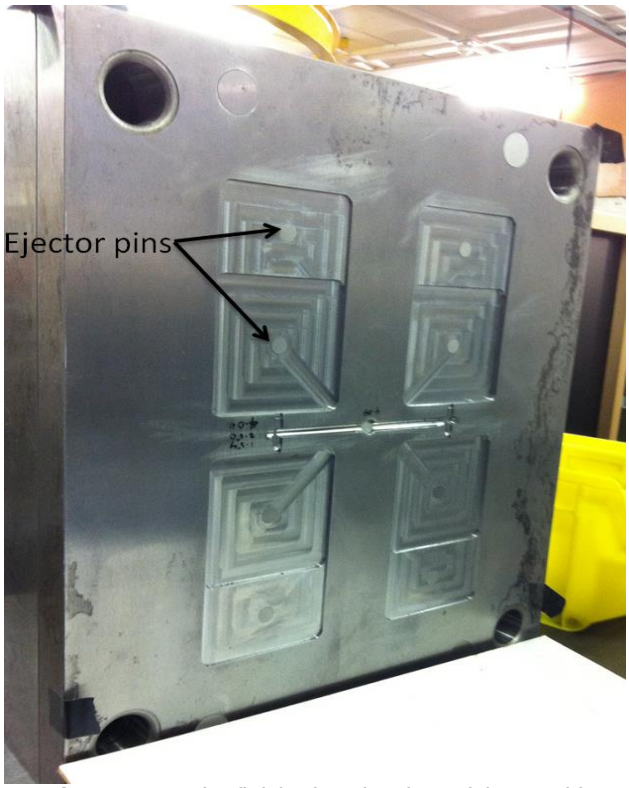

Figure 3.4-3 The finished cavity plate of the mould

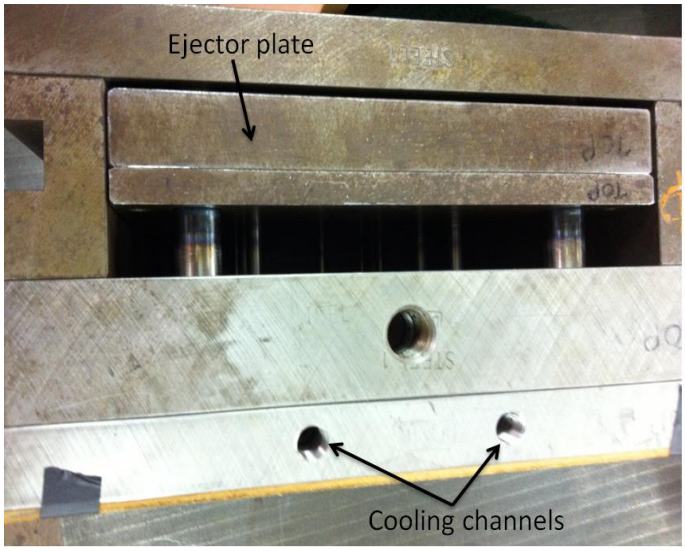

Figure 3.4-4 The ejection system and the cooling channels (top view)

The manufacturing/fabrication work on the mould was very successful. Except the slight change in the cavity wall thickness during surface polishing and the change in the layout of cooling system in the cavity plate, all the other parts of the mould were processed precisely and perfectly as designed.

Figure 3.4-5 Processing of the core plate

Figure 3.4-6 The sprue and ancillary to be installed

According to the finished mould, the final 3D model was obtained after modifying the preliminary designed model.

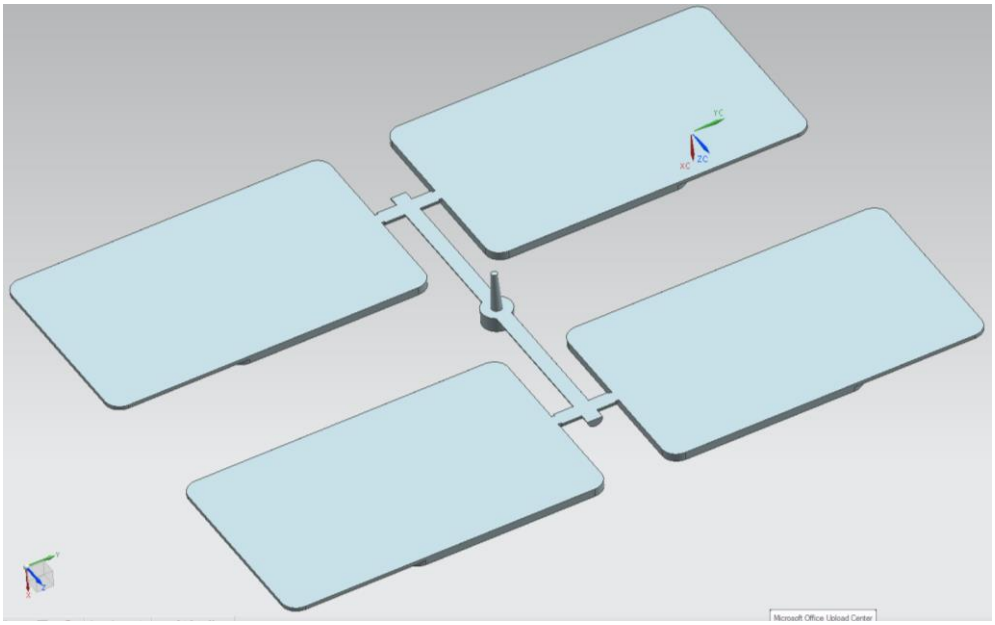

Figure 3.4-7 The final 3D model

This 3D model would be imported to Moldflow for injection moulding simulation and flow analysis of PP/clay nanocomposites, as part of the main research focus, the results would be compared and contrasted to the actual experiment with the injection moulding machine, NB62. For the next chapter, the details of experimental procedures of this research programme will be presented.

CHAPTER 4: EXPERIMENTAL

This chapter focuses on the experimental procedures utilised during the course of this research project. The chapter will be split into the following sections:

4.1 Raw Materials and Characterisation
4.2 DoE – Single Screw Extrusion of Recycled PP Blends
4.3 DoE – Optimum Formulation of PPCNs
4.4 DoE – Optimum Compounding Conditions for PPCNs
4.5 Effects of Processing Conditions on Injection Moulded Parts
4.6 Effects of Clay Concentration on Injection Moulded Parts
4.7 Effects of Wall Thickness on Injection Moulded Parts
4.8 Injection Moulding Analysis - Actual Moulding Vs. Real-Time Simulation

In this project, the raw materials were characterised first. Then single screw extrusion of recycled PP was studied using a DoE method, with the aim of exploring the capability of DoE and the underlying statistical principles. Afterwards, optimisation studies for PPCN formulation and compounding conditions were performed using this strategy. The outcomes from the optimisation studies were then applied to investigate the thin-wall injection moulding of PPCNs. The properties of thin-wall injection moulded parts were investigated to explore the effects of moulding conditions, wall thickness and clay concentration. Real-time simulation was also performed in order to compare predicted performance with that obtained in practice by the in-cavity pressure sensor. The experimental details of these studies listed above will be fully described in sections 4.1 to 4.8.

4.1 Raw Materials and Characterisation

This section will include details of the selection of specific raw materials for this research and the basic property data of those materials selected. The analytical methods that were employed to characterise these raw materials will also be described in this section.

4.1.1 Materials

a) Polypropylene (PP)

Many considerations have been taken when selecting the specific materials for this research project. There are many grades of PP available in the commercial market, and the properties of PP compounds can be very different from grade to grade and from one manufacturer to another.

Generally, commercial grades of PP are classified as homopolymer PP (PP-H) and copolymer PP (PP-C). It is well known that homopolymers, which have a relatively higher Tg, are more rigid and stiff, whilst copolymers have a lower Tg, are more flexible, tough and have better low temperature performance. Therefore, PPCNs based on PP-H materials have great potential to be widely used as automotive interior or under-bonnet parts, while PPCNs based on PP-C materials are more likely to be used automotive exterior parts. As PP-H and PP-C have their own particular merits, it was considered that both types should be included in the study. For PP-H, the mechanical tests in this research mainly focus on the yield strength and stiffness at ambient and elevated temperatures. For PP-C, the emphasis has been placed on impact toughness at ambient and low temperatures.

As real-time simulation of injection moulding is carried out with the software package Moldflow®, it would clearly be very helpful if the material had been included in the materials database within Moldflow®. If so, all the flow model coefficients would be given and accurate predictions could be made.

Table 4.1-1 Data for the selected PP materials

Grade	Type	MFI (dg min^{-1}) at 230°C, 2.16kg	Tensile modulus (MPa)	Izod impact notched (KJ m^{-2}) at 23°C	Charpy impact notched (KJ m^{-2}) at 23°C
571P	PP-H	*5.7*	*1700*	*3.0*	*4.0*
PHC26	PP-C	*8*	*1250*	*No break*	*60*

Based upon the discussion above, Sabic 571P (PP-H) and Sabic PHC26 (PP-C) were selected. Sabic 571P is a homopolymer with a MFR of 5.7 dg min^{-1} and a tensile modulus of 1.8 GPa. PHC26 is a copolymer, and it has a MFR value of 8 dg min^{-1} and a tensile modulus of 1.25 GPa. Both are covered by the database within Moldflow® and have similar MFR values. Table 4.1-1 briefly summarises the PP

materials selected, and the data sheets containing more details can found in Appendix A, section 1.

b) Nanoclay

Three nanoclays provided by three different suppliers were initially considered, and the details are summarised in Table 4.1-2. Nanomer I.44P was provided by Nanocor, Cloisite 15A was provided by Southern Clay, and DK4 was provided by Zhejiang Fenghong. The data sheets are available in Appendix A, section 1.

I.44P is dimethyl dioctadecyl ammonium chloride modified, and Cloisite15A is quaternary ammonium modified, specifically, bis-(hydrogenated tallow alkyl) dimethyl salt. Similarly, DK4 is modified by dimethyl dehydrogenated tallow ammonium chloride. It is well known that the surface modifiers on clay can enlarge the interlayer spacing, reducing the attraction between the layers and platelet surface polarity, thereby making the diffusion of polymer into the gallery favourable.[233] The chain length of the surface modifier may affect the interlayer spacing of modified clay.[234] Pukanszky *et al.*[235] point out that the interlayer spacing of organoclay is strongly affected the surfactant orientation among the clay galleries. Tilted orientation of the surfactant molecule, leads to larger gallery distance, which makes intercalation and exfoliation easier. It is reported in their study that the use of surfactant with two long aliphatic chains, one of which orientates vertically to clay surface, leads to large interlayer spacing.

The three nanoclays considered have similar applications, but different interlayer spacings. As DK4 has the largest interlayer spacing (d_{IL}), it was thus considered to be the most ideal nanoclay to make PPCNs, and was selected for this research project.

Table 4.1-2 Data for the nanoclays

Grades	Organic modifier	Density (g cm^{-3})	d_{001} (nm)	d_{IL} (nm)
I.44P	Dimethyl dioctadecyl ammonium chloride	1.90	2.4-2.6	1.45-1.65
Closite15A	Dimethyl, dehydrogenated tallow, quaternary ammonium chloride	1.66	3.15	2.20
DK4	Dimethyl dehydrogenated tallow ammonium chloride	1.70	3.60	2.65

c) Compatibiliser & co-intercalant

The addition of suitable compatibilisers into PP/clay systems is known to facilitate the formation of intercalated/exfoliated nano-scale structures. It is well known that maleic anhydride grafted PP (PP-g-MA) is the most widely used compatibiliser for PP/clay nanocomposites, thus it was selected for this research project. The PP-g-MA used was provided by the Chemtura Corp. with a trade name Polybond 3200. Brief information of Polybond 3200 is given Table 4.1-3.

Table 4.1-3 Data for Polybond 3200

Appearance	MFI (dg min^{-1}) at 230°C, 2.16kg	Density at 23°C (cm^{-3})	Melting Point (°C)	Maleic Anhydride Level (wt%)
Pellets	115	0.91	157	1.0

As mentioned previously in the literature review, Ratnayake *et al.*[11,12] reported that the co-intercalant, short chain amide molecules (AM), can migrate into the clay galleries and significantly enhance the intercalation/exfoliation of clay in the bulk PP in the presence of PP-g-MA, due to the complex chemical interactions between AM, clay and the maleic anhydride functional groups in PP-g-MA. Thus, short-chain AM component was considered as a necessary ingredient for PP/clay nanocomposites in this study. Erucamide (13-cis-docosenamide) at 99.0 % purity, supplied by Sigma-Aldrich, was selected as the short-chain AM component. Datasheets of Polybond 3200 and Erucamide are also available in Appendix A, section 1.

Table 4.1-4 Data for Erucamide

Formal Name	Molecular formula	Formula weight	Formulation
(z)-13-docosenamide	$C_{22}H_{43}NO$	337.6g mol^{-1}	A crystalline solid

4.1.2 Characterisation of Raw Materials

a) Nanoclay

X-ray diffraction (XRD) analysis was performed on the raw nanoclay powders using D2 PHASER Desktop Diffractometer. The diffractometer was operated at 30 kV and 10 mA with Cu-K$_\alpha$ X-ray beam (wavelength $\lambda = 0.15406\ nm$). The scanned range was $2\theta = 0 - 10°$ with a scan rate of 0.02° s^{-1}. The XRD analysis was carried out for all the three nanoclays and the interlayer spacing was calculated according Bragg's law ($n\lambda = 2d \sin\theta$).

Thermal gravimetric analysis (TGA) was performed to investigate the thermal stability of the organic modifiers on the clay surface using TA Instruments Q5000IR. For the analysis, the clay powders were heated up from 20 to 300 °C at a rate of 15 °C min^{-1} in an air environment, and the weight change against temperature was recorded. The analysis was carried out for all the three nanoclays.

b) Polypropylene

Melt flow index (MFI) test was operated for Sabic 571P (PP-H) and PHC26 (PP-C) to verify the MFI data given by the supplier. A MP600 Tinius Olsen melt flow indexer, was used to perform the test following Procedure B of ASTM D1238 (230 °C, 2.16 kg).

Capillary rheometry testing was carried out using Rosand RH7 Rheometer, in order to plot flow curves for the two grades of PP over the processing temperature range. Seven stages of piston speed, hence shear rate were selected. The shear rate started from 20 s^{-1} then increased to 43 s^{-1}, 93 s^{-1}, 200 s^{-1}, 430 s^{-1}, 929 s^{-1} and 2000 s^{-1}, then gradually returned to 20 s^{-1} the same way. The experiment was conducted at 200 °C, 220 °C and 240 °C with two dies that have different length. The sizes of the two dies used for the test were 16x1 mm and 20x1 mm, so die lengths were 16 mm and 20 mm respectively with an internal diameter of 1mm for both. A zero length die with negligible die length was also used to make corrections for the end effects and extensional flows within the two dies. The two-die method on the RH7 Rheometer to study polymer melt rheology has been thoroughly presented by Cogswell.[236] The flow shear curves generated from the data were then compared with the flow curves given by the database of Moldflow®, to verify the correlation between the practical data and the information in the database for simulation.

Differential scanning calorimetry (DSC) was conducted for PP-H, PP-C and PPgMA granules using TA Instruments Q20, in order to study their melting and crystallisation behaviour. A sample about 10 mg was prepared for each PP. During the test, the samples were heated up to 200 °C from ambient temperature and held for one minute to remove the thermal history, and then cooled down to room temperature and heated up to 200 °C again. The cooling/heating rates were set as 10 °C min^{-1}.

The results and analysis of this study are presented in section 5.1 in Chapter 5.

4.2 DoE – Single Screw Extrusion of Recycled PP Blends

The first phase of single screw extrusion research was an independent study using the Haake Polylab system, and its initial objective was to develop a strong understanding of the DoE approach and to become with the DoE software package, Design Expert®. This section will describe the experimental procedure of single screw extrusion in detail.

4.2.1 Materials

The materials selected in section 4.1 were not used for this independent study. Two other grades of PP, a recycled compound (A850) with MFI = 9.5 dg min^{-1} supplied by Regain Polymers Ltd., and general extrusion homopolymer grade (Sabic 531P) with MFI = 0.3 dg min^{-1}, were used. The two polymers were selected in order to obtain blends with a large viscosity variation across the composition range. The melt flow index of each material was verified by measurements carried out according to ISO1133. The table below summaries the two grades of PP used.

Table 4.2-1 Data for the selected PP materials (Provided by the supplier)

Grade	Type	MFI (dg min^{-1}) at 230°C, 2.16kg	Izod impact notched (kJ m^{-2}) at 23°C
531P	General extrusion PP-H	0.3	6.0
A850	Recycled compound	9.5	>8

No further measurements were carried out since the trends in melt flow characteristics of miscible blends are predictable from existing knowledge of the individual materials used. For instance, it is known that the decrease in molecular weight of polypropylene taking place in service and through recycling operations reduces the shear thinning effect on viscosity. The resulting change in rheological behaviour, however, is not expected to have a significant effect on the interpretation of the data related to screw speed, which is the only relevant related process variable.

4.2.2 Experimental Design

a) Selection of factors and responses

In addition to the composition weight ratio of the mixture, barrel temperature, screw speed and other factors known to affect the optimisation of single screw extrusion operations were studied and varied according to the details outlined in Table 4.2-2.

Table 4.2-2 The selected factor ranges and levels

	Factor variables	Factor ranges	Low (-)	High (+)
A	**Barrel heating temperature (°C)**	180 - 240	192.2	227.8
B	**Screw speed (rpm)**	20 - 120	40.3	99.7
C	**Content of Recycled PP (%)**	0 - 100	20.3	79.7

The responses to the selected input factors include:

- Melt pressure, owing to the effect on energy consumption and die design;
- Temperature difference between the die and the actual polymer melt temperature at the die exit (measured by a deep-set thermocouple), due to shear heating;
- Extruder output as the factor determining the production capability. Given the close similarity in melt-state density of the constituent polymers, mass output was used in the analysis as it would not be affected by the composition ratio;
- Screw torque, as the factor determining the mechanical energy for heat generation and power consumption.

b) Selection of factor ranges

The temperature increment between the three zones along the barrel was set at 10°C, while the temperature of metering zone was taken as the value at the section nearest to the die, with each of the two preceding section stepped down by 10 °C. For example, a barrel heating temperature of 180 °C actually represents three zone temperatures, respectively 160, 170 and 180 °C. The other factor ranges were set around the general operating conditions, as outlined in Table 4.2-2.

c) Constructing the design

As presented in the literature review (section 2.3), within a typical design of experiments approach, a central composite design (CCD) is widely used to analyse a second order response surface. Generally, 2^k factorial runs, 2k axial runs, and at least one centre point are required by a CCD, for a set of investigations based upon k factors. Thus, each numeric factor is varied over 5 levels: ± alpha (axial points), ± 1 (factorial points) and the centre point (0,0).

The sparsity of effects principle states that the direct effects and two-factor interactions usually dominate in a system whilst the higher order interactions are negligible. For this study, a CCD in 3 factors was employed for fitting a second order surface response model. Design Expert® software, version 8.0.7.1 (Stat-Ease, Minneapolis, USA) was used to build the response surface design. As the axial points are more extreme than the factorial points (see Figure 2.3-3), the factor ranges were then entered into the software as the 'alpha' (axial) points. Otherwise, the screw speed and the recycled PP concentration would have negative values at axial points if the factor ranges were entered as factorial points.

A design matrix generated by the software is shown in Table 4.2-3, which contains 8 factorial runs, 6 axial runs and 6 centre runs. Initially, a full second order regression model was selected for each response, shown as follows:

$$y = \beta_0 + \beta_1 X_1 + \beta_2 X_2 + \beta_3 X_3 + \beta_{12} X_1 X_2 + \beta_{13} X_1 X_3 + \beta_{23} X_2 X_3 + \beta_{11} X_1^2 + \beta_{22} X_2^2 + \beta_{33} X_3^2 + \varepsilon \quad (4.1\text{-}1)$$

where y is the response, X_1, X_2, X_3 are the independent factors or variables, β_1, β_2, β_3, etc. are the regression coefficients, and ϵ is a random error term. In the equation, linear terms of the form $\beta_i X_i$ are the main / direct effects, two-factor interactions are in the form of $\beta_{ij} X_i X_j$, and quadratic terms of the form $\beta_{ii} x_i^2$ allow for curvature in the effect of a variable on the overall response. According to Montgomery[32], the estimate of β_0 is the grand average of all observations and the estimates of the other coefficients β_i are one-half the effect estimate for the corresponding factor. The Design Expert® software uses symbols A, B and C to represent the variables.0.

Table 4.2-3 Design matrix generated by Design Expert® (A = barrel temperature, B = screw speed, C = blend concentration of A850 Recycled PP)

Std Order	Run	A (^oC)	B (rpm)	C (%)	Coded A	Coded B	Coded C
1	15	192.2	40.3	20.3	-1	-1	-1
2	9	227.8	40.3	20.3	1	-1	-1
3	18	192.2	99.7	20.3	-1	1	-1
4	14	227.8	99.7	20.3	1	1	-1
5	16	192.2	40.3	79.7	-1	-1	1
6	5	227.8	40.3	79.7	1	-1	1
7	7	192.2	99.7	79.7	-1	1	1
8	4	227.8	99.7	79.7	1	1	1
9	8	180.0	70.0	50.0	-1.68	0	0
10	13	240.0	70.0	50.0	1.68	0	0
11	20	210.0	20.0	50.0	0	-1.68	0
12	6	210.0	120.0	50.0	0	1.68	0
13	2	210.0	70.0	0.0	0	0	-1.68
14	11	210.0	70.0	100.0	0	0	1.68
15	3	210.0	70.0	50.0	0	0	0
16	19	210.0	70.0	50.0	0	0	0
17	17	210.0	70.0	50.0	0	0	0
18	10	210.0	70.0	50.0	0	0	0
19	12	210.0	70.0	50.0	0	0	0
20	1	210.0	70.0	50.0	0	0	0

4.2.3 Analysis of Variance

Analysis of variance (ANOVA) was performed by the software to determine the significance of the models. F-ratios and p-values were calculated and compared. The calculation methodology cited by Montgomery[32] has been briefly introduced in the literature review (section 2.3), which will not be repeated in this section.

In this study, the full second order regression model for each response was simplified by removing the negligible terms with p-values greater than 0.10. On the other hand, the terms with p-values lower than 0.05 were considered as important and kept in the models. Residual analysis was also carried out to confirm the adequacy of the model used, which will be discussed separately in section 5.9.

4.2.4 Equipment and Procedure

The extrusion equipment used in the experiment was Haake Rheomix 252p single screw extruder (Thermo Fisher Scientific Inc.) with screw diameter, D = 19.05 mm and length L = 25D, designed as a standard single thread screw with compression ratio 4:1. A rectangular-section 'sheet & ribbon' die (width 25 mm and a slit height of 1 mm) was used. According to the design matrix, PP mixtures with different amounts of each polymer were prepared by tumble blending prior to extrusion.

The barrel zone temperatures, die temperature, and screw speed were set as described in section 4.2.2, consistent with the design matrix. The single screw extruder was continuously flood-fed and whenever the extrusion conditions were changed, sufficient time was given for the system to stabilise before steady-state measurements were made. Experiments were carried out following the randomised run order given by the design matrix. Melt pressure (ΔP) at the end of the metering zone and screw torque (M) data were monitored continuously on the extruder and analysed within the software. Some slight fluctuations were evident, so that the nearest whole numbers were taken as the resulting values. The extruded products (for 1-minute time increments) were collected and weighed to calculate the process mass output ($\dot{m}$). An infrared thermometer was used to measure melt temperature fluctuations at the die exit, to determine the temperature difference between the die and the melt (ΔT).

4.2.5 Process Optimisation

After all the resultant process data were entered into Design Expert® software, predictive models for the responses were determined and the related process optimisation was evaluated automatically after the significance criteria were set. These criteria were simply 'high output, low pressure' conditions. 240 bar and 71 bar were the highest and lowest melt pressures obtained in the experiment, while 68.5 and 12.3 g min^{-1} were the highest and lowest mass output reached. To optimise the process towards optimum conditions in this experiment, it was assumed that the melt pressure should not exceed 120 bar, while mass output should not drop below 50 g min^{-1}. For improved temperature control, the maximum temperature difference

between the die and the melt was set to 10 °C, as indicated earlier. Finally overlay plots were generated based on the above criteria.

The experimental results are analysed and discussed in section 5.2, Chapter 5.

4.3 DoE – Optimum Formulation of PP/Clay Nanocomposites

The results of the previous independent study on single screw extrusion illustrate that the DoE approach is such a powerful statistical tool and can generate accurate predictive models for a multi-factor system. In this experiment, it was employed to optimise the formulation of PP/clay nanocomposites, and the details of experimental are presented in this section.

4.3.1 Materials

The materials involved in this experiment were PP homopolymer (Sabic 571P, coded PP-H), DK4 (organoclay), Polybond 3200 (PP-g-MA) and Erucamide (AM component). The details for the materials used have been presented previously in section 4.1.

4.3.2 Experimental Design

a) Selection of factors and responses

To achieve the optimum clay intercalation in the PP matrix, the composition of PPCNs was studied in detail, using this approach. Following the research done by Ratnayake *et al*[11,12], organoclay, compatibiliser (PPgMA) and co-intercalant (AM component) were selected as the formulation variables.

In addition to the concentration of organoclay, the weight fractions of PPgMA and AM component were varied and studied according to the details given in Table 4.3-1.

Table 4.3-1 The selected factors ranges and levels

	Factor variables	Factor ranges	Low (-)	High (+)
A	**Erucamide (wt%)**	0.16 – 1.84	0.5	1.5
B	**Polybond 3200 (wt%)**	0.64-7.36	2	6
C	**DK4 (wt%)**	0.64-7.36	2	6

The responses selected to the input variables include: (a) Interplanar spacing of clay platelets, d_{001}, which reveals the intercalation behaviour of the clay in PP matrix; (b) Tensile modulus and (c) Tensile strength, which reveals tensile properties of the PPCNs made with different formulations.

b) Selection of factor ranges

The weight fractions of organoclay and PPgMA were set around 5%, the general concentration used for organoclay and compatibiliser in PPCNs. Amide component, a more expensive additive compared to clay and PPgMA, has been widely used as a slip agent for PP processing in industry. In this research, it was used as co-intercalant[11,12] and a lower concentration, around 1 %, was selected.

c) Constructing the design

A central composite design (CCD), which has been used in the previous DoE study (section 4.2), was also employed for this experiment. A design matrix was generated by Design Expert®, after typing the selected factors and the corresponding ranges into the software package. In this experiment, the factor ranges were entered into the software as factorial points (±1).

The design matrix generated is shown in Table 4.3-2, which contains 8 factorial runs (standard order 1-8), 6 axial runs (standard order 9-14) and 6 centre runs (standard order 15-20). Initially, a full second order regression model was selected for each response (see Equation 4.1-1).

Table 4.3-2 Design matrix generated by Design Expert® (A= AM, B=PPgMA, C= DK4 organoclay)

Std Order	Run	A (%)	B (%)	C (%)	Coded A	Coded B	Coded C
1	17	0.50	2.00	2.00	-1.00	-1.00	-1.00
2	5	1.50	2.00	2.00	1.00	-1.00	-1.00
3	11	0.50	6.00	2.00	-1.00	1.00	-1.00
4	13	1.50	6.00	2.00	1.00	1.00	-1.00
5	14	0.50	2.00	6.00	-1.00	-1.00	1.00
6	18	1.50	2.00	6.00	1.00	-1.00	1.00
7	7	0.50	6.00	6.00	-1.00	1.00	1.00
8	10	1.50	6.00	6.00	1.00	1.00	1.00
9	8	0.16	4.00	4.00	-1.68	0.00	0.00
10	16	1.84	4.00	4.00	1.68	0.00	0.00
11	3	1.00	0.64	4.00	0.00	-1.68	0.00
12	20	1.00	7.36	4.00	0.00	1.68	0.00
13	19	1.00	4.00	0.64	0.00	0.00	-1.68
14	2	1.00	4.00	7.36	0.00	0.00	1.68
15	12	1.00	4.00	4.00	0.00	0.00	0.00
16	4	1.00	4.00	4.00	0.00	0.00	0.00
17	6	1.00	4.00	4.00	0.00	0.00	0.00
18	9	1.00	4.00	4.00	0.00	0.00	0.00
19	15	1.00	4.00	4.00	0.00	0.00	0.00
20	1	1.00	4.00	4.00	0.00	0.00	0.00

4.3.3 Analysis of Variance

Analysis of variance (ANOVA) was also carried out by Design Expert® to determine the significance of the regression models. F-ratios and p-values of the model terms were calculated and compared. The full regression model for each response was simplified by removing the negligible terms with p-values greater than 0.10. On the other hand, the terms with p-values lower than 0.05 were considered as significant and kept in the models.

4.3.4 Equipment and Procedure

The batch mixer used in the experiment was Haake™ Rheomix OS Laboratory Mixer (Thermo Fisher Scientific Inc.) with roller rotors. The fill factor for the mixing chamber was selected as 75 %.

According to the design matrix in Table 4.3-2, PP mixtures with different amounts of ingredients were prepared and then fed into the mixing chamber. The chamber

temperature and rotor speed were set at 185 °C and 100 rpm respectively. The mixing time was set as 6 minutes for each batch. Experiments were carried out following the randomised run order given by the design matrix. After each mixing experiment, the empty chamber was purged by adding LDPE and mixing for 3 minutes, and then carefully cleaned with a cleaning brush.

The PPCNs obtained from the batch mixer were then compression moulded into flat sheets (90 x 90 x 1.2 mm). Compression moulding was carried out at 5 tonnes for 9 minutes, at 190 °C. Standard tensile bars were then cut from the PPCN sheets by a cutting machine, according to ISO527-2-5A.

Tensile testing was performed at room temperature to study the tensile properties of PPCNs obtained. The extension rate was set as 50 mm min^{-1}, and at least 8 samples for each batch were tested to obtain the average values for tensile modulus and strength.

To study the intercalation/exfoliation behaviour of clay in PP matrix, X-ray diffraction (XRD) analysis was carried out at room temperature using Bruker D2 Phaser Benchtop diffractometer. The XRD instrument was operated at 30 kV and 10 mA with Cu-K_a X-ray beam (λ = 0.15406 nm). The scanning range was 2θ= 1-10°, with scan rate of 0.02° s^{-1}. The XRD samples were obtained by cutting compression moulded sheets into strips.

4.3.5 Formulation Optimisation

Predictive models for the responses were determined after all the resultant process data were entered into Design Expert® software. The formulation optimisation for PPCNs was achieved, based on the simple criteria that maximising the interplanar spacing, d_{001}.

The results of this experiment are presented and discussed in a later section (5.3) in chapter 5. The next section will describe the experimental details of the study on optimisation of compounding conditions.

4.4 DoE – Optimum Compounding Conditions for PPCNs

The formulation of PPCNs has been optimised in the previous experiment with the aid of DoE approach. In this section, a similar approach was employed to optimise the compounding conditions for PPCNs, while the optimum formulation from the previous work was also applied.

4.4.1 Materials and formulations

Sabic 571P (PP-H), DK4 (organoclay), Polybond3200 (PPgMA) and Erucamide (AM component) were compounded to make PPCNs, according to the optimised formulation obtained from the previous study. The formulation used is shown in Table 4.4-1

Table 4.4-1 Formulation of PPCNs

Materials	PP-H	PPgMA	Clay	AM
Composition (wt %)	90.5	4	4	1.5

4.4.2 Experimental design

a) Selection of factors and responses

Twin screw extrusion and twin rotor batch mixing are different processing techniques, therefore different input variables were selected for DoE analysis. Feed rate and screw speed were the selected as input factors for the continuous twin screw extrusion process, while mixing time and rotor speed were selected for the twin rotor mixer. Considering the possible degradation of organoclay, [131] processing temperature was thus not considered as an input variable in this study. The details of factor ranges and levels are shown in Table 4.1-2.

The selected responses to the input variables includes: (a) Interplanar spacing of clay platelets, d_{001}, which reveals the intercalation behaviour of the clay in PP matrix; (b) Tensile modulus and (c) Tensile strength, which reveals the tensile properties of the PPCNs prepared by the two different methods and under different conditions.

Table 4.4-2 The selected factors ranges and levels

Methods	Factors	Factor ranges	Low level (-1)	High level (+1)
APV	Feed rate (kg hr^{-1})	2-6	2.6	5.4
	Screw speed (rpm)	100-500	158.6	441.4
Haake	*Mixing time (min.)*	*2-12*	*3.5*	*10.5*
	Rotor speed (rpm)	*20-120*	*34.6*	*105.4*

b) Selection of factor ranges

The selected factor ranges were mainly set around the general operating conditions, and the capacity of the equipment, such as maximum available screw speed or rotor speed, which were considered when selecting factor ranges. The selected factor ranges for each method are outlined in Table 4.1-2.

c) Constructing the design

A central composite design (CCD) was selected for this experiment. A design matrix for each processing method was generated by Design Expert® after typing the selected factors and the corresponding ranges into the software package. In this experiment, the factor ranges were entered into the software as axial points, in order to avoid the situation that axial points would have negative values when the factor ranges were entered as factorial points.

Table 4.4-3 Design matrix for twin screw extrusion (A=feed rate, B=screw speed)

Std Order	Run	A (kg h^{-1})	B (rpm)	Coded A	Coded B
1	3	2.6	158.6	-1	-1
2	5	5.4	158.6	1	-1
3	13	2.6	441.4	-1	1
4	12	5.4	441.4	1	1
5	4	2	300	-1.41	0
6	10	6	300	1.41	0
7	1	4	100	0	-1.41
8	7	4	500	0	1.41
9	2	4	300	0	0
10	11	4	300	0	0
11	8	4	300	0	0
12	6	4	300	0	0
13	9	4	300	0	0

Table 4.4-3 and 4.4-4 are the design matrices generated by Design Expert®. For each processing method, a full second order regression model was selected for the response variables, initially (Equation 4.1).

Table 4.4-4 Design matrix for the twin rotor mixer (A=mixing time, B=rotor speed)

Std Order	Run	A (min)	B (rpm)	Coded A	Coded B
1	11	3.5	34.6	-1	-1
2	6	10.5	34.6	1	-1
3	1	3.5	105.4	-1	1
4	2	10.5	105.4	1	1
5	7	2	70	-1.41	0
6	8	12	70	1.41	0
7	9	7	20	0	-1.41
8	5	7	120	0	1.41
9	10	7	70	0	0
10	4	7	70	0	0
11	3	7	70	0	0

4.4.3 Analysis of Variance

Analysis of variance (ANOVA) was also carried out by Design Expert® to determine the significance of the regression models. F-ratios and p-values of the model terms were calculated and compared. The full regression model for each response was simplified by removing the negligible terms with p-values greater than 0.10. On the other hand, the terms with p-values lower than 0.05 were considered as significant and were kept in the models.

4.4.4 Equipment and Procedure

Twin screw extrusion was carried out using an APV MP30TC twin screw extruder (D = 30 mm, L/D = 30:1). Processing temperatures of the extruder from the feed zone to the die were set as 165, 165, 170, 180, 185 and 185 °C, respectively. According to the formulation in Table 4.4-1, the mixture was prepared by tumble blending prior to extrusion. The PPCN extrudate was quenched in a water bath, then dried and granulated by the pelletiser/cooler equipped. When processing settings were changed, sufficient time was given for the system to stabilise and reach steady-state conditions before PPCN pellets were collected. The experiment was carried out following the randomised run order given by the design matrix in Table 4.4-3.

Batch mixing was done using a Haake™ Rheomix OS Laboratory Mixer (Thermo Fisher Scientific Inc.) with roller rotors. The fill factor used was 75 % and the mixing temperature was set as 185 °C. PP and other ingredients prepared according to Table 4.4-1 were fed into the mixing chamber, and the experiments were carried out following the randomised run order given by the design matrix in Table 4.4-4. After each mixing experiment, the emptied chamber was purged by adding LDPE into the chamber and mixing for 3 minutes, and then carefully cleaned with a hand brush.

The PPCNs obtained from the batch mixer were then compression moulded into flat sheets (90 x 90 x 1.2 mm). Compression moulding was carried out at 5 tonnes for 9 minutes, at 190°C. Standard tensile bars were then cut from the PPCN sheets by a cutting machine, according to ISO527-2-5A. Tensile testing was performed at room temperature to study the tensile properties of PPCNs obtained. The extension rate

was set as 50 mm min^{-1}, and at least 8 samples for each batch were tested to obtain average values for tensile modulus and yield strength.

To study the intercalation/exfoliation behaviour of clay in the PP matrix, X-ray diffraction (XRD) analysis was carried out at room temperature using Bruker D2 Phaser Benchtop diffractometer. The XRD instrument was operated at 30 kV and 10 mA with Cu-K_a X-ray beam (λ = 0.15406 nm). The scanning range was 2θ= 1-10°, with scan rate of 0.02° s^{-1}. The XRD samples were obtained by cutting compression moulded sheets into strips.

Transmission electron microscopy (TEM) analysis was carried out to observe the intercalated/exfoliated structures of clay in the PP matrix. The PP/clay nanocomposites prepared at the centre points for both mixing methods were first mounted in epoxy and then ultramicrotomed with a diamond knife on a Huxley Ultra-microtome (Cambridge Instrument Company) at room temperature to give sections with a nominal thickness around 90 nm. The ultrathin sections were then transferred to 200-mesh copper grids. Images were obtained at an accelerating voltage of 80 kV with a JEOL, JEM-2000FX transmission electron microscope.

4.4.5 Compounding Conditions Optimisation

After entry of all the resultant data into the DoE software package (Design Expert®) predictive regression models for the selected responses of each processing method were obtained. Maximising the interplanar spacing of clay, d_{001}, was used as the primary criterion to optimise the settings for each processing method. Also, the small scale batch mixing, and larger scale continuous mixing, twin screw extrusion, were compared and contrasted, in terms of the structure and functional properties of PPCNs including clay dispersion and tensile properties. The results of this experiment are presented and discussed later in section 5.4.

4.5 Effects of Processing Conditions on Injection Moulded Parts

The optimum formulation of PPCNs and compounding conditions were investigated in the experiments described previously (sections 4.3 and 4.4). After that, the research moved into the next phase, thin-wall injection moulding of PPCNs. The optimum formulation and compounding conditions were used to make PPCN pellets for the injection moulding which was performed with the specially designed mould tool that has been presented in Chapter 3. This section will describe the experimental procedures of the study on effects of processing conditions on injection moulded parts.

4.5.1 Materials

Materials used in this experiment were Sabic 571P (PP-H), Sabic PHC26 (PP-C), DK4 (organoclay), Polybond 3200 (PPgMA) and Erucamide (AM component). The formulation of the PPCNs is shown in Table 4.5-1, which is the optimum formulation of PPCNs based on results and work presented earlier.

Table 4.5-1 Formulation of PPCNs

Materials	PP	PPgMA	Clay	AM
Composition (wt %)	90.5	4	4	1.5

4.5.2 Preparation of PPCN Pellets

The compounding of PPCNs was carried out by twin screw extrusion with APV MP30TC twin screw extruder (D = 30 mm, L/D = 30:1). Processing temperatures of the extruder from the feed zone to the die were set as 165, 165, 170, 180, 185 and 185 °C, respectively. The screw speed and feed rate were set as 160 rpm and 5.4 kg h^{-1} respectively, which were considered to the optimum compounding conditions according to the previous DoE study for optimum compounding conditions. The PPCN extrudate was quenched by a water bath, then dried and granulated by the pelletiser/cooler equipped

According to the formulation in Table 4.5-1, PP mixtures were prepared by tumble blending prior to extrusion. Additionally, both pure PP-H and PP-C pellets were

extruded by the twin screw extruder under the same conditions to let the control materials have the same processing history. The extrudate was cooled down by water bath, then dried and then cut into pellets by the automatic cutter equipment.

4.5.3 Injection Moulding

a) Equipment

The PPCN and pure PP pellets obtained from the twin screw extrusion process were then used for the study of injection moulding. The moulding process was carried out by Negri-Bossi NB62 injection moulding machine with 'Dimi EL-2' control, and the injection mould used in this research project was the 4-piece mould, which has been described in detail previously (Chapter 3). This moulding tool was designed specifically to allow studies of injection moulded PPCN materials in thin sections.

b) Determination of injection stroke and shot size

The initial settings of the injection machine are listed as follows:

Table 4.5-2 Initial settings

Moulding parameters	settings
Melt temperature (temperature of nozzle and barrel zones)	190 °C/180 °C/175° C /170 °C
Mould temperature	25 °C
Shot size	10 mm
Screw position trip	1 mm
Injection speed	20 %
Hold on pressure/time	All zero
Cooling time	30 s

The injection screw stroke was increased from initial 10 mm in 5 mm increments, until the mould was full. Then both stroke size and screw position trip were increased by 10 mm, and were maintained as constant for the whole study of injection moulding.

c) Determination of hold-on time and pressure

After shot size and screw position trip were determined, the hold-on pressure was set to 10 bar for 2 seconds. Three mouldings were collected and the weight of each moulding (component only) was measured and recorded. The hold-on time was increased systematically in increments of 2 s and a plot of weight against hold-on time was plotted to determine the duration of packing phase.

Once the hold-on time was determined, the hold-on pressure was varied around the initial 10 bar. Three mouldings were collected for each hold-on pressure and the weight of each moulding (component only) was measured to determine the optimum hold-on pressure.

d) Variation in moulding conditions

Once optimum hold-on time and pressure were determined, they were used and fixed throughout the study of injection moulding. Melt temperature and cooling time also remained constant in all cases.

Injection speed and mould temperature were selected as the variables in this experiment, since they are known to have influence on structure of moulded parts.[27] Considering the degradation of the organo clay intercalant starts around 180 °C, as indicated by the TGA data (Figure 5.1-2, Chapter 5), melt temperature was thus not selected as a process variable in this experiment. Injection speed is expressed in the percentage of full speed. They were varied according to the Table 4.5-3.

Table 4.5-3 Variation in injection speed and mould temperature

Set	Injection Speed (%)	Mould temperature (°C)
1	10	25
2	20	
3	30	
4	40	
5	20	35
6		45
7		55

e) Real-time data acquisition

As mentioned previously in Chapter 3, a pressure transducer has been fixed in a carefully chosen position within the cavity. Therefore, real-time pressure data in the cavity during a consistent injection moulding cycle can be collated.

For each set of samples, pressure data was collected for three cycles. The real-time pressure data collected from the actual injection moulding have been compared to Moldflow® predictions, which will be fully discussed in section 5.8.

4.5.4 Coding System

Table 4.5-4 and 4.5-5 show the codes used for the injection moulded parts studied in this experimental.

Table 4.5-4 Codes for injection moulded PP

No.	PP type	Injection speed (%)	Mould temperature (°C)	Code
1	PP-H	10	25	PPH-10-25
2	PP-H	20	25	PPH-20-25
3	PP-H	30	25	PPH-30-25
4	PP-H	40	25	PPH-40-25
5	PP-H	20	35	PPH-20-35
6	PP-H	20	45	PPH-20-45
7	PP-H	20	55	PPH-20-55
8	PP-C	10	25	PPC-10-25
9	PP-C	20	25	PPC-20-25
10	PP-C	30	25	PPC-30-25
11	PP-C	40	25	PPC-40-25
12	PP-C	20	35	PPC-20-35
13	PP-C	20	45	PPC-20-45
14	PP-C	20	55	PPC-20-55

Table 4.5-5 Codes for injection moulded PPCNs

No.	PP type	Injection speed (%)	Mould temperature (°C)	Code
1	PP-H	10	25	PPCNH-10-25
2	PP-H	20	25	PPCNH-20-25
3	PP-H	30	25	PPCNH-30-25
4	PP-H	40	25	PPCNH-40-25
5	PP-H	20	35	PPCNH-20-35
6	PP-H	20	45	PPCNH-20-45
7	PP-H	20	55	PPCNH-20-55
8	PP-C	10	25	PPCNC-10-25
9	PP-C	20	25	PPCNC-20-25
10	PP-C	30	25	PPCNC-30-25
11	PP-C	40	25	PPCNC-40-25
12	PP-C	20	35	PPCNC-20-35
13	PP-C	20	45	PPCNC-20-45
14	PP-C	20	55	PPCNC-20-55

4.5.5 Characterisation of Injection Moulded Parts

a) Mechanical testing

PP homopolymers (PP-H) are widely used in automotive industry as interior parts *etc.* for their good strength and stiffness. Therefore, tensile tests focused on the injection moulded parts based on PP-H, to study the effects of processing conditions on the tensile properties of injection moulded parts. As shown in Figure 4.5-1, standard tensile specimens were cut from the thin sections of the injection moulded parts by a manual cutter, along the flow direction of polymer melt during injection moulding.

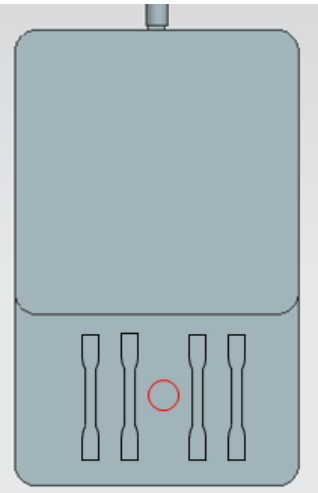

Figure 4.5-1 Position of tensile specimens cut from the injection moulded parts

Due to the presence of ejector pin in the core plate, there is always a circular scar on the injection moulded parts, which is shown as the red circle in Figure 4.5-1. When cutting specimens from the parts, the scar area was avoided. The standard tensile specimens cut from the parts were in accordance with ISO 527-2-1BB. For each processing condition, at least eight tensile specimens were prepared and tested at room temperature of 20 °C, to get the average values for tensile modulus and strength. The crosshead speed used for the test was 50 mm min^{-1}.

Tensile testing was also carried out at for injection moulded parts based on PP-C. Tensile tests were performed at room temperature of 20 °C and 80 °C on PPC-20-25 and PPCNC-20-25, to estimate the performance of PPCNs at elevated temperatures. To reveal the effect of molecular and particle orientation on tensile properties, the samples cut from PPC-20-25 and PPCNC-20-25 in the transverse direction, as shown in Figure 4.5-2, were also tested at room temperature.

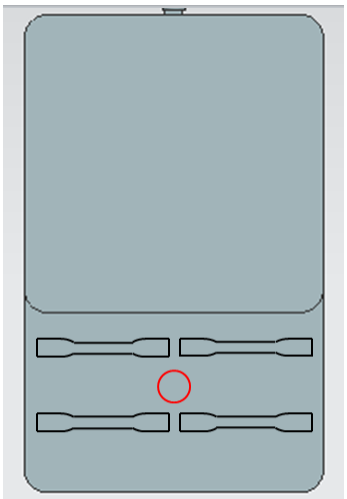

Figure 4.5-2 Position of tensile specimens cut from the injection moulded parts

In comparison to PP-H materials, PP-C materials are widely used as automotive exterior components for their good toughness. Thus, falling weight impact testing was performed for the injection moulded parts based on PP-C, to investigate the effects of processing conditions on the toughness of injection moulded parts. The test was carried out on the thick portion of the injection moulded parts which was specially designed for falling weight impact tests as discussed in Chapter 3. Considering the automotive exterior parts often need to work at low temperatures, the test was thus performed at -20 °C and at least five moulded samples for each injection moulding condition were tested to calculate the average values and standard deviations. The mass used was 10 kg and the striker mass was 0.1 kg, the height of the striker was set as 0.5 m. Therefore, the striker impacted the test specimen at a velocity of 3.12 m s^{-1} and with 49.3 J of potential energy.

b) XRD

To study the effect of injection moulding conditions on the intercalation/exfoliation behaviour of clay in moulded PPCNs, X-ray diffraction (XRD) analysis was carried out at room temperature using Bruker D2 Phaser Benchtop diffractometer. The XRD instrument was operated at 30 kV and 10 mA with Cu-K_a X-ray beam (λ = 0.15406 nm). The scanning range was 2θ= 1-10°, with scan rate of 0.02° s^{-1}, and rotational speed of 15° min^{-1}. The XRD samples were square and cut from the middle of the thin sections of the injection moulded parts, as shown in Figure 4.5-3 below. The injection moulded PPCNs based on both PP-C and PP-H were examined in this way.

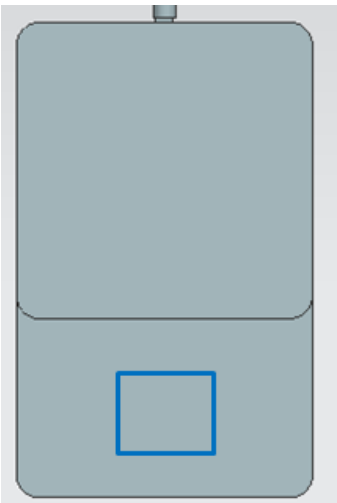

Figure 4.5-3 Position of XRD specimen cut from the injection moulded parts

c) OM

For optical microscopy (OM), small rectangular samples about 10x5 mm were cut from the square XRD samples. By using a few drops of distilled water and several short blasts of CO_2, the OM samples were mounted in ice on the brass block of a M.S.E. sledge microtome. Thin films about 10 μm were obtained by microtoming the samples using a glass blade. The thin films were then transferred to glass slides and were dried by touching to their sides with a piece of filter paper. Then the thin specimens were mounted in Euparal and covered by glass coverslips. Images were taken with Leica DMRX optical microscope using bright field mode and polarised light. Figure 4.5-4 clear points out the plane and position that the OM sample was cut from the injection moulded parts (see red circle).

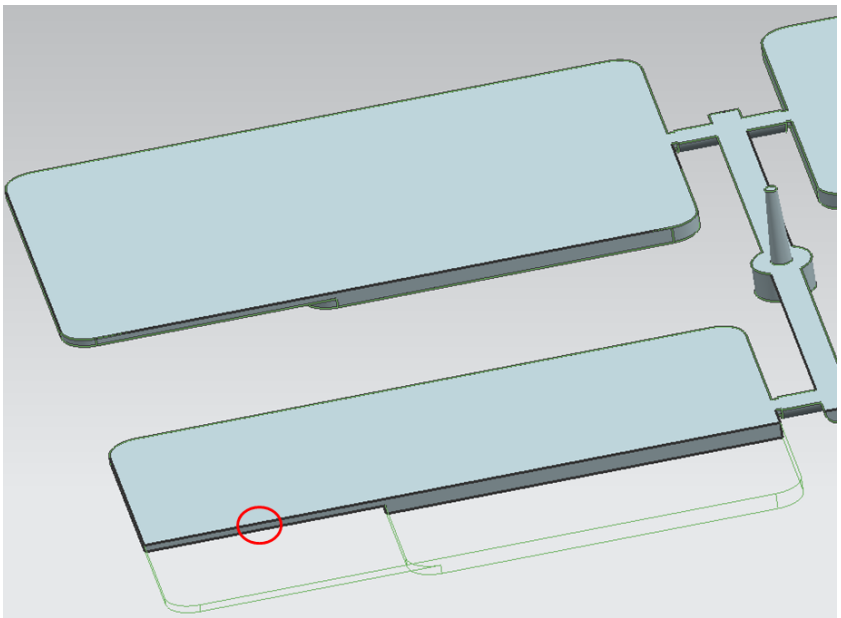

Figure 4.5-4 The plane and position where the samples were cut

d) DSC

Differential scanning calorimetry (DSC) was conducted using TA Instruments Q20, in order to study the effects of processing conditions on the crystallisation behaviour of injection moulded PPCNs. A sample about 10 mg was cut from the rectangular XRD specimens that were cut from the middle parts of thin sections of injection moulded parts. The samples were equilibrated at 25 °C and then heated up to 200 °C at the rate of 10 °C min^{-1}.

e) TEM

A small piece of sample cut from the thin section of injection moulded parts (Figure 4.5-4), and was first mounted in epoxy and then ultramicrotomed with a diamond knife on a Huxley Ultra-microtome (Cambridge Instrument Company) at room temperature to give ultrathin sections with a nominal thickness around 90 nm. The ultrathin sections were then transferred to 200-mesh copper grids. Images were obtained at an accelerating voltage of 80 kV with a JEOL, JEM-2000FX transmission electron microscope. TEM was performed for samples PPCNC-10-25, PPCNC-20-25 and PPCNC-30-25.

The results of this experiment are presented and discussed later in section 5.5, Chapter 5.

4.6 Effects of Clay Concentration on Injection Moulded Parts

Although the optimum formulation of PPCNs has been found previously using DoE approach (section 5.3), it is still nevertheless worthwhile to investigate the effects of clay on injection moulded parts. Furthermore, this study was based on the PP copolymer, while the study of optimum formulation was based on PP homopolymer.

4.6.1 Materials

Sabic PHC26 (PP-C), DK4 (organoclay), Polybond 3200 (PP-g-MA) and Erucamide (AM component) were used in this study. The concentrations of PPgMA and AM component were kept as 4 wt% and 1.5 wt% respectively, whilst the concentration of clay was varied from 1 wt% to 5 wt%. The PP-C material was used as the control group. The formulations of PPCNs and their corresponding codes are summarised in Table 4.6-1.

Table 4.6-1 Formulations of PPCNs and their codes

Batch	Clay (wt %)	PP-C (wt %)	PPgMA (wt %)	AM (wt %)	Code
1	1.0	93.5	4.0	1.5	PPCNC-C1
2	2.0	92.5	4.0	1.5	PPCNC-C2
3	3.0	91.5	4.0	1.5	PPCNC-C3
4	4.0	90.5	4.0	1.5	PPCNC-C4
5	5.0	89.5	4.0	1.5	PPCNC-C5
6	0	100	0	0	PPC-C0

4.6.2 Preparation of PPCN Materials

The twin screw extrusion process described in section 4.5.2 was used to compound the PPCNs. The mixtures of PP granules and the other ingredients were prepared by tumble blending prior to extrusion. After the collection of PPCN pellets was completed and the next batch of mixture was added into the hopper, sufficient time was given to purge the extruder and reach steady-state conditions before PPCN pellets were collected.

4.6.3 Injection Moulding

The PPCN pellets obtained from the twin screw extrusion process were then used for the study of injection moulding. The moulding process was carried out by Negri-Bossi NB62 injection moulding machine with 'Dimi EL-2' control, and the injection mould used was the 4-piece mould, which was specially designed for this research project and has been fully described in Chapter 3. The settings of the injection machine are listed as below:

Table 4.6-2 Settings for the injection machine

Moulding parameters	Settings
Melt temperature (temperature of nozzle and barrel zones)	190 °C/180 °C/175 °C/170 °C
Mould temperature	25 °C
Screw stroke	130 mm
Screw position trip	10 mm
Injection speed	30 %
Hold on pressure/time	5 bar/ 6 s
Cooling time	30 s

When the batch of PPCN pellets was changed, the barrel of the injection machine was carefully purged before the injection moulded parts were collected.

The real-time pressure data in the cavity during a consistent injection moulding cycle was collated by the pressure transducer installed within the cavity. For each set of samples, pressure data was collected for three cycles.

4.6.4 Characterisation of Injection Moulded Parts

X-ray diffraction (XRD) and differential scanning calorimetry (DSC) tests were carried out for the injection moulded parts with different clay concentrations. The test conditions described in section 4.5.5, were also applied to this study.

Transmission electron microscopy (TEM) analysis was performed for samples PPCNC-C1 and PPCNC-C4, and falling weight impact tests (FWIT) were carried out for all samples at both 20 °C and -20 °C. The test procedures for TEM analysis and FWIT tests followed the description in section 4.5.5.

Dynamic mechanic analysis (DMA) was performed on the flat strips (about 55 x 12 x 1.2 mm) cut from sample PPC-C0, PPCNC-4 using TA Instruments Q800, to investigate the effect of clay on Tg. Dynamic mechanic analysis (DMA) was performed on the flat strips (about 35 x 13.2 x 1.2 mm) cut from sample PPC-C0, PPCNC-4. The vibration frequency was 1 Hz in a nitrogen atmosphere and the temperatures ranged from -50 to 50°C at a heating rate of 3°C min^{-1}.

The facture surfaces of PPCNC-C1 and PPCNC-C3 were investigated using the high resolution field emission gun scanning electron microscope (FEG-SEM), Carl Zeiss 1053VP. The fractured surfaces were coated with gold, and images were taken at magnification of 1000x and 5000x with an accelerating voltage of 5 kV and working distance of 10 mm.

The results of this experiment is presented and discussed in section 5.6. The experimental procedures relating to the study on the effect of wall thickness of injection moulded parts will be described next.

4.7 Effects of Wall Thickness on Injection Moulded Parts

As described previously in Chapter 3 for mould tool design, the cavities in the mould were specially designed to have different thicknesses, in order to investigate the effects of wall thickness on injection moulded PP nanocomposite parts, using PP nanocomposites.

4.7.1 Materials and Sample Preparation

To investigate the effect of wall thickness, the test specimens in this experiment were directly cut from the injection moulded parts using compounds PPCNH-30-25 and PPCNC-30-25, which have been produced previously (see section 4.5), for the study of processing conditions. PPCNH-30-25 and PPCNC-30-25 were the injection moulded PPCN parts based on PP-H and PP-C respectively.

Information about the original materials, formulation of the PPCN compounds, melt-compounding process and injection moulding process used to produce PPCNH-30-25 and PPCNC-30-25, has been presented in section 4.5, thus, it is not described again in this section.

4.7.2 Coding of Samples

To make the description and results simpler and clearer, the samples have been coded as shown in the table below.

Table 4.7-1 Codes for the samples

Injection moulded parts	Section studied	Code
PPCNH-30-25	Thin	PPCNH-t
PPCNH-30-25	Thick	PPCNH-T
PPCNC-30-25	Thin	PPCNC-t
PPCNC-30-25	Thick	PPCNC-T

4.7.3 Characterisation of Injection Moulded Parts

a) Tensile testing

Tensile tests were performed on the thicker sections of injection moulded parts. The standard test specimens, ISO 527-2-1BB, were cut from the thick sections as shown in Figure 4.7-1. The round surface scar highlighted by the red circle in the figure was caused by the ejector pin, and it was avoided when cutting samples. At least eight tensile specimens were prepared and tested at room temperature (20 °C), to obtain the average values for tensile modulus and yield strength. The crosshead speed used for the test was 50 mm min^{-1}.

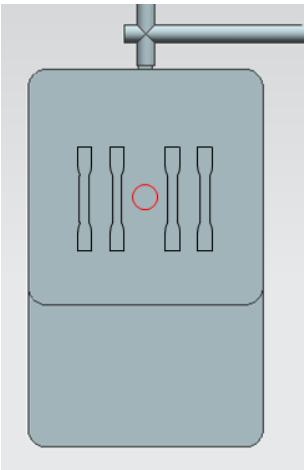

Figure 4.7-1 Position of tensile specimens cut from the thick section

b) XRD

X-ray diffraction (XRD) and differential scanning calorimetry (DSC) tests were carried out for the thick sections of the injection moulded parts. Small squares about 20x20 mm were cut off from the middle of the thick sections of the injection moulded parts, as shown in Figure 4.7-2 below.

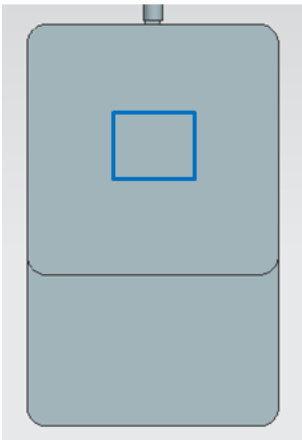

Figure 4.7-2 Position of XRD specimen cut from the injection moulded parts

X-ray diffraction (XRD) analysis was carried out at room temperature using Bruker D2 Phaser Benchtop diffractometer. The XRD instrument was operated at 30 kV and 10 mA with Cu-K_a X-ray beam (λ = 0.15406 nm). The scanning range was 2θ = 1-10°, with scan rate of 0.02° s^{-1}, and rotational speed of 15° min^{-1}.

c) OM

For optical microscopy (OM), small rectangular samples about 10x5 mm were cut from the square XRD samples. By using a few drops of distilled water and several short blasts of CO_2, the OM samples were mounted in ice on the brass block of a M.S.E. sledge microtome. Thin films about 10 μm were obtained by microtoming the samples using a glass blade. The thin films were then transferred to glass slides and were dried by touching to their sides with a piece of filter paper. Then the thin specimens were mounted in Euparal and covered by glass coverslips. Images were taken with Leica DMRX optical microscope using bright field mode and polarised light. The blue circle in Figure 4.7-3 shows where the samples were cut from the thick section, while the red circle shows where the samples were cut from the thin sections in the previous experiments (section 4.5).

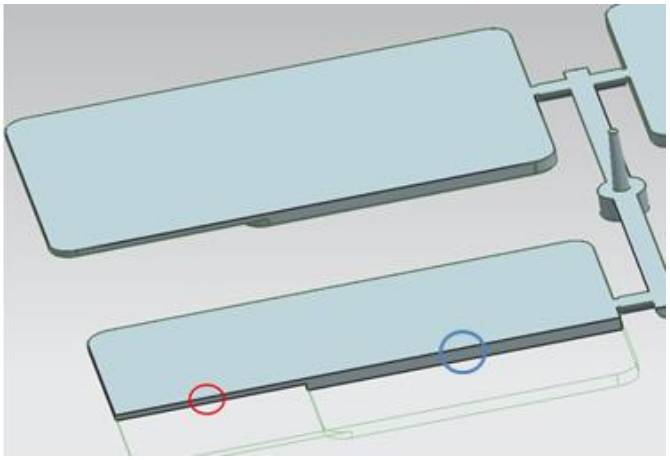

Figure 4.7-3 The plane and position where the OM samples were cut.

d) DSC

DSC samples about 10 mg were cut from the corners of the square XRD samples. During the test, the samples were calibrated at 25 °C first and then heated up to 200 °C at a rate of 10 °C min^{-1}, to study the effects of wall thickness on the crystallinity of moulded parts.

e) TEM

TEM were performed for samples PPCNC-T and PPCNC-t. The test procedures described in section 4.5.5 was applied.

Overall, all the tests performed in this experiment followed the same test procedures that have been described in section 4.5 for the study of processing conditions, except that the test specimens were taken from the thick sections of the injection moulded PPCNs. The test results for the thick sections in this experiment were then compared to those obtained previously for the thin sections, to analyse the effects of wall thickness on the properties of injection moulded parts. The results are presented in section 5.7.

4.8 Injection Moulding Analysis: Actual moulding vs. Real-Time Simulation

Analysis of injection moulding was performed by comparing the data acquired from the actual moulding process and real-time simulation carried out using Moldflow® software package. Direct comparison was made with the in-cavity pressure data, and frozen layer fraction figures, because such data is conveniently obtained from the actual injection moulding process that was performed under different processing conditions. Furthermore, the effect of processing conditions and wall thickness suggested by the data from actual moulding were compared to the predicted data from computer simulation of the moulding process.

The other data generated from the moulding simulation, such as clamping force, shear stress at wall, bulk shear rate, bulk temperature *etc*. were also studied and related to the experimental results that have been presented and discussed in the previous studies.

4.8.1 Data Acquired from Injection Mouldings

In this section, all the relevant moulding related data and testing data obtained from the injection moulded parts originated from the studies reported in sections 5.5 to section 5.7 is discussed. The data enable the effects of processing conditions, clay concentration and wall thickness on the properties of injection moulded part to be meaningfully elucidated. The data regarding the properties of the original materials is in section 5.1.

As the corresponding experimental procedures for the studies reported in sections 5.5 to 5.7 have been described previously in sections 4.5 to 4.7, they are not repeated in detail here. Table 4.8-1 summaries the experimental conditions of injection moulding conducted in sections 4.5 to 4.7, and the variables that have been studied previously are marked with asterisk.

Table 4.8-1 Actual moulding studied previously

Parameters	Settings
Melt temperature (temperature of nozzle and barrel zones)	190 °C/180 °C/175 °C /170 °C
Screw stroke	130 mm
Screw position trip	10 mm
Hold on pressure/time	5 bar/ 6 s
Cooling time	30 s
Injection speed *	10 %, 20 %, 30 %, 40 %
Mould temperature *	25 °C, 35 °C, 45 °C, 55 °C
Clay concentration *	1 %, 2 %, 3 %, 4 %, 5 %
Wall thickness *	1.2 mm, 2.7 mm

4.8.2 Selection of Mesh Type for Real-Time Simulation

The injection moulding simulation was performed using Autodesk Moldflow® Insight 2017. The 3D model used for the simulation has been drawn previously using Siemens UG NX 7.5 (Figure 3.4-7), and the mould tool design process has been fully described (Chapter 3). The 3D model was imported to Insight 2017 and was then meshed (Figure 4.8-1). Dual domain mesh type was selected due to its thin-wall structure. The model was meshed coarsely (including 18,430 elements), because the difference in the simulation results was negligible (<1%) in comparison to a much finer mesh (including 132,500 elements) but a significant amount of processing time was saved, as reviewed in Chapter 3.

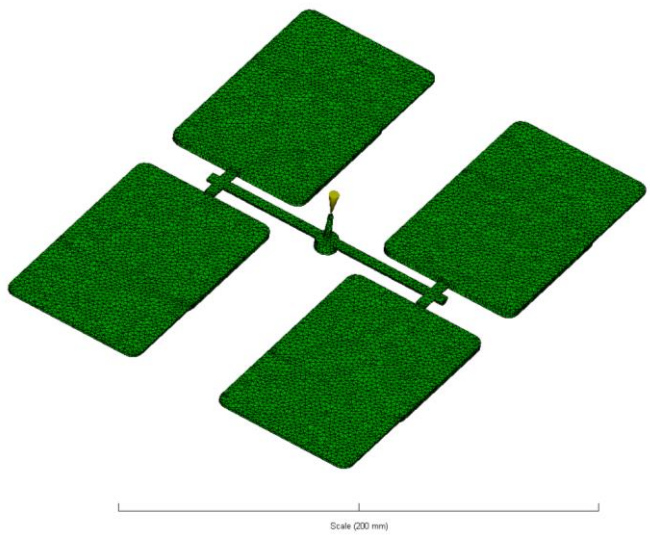

Figure 4.8-1 Meshed 3D model for simulation

4.8.3 Settings for Simulation

To make the results of injection moulding simulation more accurate and comparable to the actual moulding, the processing parameters of simulation were set as close as possible to those of the actual moulding operation.

As discussed previously in section 5.5, the actual clamp forced needed was underestimated during the mould tool design, because it was not noticed that z-axis was the default direction of mould opening in Moldflow® software package. This problem was fixed first by adjusting the coordinates, before performing the simulation.

a) Materials

As both PP-H (Sabic 571P) and PP-C (Sabic PHC26) are included in the database of Moldflow® software package, thus, they could be directly selected and used for the simulation process. In this study, PP-C was selected for the real-time simulation of injection moulding. The simulations then compared with the actual injection moulding process that was performed with PP-C or nanocomposites based on PH-C.

b) Injection time and mould temperature

The injection time used in the actual moulding operation at different injection speeds was recorded by the injection moulding machine, and is summarised in Table 4.8-2. The actual injection times were set as the injection times for the simulation process initially. In Moldflow® Insight, the actual fill time is always slightly higher than the value entered, and extra time is due to the material compressibility. Thus, the injection time entered in the simulation was carefully adjusted to make sure the fill time was as close as possible to the injection time used in the actual injection moulding operations shown in Table 4.8-2.

Table 4.8-2 Actual injection time for the actual moulding

Injection speed (% of full speed)	Actual injection time (s)
10	11.9
20	5.8
30	3.9
40	3.0

The mould temperatures of 25 °C, 35 °C, 45 °C and 55 °C used for the actual moulding operation were also used for the real-time simulation, to investigate the effects of mould temperature.

c) Switch-over from injection phase to packing phase

For the actual moulding operation, the switch-over from injection phase to packing phase was stroke-controlled, when the displacement of screw was reduced to 10 mm (screw position trip) from 130 mm (screw stroke).

According to the discussion in section 5.5.1, it is very clear that the multi-cavity system was fully filled during the injection phase even though packing phase was not applied to the moulding process yet. Therefore, ‘100 % volume filled’ was selected as the criteria for the velocity/pressure switch-over of the injection moulding simulation.

d) Hold pressure/time

As shown in Table 4.8-1, the pressure and time set for packing stage were 5 bar and 6 s. It has been discussed in section 5.5 that the 5 bar hold pressure was hydraulic pressure, which gave nominal 77 bar cavity pressure according to the pressure intensification conversion plot. 77 bar is equal to 7.7 MPa and therefore, packing pressure of 7.7 MPa and packing time of 6s were set for the packing stage of real-time simulation.

e) Other parameters

The melt temperature was set as 190 °C, and the cooling time was set as 30 s for all runs. The analysis sequence was chosen as ‘fill and pack’.

4.8.4 Data Measurements

For actual moulding, the in-cavity pressure was measured by the pressure transducer installed next to the gate in one of the four cavities (see Figure 3.3-4). Thus, the pressure at the same point was measured for the real-time simulation (red dot in Figure 4.8-2), and then was compared to the pressure data obtained from the actual moulding experiments.

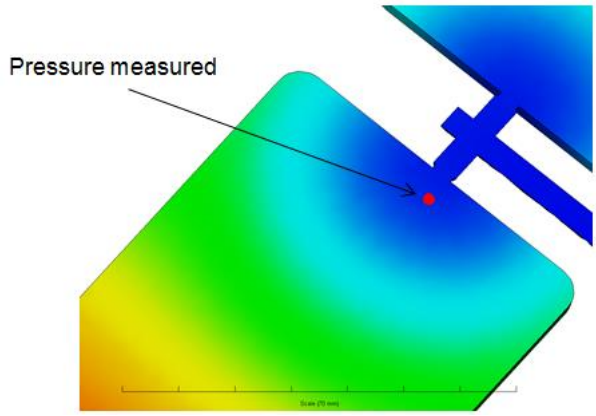

Figure 4.8-2 The position where pressure was measured

The other resulting data such as frozen layer fraction, bulk shear rate, bulk temperature and *etc*. were obtained by measuring the centres of the thick and thin sections (Figure 4.8-3). As the samples used for different tests in previous studies were all cut from the centre areas of the thin and thick sections, thus, the data measured at their central points were most representative.

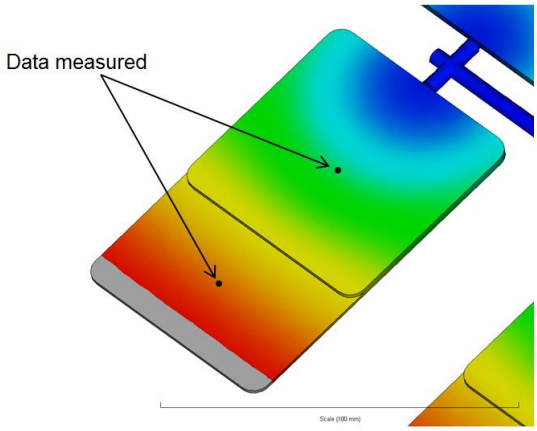

Figure 4.8-3 The positions where data was obtained

The resulting data obtained from the real-time simulation were analysed and compared to those obtained from actual moulding.

4.8.5 Coding system

The coding system used in this study was consistent with that in previous studies regarding actual injection moulding of PP-C. 'S' was added to the sample codes, denoting the simulation results.

Table 4.8-3 Codes for the actual injection moulding and real-time simulation

No.	PP type	Injection speed (%)	Mould temperature (°C)	Code (actual)	Code (simulation)
1	PP-C	10	25	PPC-10-25	PPC-10-25-S
2	PP-C	20	25	PPC-20-25	PPC-20-25-S
3	PP-C	30	25	PPC-30-25	PPC-30-25-S
4	PP-C	40	25	PPC-40-25	PPC-40-25-S
5	PP-C	20	35	PPC-20-35	PPC-20-35-S
6	PP-C	20	45	PPC-20-45	PPC-20-45-S
7	PP-C	20	55	PPC-20-55	PPC-20-55-S

The results of this study will be presented in section 5.8.

CHAPTER 5: RESULTS AND DISCUSSION

The experimental procedures have been fully described in Chapter 4, and this chapter will therefore focus on presentation of the experimental results and discussion of the observed trends ad interrelationships between them. This chapter is detailed into the following sections:

5.1 Raw Materials and Characterisation
5.2 DoE – Single Screw Extrusion of Recycled PP Blends
5.3 DoE – Optimum Formulation of PPCNs
5.4 DoE – Optimum Compounding Conditions For PPCNs
5.5 Effects of Processing Conditions on Injection Moulded Parts
5.6 Effects of Clay Concentration on Injection Moulded Parts
5.7 Effects of Wall Thickness on Injection Moulded Parts
5.8 Injection Moulding Analysis - Actual Moulding Vs. Real-Time Simulation
5.9 Discussion on DoE Approach

Clearly, the order of the sections to be discussed in this chapter is consistent with that of the experimental procedures described in Chapter 4. The discussion will start with the characterisation of raw materials, followed by the DoE studies of single screw extrusion, optimisation of PPCN formulation and compounding conditions. After that, the discussion will focus on the thin-wall injection moulding of PPCNs, specifically, the effects of moulding conditions, clay concentration and wall thickness on injection moulded parts. The comparison between the predicted performance from real-time simulation and that obtained in practice will be made and discussed. The last section will give some thoughts and comments on DoE approach, based on the three DoE studies conducted in this project.

5.1 Raw Materials and Characterisation

This section will focus on the properties of the selected raw materials. For the nanoclays, emphasis will be placed on the interlayer spacing (d_{001}) and thermal stability of their surface coating. Generally, larger interlayer spacing makes it easier for the PP chains to diffuse into the clay galleries to form intercalated/exfoliated

structures, and degradation temperature of the coating may determine the maximum processing temperature of PPCNs. For the PP materials, the rheological properties will be emphasised, as they are of critical importance to the processing of polymers.

5.1.1 Nanoclay

The XRD patterns for the three nanoclays are shown in the figure below.

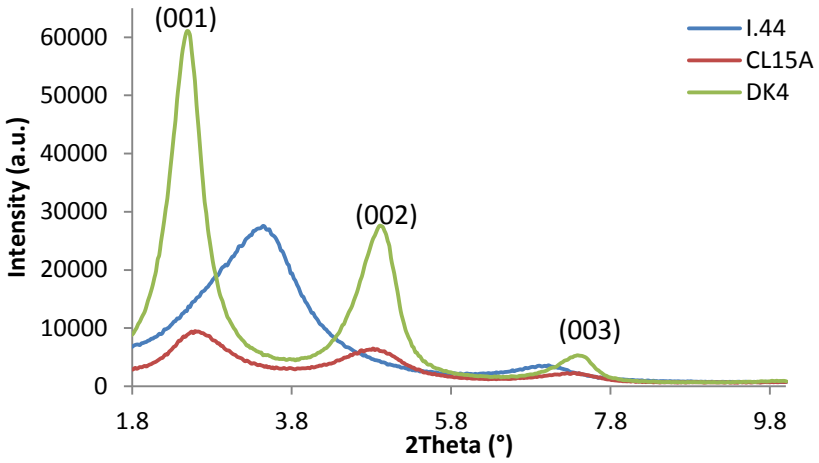

Figure 5.1-1 XRD curves for I.44, DK4 and Cloisite 15A

Based upon the XRD curves above, interlayer spacing of the nanoclays can be obtained using Bragg's law ($n\lambda = 2d\sin\theta$). The calculated interlayer spacing d-values are summarised in the Table 5.1-1.

Table 5.1-1 Calculated interlayer spacing values for the three nanoclays

Clay	d_{001} (nm)	d_{002} (nm)	d_{003} (nm)	d_{001} (nm) provided by suppliers
DK4	3.55	1.80	1.20	3.60
I.44 PS	2.58	1.27	/	2.4-2.6
Cloisite 15A	3.39	1.84	1.21	3.15

The d_{002} and d_{003} values are generated from higher order diffractions and can be easily converted into d_{001} using Bragg's law. Thus, in this study, d_{001} is used to represent the interlayer spacing of clay. Clearly, the measured data above are quite close to the d_{001} values provided by the suppliers in Table 5.1-1.

According to the d_{001} values in the table, it is clear that DK4 clay has the largest d-spacing, which implies the PP molecular chains may diffuse into the clay galleries

more easily in practice and it is thus more likely to form intercalated or exfoliated structures.

According to the review on XRD pattern of layered silicate in section 2.1.4, it is clear that DK4 is a uniformly stacked organoclay, due to the sharp and intense (001) refection and clearly evident (002) and (003) reflections. Nanocor I.44P gives a rather broad (001) reflection peak and an unobvious (002) reflection, which means there is some stacking disorder in it. As the layer thickness on the sample holder/substrate were the same for all samples, it is thus very likely that Cloisite 15A features only a small fraction of tactoids (platelet stacks) that are sufficiently uniformly spaced to give an (001) refection and possible higher order reflections. However, the (001) spacing of Cloisite 15A is not exactly two times of (002) spacing and three times of (003) spacing. This may suggest that the reflections at higher angle than (001) are not higher order reflections but fractions of the sample with smaller (001) spacing.

Very likely, the difference in basal spacing (d_{001}) is due to different chain length and orientation of the surfactants between the clay platelets,[234,235] which has discussed previously in section 4.1.1.

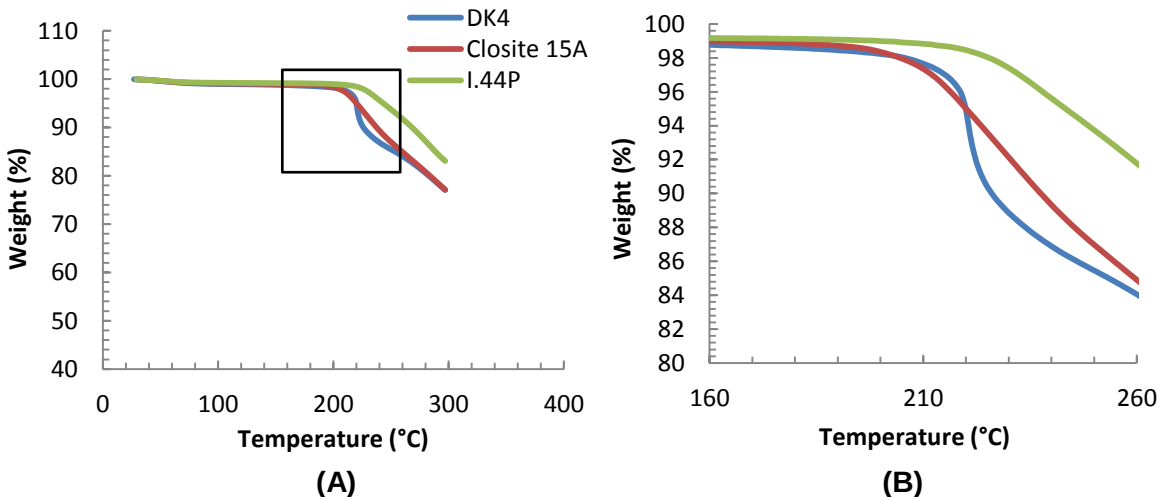

Figure 5.1-2 TGA curves for the nanoclays: (A) Original plot and (B) Zoom-in plot

The TGA curves for the three nanoclays are shown in Figure 5.1-2 (A and B). The original plot (Figure 5.1-2 A), is expanded between 160 °C (T_m of PP) and 260 °C (upper process limit of PP) to obtain the zoom-in plot (Figure 5.1-2 B). Clearly, the degradation of the organic coating on the clay surface starts at around 180 °C. This

temperature information is of great importance for the compounding and processing of PP/clay nanocomposites in this project, because it indicates that the compounding or processing temperature should be very carefully controlled. DK4 shows large drop in mass at ca. 220 °C which may indicate significant unbound organic modifier. The possible reason may be this organoclay has been modified to a level far beyond its cation exchange capacity.

5.1.2 Polypropylene

The selected PP homopolymer, Sabic 571P, and PP copolymer, Sabic PHC26, are coded as PP-H and PP-C respectively throughout this research project.

a) Melt Flow Index Testing

The table below shows the resulting data from MFI tests.

Table 5.1-2 Resulting data from MFI tests (Test condition: 230 °C, 2.16 kg)

Materials	Shear stress (Pa)	Melt density (g cm^{-3})	Flow rate (dg min^{-1})	Volume rate (cm^3 min^{-1})	Viscosity (Pa.s)	Shear rate (s^{-1})
PP-H	19592	0.736	6.10	0.82	1294	15.2
PP-C	19592	0.732	9.86	1.35	800	24.7

Clearly, PP-H has a MFI value of 6.1 dg min^{-1}, which is slightly different from the value of 5.7 dg min^{-1} provided by the supplier. PP-C has a tested value of about 9.9 dg min^{-1}, which is also different from the given value of 8.0 dg min^{-1}. The difference is not considered to be very significant and it is still in the acceptable range of variation.

The MFI values indicate that PP-H has a slight higher viscosity than PP-C, and is consistent with the results from RH7 rheometer. However, the viscosity data from the MFI test are not very accurate as the L/D ratio of the die is too low. More accurate data are derived from the RH7.

b) Capillary Rheometry Analysis

As mentioned in section 4.1.2, seven stages of piston speed, hence shear rate were selected for the capillary rheometry testing. The resultant pressure was measured at

the die entrance. The resulting viscosity data was computed automatically by the software of RH7 rheometer from the knowledge of the capillary die dimensions, piston speed and pressure. It should be noted that Bagley end correction was performed automatically by the software to compute true shear stress, while Rabinowitsch correction was carried out manually to obtain true shear rate. Finally, the true viscosity was calculated based on the true shear stress and shear rate. The examples of calculations and original data obtained are shown in Appendix A, section 2.

Obviously, seven stages of piston speed means seven shear rates, which in turn gives seven viscosity data points (see Figure 5.1-3). The flow curves of the PP materials can thus be obtained by connecting these viscosity data points (Figure 5.1-4).

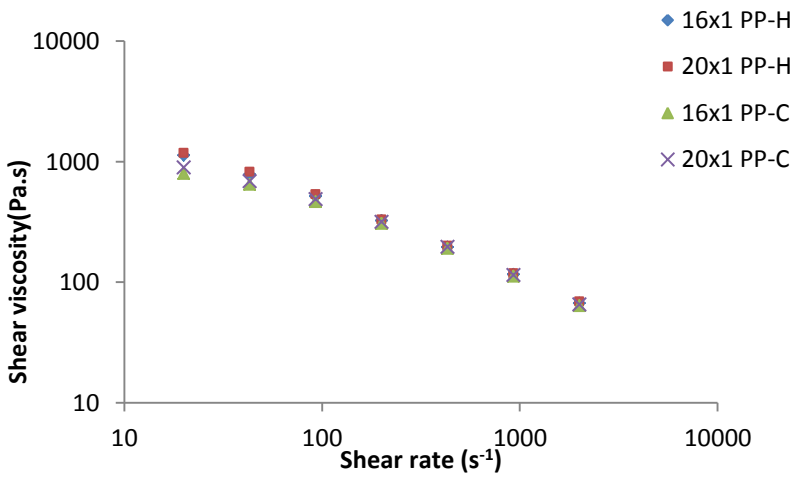

Figure 5.1-3 Viscosity vs. shear rate

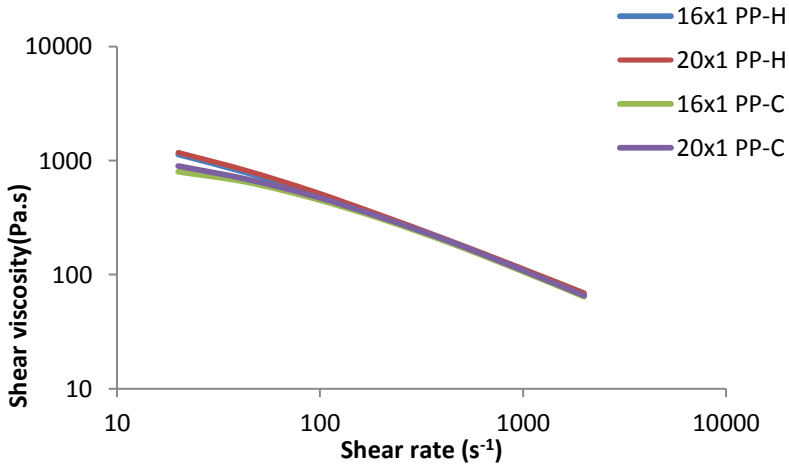

Figure 5.1-4 Flow curves for 571P and PHC 26 at 200°C with different dies

It is clear that PP-H and PP-C show some slight differences in the flow curves especially at low shear rates.

Both polymers illustrate shear thinning behaviour with increasing shear rate and the curves become linear in the power law region. At high shear rates, the curves start to converge, and this indicates that the difference in viscosity is significantly reduced at high shear rates.

The length of the die also shows limited effects on the flow curves at low shear rate. At low shear rates, it seems that the long die gives slightly higher viscosity. This may be because end effects have greater significance in the case of the short die, as the pressure drop at die entrance takes up a greater proportion of total pressure drop in comparison to the long die. Thus, the viscosity data from the long die is believed to be more accurate. At high shear rates, the effect of die length is negligible as shear thinning becomes dominating.

The effect of temperature on the flow curves can be seen clearly from the two figures below.

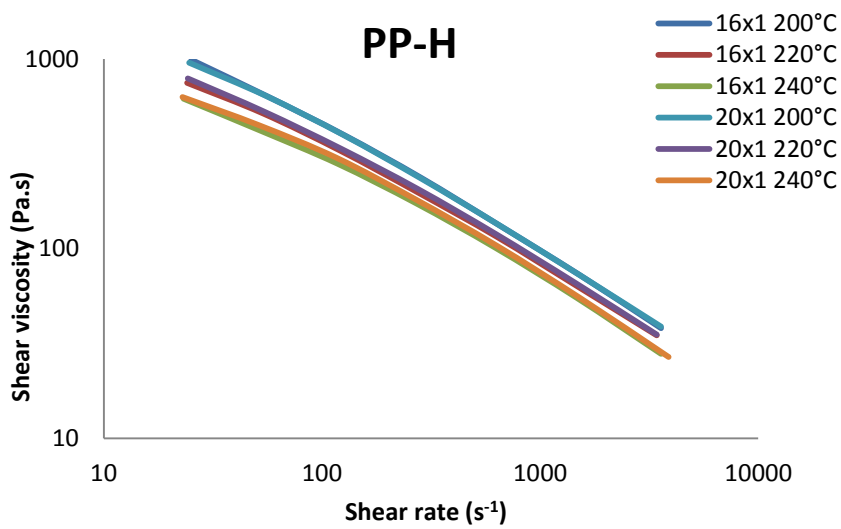

Figure 5.1-5 Flow curves for PP-H at 200, 220 and 240°C with different dies

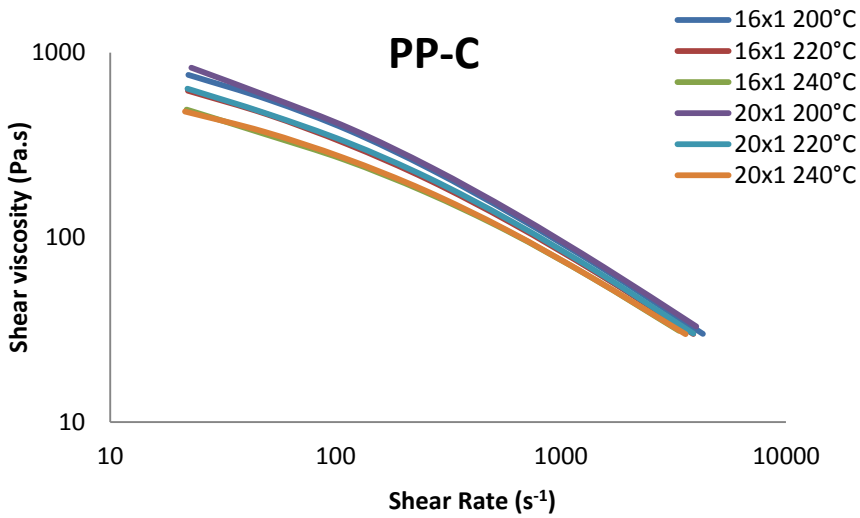

Figure 5.1-6 Flow curves for PP-C at 200, 220 and 240°C with different dies

The figures clearly illustrate that higher temperature leads lower viscosity across the shear rate range and this effect of temperature on the flow curves are expected according to the basic principles of polymer science. Figure 5.1-7 and 5.1-8 show the difference in the performance of the homopolymer and copolymer when the same die was used.

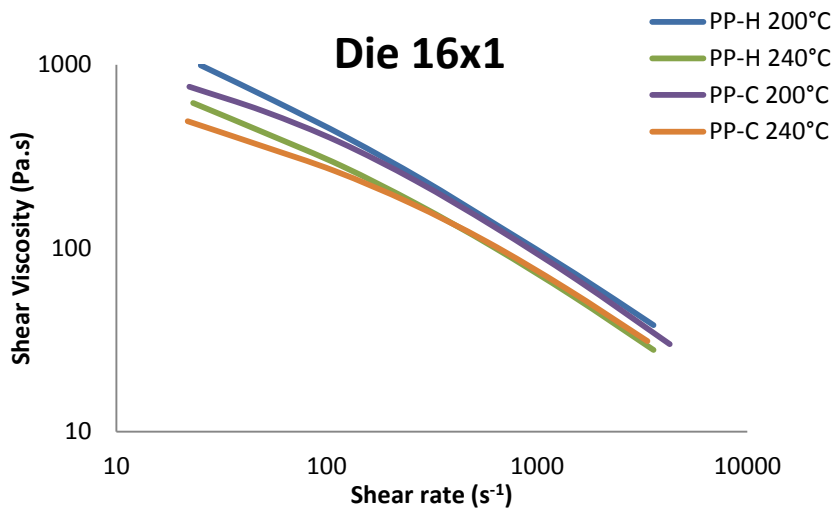

Figure 5.1-7 Flow curves for PP-H and PP-C with the 16X1 die

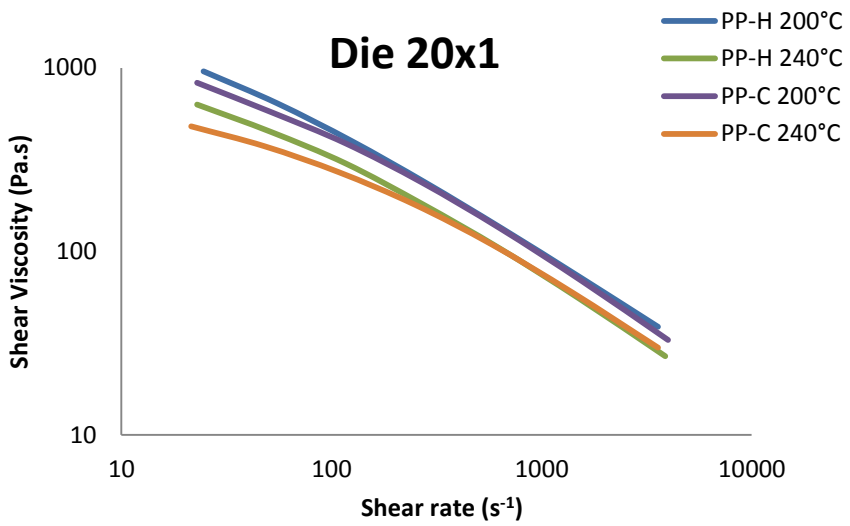

Figure 5.1-8 Flow curves for PP-H and PP-C with the 20X1 die

Clearly, at low shear rate, the copolymer and homopolymer display significant difference in viscosity, and the difference gradually disappears as the shear rate increases.

The power constants (k, n) of the two PP materials can be estimated according to the flow curves obtained from RH7 rheometry. As mentioned previously, the effect of die length is negligible at high shear rates (linear region) and the long die gives more accurate data, thus, the estimation of power constants is based on the flow curves generated with the long die. An example of estimation is given in Appendix A, section 2, and the resultant data are summarised in Table 5.1-3.

Table 5.1-3 Calculated power law coefficients

Material	Temperature (°C)	K	n	n from Moldflow
PP-H	200	8555	0.35	0.29
	220	6566	0.37	
	240	5157	0.38	
PP-C	200	6915	0.37	0.27
	220	4785	0.41	
	240	3104	0.46	

Clearly, the data show that the consistency index K decreases significantly with increasing temperature. K is no more than the viscosity at shear rate of 1 s^{-1} according to the power law, and it is thus reasonable to see such trend, considering the fact that viscosity of polymer melts decreases with increasing temperature. The power law index also shows some slight changes with temperature, which should be

constant for a given polymer. This may be due to the experimental range of shear rates being too narrow, especially towards the high shear rate region. This may allow the data points in the low shear rate region (close to non-linear region) to exert too much influence on the estimation of power law index n. The data of index n from Moldflow® are also shown in the table. They are deduced from much broader shear rate range (see Figure 5.1-9 and 5.1-10), and are more accurate and independent of temperature as expected. It should be noted that (see section 2.2.4) the analysis of polymer melt flow in Moldflow® Synergy is based on the Cross/WLF equation, where power law index n is one of the parameters.

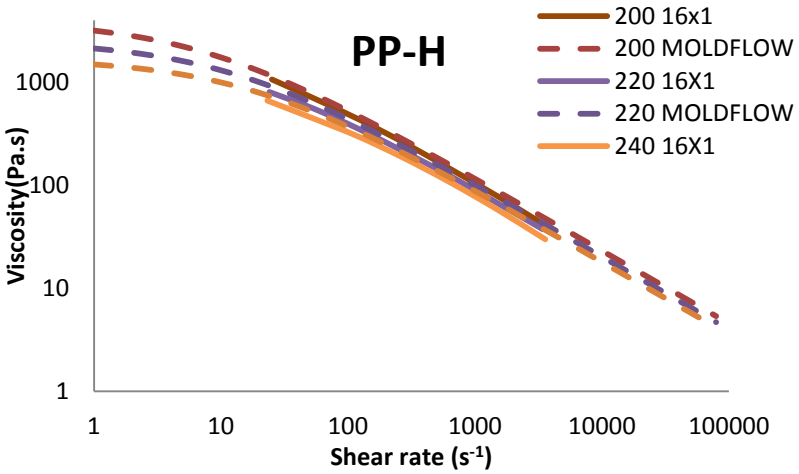

Figure 5.1-9 Flow curves from RH7 and Moldflow for PP-H

The comparison between the measured flow curves and the flow curves given by the database of Moldflow are shown in Figure 5.1-9 and 5.1-10.

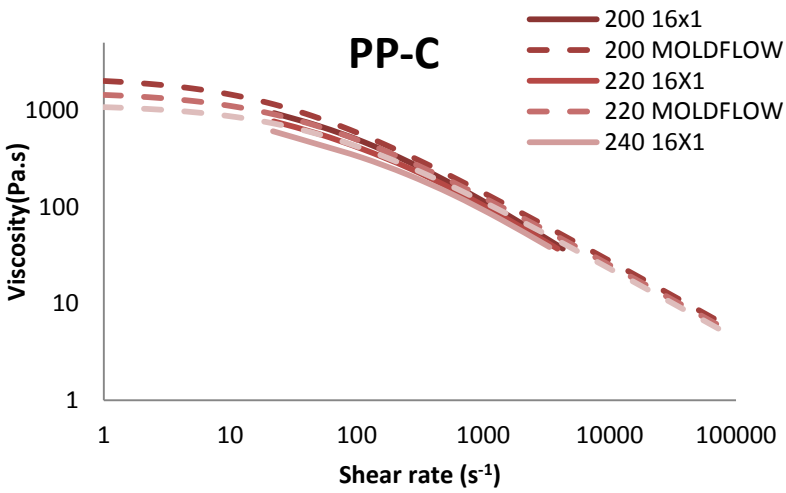

Figure 5.1-10 Flow curves from RH7 and Moldflow for PP-C

For the PP-H, the measured flow curves are very close to those obtained from Moldflow®, and there are only very slight differences between them. PP-C shows some larger discrepancy between the measured data and Moldflow® data. The difference in the flow curves will be considered when comparing the data obtained from actual injection moulding and the Moldflow® simulation of the process covered in section 5.8.

c) DSC

During the test, the samples were heated up to 200 °C from ambient temperature and held for one minute to remove the thermal history, and then cooled down to room temperature and then re-heated up to 200 °C. The cooling and heating rates were set as 10 °C min^{-1}. Emphasis is therefore placed on the data obtained from the cooling and re-heating processes.

The DSC trace for PP-H is shown as an example in Figure 5.1-11, whilst the curves for PP-C and the compatibiliser, PPgMA (maleic anhydride grafted PP) are shown in Appendix A, section 2.

From the DSC curve (Figure 5.1-11), PP-H shows onset of melting at 157 °C and onset of crystallisation at 119 °C. The peak temperatures for melting and crystallisation are 168 °C and 113 °C, respectively. The measured T_m and T_C values for PP-H are in typical ranges for PP materials.

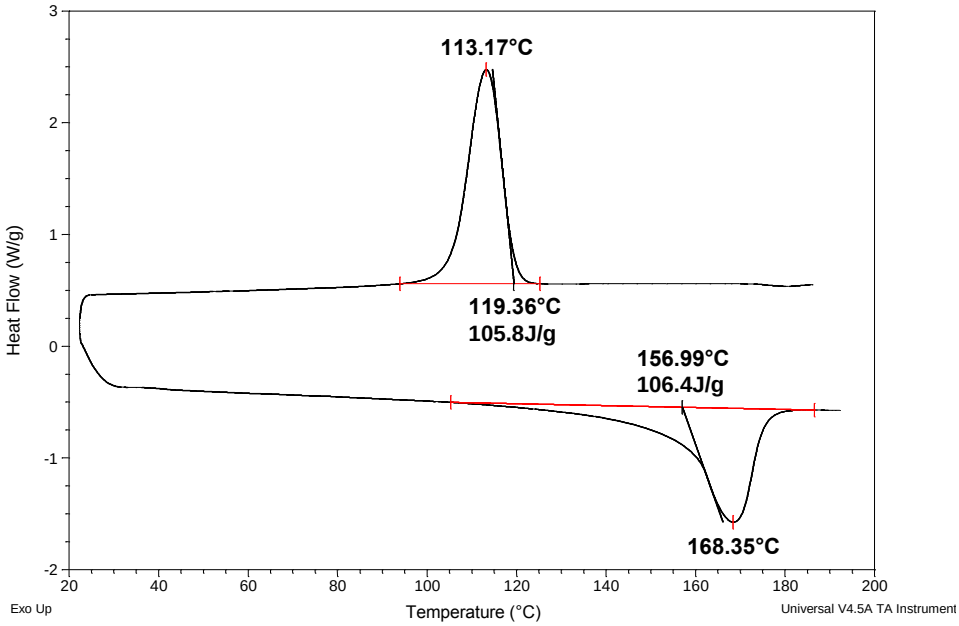

Figure 5.1-11 DSC curve of PP-H

The crystallinity of polymers is calculated with the equation:

$$crystallinity(\%) = \frac{\Delta H}{\Delta H_{100}} \tag{5.1-1}$$

where ΔH is the enthalpy of fusion, and ΔH_{100} is the enthalpy of fusion when the material has 100 % crystallinity. For PP, ΔH_{100}= 207 J g^{-1},[237] and the crystallinity of the PP materials studied can be calculated. Table 5.1-4 summarises the resulting DSC data.

Table 5.1-4 Resultant data from DSC

Materials	Tm onset (°C)	Tm peak (°C)	Tc onset (°C)	Tc peak (°C)	Enthalpy of fusion (J g^{-1})	Enthalpy of crystallisation (J g^{-1})	Crystallinity (%)
PP-H	157	168	119	113	106	105	51.2
PP-C	156	171	134	126	77	77	37.2
PPgMA	153	166	116	109	90	90	43.5

In comparison to PP-H, PP-C has a similar T_m (onset) value of 156 °C and a higher T_c (onset) value of 134 °C. The endothermic and exothermic peaks of PP-C are much smaller than these of PP-H, indicating a lower degree of crystallinity. PP-C, as a copolymer, has a lower degree of stereo-regularity for its molecular chains, compared to a homopolymer. The low regularity impairs the ability of the copolymer to crystallise. A very weak peak can be observed around 120 °C on heating and

around 100 °C on cooling from the DSC curve of PP-C, due to the crystallisable PE sequences in the copolymer. Due to the presence of nucleating agent in the PP-C, a higher Tc is obtained. The compatibiliser, PPgMA has a T_m of 153 °C and a T_C of 116 °C, and the two characteristic temperatures are very close to these of PP-H.

The materials discussed in this section are to be used for all the experiments performed in this search programme, but the experiment of single screw extrusion of recycled PP blends to be presented next in section 5.2, is an exception.

5.2 DoE – Single Screw Extrusion of Recycled PP Blends

To develop a strong understanding of the DoE approach and the underlying statistical principles, an independent study of single screw extrusion of recycled PP blends was carried out. The experimental procedure has been described in section 4.2, and this section presents and discusses the results obtained in this experiment. Table 5.2-1 summarises the experimental results.

Table 5.2-1 Melt temperature (A), screw speed (B), concentration of recycled PP (C), melt pressure (ΔP), mass output ($\dot{m}$), screw torque (M) and melt temperature rise at the die temperature (ΔT)

Std Order	Run	Coded A	Coded B	Coded C	ΔP (bar)	$\dot{m}$ (g min^{-1})	M (Nm)	ΔT (°C)
1	15	-1	-1	-1	208.0	48.5	45.0	12.8
2	9	1	-1	-1	146.0	24.2	25.0	12.2
3	18	-1	1	-1	240.0	56.8	46.0	17.8
4	14	1	1	-1	190.0	57.7	35.0	17.2
5	16	-1	-1	1	90.0	24.0	18.0	3.8
6	5	1	-1	1	71.0	16.2	11.0	3.2
7	7	-1	1	1	123.0	48.1	28.0	8.8
8	4	1	1	1	100.0	63.4	17.0	8.2
9	8	-1.68	0	0	165.0	48.6	44.0	11.0
10	13	1.68	0	0	117.0	44.2	20.0	12.0
11	20	0	-1.68	0	93.0	12.3	18.0	5.0
12	6	0	1.68	0	165.0	68.5	30.0	18.0
13	2	0	0	-1.68	237.0	41.1	65.0	15.0
14	11	0	0	1.68	80.0	41.8	13.0	9.0
15	3	0	0	0	133.0	42.8	25.0	12.0
16	19	0	0	0	137.0	42.6	24.0	10.0
17	17	0	0	0	160.0	39.0	25.0	10.0
18	10	0	0	0	141.0	42.6	24.0	11.0
19	12	0	0	0	138.0	41.9	24.0	12.0
20	1	0	0	0	141.0	41.8	25.0	10.0

The ANOVA table for melt pressure, as a typical example of the data obtained, is shown in Table 5.2-2. The ANOVA tables for the other responses are in Appendix B. The p-values of the model terms for the responses are summarised in Table 5.2-3.

Table 5.2-2 ANOVA Table for melt pressure (A = barrel temperature, B = screw speed, C = blend concentration of A850 recycled PP)

Source	Sum of Squares	Df	Mean Square	F-Value	p-value
Model	42803.808	9	4755.979	69.335	< 0.0001
A	4034.335	1	4034.335	58.815	< 0.0001
B	4915.272	1	4915.272	71.657	< 0.0001
C	32287.895	1	32287.895	470.709	< 0.0001
AB	8.000	1	8.000	0.117	0.7398
AC	612.500	1	612.500	8.929	0.0136
BC	24.500	1	24.500	0.357	0.5634
A^2	2.513	1	2.513	0.037	0.8520
B^2	210.850	1	210.850	3.074	0.1101
C^2	628.667	1	628.667	9.165	0.0127
Residual	685.942	10	68.594		

Table 5.2-3 ANOVA table of p-values (A = barrel temperature, B = screw speed, C = blend concentration of A850 recycled PP)

Source	Melt pressure	Mass output	Screw Torque	Temperature difference
A	**< 0.0001**	**0.0822**	**0.0002**	0.8946
B	**< 0.0001**	**< 0.0001**	**0.0150**	**0.0002**
C	**< 0.0001**	**0.0176**	**< 0.0001**	**0.0001**
AB	0.7398	**0.0004**	0.6932	1.0000
AC	**0.0136**	**0.0074**	0.3158	1.0000
BC	0.5634	**0.0095**	0.6932	1.0000
A^2	0.8520	0.1030	0.1450	0.9693
B^2	0.1101	0.5070	0.3964	0.9693
C^2	**0.0127**	0.8001	**0.0038**	0.7778

The initial full regression model for each response was simplified by removing the negligible terms with p-values greater than 0.10. On the other hand, the terms with p-values lower than 0.05 were considered as significant and kept in the models. The four selected responses, melt pressure (ΔP), mass output ($\dot{m}$), screw torque (M) and temperature difference between the die and polymer at the exit (ΔT) are discussed separately next, on the basis of the final predictive models obtained.

5.2.1 Melt Pressure (ΔP)

According to the p-values in Table 5.2-3, the terms A, B, C, AC and C^2 were considered as significant for melt pressure and thus the second order regression model was reduced by removing the other insignificant terms. With the computed coefficients, the final predictive equation for melt pressure with coded factors becomes:

$$\Delta P(bar) = 139.03 - 17.19A + 18.97B - 48.62C + 8.75AC + 6.91C^2 \qquad (5.2\text{-}1)$$

This equation confirms that the respective effects of the independent variables are consistent with theoretical predictions. For instance, increasing the melt temperature in the metering zone of the extruder (factor A) and the concentration of high MFI component of the PP blend (factor C) each bring about a reduction in melt viscosity and, therefore, a reduction in pressure across the die. Since melt temperature also controls shear viscosity, the interactive term AC is significant. Furthermore, one notes the large effect of factor C in Equation 5.2-1. An example of a response surface predicted by Equation 5.2-1 is shown in Figure 5.2-1. The response surface shows that melt pressure is reduced when increasing barrel temperature and the content of recycled PP. The magnitude of the change in melt pressure, with respect to variables A and C, is consistent with the interpretation above. Based on Equation 5.2-1, one 3D response surface can be plotted.

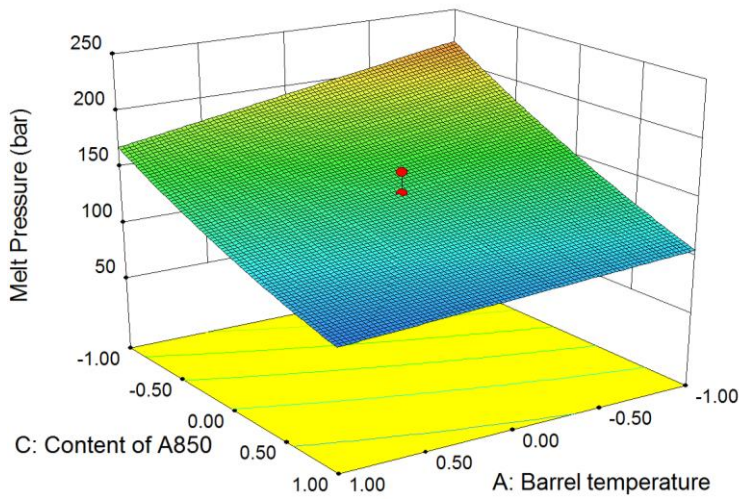

Figure 5.2-1 Melt pressure response surface for effect of PP composition ratio, factor C (content of A850) and barrel temperature, factor A. (B is set at the neutral point, i.e. zero-level).

As predicted from theoretical consideration, higher screw speed (B) leads to a greater volumetric output and results in a higher pressure even though melt viscosity would be expected to decrease to some extent due by shear-thinning effects. It should be noted, however, that the addition of the high MFI component would reduce this effect. Under any given set of process conditions, melt viscosity of the PP compounds is determined by the recycled PP composition ratio which, in turn, will reduce the sensitivity of melt viscosity to changes in barrel temperature and, consequently, its effect will be borne out on the overall response. As a result, the interaction factor AC was found to be a significant term by the ANOVA. However, while the interpretation of interactive effects can be quite complex the second order term (C^2) is significant and brings about a curvature in the response surface.

As mentioned previously the estimates of the coefficients $\hat{\beta}_i$ are one-half the effect predicted for the corresponding factor. Therefore, the first order term of C has to be considered to be the most influential on the response, which implies that melt viscosity is a dominating factor on the developed pressure in single screw extruder operations.

5.2.2 Extruder Mass Output ($\dot{m}$)

For extruder mass output, the reduced regression model with coded factors is shown by Equation 5.2-2 below.

$$\dot{m}\ (g\ min^{-1}) = 42.31 - 1.7A + 15.19B - 2.5C + 6.03AB + 3.86AC + 3.69BC \quad (5.2\text{-}2)$$

Note that although melt transport theory[177] in extrusion processes relates volumetric output (Q) to the process variables, this has no significant effect on the predictions as it is directly proportional to mass output ($\dot{m}$), due to the insignificant compressibility effects. Furthermore, the modified model implies that over the factor ranges studied, non-linear effects are not identified from the experimental results. The coefficients suggest that screw speed (B) has the most significant effect on mass output, consistent with the study of Borgaonkar and Ramani[238] and with predictions from the melt pumping analysis in single screw extrusion, consisting of laminar shear flow due to drag forces induced by screw rotation[239].

Figure 5.2-2 shows a typical Q/P diagram derived from basic theoretical considerations, which illustrates the effects of rotational screw speed ($N_B > N_A$) consistent with the dominating effect of this variable predicted by Equation 5.2-2. This figure also implies that at a given screw speed there will be only a relatively small change in the operational viscosity, as reported by Birley *et al.*[174] This also explains the small coefficients for the effect of barrel temperature and PP blend ratio (terms A and C in Equation 5.2-2), confirming that they have limited influence on mass output, despite their direct effect on melt viscosity. Therefore, output may increase or decrease as viscosity changes depending on the way the respective coefficients affect the extruder and die characteristics.

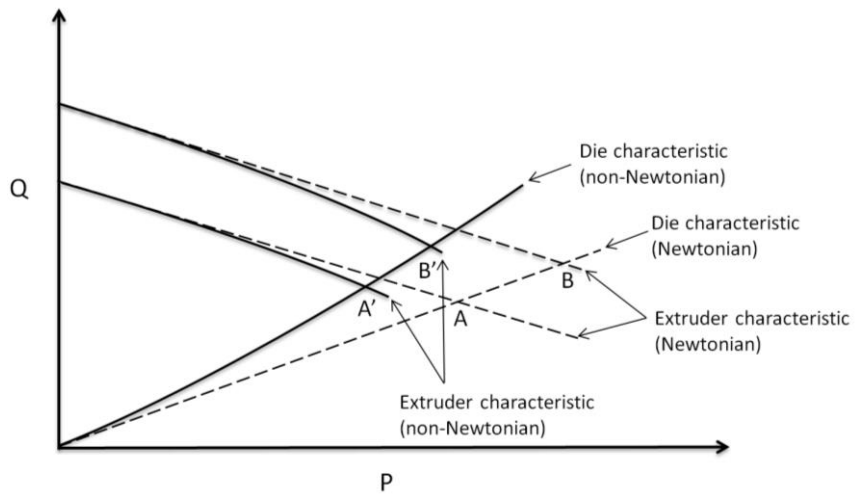

Figure 5.2-2 Schematic depiction of the volumetric output from a single screw extruder (Q) as a function of head pressure (P), defining respectively the screw and die characteristics, and their intersection as the operating condition. Solid lines represent solutions for pseudoplastic rheological behaviour and dotted lines for Newtonian flow.

Two of the ANOVA response surfaces represented by Equation 5.2-2 are shown in Figures 5.2-3 and 5.2-4, which reveal the complex nature of extrusion dynamics in predicting that all two-factor interactions are significant terms. The third response surface represented by equation 5.2-2 is shown in Appendix B.

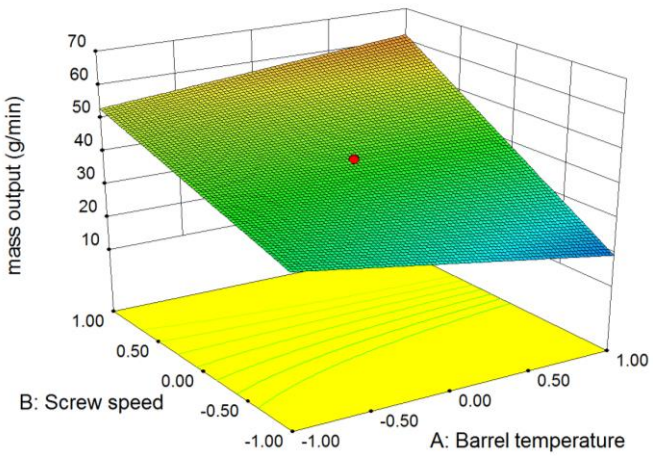

Figure 5.2-3 Response surface of mass output as a function of barrel temperature (factor A) and screw speed (factor B), (C is set at the neutral point, i.e. zero-level).

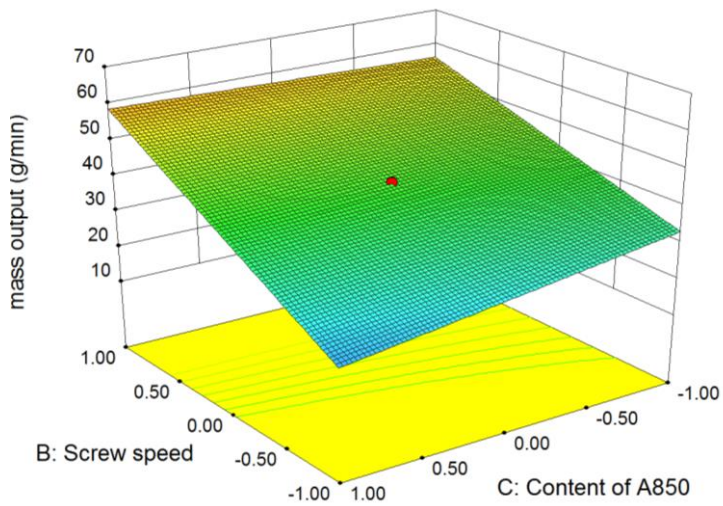

Figure 5.2-4 Response surface of mass output as a function of screw speed (factor B) and composition ratio (content of A850, factor C). A is set at the neutral point, i.e. zero-level).

Since each main factor can have a large effect on melt viscosity, it is likely that a change in one factor can influence the effect of another factor on mass output simply through their effect on viscosity. It is clear also that increasing barrel temperature and content of a low viscosity polymer blend component can significantly reduce melt pressure, albeit with a marginal predicted loss in extruder output. Since high barrel temperature increases thermal energy consumption the option of utilising low-viscosity polymers could be a viable alternative.

5.2.3 Screw Torque (M)

The torque required for screw rotation is directly related to the shear forces generated along the extruder screw-barrel assembly and indicates the transformation of electrical to mechanical energy input to comply with the set process variables. In this study the predicted model obtained for screw torque (M) becomes:

$$M(Nm) = 25.22 - 6.54A + 3.45B - 12.04C + 4C^2 \quad (5.2\text{-}3)$$

This equation predicts similar qualitative relationships to Equation 5.2-1 (melt pressure, ΔP) but without the interaction term AC; this similarity is due to the dependence of melt pressure and screw torque on shear viscosity.

The influence of screw torque mainly relates to the conditions in the metering zone of the extruder, when the melting process is complete and power requirements are dominated by the pumping of the melt through the die by the rotations of the screw. Increasing the concentration of the low viscosity blend component (factor C) has a similar effect on screw torque and this effect includes a second order term in Equation 5.2-3. Increasing screw speed also increases screw torque and machine output, despite the reduction in melt viscosity due to shear heating. One of the response surfaces predicted from Equation 5.2-3 is shown in Figure 5.2-5 where it is indicated that the lowest screw torque is obtained when barrel temperature and the low viscosity blend component are set to their highest levels, which can be directly attributed to effects on shear viscosity. Since screw torque in single screw processes determines the required mechanical energy and electrical power requirements, the analysis clearly confirms the economic advantage of using low viscosity polymers.

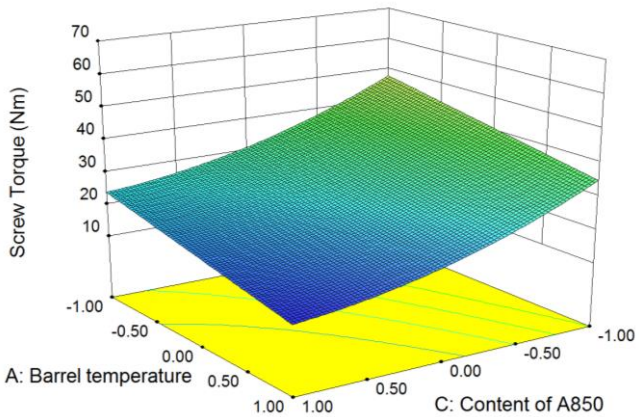

Figure 5.2-5 Response surface of screw torque as a function barrel temperature (factor A) and composition ratio (content of A850, factor C). B is set at the neutral point, i.e. zero-level).

5.2.4 Temperature Increase at the Die (ΔT)

With the aid of a p-value approach, the reduced regression model with coded factors for temperature difference (ΔT) between the barrel setting (factor A) and the extruded melt, is as follows:

$$\Delta T\ (°\mathrm{C}) = 10.95 + 3.07B - 3.37C \tag{5.2-4}$$

This response surface model is very simple, consisting only of first order terms for screw speed (B) and recycled PP concentration (C), so that the initial full second order model has been significant reduced to a simple linear model. This result implies that only factors B and C were significant with a linearly balanced counteracting response on the temperature rise, as shown in Figure 5.2-6.

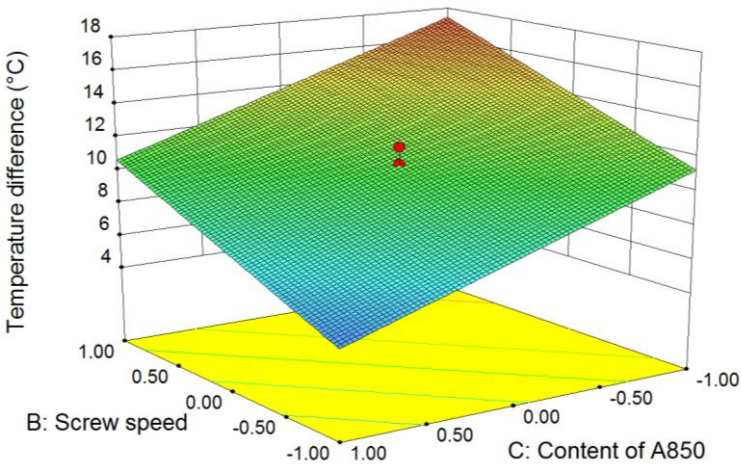

Figure 5.2-6 Response surface of die temperature rise as a function of factors screw speed (factor B) and composition ratio (content of A850, factor C). A is the neutral point, i.e. zero-level).

For simple shear flow, viscous heat dissipation per unit volume (φ_S) can be estimated by the following equation, according to Stevens and Covas [240]:

$$\phi_S = \eta.(\dot{\gamma})^2 \tag{5.2-5}$$

Using a simple power law model for the dependence of viscosity (η) on shear rate ($\dot{\gamma}$) for polymer melts, where *k* and *n* are material constants:

$$\eta = k\dot{\gamma}^{n-1} \tag{5.2-6}$$

So that substitution gives:

$$\phi_S = k.(\dot{\gamma})^{n+1} \tag{5.2-7}$$

Coefficients *k* and *n* are also temperature-sensitive, whilst shear rate $\dot{\gamma}$ is proportional to screw speed. Since the PP blend composition determines indices *k* and *n*, Equation 5.2-7 clearly indicates that screw speed (B) and recycled PP

concentration (C) are the two factors that determine shear heating, regardless of the set temperature (factor A), thereby confirming the validity of the simple relationship expressed by the parameters of Equation 5.2-4. Note that the effect of barrel temperature was too small to be identified by ANOVA as it was completely covered by the noise or experimental variation. Since as a first approximation, power law index (*n)* can be considered to be temperature independent, the barrel temperature can only be expected to affect the consistency index *k* and, therefore, is less influential than the recycled PP concentration.

The analysis shows that the temperature increment (ΔT) at the die is also significant, and therefore would have to be taken into account in some cases where either the polymer or the additives may prone to degradation as temperature rises, as it is obviously the case when chemical blowing agents are used for the production of cellular products. With the aid of a ANOVA analysis the barrel temperature can be set at a required lower level and allow the melt temperature to rise to the precise value required for initiating the decomposition of the blowing agent. On the other hand, the predictive models of temperature increment can also be used to avoid oxidative degradation. For example, when compounding PP/clay nanocomposites with a single screw extruder, the surface coating on nanoclay starts to degrade around 180 °C. Thus, the actual melt temperature needs to be considered and well controlled to avoid the loss of clay surface coating and the reduction in affinity between the PP chains and nanoclay.

5.2.5 Process Optimisation

In Figures 5.2-7 and 5.2-8 are shown examples of overlay plots generated by the software for process optimisation. The yellow areas in the graphs represent the processing conditions (‘operating windows’) that meet the defined criteria, which for the system examined are:

- Melt pressure 120 bar (maximum)
- Mass output not less than 50 g min^{-1}
- Temperature rise at the die no higher than 10 °C

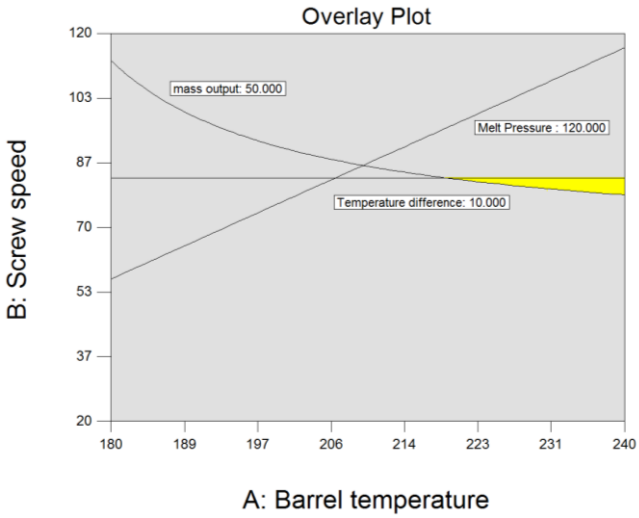

Figure 5.2-7 Overlay plot for process optimisation for composition ratio (factor C), A850 recycled PP = 70 %

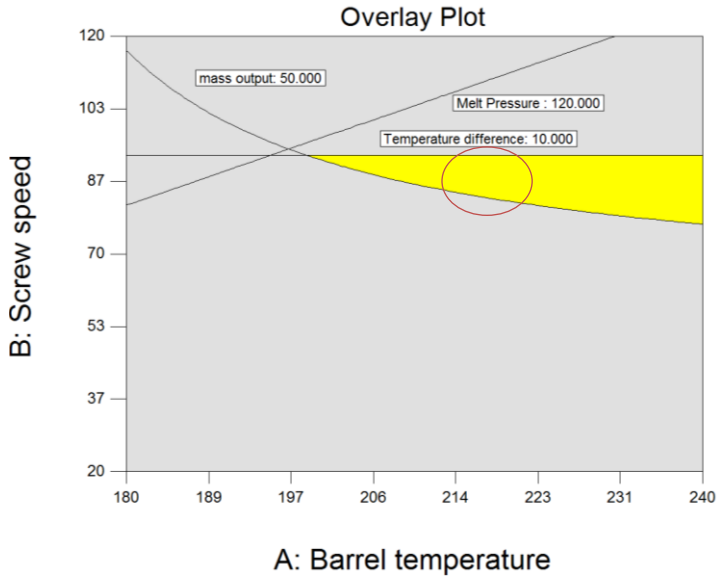

Figure 5.2-8 Overlay plot for process optimisation for composition ratio (factor C), A850 recycled PP = 90 %

These Figures show the operating conditions where recycled PP concentration is 70 % and 90 % respectively. The two axes chosen were screw speed and barrel temperature in order to emphasise the influence of melt viscosity. The plots reveal clearly that when viscosity is reduced by increasing the concentration of the high MFI recycled component in the blend, the processing operating window becomes much wider. In the case of 90 % recycled PP (Figure 5.2-8), it seems that the yellow area indicated by the rea circle is the most ideal part of the operating window, because low barrel temperature (low energy) and lower screw speed are needed.

5.2.6 Summary

A DoE approach was used to investigate single screw extrusion dynamics, in order to develop a strong understanding of the DoE approach and become familiar with it. The variables (‘factors’) studied were barrel temperature, rotational screw speed and the concentration of a low viscosity recycled component in a PP blend system. The measured responses for the steady-state process operation included melt pressure, mass output, screw torque and the temperature rise at the die.

The resulting predictive models show that within the experimental ranges of the three chosen factors, the content of recycled PP and, therefore, the melt viscosity of the feedstock have the highest effect on melt pressure and screw torque. Consistent with the trends that can be derived from extrusion theory, screw speed was found to be a predominant factor for the extruder output rate. Overall, the respective effects of the examined variables on mass output were confounded by two-factor interactions, which were proved to be statistically significant. The simple linear regression model obtained for die temperature rise implies that screw speed and recycled PP content are the most significant factors, having quantitatively similar but opposite effects. The study has provided reproducible data for single screw extrusion operations and has demonstrated that the DoE approach makes it possible to make accurate predictions for the process dynamics. A similar approach was therefore deemed to be feasible for the study of PP/clay nanocomposites, as reported next in section 5.3 and 5.4.

5.3 DoE – Optimum Formulation of PP/clay Nanocomposites

The DoE approach has been successfully applied to investigate the single screw extrusion of recycled PP blends previously. In this section, a very similar approach was employed to optimise the formulation of PP/clay nanocomposites, to achieve the maximum intercalation. Table 5.3-1 below shows the completed design matrix.

Table 5.3-1 Concentrations of AM (A), PPgMA (B) and organoclay (C), interlayer spacing (d_{001}), tensile strength (σ^*) and tensile modulus (E)

Std Order	Run	Coded A	Coded B	Coded C	d_{001} (nm)	σ^* (MPa)	E (MPa)
1	17	-1.00	-1.00	-1.00	4.55	30.9	718.1
2	5	1.00	-1.00	-1.00	4.90	30.3	723.4
3	11	-1.00	1.00	-1.00	4.46	27.0	727.4
4	13	1.00	1.00	-1.00	5.20	33.2	701.1
5	14	-1.00	-1.00	1.00	3.70	33.8	754.1
6	18	1.00	-1.00	1.00	4.55	32.6	704.5
7	7	-1.00	1.00	1.00	3.80	25.4	764.5
8	10	1.00	1.00	1.00	4.37	26.6	693.8
9	8	-1.68	0.00	0.00	3.84	33.5	749.0
10	16	1.68	0.00	0.00	5.50	27.3	676.6
11	3	0.00	-1.68	0.00	4.46	22.6	703.6
12	20	0.00	1.68	0.00	4.50	30.0	700.7
13	19	0.00	0.00	-1.68	5.20	36.0	713.6
14	2	0.00	0.00	1.68	3.80	23.2	752.5
15	12	0.00	0.00	0.00	4.46	26.0	693.6
16	4	0.00	0.00	0.00	4.64	25.4	697.5
17	6	0.00	0.00	0.00	4.41	28.2	711.4
18	9	0.00	0.00	0.00	4.50	25.2	720.6
19	15	0.00	0.00	0.00	4.60	32.7	698.7
20	1	0.00	0.00	0.00	4.50	31.8	761.1

The ANOVA table for interlayer spacing d_{001} is shown in Table 5.3-2 as a typical example of the data obtained, while the other tables are in Appendix C. Table 5.3-3 summarises the p-values of the models for the responses.

Table 5.3-2 ANOVA Table for interlayer spacing d_{001} (A = concentration of AM, B = concentration of PPgMA, C = concentration of organoclay)

Source	Sum of Squares	Df	Mean Square	F-Value	p-value
Model	3.999	9	0.444	17.03	< 0.0001
A	2.058	1	2.058	78.90	< 0.0001
B	0.003	1	0.003	0.11	0.7478
C	1.863	1	1.863	71.43	< 0.0001
AB	0.002	1	0.002	0.06	0.8146
AC	0.014	1	0.014	0.52	0.4866
BC	0.011	1	0.011	0.40	0.5398
A^2	0.013	1	0.013	0.51	0.4931
B^2	0.020	1	0.020	0.75	0.406
C^2	0.013	1	0.013	0.49	0.4991
Residual	0.26	10	0.026		

Table 5.3-3 ANOVA table of p-values (A = concentration of AM, B = concentration of PPgMA, C = concentration of organoclay)

Source	Interlayer spacing	Tensile strength	Tensile modulus
A	< 0.0001	0.7636	0.0036
B	0.7478	0.8537	0.7988
C	< 0.0001	0.1473	0.1368
AB	0.8146	0.4592	0.3448
AC	0.4866	0.6494	0.0913
BC	0.5398	0.2884	0.8160
A^2	0.4931	0.3811	0.8185
B^2	0.406	0.7075	0.6110
C^2	0.4991	0.5228	0.1235

The initial full regression model for each response was simplified by removing the negligible terms with p-values greater than 0.10. On the other hand, the terms with p-values lower than 0.05 were considered as significant and kept in the models. The three selected responses, interlayer spacing (d_{001}), tensile modulus (E) and yield strength (σ^*) will be discussed separately next, on the basis of the final predictive models obtained.

5.3.1 Interlayer Spacing (d_{001})

Figure 5.3-1 shows the XRD patterns of pure DK4 clay and a typical PPCN.

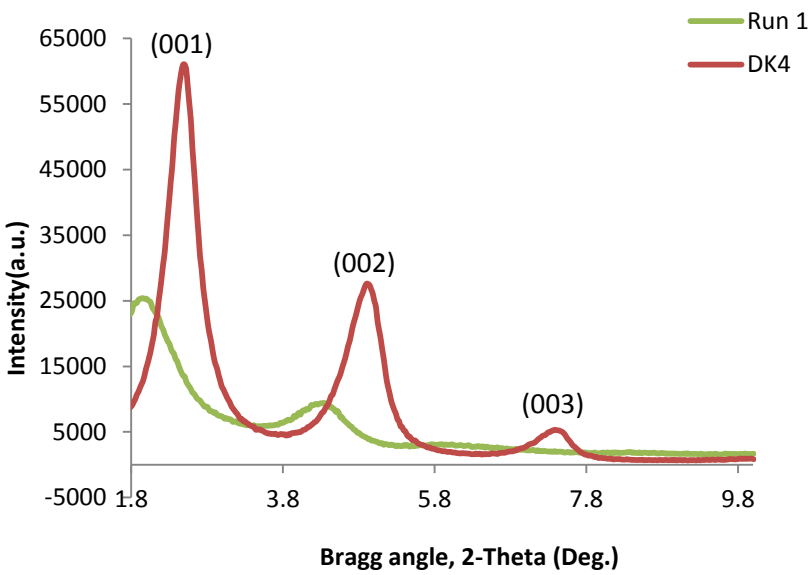

Figure 5.3-1 XRD patterns of DK4 clay and PPCN prepared by run 1 (4 % clay, 4 % PPgMA and 1 % AM, see Table 5.3-1)

It is clear that the peaks shifted towards the lower angle after the organoclay was compounded with PP and other ingredients, which indicates the expansion of clay galleries and increased intercalation. The interlayer spacing (d_{001}) for each sample has been calculated by Bragg's law ($n\lambda = 2dsin\theta$) and is summarised in Table 5.3-1.

According to the p-values in Table 5.3-3, only the terms A and C were considered as significant for interlayer spacing of clay. By removing the other insignificant terms, the full second order regression model with coded factors was reduced to Equation 5.3-1.

$$\boldsymbol{d_{001}(nm) = 4.5 + 0.39A - 0.37C} \qquad (5.3\text{-}1)$$

The equation is simple and only has first order terms for AM concentration (A) and clay concentration (C). Therefore, it simply suggests that concentrations of AM and organoclay were significant with a linearly balanced counteracting response on the interlayer spacing. Either increasing AM content or decreasing clay content will achieve a higher interlayer spacing. The implication of this equation is in good consistency with many studies reported in the literature.[11,14]

It was first reported by Ratnayake *et al* [12] that the addition of short-chain AM molecules into conventional PP/PPgMA/clay system would result in a higher interlayer spacing and promote enhancement of clay dispersion in the PP matrix. In their later study [11], the co-intercalation of PPgMA and short-chain AM molecules in

PP/clay nanocomposites was further investigated. They suggest the hydrogen bonding between the silicate layers and AM as the thermodynamic driving force for the intercalation of AM into the clay galleries, and there are complex interaction between three components, namely, the silicate layers, AM and the maleic anhydride functional groups in PPgMA. On the other hand, it has been reported in many studies that increasing clay concentration has a negative effect on the interlayer spacing of clay in the PP matrix if other ingredients remain unchanged[14,80,123]. Briefly, Equation 5.3-1 suggests that high AM concentration and low clay concentration are necessary to achieve optimum clay dispersion in the PP matrix. Also, it seems that the initially selected ratio of clay to AM component (4:1) is reasonable, which also suggests that the concentration of the relatively expensive AM component can be kept at a low level in PPCNs.

It should be borne in mind that the predictive equation is only valid in the selected experimental ranges. For example, PPgMA was not identified as a significant factor in this experiment, but it does not mean PPgMA is not an essential ingredient in PP/clay system. In actual fact, the presence of PPgMA is critical to the dispersion of organoclay in PP matrix, which has been pointed out by Ratnayake *et al* [11] and also in some other studies[14,66,105,121,241]. However, within the experimental range (0.64 % - 7.36 %) selected for PPgMA in this study, the effect of PPgMA was too small to be identified by ANOVA as it was completely covered by the noise or experimental variation.

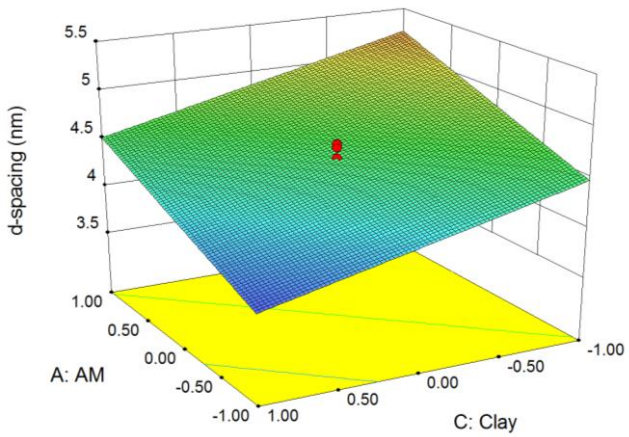

Figure 5.3-2 Response surface of interlayer spacing (d_{001}) as a function of factors AM content (factor A) and clay concentration (factor C). Factor B is set at the neutral point, i.e. zero-level).

The response surface predicted from Equation 5.3-1 is shown in Figure 5.3-2. Clearly, it is indicated that the maximum interlayer spacing can be achieved when clay concentration is at low level while AM concentration is at high level.

5.3.2 Tensile Modulus of PPCNs (E)

The raw data of tensile tests are summarised in Appendix C. For tensile modulus, the reduced regression model with coded factors is shown by Equation 5.3-2 below.

$$\boldsymbol{E(MPa) = 718.29 - 19.26A + 8.22C - 12.41AC} \qquad (5.3\text{-}2)$$

It should be noted that although factor C has a p-value slightly larger than 0.10, it has to be kept in the equation to support hierarchy as the interaction term AC needs to remain in the equation. This equation suggests similar qualitative relationships to Equation 5.3-1 but with the interaction term AC.

As mentioned previously[11,12], AM molecules tend to migrate into clay galleries and form hydrogen bonding with the modifiers on the clay surface, leading to a higher interlayer spacing and promotion of enhancement of clay dispersion in the PP matrix. Therefore, the presence of the interaction term AC in the equation is reasonable. It should be noted, however, that when the AM molecules exceed the saturation level, the excessive AM molecules may be dispersed in the matrix by reacting with the maleic anhydride groups of PPgMA.

The concentration of AM is the most influential factor according to the coefficients in the equation above. The AM is normally used as a slip agent in PP processing and it is a low molecular weight species. Therefore, if any free AM molecules are dispersed in the PP matrix, it is very likely that they would adversely influence the homogeneity and then plasticise the PP matrix, leading to reduced tensile modulus. It is thus reasonable for the term of the main effect of AM concentration (A) to have a negative coefficient of -19.26. However, it should be noted that the excessive AM content may reduce the tensile modulus of PPCNs, but the presence of AM helps intercalation/exfoliation which would increase the modulus. Thus, the addition of AM component is believed to be necessary make PPCNs.

On the other hand, clay is very a rigid and strong material compared to thermoplastics. Thus, the addition of clay would stiffen the PP matrix, provided there is good bonding between them. It is thus predicted by the equation that increasing clay content leads to increasing tensile modulus, which has been widely reported in literature.[14,80,121]

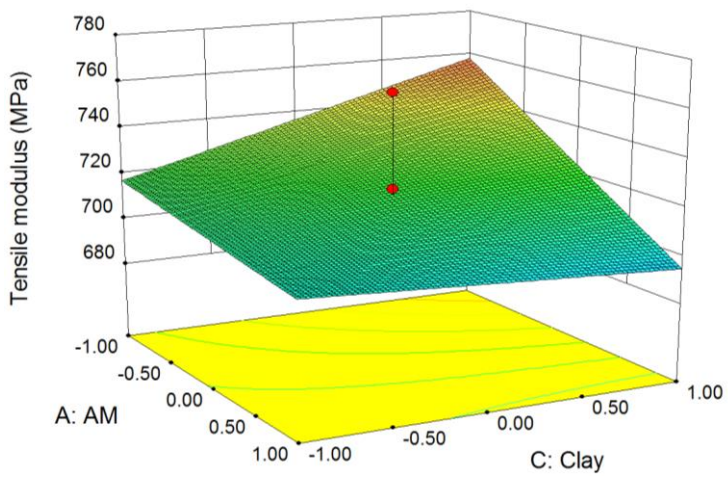

Figure 5.3-3 Response surface of tensile modulus (E) as a function of factors AM content (factor A) and clay concentration (factor C). Factor B is set at the neutral point, i.e. zero-level).

The response surface represented by Equation 5.3-2 is shown in Figure 5.3-3. The 3D surface implies that within the selected ranges, the optimum tensile modulus can be achieved if the concentration of AM is at low level while that of clay is at high level. Again, concentration of PPgMA (B) was not identified as a significant factor for the selected response, tensile modulus. In other words, the effect of PPgMA content on the tensile modulus of PPCN was negligible compared to the noise and experimental variation.

5.3.3 Yield Strength of PPCNs (σ^*)

As ductile fracture behaviour was observed for the compression moulded PPCN dumbbell samples, the yield strength was thus used as a response. A typical stress-strain graph obtained from the PPCN sample is shown as an example in Appendix C.

With the aid of p-value approach, the reduced predictive model with coded factors for tensile strength is as follow:

$$\boldsymbol{\sigma^*(MPa) = 29.09} \qquad (5.3\text{-}3)$$

The equation clearly shows that tensile strength is a constant and no factors have been identified as significant to the tensile strength. Therefore, in the selected experimental ranges, the effects of all the three factors on tensile strength were negligible compared to the noise or experimental variation. As a result, the ANOVA response surface is a horizontal flat plate as shown in Figure 5.3-4.

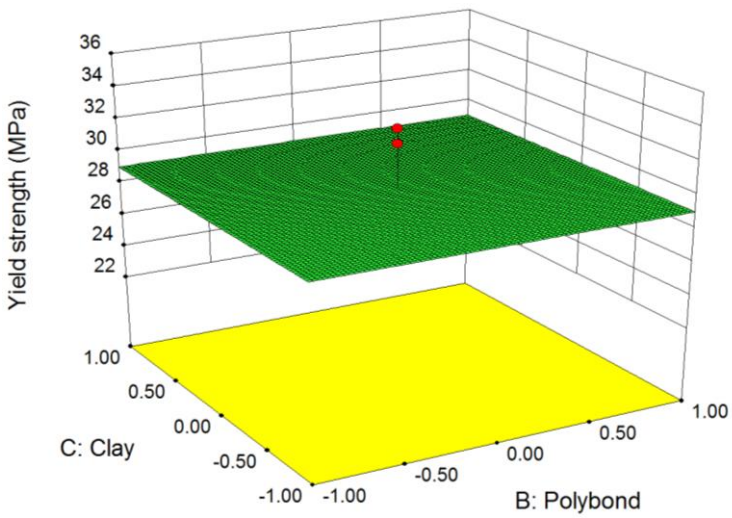

Figure 5.3-4 Response surface of tensile strength (σ^*) as a function of factors PPgMA content (factor B) and clay concentration (factor C). Factor A is set at the neutral point, i.e. zero-level).

5.3.4 Optimum Formulation and Summary

The study reported by Dong *et al*[14] reveals that the optimum formulation can be achieved when clay concentration is around 3 -5 %, and PPgMA content is two times that. However, the co-intercalant agent, AM content, was not used in their study. Therefore, the amount of PPgMA needed can be further reduced in the presence of AM content. According to the study reported by Ratnayake *et al*[11], the optimum formulation is achieved when clay, PPgMA and AM are in the ratio of 4:4:1.

Combining their studies and the resulting data and predictive equations from this study, the initial optimum formulation was set as 4 wt% clay, 4 wt% PPgMA and 1 wt% AM, which is actually the central point in this DoE study. As the maximum interlayer spacing was set as the main criterion, the optimum formulation was then slightly adjusted to 4 wt% clay, 4 wt% PPgMA and 1.5 wt% AM. The PPCNs used in all the subsequent studies on compounding conditions and injection moulding were on the basis of this optimum formulation.

5.4 DoE – Optimum Compounding Conditions for PPCNs

The formulation of PPCNs was optimised in the previous experiment with the aid of a DoE approach, and the optimum formulation obtained has been utilised in the subsequent experiments throughout this research programme. This section presents the results of the study of optimisation of the compounding conditions using a DoE approach. The experiment was carried out using a small scale twin rotor batch mixer and a large scale twin screw extruder. Table 5.4-1 summarises the experimental results from the twin screw extruder.

Table 5.4-1 Feed rate (A), screw speed (B), interlayer spacing (d_{001}), tensile modulus (E), and tensile strength (σ^*)

Std Order	Run	Coded A	Coded B	d_{001} (nm)	E (MPa)	σ^* (MPa)
1	3	-1	-1	3.94	655.7	33.9
2	5	1	-1	4.13	683.7	37.0
3	13	-1	1	3.84	628.4	34.2
4	12	1	1	4.01	632.9	36.4
5	4	-1.414	0	4.01	652.6	33.2
6	10	1.414	0	4.01	638.0	35.1
7	1	0	-1.414	3.56	670.1	33.4
8	7	0	1.414	4.55	603.9	30.5
9	2	0	0	3.87	652.0	34.6
10	11	0	0	4.20	649.4	35.0
11	8	0	0	3.94	624.1	34.6
12	6	0	0	4.20	643.5	35.0
13	9	0	0	4.05	635.0	35.2

Table 5.4-2 shows the calculated ANOVA data for tensile modulus (E), as a typical example of the data obtained for the twin screw extrusion, while the other tables are in Appendix D. Table 5.4-3 illustrates the p-values of the model terms for the responses.

Table 5.4-2 ANOVA Table for tensile modulus E. (A = feed rate, B = screw speed)

Source	Sum of Squares	Df	Mean Square	F-Value	p-value
Model	3983.273	5	796.655	5.235	0.026
A	17.560	1	17.560	0.115	0.744
B	3686.010	1	3686.010	24.220	0.002
AB	138.063	1	138.063	0.907	0.373
A^2	141.261	1	141.261	0.928	0.367
B^2	0.883	1	0.883	0.006	0.941
Residual	1065.316	7	152.188		

Table 5.4-3 ANOVA table of p-values (A = feed rate, B = screw speed)

Source	Interlayer spacing	Tensile strength	Tensile modulus
A	0.6270	0.0838	0.7441
B	0.1398	0.3037	0.0017
AB	0.9693	0.7576	0.3726
A^2	0.7300	0.6963	0.3674
B^2	0.9060	0.1403	0.9414

The experimental results for the twin rotor mixer, corresponding ANOVA data for tensile modulus and the calculated p-values of the model terms for responses are summarised in Table 5.4-4 to Table 5.4-6, respectively. The other ANOVA tables are in Appendix D.

Table 5.4-4 Mixing time (A), rotor speed (B), interlayer spacing (d_{001}), tensile modulus (E), and tensile strength (σ^*)

Std order	Run	Coded A	Coded B	d_{001} (nm)	E (MPa)	σ^* (MPa)
1	11	-1	-1	5.91	677.7	30.8
2	6	1	-1	5.87	672.5	23.7
3	1	-1	1	5.79	669.1	29.0
4	2	1	1	5.75	704.5	29.4
5	7	-1.41	0	5.99	695.1	27.3
6	8	1.41	0	5.64	690.1	32.5
7	9	0	-1.41	6.15	696.6	32.6
8	5	0	1.41	5.68	676.8	26.1
9	10	0	0	5.83	683.8	30.0
10	4	0	0	5.83	672.1	29.8
11	3	0	0	5.61	681.1	26.8

Table 5.4-5 ANOVA Table for tensile modulus E. (A = mixing time, B = rotor speed)

Source	Sum of Squares	Df	Mean Square	F-Value	p-value
Model	602.370	5	120.470	0.820	0.582
A	67.060	1	67.060	0.460	0.528
B	2.590	1	2.590	0.018	0.899
AB	412.120	1	412.120	2.820	0.154
A^2	119.980	1	119.980	0.820	0.407
B^2	15.830	1	15.830	0.110	0.756
Residual	731.130	5	146.230		

Table 5.4-6 ANOVA table of p-values (A = mixing time, B = rotor speed)

Source	Interlayer spacing	Tensile strength	Tensile modulus
A	0.1775	0.9478	0.528
B	0.0538	0.6017	0.899
AB	0.9954	0.3152	0.154
A^2	0.7114	0.9108	0.407
B^2	0.2375	0.9419	0.756

The initial full regression model for each response was simplified by removing the negligible terms with p-values greater than 0.10. On the other hand, the terms with p-values lower than 0.05 were considered as significant and retained. The three selected responses, interlayer spacing (d_{001}), tensile modulus (E) and yield strength ($\boldsymbol{\sigma}^*$) will be discussed separately, on the basis of the final predictive models obtained.

Section 5.4.1 focuses on the effect of compounding conditions on the basal spacing of the clay (d_{001}). Section 5.4.2 and 5.4.3 analyse the influence of compounding conditions on tensile modulus and yield strength, respectively. Optimisation of processing conditions will be discussed in section 5.4.4.

5.4.1 Interlayer Spacing of clay (d_{001})

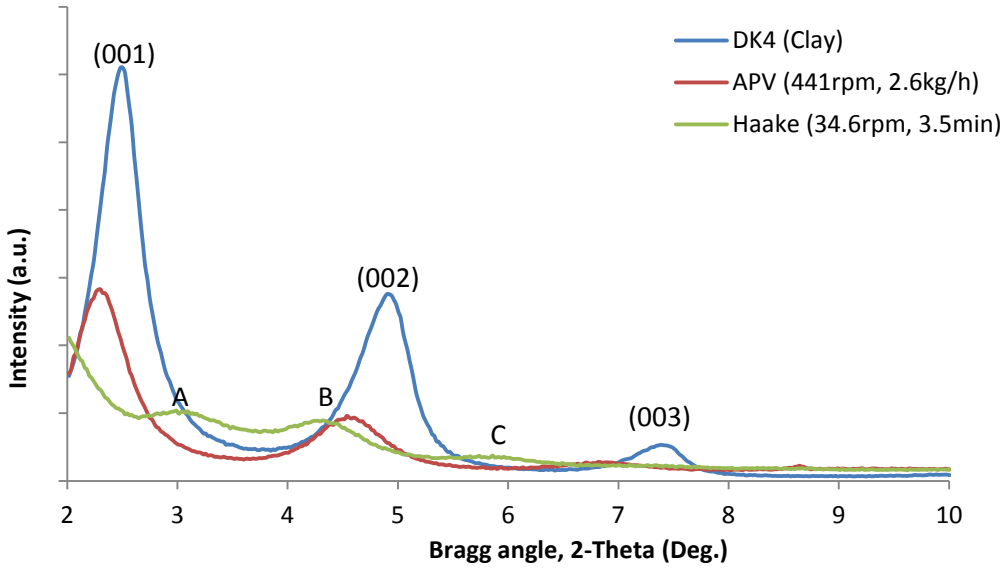

Figure 5.4-1 XRD patterns for pure organoclay and PPCNs prepared by the two methods

Figure 5.4-1 displays the XRD patterns of pure organoclay and a typical PPCN sample prepared by the two different compounding methods. Clearly, the (001) peak has shifted to lower diffraction angles after each of the melt compounding processes. The interlayer spacing (d_{001}) for each sample has been calculated by Bragg's law ($n\lambda = 2dsin\theta$) and typed into the design matrices.

It should be noted that for the samples prepared by the Haake twin rotor mixer, d_{001} values were deduced from higher order reflections, as their d_{001} peaks dropped below 2θ = 2°, indicating d_{001} greater than 4.41 nm (at 2θ = 2°), arising from particularly effective intercalation. The reflections of the DK4 based composited mixed in the Haake mixer have been labelled A, B and C in Figure 5.4-1. The calculated spacings for the three reflections are 2.95 nm, 2.02 nm and 1.51 nm, respectively. The calculated spacing values and their relationships show clearly that not all the three weak reflections are due to higher order reflections. Peak B has a spacing value (2.02 nm) that is smaller than the half of 4.41 nm (at 2θ = 2°), which strongly suggests that peak A is most likely to be the actual (002) reflection associated with the (001) reflection that has dropped below 2θ = 2°. Therefore, the d_{001} value was deduced from the (002) reflection at peak A, in this study. The reflections at peak B and C may be due to inhomogeneous dispersion and degradation of the surfactant, leading to a tactoids with differing (001) spacings.

a) APV twin screw extruder

According to the p-values listed in Table 5.4-3, there seem to be no significant terms for the response of interlayer spacing of clay in the PPCNs prepared by APV twin screw extrusion. However, after removing the other insignificant terms, the p-value of term B dropped from 0.1398 to 0.0671, which is barely significant (between 0.05 and 0.1). Therefore, the final predictive equation becomes:

$$d_{001}(mn) = 4.02 + 0.15B \tag{5.4-1}$$

This equation is very simple and implies that high screw speed (B) promotes better dispersion of organoclay in PP matrix in the selected experimental ranges, which is consistent with some studies reported in literature [17,128,242]. This result is very likely due to the simple fact that shear rate is proportional to screw speed, and greater hydrodynamic stress within the mixing zones of the extruder is generated under higher shear rate, which improves the dispersion of clay.

It is well known that for a given starve-fed twin screw extruder, shear rate is also affected by feed rate. However, the effect of feed rate on shear rate, especially in the fully filled zones of a extruder, is still very limited compared to that of screw speed [189]. Additionally, the variation range of feed rate was relatively narrow in this experiment, so that the influence of feed rate on shear rate was too weak to cause any effective change in d_{001}. As a result, feed rate was not identified as statically significant.

In general, a good dispersion of clay in PP matrix relies not only on shear rate but also on residence time [127,243]. A suitable residence time should be long enough for the PP chains to diffuse into the clay galleries but shorter than the time for the degradation of polymer and clay surfactant. It is known that, in a co-rotating twin screw extruder, the average residence time can be estimated by [187]:

$$\bar{t} = \frac{A}{Q} + \frac{B}{N} \tag{5.4-2}$$

where A and B are constant for specific screw configurations, Q is volumetric throughput and N is screw speed.

According to Equation 5.4-2, the average residence time is determined by overall feed rate and screw speed together for a given twin screw extruder. Therefore, the

effect of screw speed implied by Equation 5.4-1 might be an overall effect induced by shear rate and residence time. However, Equation 5.4-2 implies that increasing screw speed will reduce residence time. Therefore, the effect of shear rate and shear stress was clear much more important than residence time difference in this experiment.

Feed rate was not identified as statistically significant to the response, d_{001}, in the range of 2 kg/h to 6 kg/h, although Equation 5.4-2 suggests that it influences residence time. Feed rate has very a limited effect on shear rate compared to screw speed as mentioned previously, and shear rate was the dominating factor influencing the dispersion of clay in this experiment. Therefore, in this relatively narrow experimental range, the minor effect of feed rate was completely masked by the noise and or experimental variation and other effects, such as screw speed. The effects of feed rate on clay dispersion in much broader variation ranges, have been reported in literature[128,243].

A response surface predicted by Equation 5.4-1 is shown in Figure 5.4-2. It shows that interlayer spacing is increased linearly when increasing screw speed, while feed rate has no effect on the interlayer spacing.

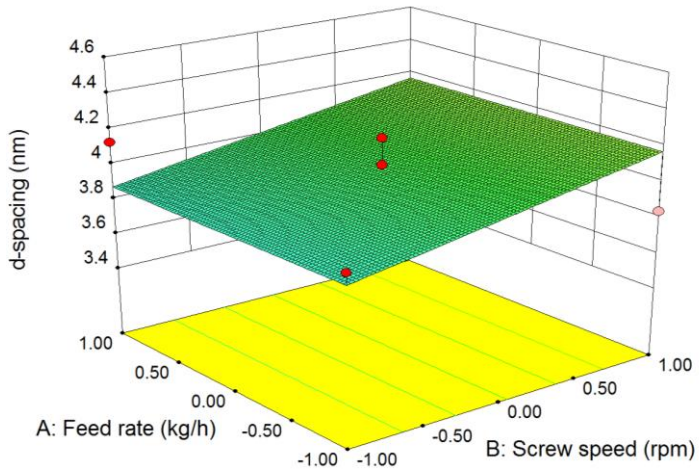

Figure 5.4-2 Response surface of d_{001} for effect of feed rate (A) and screw speed (B). (APV extruder)

b) Haake twin rotor mixer

Similarly, after removing the insignificant terms according to the p-values, the reduced regression model with coded factors for interlayer spacing of clay in the PPCNs prepared by the Haake twin rotor mixer is as follows:

$$d_{001}(mn) = 5.82 - 0.11B \quad (5.4\text{-}3)$$

The equation predicts very similar qualitative relationships to Equation 5.4-1, but with negative coefficient for rotor speed (B). This similarity is very likely due to the dominating effect of shear rate on the dispersion of clay.

The negative coefficient for rotor speed indicates that interlayer spacing of clay is decreased when increasing rotor speed. This seemingly contradictory observation is most likely due to the excessively intense shear conditions in the twin rotor mixer, which generated high shear heat, resulting in degradation of clay surfactant and reduced clay-polymer affinity. During the experiment, the actual chamber temperature of the twin rotor mixer dropped a little bit from the set temperature of 185 °C when the PP granules and other ingredients were added. It then increased rapidly and exceeded the set temperature, and soon the increase of temperature slowed down gradually and the actual temperature tended to level off with time. The actual temperature at the end of mixing varied from 188 to around 200 °C, depending on the mixing time and rotor speed used. Briefly, either increasing rotor speed or mixing time led to increased actual temperature. It is thus very likely that high rotor speed resulted in more loss of surface coating on clay sheets, although it provided high shear rate which was good for the intercalation and exfoliation of clay. As losing surface coating was the dominating effect, thus the term of rotor speed in Equation 5.4-3 has a negative coefficient.

In comparison, the APV twin screw extruder had electric cast slab heaters and water cooling within the barrel to control temperature consistently. Processing temperatures of the extruder from the feed zone to the die were set as 165, 165, 170, 180, 185 and 185 °C, respectively. During the experiment, when the maximum screw speed was 300 rpm, the actual temperature of the material in the extruder was no higher than 185 °C. When the screw speed reached 500 rpm, the actual temperature of the material only slightly exceeded 190 °C in the mixing zones of the extruder. Moreover, the rate of intercalant oxidation in the Haake twin rotor mixer may be higher than in the twin screw extruder as the former is more open to the atmosphere than the latter. Degradation of the surfactant may therefore be more rapid and more severe than in equivalent composites processed in the twin screw extruder. Thus, the degradation of the coating on clay was less likely to happen in the twin screw

extruder, and the overall effect of increasing screw speed was still promoting the dispersion of clay, resulting in a positive coefficient for the term of screw speed in Equation 5.4-2.

On the other hand, mixing time (A) was not identified as a significant factor, which is very likely due to its competing effects on the clay dispersion. Similarly, increasing mixing time benefited the diffusion of PP chains into clay galleries, but this was counter balanced by grater degradation of the surface coating on clay platelets, as the melt temperature exceeded 180 °C for extended periods of time. The overall effect of mixing time was then neutralised by the competing effects and was not identified as a significant factor in the experiment.

Figure 5.4-3 shows the response surface represented by Equation 5.4-3, which reveals the simple relationship between the rotor speed and the interlayer spacing of clay in the PPCNs.

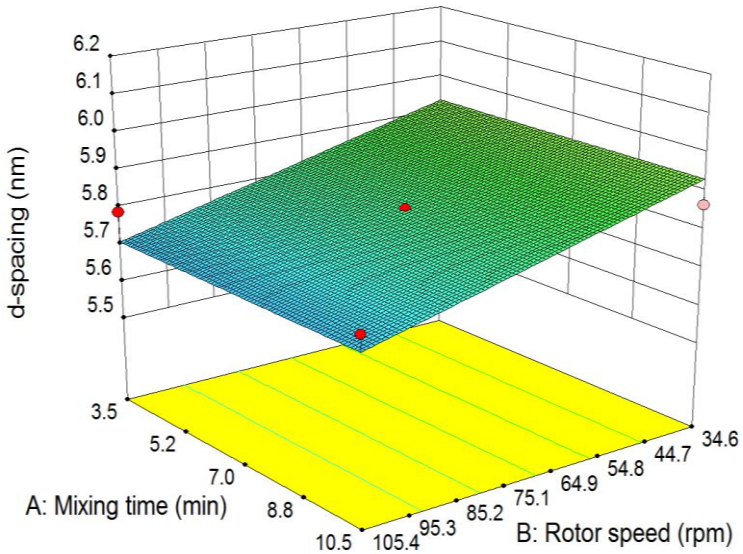

Figure 5.4-3 Response surface of d_{001} for effect of mixing time (A) and rotor speed (B). (Haake mixer)

c) Comparison of the two compounding methods

It should be noted that the intercepts in the predictive regression models are the grand averages of all observations. According to Equation 5.4-1 and 5.4-3, it is very clear that the average value of d_{001} was 5.82 nm for PPCNs prepared by the twin rotor mixer and 4.02 nm for those prepared by the twin screw extruder. The much higher value of interlayer spacing for PPCNs made by the twin rotor mixer indicates

a higher degree of intercalation. Therefore, it seems that the twin rotor mixer is a more efficient and effective method to compound PPCNs, in comparison to the screw profile used with the twin screw extruder.

Considering the high level of intercalation and the negative effect of rotor speed on d_{001}, it appears that the shear condition is more extreme in the twin rotor mixer, with respect to the rotor/screw profile designs used in this study. However, the TEM graphs in Figure 5.4-4 shows the contrary.

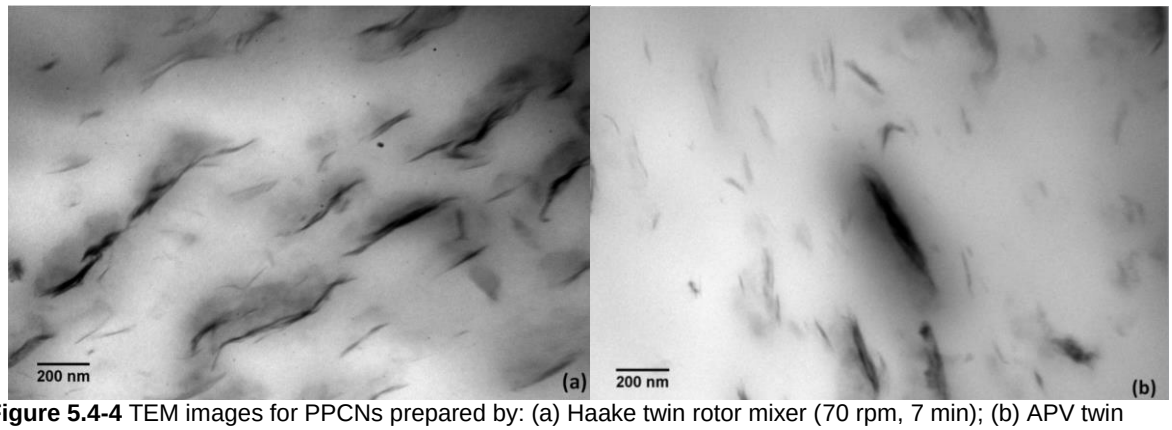

Figure 5.4-4 TEM images for PPCNs prepared by: (a) Haake twin rotor mixer (70 rpm, 7 min); (b) APV twin screw extruder (300 rpm, 4 kg/h)

Firstly, the TEM images confirm that the clay is only partially exfoliated in the PP matrices because both individual clay sheets and thick clay stacks can be observed. In comparison to Figure 5.4-4 (a), it is quite clear that there are more individual clay sheets in Figure 5.4-4 (b), but it seems that they have been separated, then fragmented into smaller particles with greatly reduced aspect ratios. This might suggest that the shear condition in the twin screw extruder was actually too extreme compared to the twin rotor mixer. As mentioned previously, the actual temperature in the extruder was relatively well controlled, thus, degradation of the clay surface coating was less likely to happen in the twin screw extruder although the shear conditions were more extreme.

Interestingly, the results indicate that the interlayer spacing of PPCNs prepared by the twin screw extruder was much lower, although the twin screw extruder provided more extreme shear conditions. Considering the XRD results and the TEM images, it seems that the extreme shear conditions promoted the delamination of clay sheets to achieve high exfoliation, but it might not be that helpful to improve the diffusion of PP chains into the clay galleries to achieve high intercalation. Additionally, Figure

5.4-4 (b) also displays the presence of big clay tactoids among the individual clay sheets, which implies that the mixing effect of the twin screw extruder was not quite uniform.

On the other hand, the dispersion of clay shown in Figure 5.4-4 (a) is very uniform and consistent. Although there were relatively less individual clay sheets, the clay platelets were not fragmented significantly and the aspect ratio was maintained well compared to the PPCNs prepared by the twin screw extruder. The TEM graphs suggest that the twin rotor mixer is more effective and desirable when compounding PPCNs in comparison to the twin screw extruder with the given screw design.

The difference in the dispersion of clay revealed by d_{001} data and TEM images implies that there might be significant difference in the tensile properties of PPCNs prepared by the two different methods.

5.4.2 Tensile Modulus of PPCNs (E)

As described in section 4.4.4, the PPCNs compounded by the two methods were compression moulded into flat sheets and then tensile samples were cut from the sheets by the cutter, according to ISO527-2-5A. The raw data is summarised in Appendix D.

a) APV twin screw extruder

The reduced regression model with coded factor for PPCNs prepared by APV twin screw extruder is shown by Equation 5.4-4 below.

$$E(MPa) = 643.79 - 21.47B \qquad (5.4\text{-}4)$$

The model is also very simple, and only extruder screw speed (B) was identified as statistically significant. It predicts similar qualitative relationships to Equation 5.4-2, but the screw speed shows negative effects on the tensile modulus of PPCNs. Again, feed rate was not identified as a significant factor. According to the previous discussion regarding the dispersion of clay, feed rate showed very limited effect compare to screw speed, and the effect was completely masked. As the dispersion

of clay significantly affects the interfacial area and hence the reinforcing capacity of PPCNs, it is thus reasonable that feed rate was identified as insignificant again.

It is well known that the reinforcing effect of filler is significantly affected by its aspect ratio. Normally, better reinforcement can be achieved with higher aspect ratio. As shown in Figure 5.4-4(b), the shear conditions in the twin screw extruder resulted in breakdown of the clay sheets and reduced aspect ratio. Increasing screw speed increases the shear rate/stress, which can thus fragment more clay sheets in the flow field reduce the aspect ratio further. Additionally, increased shear rate generates more shear heat and might cause chain session for the PP matrix and degradation of coating on clay. Therefore, it was expected that the screw speed would show a negative effect on the tensile modulus of PPCNs, given the earlier observations (TEM image).

The response surface represented by Equation 5.4-4 is shown in Figure 5.4-5.

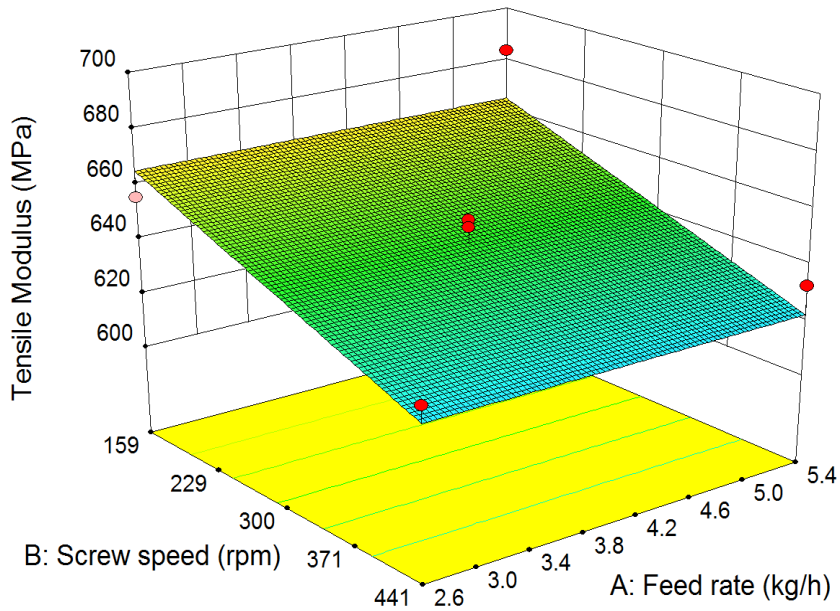

Figure 5.4-5 Response surface of tensile modulus effect of feed rate (A) and screw speed (B). (APV extruder)

b) Haake twin rotor mixer

After removing the insignificant terms, the final predictive models for PPCNs compounded in the twin rotor mixer is shown as follow:

$$E(MPa) = 683.58 \tag{5.4-5}$$

Within the levels of variation observed, the model shows a constant value of modulus, which suggests that there are no significant factors to the response of tensile modulus. As discussed previously, the XRD results and TEM images strongly imply that the Haake twin rotor mixer was very effective and efficient when compounding PPCNs, in comparison to the APV twin screw extruder. Therefore, in the selected variation ranges for processing conditions, it is very likely that the dispersion of clay and its reinforcing effect was similar regardless of mixing conditions. Thus, the change in the processing condition has very limited effect on the tensile modulus of PPCNs prepared by the twin rotor mixer. Figure 5.4-6 shows the response surface predicted by Equation 5.4-5 above.

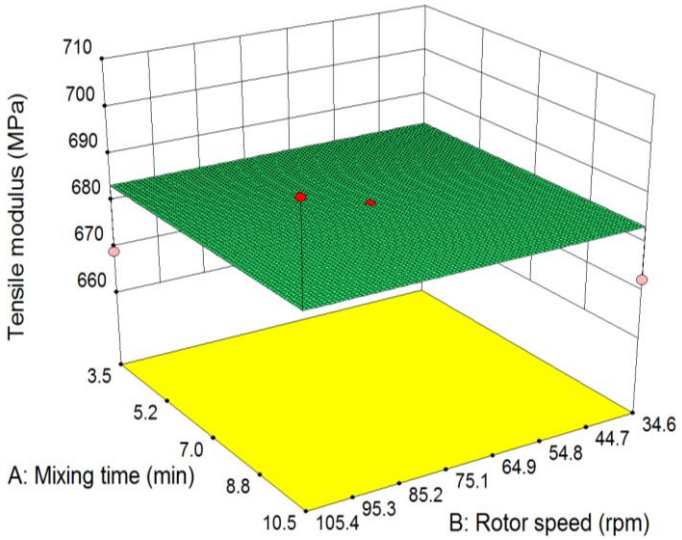

Figure 5.4-6 Response surface of tensile modulus for effect of mixing time (A) and rotor speed (B). (Haake extruder)

c) Comparison of the two methods

The intercepts in Equation 5.4-4 and 5.4-5 are the grand average values of tensile modulus for PPCNs prepared by the two different methods. Therefore, the average modulus for the PPCNs compounded by the twin screw extruder was 644 MPa while that for the PPCNs prepared by the twin rotor mixer was 683 MPa. Clearly, the average tensile modulus show good consistency with the interlayer spacing (d_{001}) and aspect ratios of clay discussed in the previous section. Higher tensile modulus was thus expected for the PP/clay nanocomposites prepared by the twin rotor mixer.

The preliminary results suggest that the shear conditions in the processing equipment had significant effects on the dispersion of clay and thus the reinforcing effects achieved. Generally, the flow is very complex in a twin rotor mixer or a twin screw extruder, thus it is very difficult to define the shear conditions precisely, especially in a twin screw extruder which always possesses different screw zones with different functions. However, it seems worthwhile to estimate the magnitude of the maximum shear rate that might occur in the twin rotor mixer and twin screw extruder in the experiment.

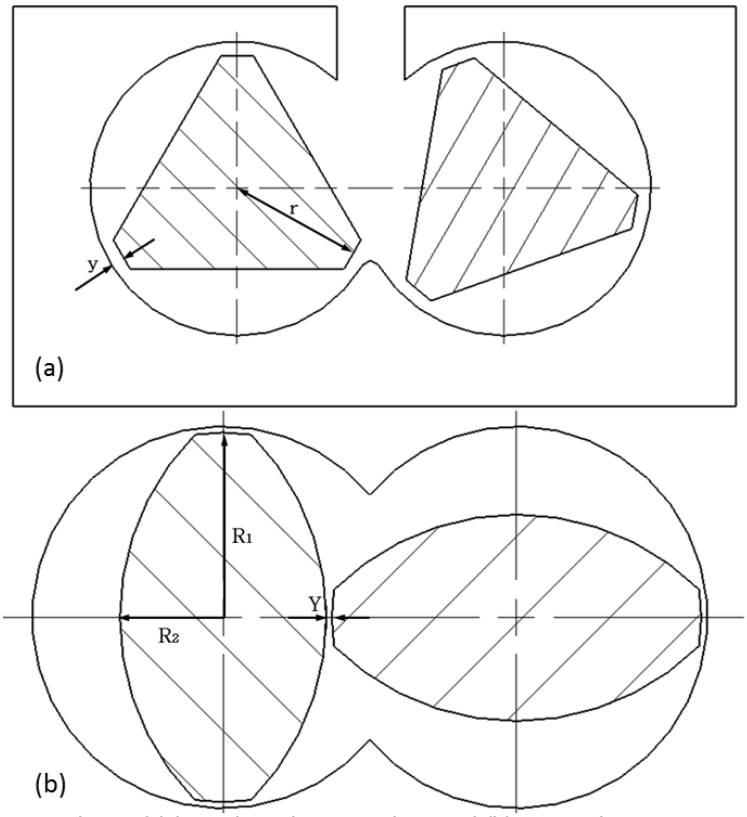

Figure 5.4-7 Cross sections of (a) Haake twin rotor mixer and (b) APV twin screw extruder (mixing zone)

In Haake twin rotor mixer, the left rotor rotates clockwise while the right one anti-clockwise and they rotates at a speed ratio of 3:2. In Figure 5.4-7(a), y represents the smallest gap between the left rotor and bowl chamber wall is, which offers the maximum shear rate during mixing. Correspondingly, r is the largest radius of the roller blade. The calculation for maximum shear rate in the twin rotor mixer is based on the central point (70 rpm, 7 min).

For the Haake mixer, it is known that the smallest gap (y) is 1.4 mm and the largest radius (r) of the roller blade is 18.2 mm, and the rotor speed (N) is 70 rpm.

The angular speed (n) in rad s^{-1} is equal to:

$$n = \frac{2\pi \cdot N}{60} = 7.3\ rad\ s^{-1} \tag{5.4-6}$$

The circumferential speed (v) is thus equal to:

$$v = n \cdot r = 7.3 \cdot 18.2\ mm\ s^{-1} = 132.9\ mm\ s^{-1} \tag{5.4-7}$$

The maximum shear rate ($\dot{\gamma}_{max}$) with the above speed v is:

$$\dot{\gamma}_{max} = \frac{v}{y} = \frac{132.9}{1.4} s^{-1} = 94.9\ s^{-1} \tag{5.4-8}$$

It is well known that mixing mainly takes place in kneading paddles in a twin screw extruder. The cross-section of kneading paddles is shown in Figure 5.4-7 (b). Y represents the clearance between the tips of kneading paddles, where the maximum shear rate is most likely to appear. R_1 and R_2 are the outer radius and inner radius of the kneading paddles. It is known that the ratio of R_1/R_2 is equal to1.82 and Y is about 0.8 mm for the APV MP series for laboratory and pilot scale. It is known that R_1 = 15 mm, thus R_2 is thus around 8.2 mm. Similarly, the estimation of maximum shear rate in the twin screw extruder is based on the central point (300 rpm, 4 kg) in the DoE design, and thus N is equal to 300 rpm.

The circumferential speeds are equal to:

$$v_1 = \frac{2\pi \cdot N}{60} \cdot R_1 = 471\ mm\ s^{-1} \tag{5.4-9}$$

$$v_2 = \frac{2\pi \cdot N}{60} \cdot R_2 = 257.5\ mm\ s^{-1} \tag{5.4-10}$$

As it is a co-rotating twin screw extruder, thus the calculated speeds above are applied to the clearance Y in the reverse direction.

The maximum shear rate ($\dot{\gamma}_{max}$) based on the above speeds is:

$$\dot{\gamma}_{max} = \frac{v_1 + v_2}{Y} = 910.6\ s^{-1} \tag{5.4-11}$$

According to the calculations above, the possible maximum shear rate in the twin rotor is about 94.9 mm s^{-1} at the central point (70 rpm, 7 min), which is almost in an order of magnitude less than that in the twin screw extruder at the central point (300 rpm, 4 kg/h). This big difference in shear rate explains the breakdown of the clay

platelets shown in Figure 5.4-4(b) and the lower modulus of the PPCNs prepared by the extruder. The calculated shear rates also imply that an extremely intensive shear condition is not necessary for high levels of intercalation, considering the smaller d_{001} values of the PPCNs prepared by the extruder.

5.4.3 Yield Strength of PPCNs (σ^*)

In addition to tensile modulus, the yield strength of the PPCNs prepared by the two compounding methods was also measured, to investigate the effects of processing conditions.

a) APV twin screw extruder

For yield strength of PPCNs prepared by the twin screw extruder, the reduced regression model with coded factors is shown by Equation 5.4-12 below.

$$\sigma^*(APV) = 34.47 + A \qquad (5.4\text{-}12)$$

This simple equation shows that only feed rate (A) was identified as a significant factor to the response, yield strength. The positive coefficient means that increasing feed rate leads to an increase in the yield strength.

According to the previous discussion, the shear condition in the twin screw extruder was very extreme and led to breakdown of the clay platelets and hence reduced aspect ratio. As suggested by Equation 5.4-2, increasing feed rate reduces residence time. During compounding, the reduced residence time may lead to less loss in aspect ratio, although the shear rate in the extruder was increased slightly when increasing feed rate. As mentioned previously, the effect of feed rate on shear rate was very limited compared to that of screw speed, especially in the narrow variation range. Thus, the overall effect of increasing feed rate was to increase yield strength.

On the other hand, increasing screw speed can also reduce residence time, but it makes the shear condition much more extreme. It is hence very likely that those comparable competing effects caused screw speed to be an insignificant factor. The response surface for Equation 5.4-12 is shown in Figure 5.4-8.

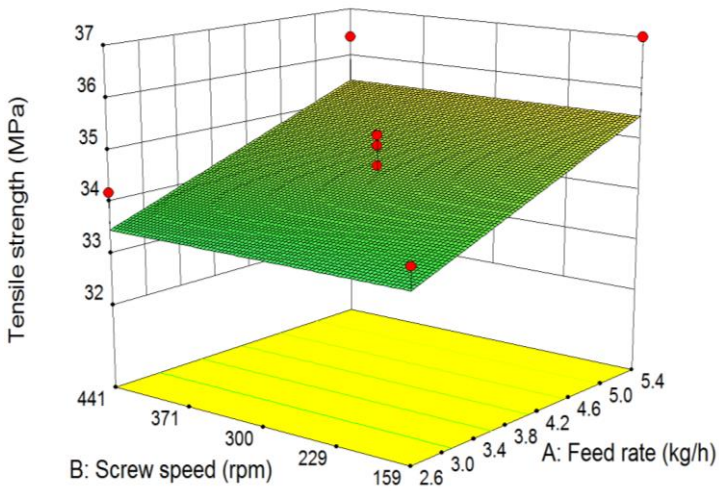

Figure 5.4-8 Response surface of tensile strength effect of feed rate (A) and screw speed (B).

b) Haake twin rotor mixer

The final predictive model for yield strength of PPCNs prepared by the twin rotor mixer is shown in Equation 5.4-13 below:

$$\sigma^*(Haake) = 28.91 \tag{5.4-13}$$

The model implies a constant value of σ^* (very similar to Equation 5.4-5). No factors were identified as significant for the response. Therefore, the results suggest that the tensile modulus and yield strength of PPCNs prepared using the twin rotor mixer were not affected by the change in processing conditions. This indicates that the dispersion of clay in the PPCNs prepared by the twin rotor mixer was very similar regardless the variation in processing conditions over the selected ranges. The response surface represented by Equation 5.4-12 is shown in Figure 5.4-9.

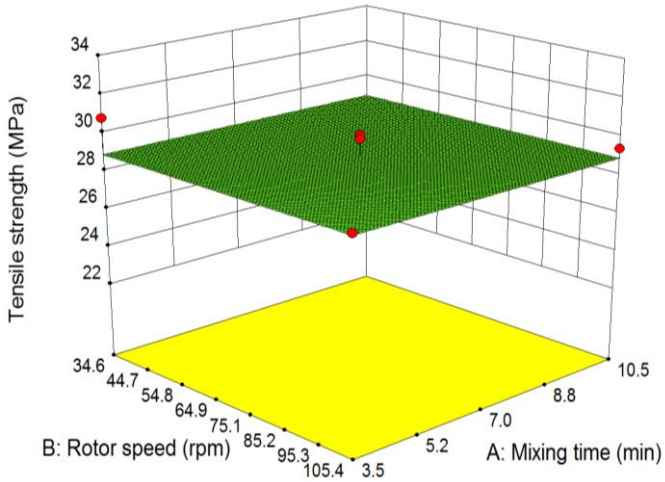

Figure 5.4-9 Response surface of yield strength for effect of mixing time (A) and rotor speed (B).

c) Comparison of the two methods

According to the intercepts in Equation 5.4-12 and 5.4-13, it is clear the average yield strengths were 34.5 MPa and 28.9 MPa for the PPCNs prepared by the twin screw extruder and twin rotor mixer, respectively.

The yield strength of PPCNs prepared by the twin rotor mixer was significantly lower, although the intercalation (d_{001}) and tensile modulus was higher. Considering the PPCNs prepared by twin screw extruder had higher level of exfoliation, this result implies that for yield strength, exfoliation is more important. The possible reason is that more interphase and bonding were able to be created between the clay and PP matrix, at higher level of exfoliation. When the PPCN samples prepared by the twin screw extruder were under load, more stress could be effectively transferred to the stiff clay sheets. As a result, the PPCN samples prepared by the twin screw extruder could undertake higher load before yielding, leading to higher yield strength.

5.4.4 Process Optimisation and Summary

Based on the discussion above, Table 5.4-7 below summaries and compares the two different mixing methods.

Table 5.4-7 Summaries of the two compounding methods

	APV twin screw extruder	Haake twin rotor mixer
Shear rate	• Extreme • $\dot{\gamma}_{max} = 911\ s^{-1}$ (central point) • Controlled by screw speed and feed rate for a given screw design	• Medium • $\dot{\gamma}_{max} = 94.9\ s^{-1}$ (central point) • Controlled by rotor speed
Residence time	• Controlled by screw speed and feed rate • Less important than shear rate to the dispersion of clay in this experiment	• Controlled by mixing time • Showed no effect on clay dispersion and tensile properties
Intercalation	• Lower • Increased with increasing screw speed	• Higher • Decreased with increasing rotor speed
Exfoliation	• Higher • Due to the extreme shear conditions	• Lower • Due to the medium shear conditions
Aspect ratio	• Lower • Fragmented by extreme shear rate	• Higher • Maintained well
Tensile modulus	• Lower • Due to reduced aspect ratio and chain scissions • Decreases with increasing screw speed	• Higher • Due to higher aspect ratio • Constant
Yield strength	• Higher • Due to higher level of exfoliation • Increases with increasing feed rate	• Lower • Due to lower level of exfoliation • Constant

As Haake twin rotor mixer is only for small-scale mixing, and it is not a continuous process, it is thus not suitable for compounding PPCNs in large quantities. In this project, APV twin screw extruder would be used to produce the PPCN pellets for injection moulding. Therefore, optimisation was only considered for the twin screw extruder with the existing screw design.

The preliminary results show that the shear conditions were very extreme in the twin screw extruder, which fragmented the platelets and caused chain scissions. According to Equation 5.4-4 and 5.4-12, the lowest screw speed and highest feed rate were thus considered to be the optimum compounding conditions, although the maximum interlayer spacing (d_{001}) for clay would not be achieved under the conditions. It should be noted that the above optimisation is only for the twin screw extruder with existing screw design, which would be used to manufacture the PPCN compounds for injection moulding in this project.

However, to further optimise compounding conditions for twin screw extrusion, the process/mixing zones of the screws need to be designed to:

- Achieve higher intercalation
- Achieve higher exfoliation
- Avoid excessive breakdown of the clay particles
- Avoid excessive temperatures

This would need an in-depth study of compounding, examining:

- Different screw designs
- Material analysis from different positions along the screws

After the optimum formulation of PPCNs and compounding conditions were found with the aid of DoE approach, they were used to manufacture the PPCN compounds for the subsequent thin wall injection moulding. Then research moved into the next phase. The effects of moulding conditions on the properties of thin wall injection moulded PPCNs will be discussed in the next section, based upon the experimental results.

5.5 Effects of Processing Conditions on Injection Moulded Parts

After the formulations of PPCNs and compounding conditions were optimised with the aid of DoE approach (sections 5.3 and 5.4), the research then moved into the next phase, thin-wall injection moulding of PPCNs. The optimum formulation and compounding conditions obtained in the earlier work were used to compound PPCN pellets for thin-wall injection moulding. This section will present the setting-up of injection moulding process, and also discuss the effects of processing conditions on injection moulded PPCN parts.

5.5.1 Injection Stroke and Shot Size

Figure 5.5-1 shows the injection moulded parts obtained with increasing shot size. It is clear that when shot size was increased to 120 mm, the cavity volume was completely filled. Then 10 mm was added to both shot size and screw position trip, and the resulting stroke of 130 mm and screw position trip of 10 mm available for packing remained throughout the study of injection moulding.

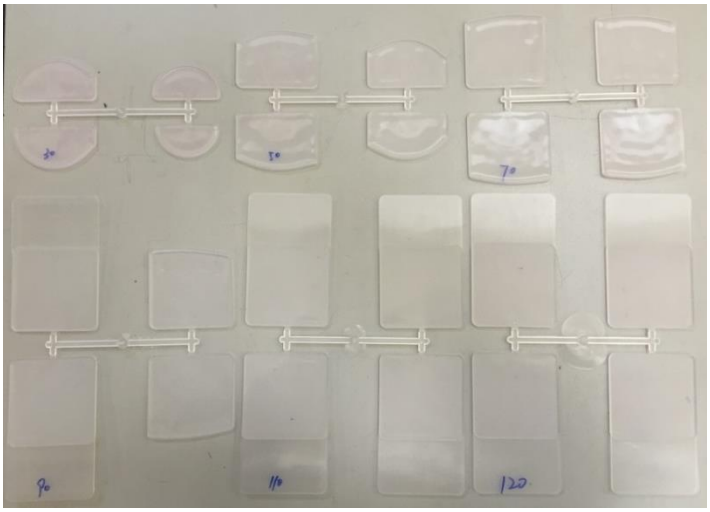

Figure 5.5-1 Injection moulded parts with increasing stroke shot size

5.5.2 Experimental Determination of Hold-On Time and Pressure

Table 5.5-1 summaries the average weight of the mouldings produced (component only) under different hold-on times.

Table 5.5-1 Moulding weight vs. hold-on time at hold-on pressure of 10bar

Hold-on time (s)	2	4	6	8	10
Average mass (g)	54.1	54.5	54.9	54.9	54.8
Standard deviation	0.38	0.12	0.26	0.26	0.35

Figure 5.5-2 shows the plot of weight versus hold-on time, on the basis of the data in Table 5.5-1.

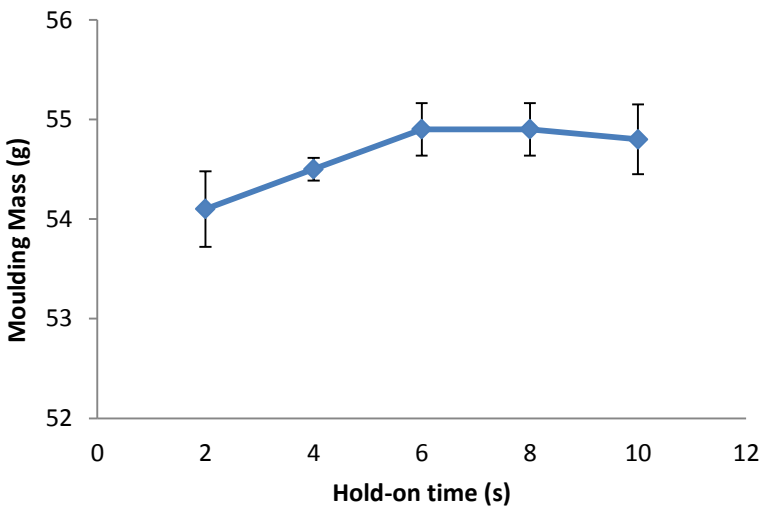

Figure 5.5-2 Moulding weight vs. hold-on time under 10bar hold-on pressure

Clearly, the plot shows that when hold-on is shorter than 6 s, increasing hold-on time leads to an increase in the mass of moulded parts. However, once the hold-on time reaches 6 s and above, the mass of injection moulded parts tends to remain as constant. This result simply implies that during the packing phase or hold-on phase, the gate was completed frozen after around 6 seconds, after which no material or packing pressure can be transmitted into the cavity to achieve further packing of the parts.

The gate is the location at which the molten plastic enters the mould cavity. Figure 5.5-3 highlights the gate, which determines the length of hold-on phase. According to the result, the hold-time was chosen as 6 s throughout the study of injection moulding.

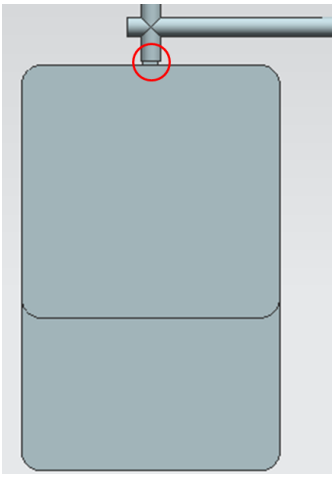

Figure 5.5-3 Gate of the moulding

Similarly, Figure 5.5-4 shows the plot of moulding weight vs. hold-on pressure under the hold-on time of 6 seconds.

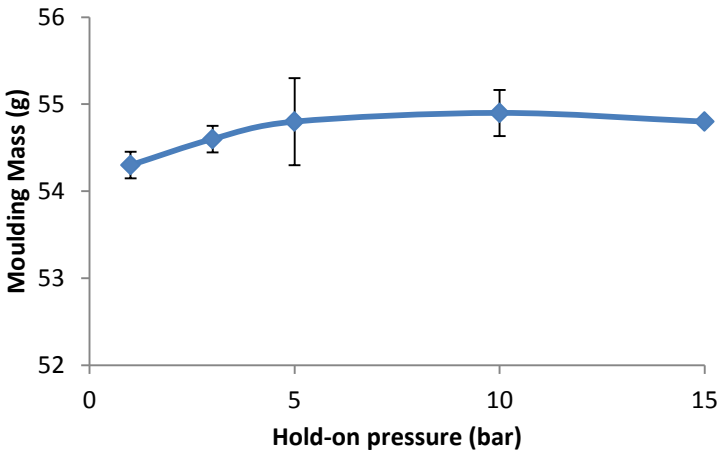

Figure 5.5-4 Mould weight vs. hold-on pressure (hold-on time: 6s)

It is clear from the plot that increasing hold-on pressure causes slightly increasing moulding mass before the hold-on pressure reaches around 10 bar. This is because the moulded parts were just relatively denser under higher hold-on pressure. In this experiment, the criteria used to choose hold-on pressure was that minimising packing pressure as long as it could assure the quality of injection moulded parts.

The weight of injection moulded parts produced under 5 bar hold-on pressure was only 0.1 g less than those produced under 10 bar hold-on pressure. After inspecting the moulded parts, it was found that the quality of the parts produced under 5bar hold-pressure was very good and acceptable, without any visible defects. Therefore, 5 bar was considered as the optimum hold-on pressure.

According to the results above, the optimum hold-on time and pressure for this injection moulding task were 6 s and 5 bar, respectively. They were then used as the default settings throughout the study.

Therefore, the basic settings for the study of injection moulding process are shown in Table 5.5-2. The variations made to study the effects of processing conditions were all on the basis of these basic settings.

Table 5.5-2 Basic settings for injection moulding process

Moulding parameters	settings
Melt temperature (temperature of nozzle and barrel zones)	190 °C/180 °C/175 °C/170 °C
Mould temperature	25 °C
Shot size	130 mm
Screw position trip	10 mm
Injection speed	20 %
Hold on pressure/time	5 bar / 6 s
Cooling time	30 s

5.5.3 Interpretation of Real-Time Data Acquired

After a consistent processing cycle was achieved, the real-time data of in-cavity pressure was collected for each moulding condition. Figure 5.5-5 shows a typical plot pressure/screw position vs. time obtained under the basic processing conditions determined in Table 5.5-2.

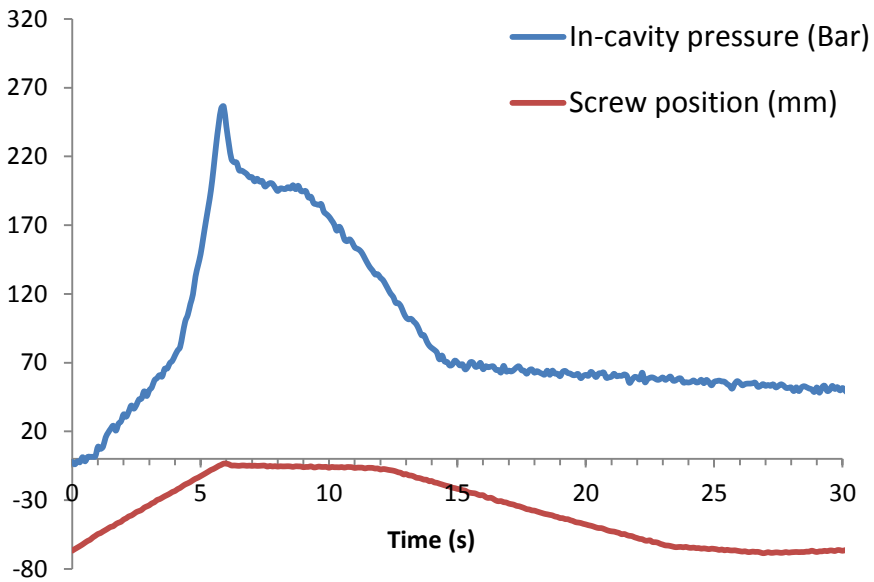

Figure 5.5-5 In-cavity pressure-time plot for PPCNH-20-25

The blue curve illustrates the change of in-cavity pressure during a moulding cycle while the red line shows the change in screw position.

- Screw Positon

According to the screw position curve in the graph, it is clear that the first phase is mould filling, because the screw moves forward at a constant speed (upward gradient). This phase lasts less than 6 seconds in the graph, while the actual injection time given by the injection moulding machine under the injection speed of 20 % was 5.79 seconds, which shows very good consistency. After that, the screw remains almost stationary for about 6 seconds (see graph), this corresponds to the selected packing time of 6 s. When the packing phase ends, the screw rotates and moves backward (downward gradient), and then remains stationary until the next cycle (horizontal).

- Pressure

During the moulding filling stage, the in-cavity pressure curve shows little change during the first half second, because the polymer melt is still flowing through the feed system and has not yet reached the pressure transducer position. After the first half second, cavity pressure builds up rapidly at a near-constant rate, which is due to the polymer flow past the pressure transducer and started filling the thick section of the cavity. According to the graph, in the last second of the mould filling stage, cavity pressure increases at a much higher rate. This is because the polymer melt starts filling the thin section of the cavity, which is a thinner/restricted section and thus higher pressure is required.

According to polymer rheology, it is known that:

$$\tau = \frac{H \cdot \Delta P}{2L} \tag{5.5-1}$$

$$\dot{\gamma} = \frac{6Q}{WH^2} \tag{5.5-2}$$

Power law is:

$$\tau = k \cdot (\dot{\gamma})^n \tag{5.5-3}$$

By substituting τ and $\dot{\gamma}$ into the power law, it can thus be obtained:

$$\Delta P = \frac{2LK}{H^{2n+1}} (\frac{6Q}{W})^n \tag{5.5-4}$$

where ΔP is pressure, L is channel length, H is channel depth, W is channel width, Q is volumetric flow rate, n and K are power law constants. Therefore, if H (thickness) is decreased, then pressure ΔP increases, at the same flow rate.

Normally, when 95 % of cavity is filled or injection pressure reaches a certain point, mould filling stage switches to hold-on stage. At this switch-over point, mould filling ends but hold-on stage starts, and the injection moulding process switches from ram velocity control to pressure control. In this study, the switch-over point was controlled by the screw position, namely, by the shot size of 130 mm and screw position trip of 10 mm. When the screw reached 10 mm from 130 mm, filling stage switched to hold-on stage automatically.

The switch-over point and the length of mould filling and hold-on phase can be identified from the pressure-time plot with the aid of actual injection time and hold-on time. During the moulding process, the actual injection time given by the machine was 5.79 s and hold-on time was set as 6 s. Therefore, switch-over happened at t = 5.79 s and hold-on phase ended at t = 11.79s. Figure 5.5-6 can be plotted to illustrate the filling stage and packing stage.

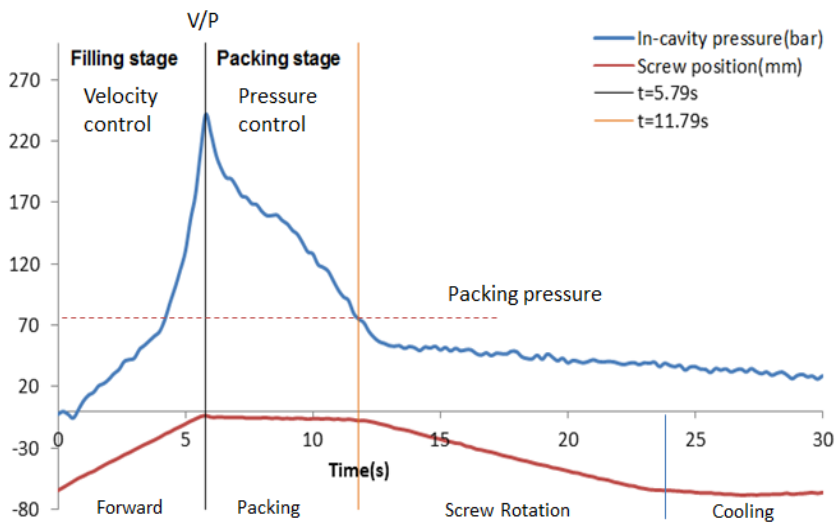

Figure 5.5-6 Complete cycle, showing different phases

Clearly, in-cavity pressure reaches its maximum value at the switch-over point in the graph, because the hold-on pressure selected was lower than the maximum injection pressure achieved during mould filling. It should be noted that the packing pressure set for the injection moulding process is not the cavity pressure but the hydraulic pressure. According to the pressure conversion plot provided on the machine, 5 bar hydraulic pressure gives about 77 bar pressure at the front of the screw.

During packing phase or hold-on phase, the screw applies a selected pressure to compensate the thermal shrinkage due to the solidification of polymer melt. Therefore, a small forward movement would be expected normally. However, in the experiment, the in-cavity pressure has reached around 250 bar just before the switch-over point, but in the next moment, the pressure applied by the screw was suddenly reduced to 77 bar for packing. The big difference in pressure (about 173 bar) pushed the screw backward slightly during packing phase to release the pressure difference. The backward movement of screw, as well as the solidification of the melts and freeze of the gate, results in the pressure drop during packing.

The graph shows that when packing stage ends, the screw rotates immediately and prepare for the next cycle. On the other hand, the in-cavity pressure keeps decreasing and is not affected by the movement of the screw due to the frozen gate. Normally, in-cavity pressure drops to zero at the end of a moulding cycle after the material has fully solidified in the cavity. It was not the case in this study, because the in-cavity pressure is around 50 bar at the end of the cycle as shown in Figure 5.5-5. Clamp force required is thus examined next to check the possible issue of moulding opening.

- Clamp force

The maximum clamping force of Negri Bossi NB62 is 62 tonnes, which is about 620 kN. The clamping force required, F, can be estimated by the equation:

$$F = P_{max} \cdot A \tag{5.5-5}$$

where P_{max} is the maximum injection pressure, A is the projected area of the parts and feed system.

According to the drawing of mould tool design shown in Figure 5.5.-7, the approximate projected area can be quickly estimated by considering the components only. The projected area of the four components is:

$$A_{cavity} = 106\ mm \times 60\ mm \times 4 = 25440\ mm^2 \tag{5.5-6}$$

The maximum injection pressure is about 250 bar according to Figure 5.5-6. As 10 bar is equal to 1 MPa and thus 1 N mm^{-2}, 250 bar is thus equal to 25 N mm^{-2}.

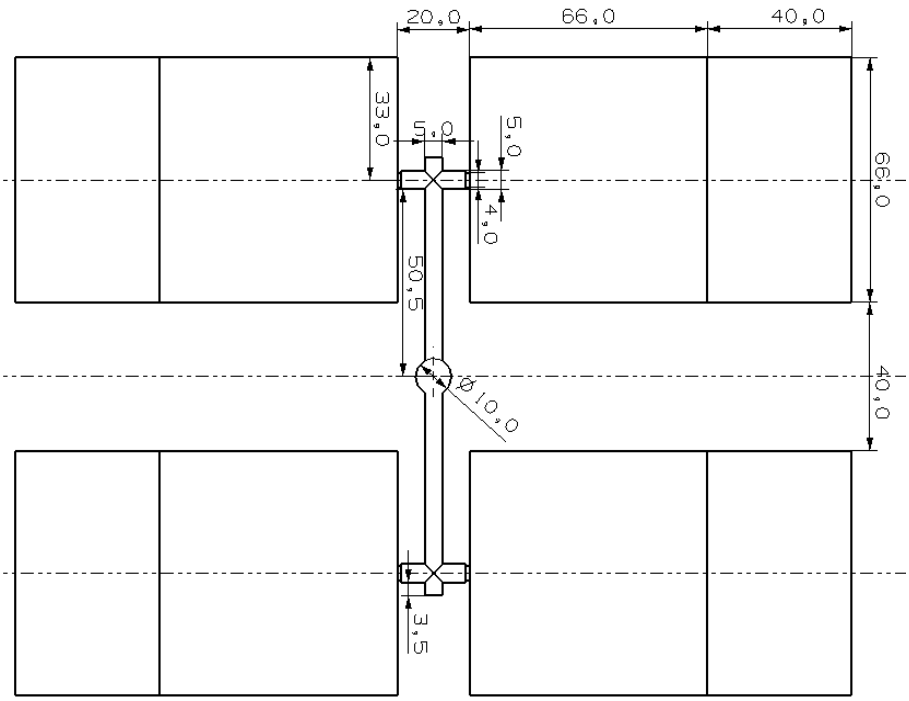

Figure 5.5-7 Projected area of the cavities

The clamping force can be roughly estimated:

$$F = 25440\ mm^2 \times 25\ N/mm^2 = 636\ kN\ > 620\ kN \tag{5.5-7}$$

Apparently, the required clamping force has exceeded the capacity of the injection moulding machine (62 tonnes). In actual fact, during the mould filling stage, the mould was opened slightly, resulting in injection moulded parts that were thicker than the cavity depth after solidification. As a result, the solidified parts after cooling were still thicker than the cavity depth, transmitting the clamp force to the pressure transducer. This is described in Figure 5.5-8.

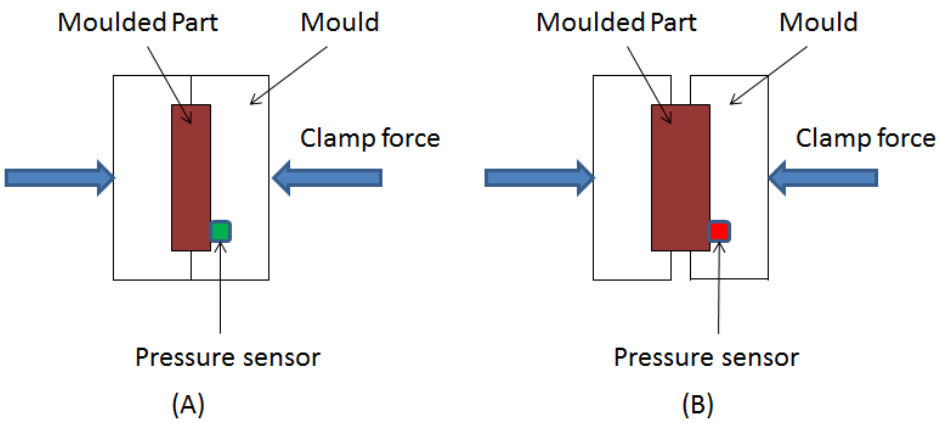

Figure 5.5-8 At the end of injection moulding cycle, the pressure sensor detects: (A) no pressure in normal case; (B) some pressure when moulded part is thicker than cavity depth

The actual thickness of injection moulded parts confirms that the mould opened slightly during the mould filling stage. The thickness of injection moulded parts is 1.36 mm and 2.77 mm for thin and thick section respectively, while that of cavity depth is 1.20 mm and 2.70 mm respectively.

As the default mould opening direction in Moldflow® software was other than the actual direction, the clamping force was not calculated correctly and thus failed to give a warning about this.

5.5.4 Effects on In-Cavity Pressure

(a) Effects of injection speed/time

Figure 5.5-9 shows pressure-time plots obtained under different injection speeds for PPCNs based on PP-H (PPCNH). The plots for PPCNs based on PP-C (PPCNC) are in shown Appendix E.

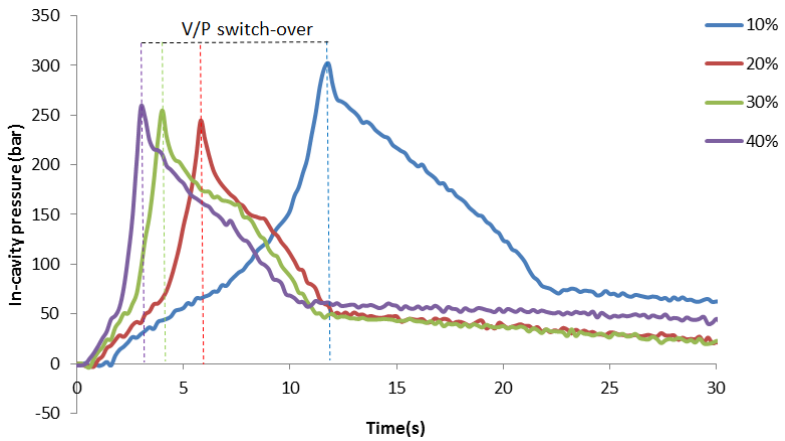

Figure 5.5-9 Pressure-time plots obtained for PPCNH under different injection speeds(%)

Injection speed has a great influence on the pressure-time plot, which is consistent with theoretical predictions. For example, injection speed determines how fast the in-cavity pressure is built up, the injection pressure needed, as well as the length (injection time) of filling stage. Clearly, Figure 5.5-9 shows that at higher injection speed, in-cavity pressure rises faster, mould filling lasts shorter and the maximum in-cavity pressure or injection pressure needed is higher.

It should be noted that the pressure curve for 10 % injection speed is exceptional, for its extremely high maximum in-cavity pressure. In actual fact, short shot occurred when using 10 % injection speed during the experiment, which reveals that the injection pressure needed to fill the mould has exceeded the maximum pressure that the injection moulding machine can provide. Figure 5.5-10 shows the plot of injection pressure vs. injection time. The figure shows that low injection speed or flow rate requires massive pressure, and the pressure drops first and then increases with increasing injection speed or flow rate. This phenomenon is in agreement with the theory, which will be explained next.

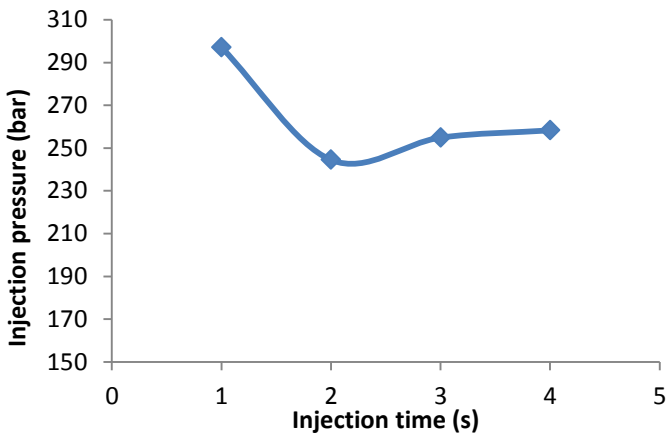

Figure 5.5-10 Injection pressure vs. injection time

Injection moulding is a non-isothermal process, as there are significant temperature difference between polymer melt and cavity wall. Once the hot melt is in contact with the cold metal cavity wall surface, it loses heat fast and freezes rapidly forming frozen layer on the wall surface. The presence of the frozen layer leads to decreasing channel depth and thus requires more pressure to fill the mould, in comparison to isothermal process. The sketch in Figure 5.5-11 shows the reduced channel depth due to the presence of frozen layer.

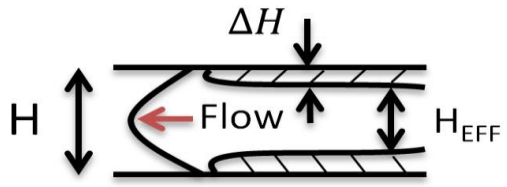

Figure 5.5-11 Decreasing channel depth in non-isothermal flow

The calculation methodology originally cited by Lenk[195], for pressure drop during mould filling is briefly shown here. The effective channel depth is:

$$H_{EFF} = (H - 2\Delta H) \tag{5.5-8}$$

where H is the channel depth, ΔH is the thickness of frozen layer.

It is known that:

$$\Delta H = Ct^{1/3} \tag{5.5-9}$$

Therefore:

$$H_{EFF} = (H - 2Ct^{\frac{1}{3}}) \tag{5.5-10}$$

where C is freeze-off constant, t is filling time.

Using the power law model for shear flow, the pressure drop for mould filling can be estimated by the following equation:

$$\Delta P = \frac{2LK(\frac{6Q}{W})^n}{H^{2n+1}\left[1-\frac{2C}{H^{2/3}}(\frac{WHL}{Q})^{1/3}\right]^{2n+1}} \tag{5.5-11}$$

where W, H and L are the channel width, depth and length respectively, K is the power law consistency index, n is the power law index, Q is the volume flow rate. As presented in the literature review, there are some other models that could be used to describe the flow of polymers such as Cross/WLF model, which also takes pressure sensitivity and temperature sensitivity into consideration in addition to shear rate sensitivity. The Moldflow software is based on Cross/WLF model. The data obtained from Moldflow simulations and actual injection moulding will be compared later in section 5.8.

A brief sketch describing the relationship between pressure drop ΔP and flow rate Q described by Equation 5.5-11, can be plotted as follow:

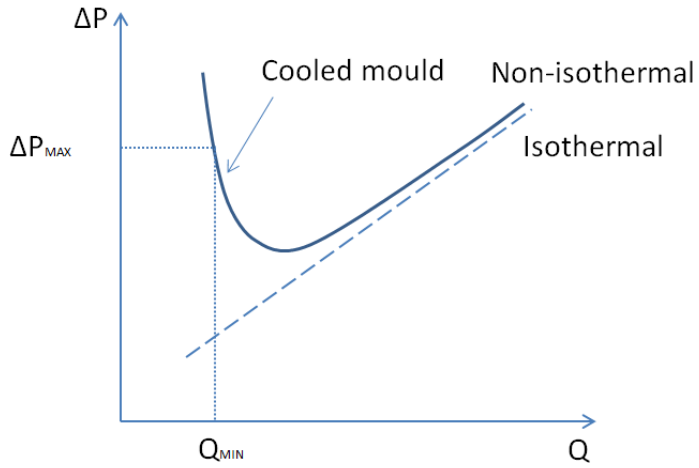

Figure 5.5-12 Pressure drop (ΔP) vs. flow rate (Q)

Therefore, for a given injection moulding machine, when injection speed is low enough to give a flow rate smaller than Q_{MIN}, then the pressure required to fill the mould might exceed the maximum pressure (ΔP_{MAX}) that the machine can provide, resulting in short shot. This explains the extreme high in-cavity pressure for 10 % injection speed in Figure 5.5-10.

Figure 5.5-13 shows how injection speed affect the injection pressure needed to fill the mould, which also qualitatively explains the relationship between the maximum in-cavity pressures in Figure 5.5-10.

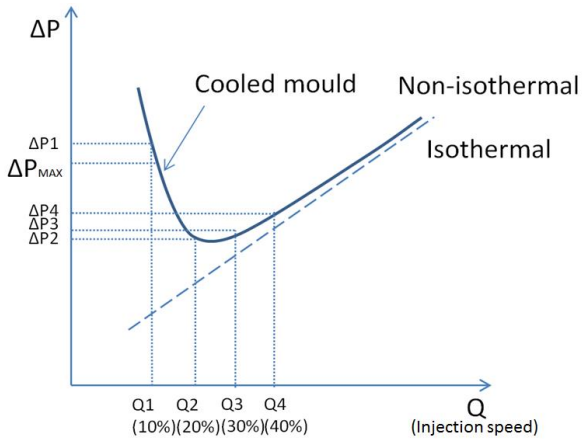

Figure 5.5-13 Effect of injection speed on pressure drop

As explained previously, the clamping force was not sufficient, so the mould was opened slightly during mould filling resulting in thicker moulded parts. As a result, the in-cavity pressure never dropped to zero at the end of cooling stage. As 10 % injection speed needs highest in-cavity pressure during mould filling, it thus has highest pressure at the end of cooling for the thickest moulded parts. For the same

reason, the in-cavity pressure of 40 % injection speed is ranked second at the end of cooling. The pressure at the end of the cycle shows no significant difference for the injection speeds of 30 % and 20 %.

b) Effects of mould temperature

Pressure-time plots for PPCNH samples different mould temperatures are shown in Figure 5.5-14. The plots for PPCNC samples are in shown Appendix E

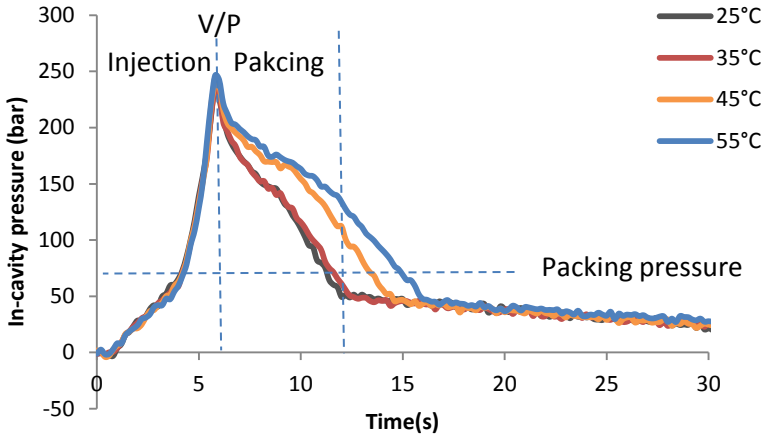

Figure 5.5-14 Pressure-time plots obtained for PPCNH under different mould temperatures

Figure 5.5-15 shows the plot of mould temperature vs. injection pressure. Clearly, mould temperature has very little effect on the injection pressure, in the selected experimental range (25-55 °C). In comparison, injection speed is a dominating factor that determines the injection pressure.

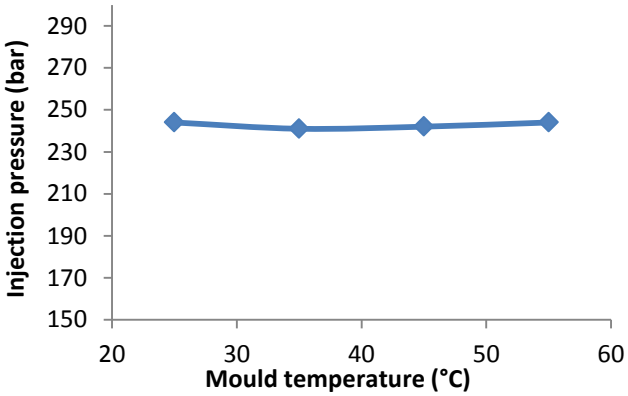

Figure 5.5-15 Mould temperature vs. Injection pressure

Although mould temperature has little influence on injection phase, it significantly affects the pressure profile in packing phase as shown in Figure 5.5-14. This is

because high mould temperature helps to transmit the pressure for a longer time, as the freeze of gate is delayed.

Mould temperature also affects the cooling of moulded parts. The figure shows that high mould temperature slows down the cooling process, thus the change of in-cavity pressure. However, the cooling time used in this study was very sufficient, and the all in-cavity pressures dropped to the same level at the end of the moulding cycle.

Clearly, pressure-time plot implies that injection speed has significant effects on in-cavity pressure. Thus, molecular and particle orientation is very likely to be affected by injection speed as well. On the other hand, as cooling rate is affected by mould temperature, the crystallisation of PP and formulation of frozen layer during mould filling are expected to be affected. Therefore, differences in the properties of injection moulded parts would be expected, and this will be discussed next.

5.5.5 Effects on Tensile Properties

To investigate the effects of processing conditions on the mechanical properties of injection moulded parts, tensile tests were carried out. As mentioned previously, due to the relatively high stiffness and rigidity among common commercial thermoplastics, PP-H materials have great potential to be widely used as automotive interior or under-bonnet parts. Therefore, the tensile tests were mainly carried out on PPH and PPCNH samples produced under different injection moulding conditions, to determine modulus and strength data. The resulting data for tensile tests are summarised in Appendix E. The coding system has been presented in section 4.5.

a) Injection speed

According to the resulting data, the plots of tensile properties vs. processing conditions can be obtained.

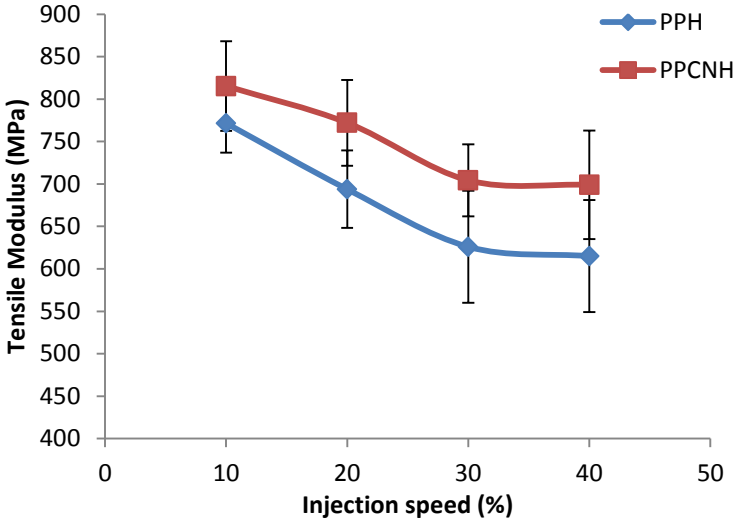

Figure 5.5-16 Tensile modulus vs. injection speed

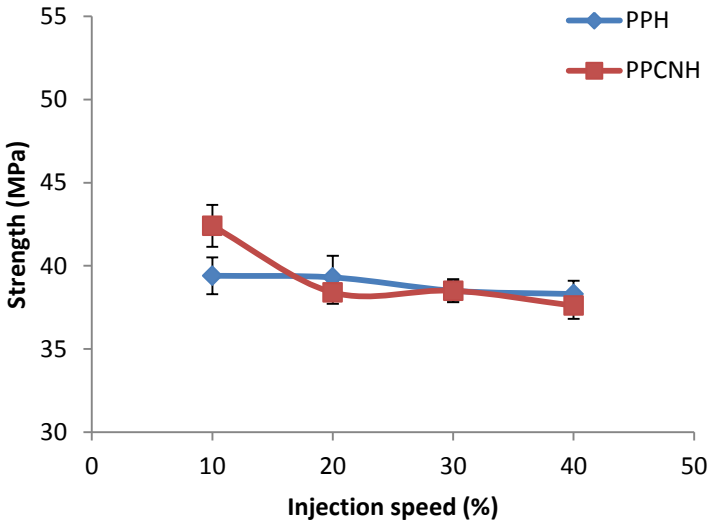

Figure 5.5-17 Yield strength vs. injection speed

Figure 5.5-16 and 5.5-17 shows the effect of injection speed on the tensile properties of injection moulded PPH and PPCNH samples. Apparent, PPCNH samples, as the nanocomposites, show improved tensile modulus compared to PPH samples (about 10 to 14 % improvement). This is a very desirable result considering the potential application of automotive interior parts where stiffness is required.

When increasing injection speed from 10 % to 40 %, the tensile modulus of PPH samples decreases from 772 to 615 MPa, while that of PPCNH samples decreases from 815 to 699 MPa. On the other hand, the yield strength of PPH reduces from 39.4 to 37.5 MPa, and that of PPCNH decreases from 42.4 to 37.6 MPa.

Therefore, it is clear that increasing injection speed leads to greatly reduced tensile modulus and yield strength for the thin-wall injection moulded PPH and PPCNH parts, which is in good agreement with the reported studies on injection moulding of PP and filled PP.[27,196,208]

b) Mould temperature

The effect of mould temperature on tensile properties is shown in Figure 5.5-18 and 5.5-19. The trends shown in the graphs are not very distinctive, and the effects of mould temperature are not very significant, showing that mould temperature has limited effect compared to injection speed for relatively thin parts.

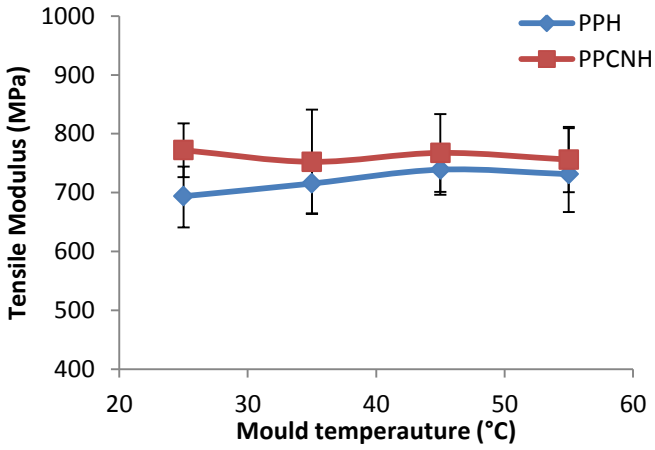

Figure 5.5-18 Tensile modulus vs. mould temperature

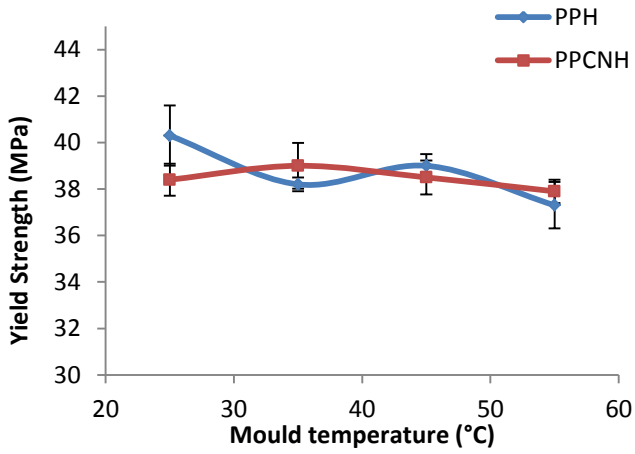

Figure 5.5-19 Yield strength vs. mould temperature

c) Flow direction

To reveal the effects of molecular and particle orientation on the tensile properties, additional tensile tests were carried out. The dumbbell specimens of PPC-20-25 and PPCNC-20-25 were cut both parallel (0°) and perpendicular (90°) to the flow direction (see Figure 4.5-1 and 4.5-2). The resultant data of the tensile tests is summarised in Appendix E.

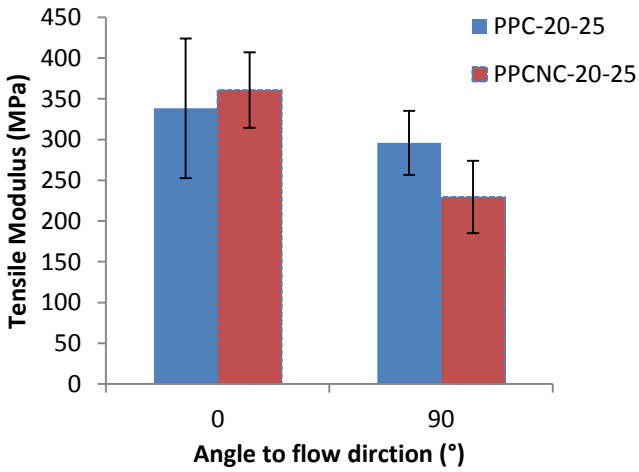

Figure 5.5-20 Tensile modulus vs. angle to flow direction

Figure 5.5-20 and 5.5-21 show the effects of molecular and particle orientation on the tensile properties. Clearly, the result suggests that the thin-wall injection moulded PPC parts are much stronger and stiffer parallel to the flow direction in which the molecular chains and particles are oriented. The tensile modulus of PPC reduces by 12.4 % from the flow direction to the transverse direction. In comparison, the tensile modulus of PPCNC samples decreases by 36.4 % under the same conditions. Additionally, the graph indicates that the thin-wall moulded PPCNC samples are about 6.5 % stiffer than PPC in the flow direction, but are 23 % softer than PP in the transverse direction. From the flow direction to the transverse direction, the yield strength of PP-C reduces by 8.3 %, while that of PPCNC decreases by 13.6 %. This suggests that the nanocomposites are more anisotropic than pure PP because the orientation of clay platelets also has certain effects on the tensile properties, in addition to the orientation of polymer chains.

Overall, the tensile tests results imply that the flow direction, thus the particle and molecular orientation, has a great influence on the tensile properties of thin-wall injection moulded PPC and PPCNC samples.

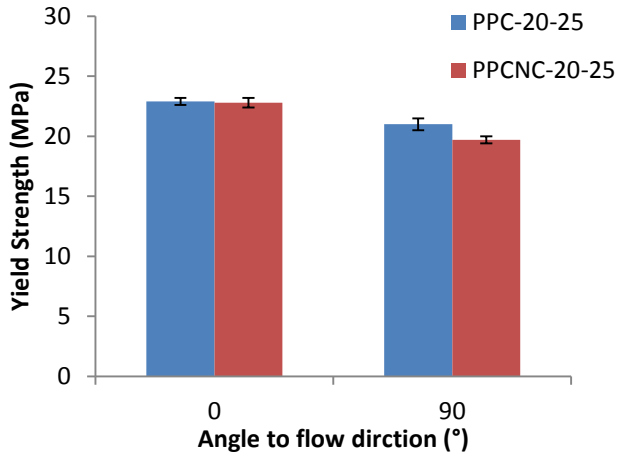

Figure 5.5-21 Yield strength vs. angle to flow direction

d) Testing at elevated temperatures

On sunny summer days, the temperature inside a car or in the engine component can rise considerably with localised temperature reaching 80 °C easily. Therefore, the plastic automotive interior parts need to maintain rigidity at elevated temperature. Tensile tests were also performed at 80 °C for PPH-30-25 and PPCNH-30-25, in order to verify that PP nanocomposites retained higher modulus than the pure PP parts. The resultant data are summarised in Appendix E.

The results are summarised in Table 5.5-3.

Table 5.5-3 Results for tensile tests performed at 20 °C and 80 °C

Sample	Temperature	Modulus	Strength
PPH-30-25	20	626 ± 42.6	38.5 ± 0.7
PPCNH-30-25		704.3 ± 65.9	38.5 ± 0.6
PPH-30-25	80	147.6 ± 12.6	16.5 ± 1.3
PPCNH-30-25		163.0 ±14.8	16.6 ± 0.5

It is well known that when it is above the glass transition temperature, T_g, the amorphous phase within polymers becomes softer and weaker and starts to flow gradually with increasing temperature. Semi-crystalline polymers show some reduction in stiffness and strength due to the presence of the amorphous regions, but they do not flow below T_m as the crystalline regions function as physical crosslinks, constraining deformation. As PP is a typical semi-crystalline polymer, it was thus expected to see a reduced tensile modulus and yield strength at 80 °C.

According to the results, at 20 °C, the tensile modulus of PPCNH-30-25 nanocomposite was 12.3 % higher than that of PPH-30-25. At 80 °C, although there was significant reduction in tensile modulus, PPCNH-30-25 still had a tensile modulus that was 10.4 % higher than that of PPH-30-25. However, the yield strengths of PPCNH-30-25 and PPH-30-25 were very close at both 20 °C and 80 °C. This result confirms the advantages of nanocomposites over pure PP, in terms of modulus enhancement.

5.5.6 Effects on Impact Properties

PP-C materials have the great potential to be used as automotive exterior parts such as car bumpers, for their excellent toughness compared to PP-H materials. Low temperature toughness is important for the application of automotive exterior parts, as the outdoor temperature can drop below zero in many climates, in winter. Therefore, the falling weight impact testing (FWIT) was carried out at -20 °C for PPCNC parts produced under different processing conditions. All the tested samples showed brittle failure during the FWIT.

The FWIT result for virgin PPC samples will be discussed in section 5.7 where the effect of clay concentration is the focus. As the failure energy is defined as the energy absorbed by the material before factruture, failure energy (U) was thus selected to represent the toughness of the material studied in this experiment. The resulting data are summarised in Appendix E.

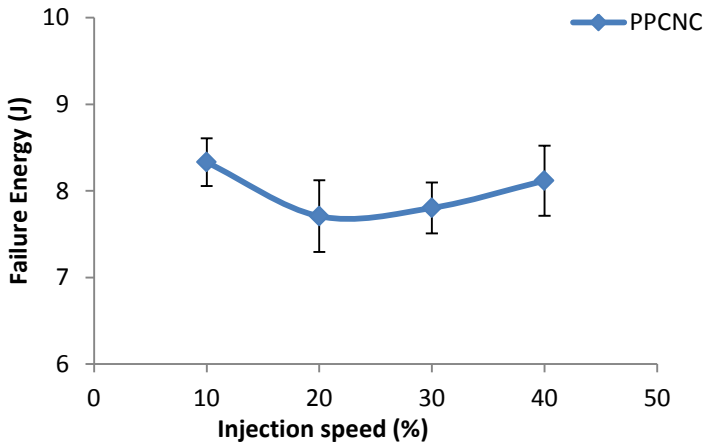

Figure 5.5-22 Failure energy vs. injection speed for moulded nanocomposites

In Figure 5.5-22, the trend of failure energy with increasing injection speed is very similar to that of the maximum in-cavity pressure shown in Figure 5.5-10. As discussed previously in section 5.5.3, the mould was opened slightly for a very short time during mould filling due to the unsufficient clamping force, resulting in a thicker moulded part. The thickness of the thick section of PPCNC samples is summarised in Appendix E. The plot of actual thickness of the thick section of injection moulded nanocomposites against injection speed is shown in Figure 5.5-23.

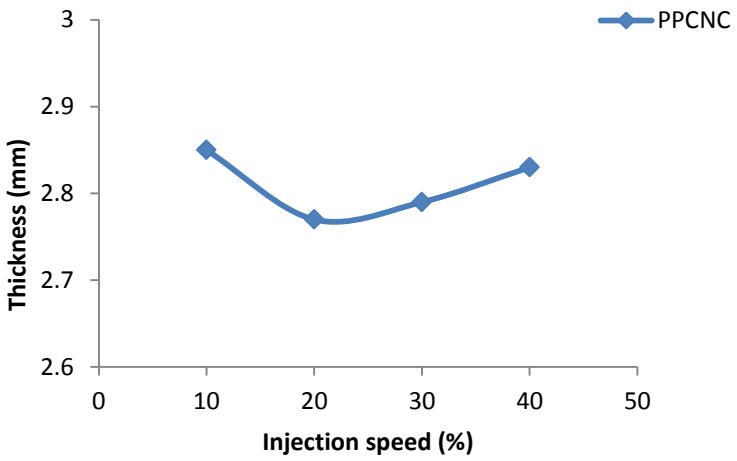

Figure 5.5-23 Thickness of thick section vs. injection speed

Considering the different thicknesses of moulded parts might strongly affect the measured failure energy, the resulting data are thus normalised to eliminate the effects of part thickness:

$$U^* = \frac{U}{H} \tag{5.5-12}$$

where U* is normalised failure energy, U is measured failure energy and H is the thickness of moulded parts.

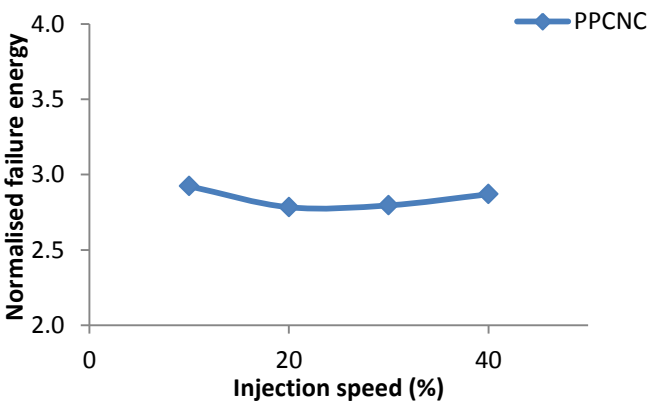

Figure 5.5-24 Normalised failure energy vs. injection speed

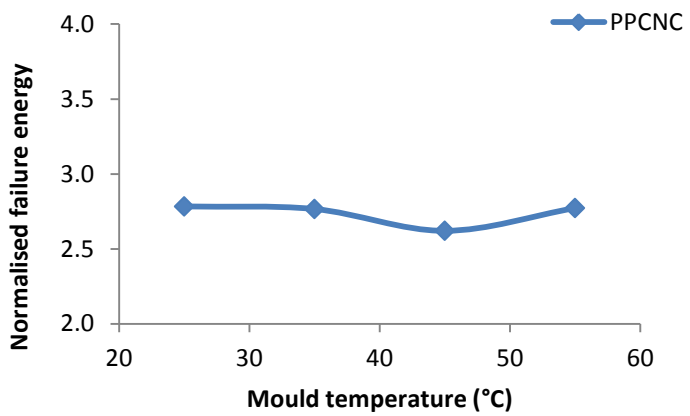

Figure 5.5-25 Failure energy vs. mould temperature

The plots of normalised failure energy vs. injection speed and mould temperature show no distinctive trends. It seems that injection speed and mould temperature have very limited effects on the toughness of injection moulded parts.

So far, very little work has been reported on the effects of moulding conditions on the mechanical properties of thin-wall injection moulded PP nanocomposites. Therefore, XRD, DSC, TEM, OM have been employed to investigate the effects of moulding conditions.

5.5.7 Effects on Crystallinity

DSC curves for PPCNH and PPCNC samples produced under different processing conditions are shown in Appendix E. It is known that for completely crystallised PP, the enthalpy of fusion ΔH_{100}= 207 J g^{-1},[237] from which the crystallinities of injection moulded PP nanocomposite parts have been calculated according to the following equations:

$$X_{cr}(\%) = \frac{\Delta H_f}{\omega_{PP} \cdot \Delta H_{100}} \quad (5.5\text{-}13)$$

The calculated crystallinities for all samples listed in Table 5.5-4.

Table 5.5-4 DSC results for PPCNH and PPCNC samples

Sample Code	Enthalpy of fusion (J g^{-1})	Crystallinity (%)	Melting point(°C)
PPCNH-10-25	84.1	44.5	166
PPCNH-20-25	84.9	44.9	167
PPCNH-30-25	85.7	45.3	166
PPCNH-40-25	87.2	46.1	166
PPCNH-20-35	85.2	45.0	167
PPCNH-20-45	85.5	45.2	167
PPCNH-20-55	86.4	45.7	166
PPCNC-10-25	60.7	31.9	168
PPCNC-20-25	62.2	32.8	167
PPCNC-30-25	64.0	33.7	167
PPCNC-40-25	65.3	34.4	167
PPCNC-20-35	66.1	34.8	166
PPCNC-20-45	67.0	35.3	166
PPCNC-20-55	67.3	35.4	166

It is well known that the crystallinity of semi-crystalline polymers significantly affects their mechanical properties. Therefore, the crystallinities of injection moulded nanocomposite parts have been plotted against the processing conditions, as shown in Figure 5.5-28 and 5.5-29.

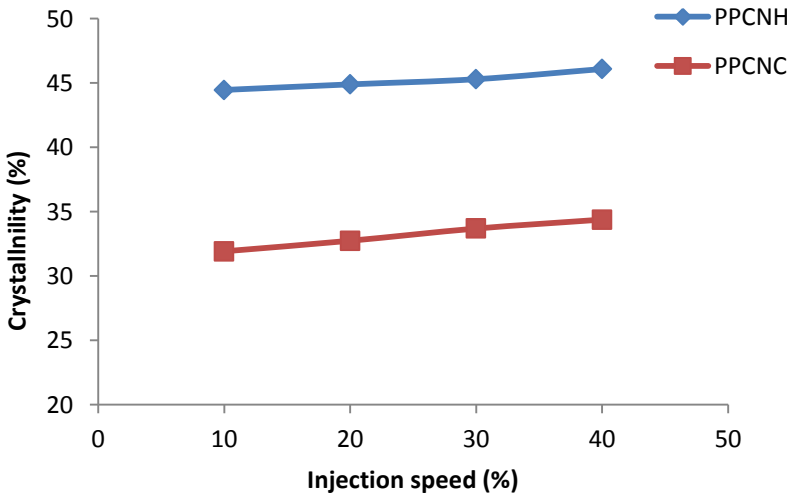

Figure 5.5-26 Crystallinity vs. injection speed

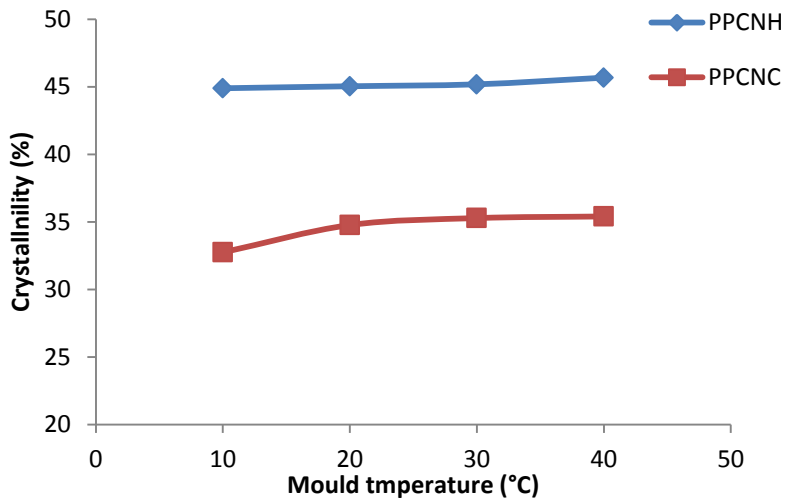

Figure 5.5-27 Crystallinity vs. mould temperature

Clearly, the graphs above show that when increasing injection speed or mould temperature, crystallinity will increase to a very limited extent.

Increasing injection speed leads to increased volumetric flow, and thus increased shear rate/stress, which is a critical factor for flow-induced orientation of polymer chains. Therefore, during mould filling, there are more PP molecular chains and clay particles that are oriented in the direction of flow, at a higher injection speed.

After investigating orientation-induced crystallisation of isotactic PP, Liu *et al.*[244] indicate that the crystallisation process is remarkably affected by the preorientation of the molecular chains. Compared to random coiled polymer chains, the oriented polymer chains are closer to their state in the crystal phase, thus, it is easier to organise the preordered chain segments into a crystal lattice and there is less energy barrier to overcome.

On the other hand, high injection speed means less injection time. The actual injection times for different injection speeds are summarised in Table 5.5-5.

Table 5.5-5 Injection speed vs. actual injection time

Injection speed (%)	Actual injection time (s)
10	11.89
20	5.79
30	3.91
40	2.96

With higher injection speed, there is less heat loss during mould filling stage, but more shear heat generated when the melt passes through the gate and along the cavity. Thus, the material in the cavity has a higher temperature at the switch-over point. In other words, the core of the part remains hot for longer time, and this may allow more orientated polymer molecules to relax to their coiled equilibrium state, reducing preorientation. On the other hand, remaining hotter for a longer time also allows more crystallisation to occur. As a result of the competing effects, increasing injection speed can only lead to a slight increase in crystallinity.

Increasing mould temperature reduces the heat loss rate during mould filling as well as the rate of cooling. Again, greater time is allowed to stay within crystallisation temperature region, and thus more crystallisation may be achieved although there is more relaxation for flow induced orientation. Crystallinity increases slightly with increasing mould temperature, as shown.

However, the effect of processing conditions on the crystallinity of injection moulded parts is believed to be very limited in this study, according to the preliminary results. The difference in the degree of crystallinity caused by varied processing conditions is only about 1 to 2 %, which is not likely to cause any significant changes in mechanical properties.

5.5.8 Effects on Clay Dispersion

Intensive shear stress and shear rate are involved during injection moulding process. When processing conditions are changed, the dispersion of clay in PP matrix may also be affected.

A gate is normally the smallest flow channel in a feed system, thus, when volumetric flow rate remains constant, shear rate and stress is most extreme in the gate region. In this study, the nominal shear rate in the rectangular gate can be briefly estimated by the equation:

$$\dot{\gamma} = \frac{6Q}{WH^2} \tag{5.5-14}$$

Where Q is volumetric flow rate, W is channel width and H is channel height. The size of the gate in this study is 4x1x1 mm. The volumetric flow rate then can be calculated according to the actual injection time and shot volume.

The diameter of the screw in the barrel is 28 mm, which gives a cross-sectional area of 615.75 mm^2. During mould filling stage, the distance that the screw moves is 110mm. Therefore, the shot volume is about 68062 mm^3. For 10 % injection speed, the actual injection time is 11.86 s.

$$Q = \frac{68062mm^3}{11.86s} = 5739\ mm^3\ s^{-1} \tag{5.5-15}$$

By substituting into Equation 5.5-14

$$\dot{\gamma} = \frac{6\times5738.79mm^3\ s^{-1}}{4mm\times(1mm)^2} = 8608\ s^{-1} \tag{5.5-16}$$

Table 5.5-6 summaries the shear rates calculated for the different injection speeds. It is clear that the nominal shear rate has reached $10^5\ s^{-1}$ level when injection speed is 20 % or above.

Table 5.5-6 Nominal shear rate in the gate region

Injection speed (%)	Actual Injection time (s)	Volumetric flow rate ($mm^3\ s^{-1}$)	Shear rate (s^{-1})
10	11.86	5739	8608
20	5.79	11755	17633
30	3.91	17407	26111
40	2.96	229934	34491

Figure 5.5-30 shows a typical XRD pattern for injection moulded PPCN parts based on PP-H and PP-C.

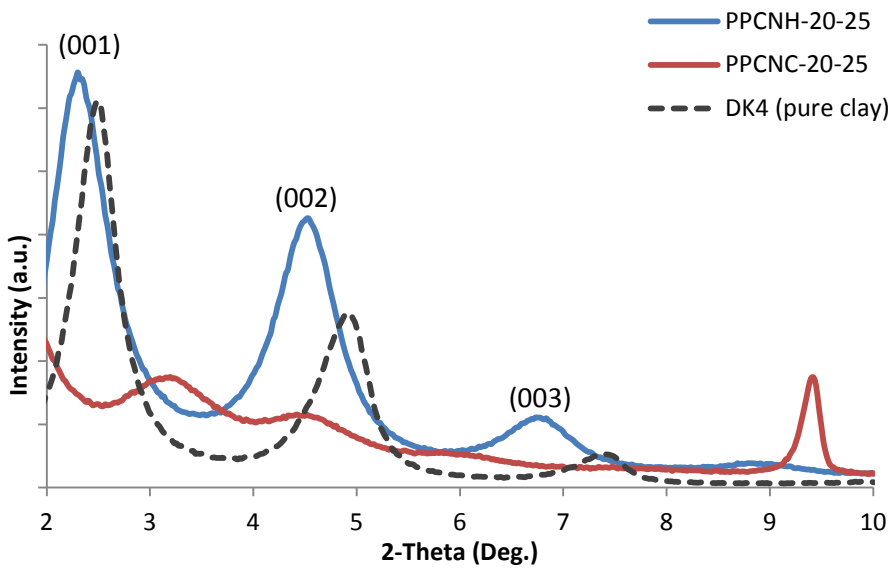

Figure 5.5-28 XRD patterns for injection moulded parts

Clearly, the (001) peak has shifted to lower diffraction angles after compounding and injection moulding. The interlayer spacing (d_{001}) for each sample has been calculated by Bragg's law ($n\lambda = 2d\sin\theta$) and summarised in Appendix E. For PPCNC samples, d_{001} values were deduced from d_{002} as their d_{001} peaks dropped below 2θ = 2°, indicating high degree of intercalation.

In addition to the shift of diffraction peak towards lower angle, sample PPCNH-20-25 also shows higher diffraction intensity even than the pure clay powder, which indicates there might be high level of orientation of clay stacks in the moulded parts. In contrast, PPCNC-20-25 shows very low peak intensity although it had the same concentration of clay inside the part. This simply implies that most clay stacks may have been broken down into individual sheets and dispersed well in the PP matrix, and this is consistent with the big shift of the (001) peak towards a lower angle. It is believed that exfoliated structure is more likely to be achieved with higher interlayer spacing, because when the spacing reaches a critical point, the static force will be too weak to hold the clay sheets together, leading to exfoliation.

The PP-C based composites showed greater exfoliation than the equivalent composite based on PP-H may be due to the presence of nucleating agent in the PP-C, which shows a reflection peak at ca. 2θ = 9.5° in Figure 5.5-30. Therefore, there might be some complex interactions among the nucleating agent, nanoclay, PP-g-MA, AM, PP and even the crystallisable PE sequences. Also, the presence of nucleating agent greatly affects the crystallisation mechanism, and Hedge *et al.*[152]

suggest that alone with the thermodynamic driving force, which causes the clay platelet to agglomerate, spherulite formation also drives the ultimate morphology of organoclay. The difference in the intercalation/exfoliation behaviour of clay in the PP-H and PP-C based composites is very interesting and worth further investigation in the future. This section focuses on thin wall injection moulding of PPCNs, and it is thus not fully discussed here.

The plots of basal spacing vs. processing conditions are shown in Figure 5.5-31 and 5.5-32.

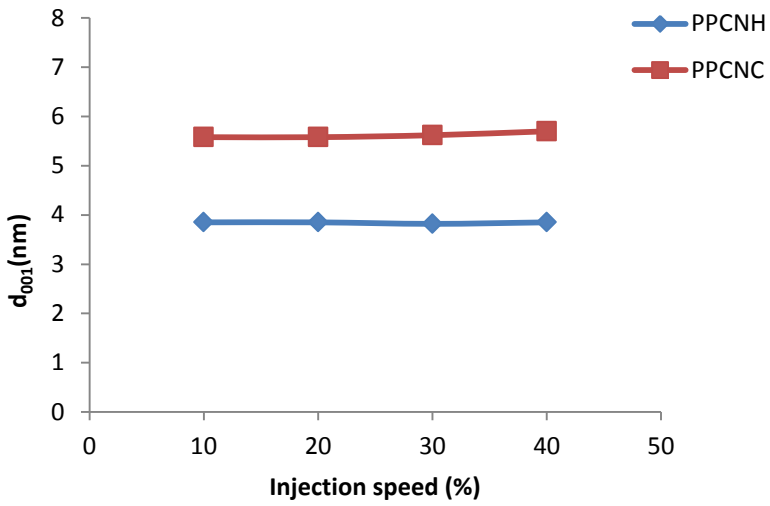

Figure 5.5-29 Interlayer spacing vs. injection speed

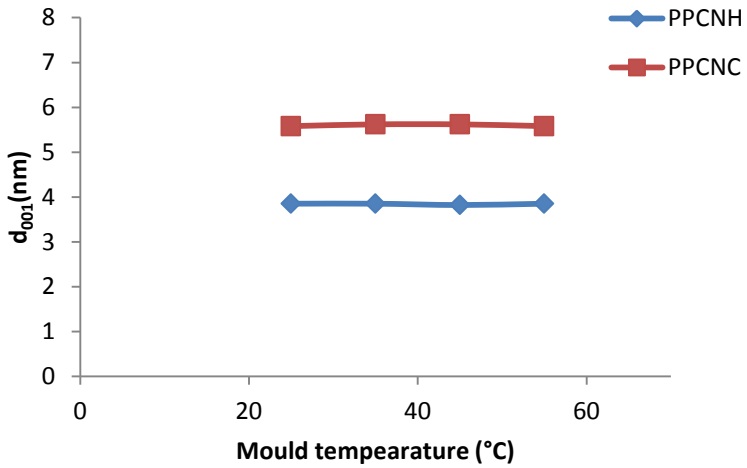

Figure 5.5-30 Interlayer spacing vs. mould temperature

In actual fact, the XRD results show no clear trend for interlayer spacing of clay. By combining the XRD results from section 5.4, the XRD patterns of compounded PPCN and the final injection moulded PPCN can be compared. This shows the

importance of the preparation/compounding/mixing stages, because all the exfoliation/intercalation is created at an earlier stage.

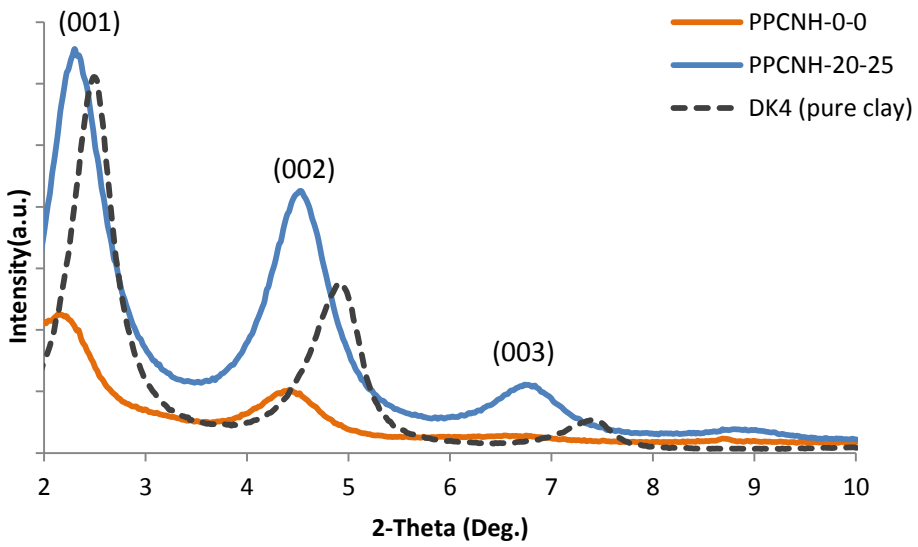

Figure 5.5-31 XRD patterns

Sample PPCNH-0-0 refers to the PPCNH compounded by APV twin screw extruder under the optimised conditions, but it has not been injection moulded yet. Clearly, the low peak intensity of PPCNH-0-0 indicates the random orientation of clay. However, the (001) peak of PPCNH-0-0 occurs at a lower diffraction angle. The calculated interlayer spacing for PPCNH-0-0 is 4.13 nm, while that for PPCNH-20-25 is 3.85 nm, which indicates that a reduction in clay layer separation took place during injection moulding. The melt temperature for during injection moulding was 190 °C, and there was also strong shear heat at the gate. As mentioned previously in section 5.1, the TGA curves suggest that the degradation of the organic surfactant on clay starts from 180 °C. Therefore, the compaction phenomenon of clay is most likely due to the thermal degradation of the surface coating on the clay sheets, which led to reduced affinity between the clay and the PP matrix and thus reduced interlayer spacing.

Figure 5.5-34 shows the TEM images for nanocomposite sample PPCNC-10-25, while the other images for PPCNC-2-25 and PPCNC-30-25 are in Appendix E.

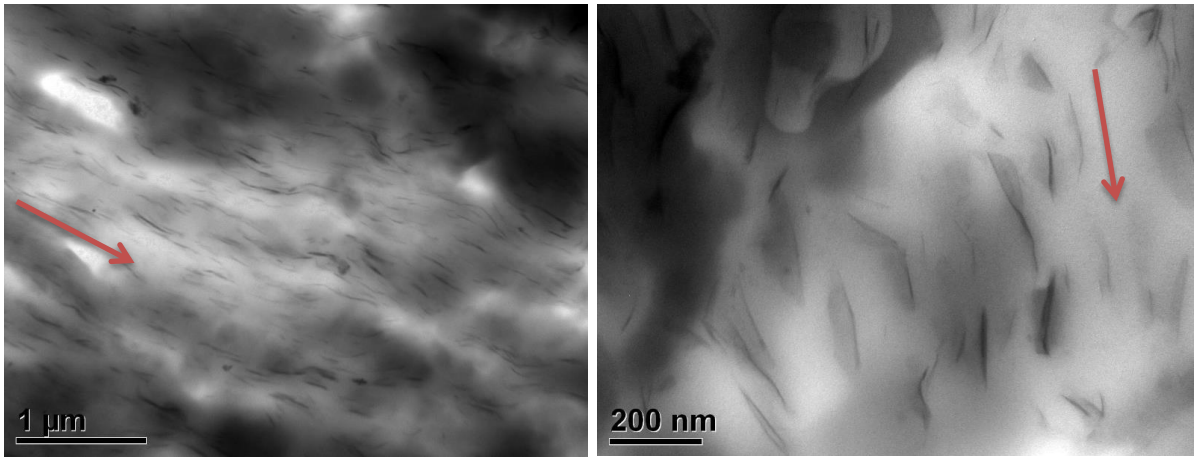

Figure 5.5-32 TEM images for PPCNC-10-25 at (a) 30,000x magnification and (b) 100,000x magnification

Clearly, the TEM images show that the clay particles are highly oriented in the flow direction, and the red arrows indicate the flow direction. This is in good agreement with the enhancement in XRD peak intensity of the moulded nanocomposite part shown in Figure 5.5-33. As both the PP molecular chains and clay particles are oriented in the flow direction, the injection moulded parts are thus much stiffer and stronger in the flow direction than the transverse direction (see section 5.5.5).

5.5.9 Effects on Morphology

As presented in the literature review (section 2.2.3), the mould filling stage is a non-isothermal process, and there is a highly oriented layer frozen immediately below the part surface, due to a combination of high shear stress and high cooling rate adjacent to the mould wall. Because of the insulating effect of the frozen layers, the polymer melt in the hot core is able to relax to a higher extent. For injection moulded PP parts, at least two regions are noticeable across a specimen thickness.[196–198] The first frozen surface layer is called 'the skin', while the zone in the middle of the cavity is called 'the core'. The region between them is called 'the shear zone' due to the foundation flow.[196] The skin layer possesses a highly oriented non-spherulitic, shish-kebab like structure, while the core has common spherulitic structure (see Figure 2.2-12).[199] Therefore, the highly oriented non-spherulitic skin or frozen layer and the spherulitic core can be recognised easily by optical microscope (OM) with polarised light. In this experiment, the thin sections of injection moulded parts were examined by OM.

The OM images of sample PPCNH-30-25 at different magnifications are shown in Figure 5.5-35 and 5.5-36. The OM images for the other samples are all shown in Appendix E.

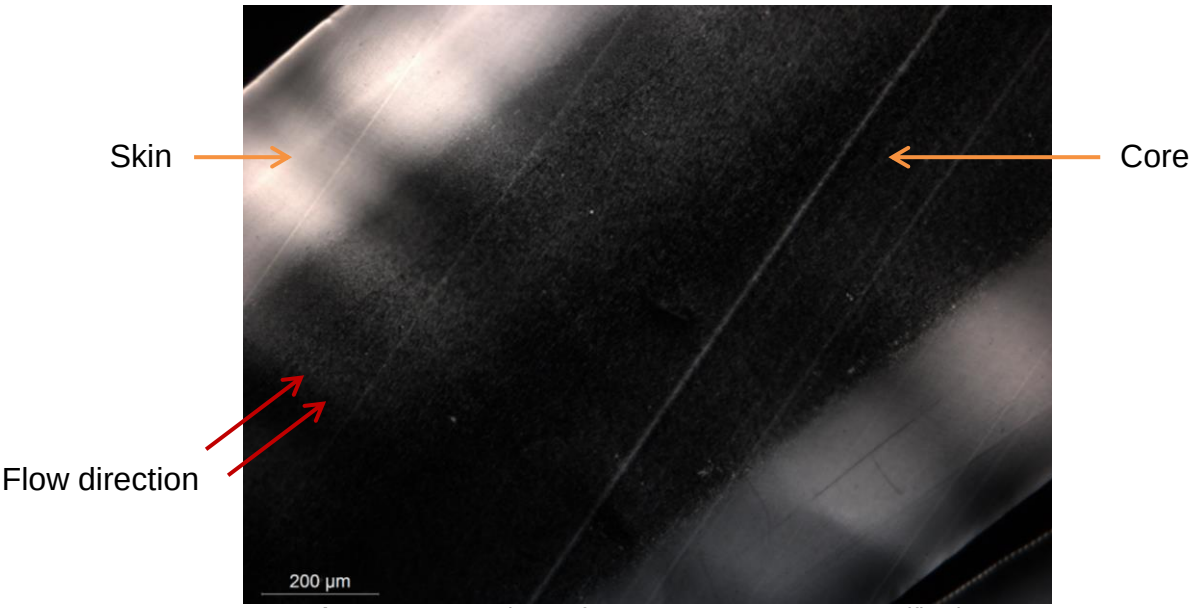

Figure 5.5-33 OM image for PPCNH-30-25 at 50x magnification

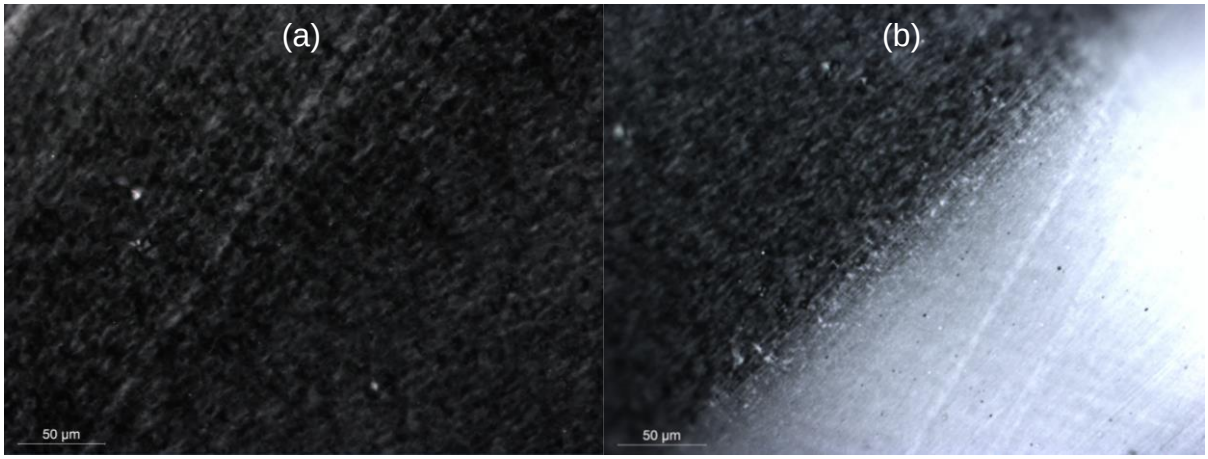

Figure 5.5-34 OM images for PPCHN-30-25 at 100x magnification: (a) spherulitic core, (b) boundary between the spherulitic core and non-spherulitic skin

The OM images obtained are in good agreement with the literature, and the spherulitic core and highly oriented non-spherulitic skin can be recognised clearly. Very fine spherulites can be seen in the core region. The thickness of the part and frozen layer (skin) has been measured using the software ImageJ, on the basis of the OM images. The fraction of frozen layer can be calculated by:

$$Frozen\ layer\ fraction = \frac{thickness\ of\ frozen\ layer}{thickness\ of\ part} \tag{5.5-17}$$

The measured frozen layer thickness and part thickness as well as the calculated frozen layer fraction are summarised in Appendix E.

Plots of frozen layer fraction against processing conditions are shown in Figure 5.5-37 and 5.5-38 below. Because the thickness of thin-wall injection moulded parts is low, the frozen layer fraction values are all relatively high.

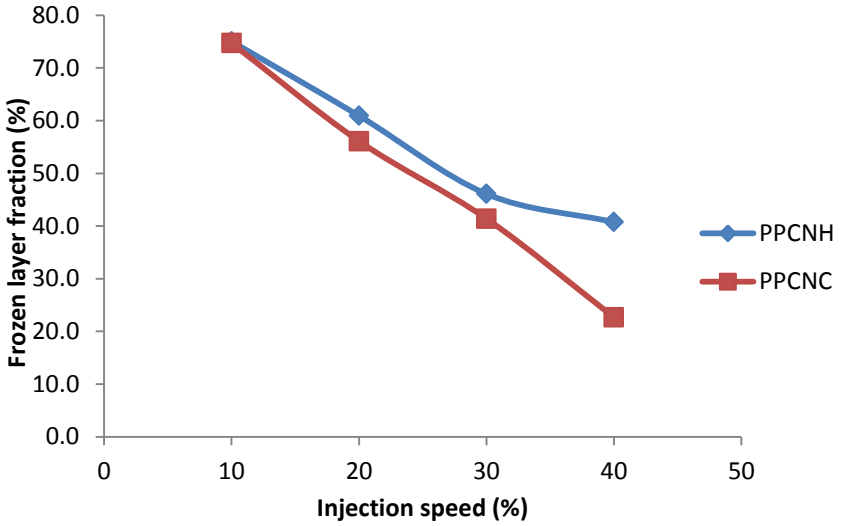

Figure 5.5-35 Frozen layer fraction vs. injection speed

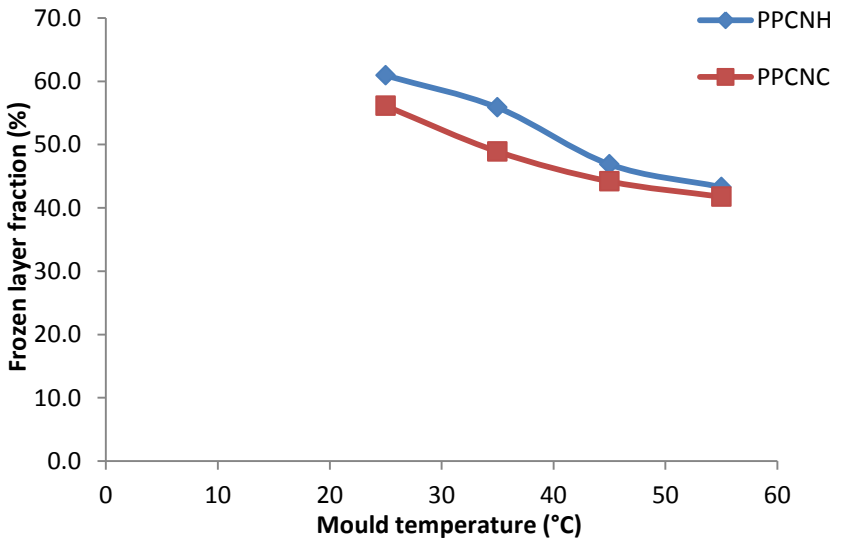

Figure 5.5-36 Frozen layer fraction vs. mould temperature

Clearly, the frozen layer fraction increases with decreasing injection speed or mould temperature, which is consistent with many studies reported so far.[27,196,202,205,208]

It is known that Fourier's dimensionless groups can be used to describe the process of frozen layer development under unsteady state. The method is helpful to describe

the initial growth of frozen layer before the balanced state is achieved or the growth of frozen layer after the balanced state finishes. The calculation methodology originally cited by Lenk[195] is briefly introduced here

The dimensionless time F_0 and dimensionless temperature θ are:

$$F_0 = \frac{\alpha t}{x^2} \tag{5.5-18}$$

$$\theta = \frac{T - T_C}{T_M - T_C} \tag{5.5-19}$$

Where α is thermal diffusivity, t is time, x is the distance from mould surface, T_c is mould temperature, T_m is melt temperature and T is the temperature at distance x. Apparently, the condition to define frozen layer thickness (ΔH) is: $x = \Delta H$ at $T = T_f$, where T_f is the temperature at which the polymer melt freezes.

It is known when θ < 0.8, the Fourier's equation can be expressed by:

$$\theta = \frac{1}{2{F_0}^{1/2}} \tag{5.5-20}$$

For frozen layer, $x = \Delta H$ at $T = T_f$. After substituting for F_0, and θ from (5.5-18) and (5.5-19) the following equation can be obtained:

$$\Delta H = 2\alpha^{1/2}\left(\frac{T_f - T_C}{T_M - T_C}\right)t^{1/2} \tag{5.5-21}$$

Clearly, Equation (5.5-20) implies that for a given material and fixed processing conditions, frozen layer thickness is proportion to the square root of time, $t^{1/2}$. The equation also shows that the processing conditions (Tm, Tc) and the thermal properties of materials (α, Tf) affect the development of frozen layer. For example, increasing cavity temperature Tc decreases $\left(\frac{T_f - T_C}{T_M - T_C}\right)$, slowing down the growth of frozen layer ΔH. The faster the frozen layer grows, the more orientation will be frozen-in. At higher injection speed, the actual Tm is higher due to less heat loss within the same time, which reduces $\left(\frac{T_f - T_C}{T_M - T_C}\right)$ as well and thus slows down the development of frozen layer. If a material has a lower α or Tf, its frozen layer develops slower.

The frozen layer that can be identified by optical microscopy with polarised light consists of both the initial balanced frozen layer during mould filling and the frozen layer that forms immediately when the flow stops where the oriented polymer chains are unable to relax in time. However, if the mould filling is fast enough, the flow may stop before the balanced frozen layer is achieved.

In recent years, Viana *et al.*,[202,208] has proposed a new way to interpret the development of the skin layer, in the light of two main factors: time allowed for relaxation of the flow induced particle/molecular orientation until crystallisation temperature is achieved, t_r, and the relaxation time of the material, λ.

- If $t_r > \lambda$, the flow induced molecular orientation is able to completely relax, leading to the development of spherulitic-like structure.
- If $t_r < \lambda$, the flow induced molecular orientation has not enough time relax before crystallisation, originating the development of a highly oriented skin layer.

According to the results of their study,[202,208] increasing injection flow rate leads to increased temperature and melt shear. The increase in melt shear has two competing effects: it increases the crystallisation temperature, reducing the time to reach the crystallisation (thinner skin); and it reduces material relaxation time (thicker skin). However, the concomitant increase of the melt temperature caused by higher flow rate leads to thinner skin. Therefore, the final balance seems to be reduction of skin thickness with increasing injection speed. On the other hand, decreasing mould temperature increases cooling rate. As a result, the time to reach the crystallisation temperature is reduced (thicker skin), but the crystallisation temperature is also reduced, increasing the time reach the crystallisation temperature (thinner layer). Therefore, mould temperature has a relatively small influence in terms of development of the skin layer.

Comparing Figure 5.5-39 and 5.5-40, it is clear that within the studied processing window, injection speed has a more significant effect on the frozen layer fraction, which is in agreement with the studies mentioned above. Under all processing conditions, PPCNH samples show higher frozen layer fraction than PPCNC samples.

In section 5.5.5, it is clear that the tensile properties decrease with increasing injection speed, and frozen layer fraction shows very similar trend. It is reported that

the frozen layer or skin is much stiffer and stronger than the core.[196] Moreover, it is found that a thicker skin is simultaneously more oriented and crystalline, but the spherulitic core is less crystalline. [27,202] For thin-wall injection moulding, the thickness of mould parts is very low and the thus values of frozen layer fraction is quite high (up to 75 %). Thus, it is highly likely that the reduction in the tensile modulus with increasing injection speed is due to the reduction of skin layer thickness, level of orientation and crystallinity in the skin. Tensile modulus of PPCNH samples is plotted against frozen layer fraction in Figure 5.5-41 to show their relationship.

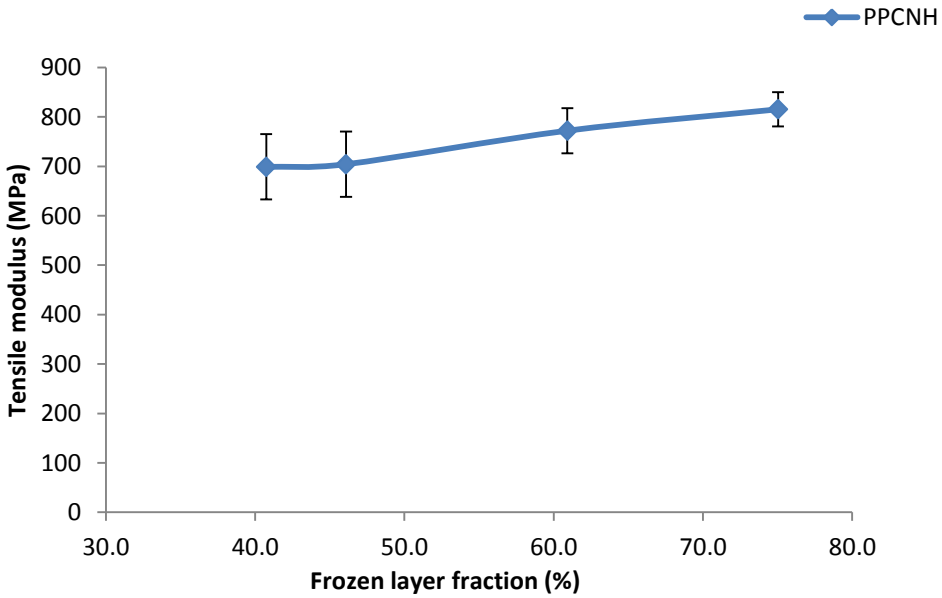

Figure 5.5-37 Tensile modulus vs. frozen layer fraction

It is well known that crystallinity of semi-crystalline polymers has a significant effect on their mechanical properties. In general, a polymer is stiffer with higher degree of crystallinity because the crystalline regions are very rigid compared to the amorphous regions in the polymer, especially for polymer with a relatively low Tg. In Figure 5.5-30, it is clear that increasing injection speed leads to a slight increase in crystallinity. However, the effect of the slightly increased crystallinity on tensile properties is probably overcome by the strong effect of the frozen layers. In comparison to injection speed, mould temperature, within range selected for this investigation, has a very limited effect on the mechanical properties of injection moulded parts.

In terms of impact toughness, both injection speed and mould temperature have no distinctive effects, despite the changes in frozen layer, crystallinity and *etc*.

Considering the fact that multiaxial stress is applied during FWIT and the particle and molecular orientation aid cracks grow in the orientation direction, stable impact toughness for thin-wall injection moulded PP nanocomposite parts produced under different moulding conditions is thus considered to be favourable.

5.5.10 Summary

In this section, the effects of processing conditions, namely, injection speed and mould temperature, have been investigated.

The results shows show that the maximum in-cavity pressure increased significantly with increasing injection speed. As the clamping force was not sufficient during mould filling, the mould was opened very slightly for a short time under the high in-cavity pressure during injection stage, resulting in increased part thickness. Therefore, increasing injection speed also increased the part thickness. On the other hand, mould temperature showed very minor effect on the in-cavity pressure as well as the part thickness. The in-cavity pressure data obtained in actual moulding will be compared with that obtained from Moldflow simulations in section 5.8.

Within the selected processing window, tensile modulus and yield strength of thin wall injection moulded PPCN parts increase significantly with decreasing injection speed, which is in good agreement with the reported studies on injection moulding of PP or filled PP.[27,196,208] This is highly likely due to the significant increase in the highly oriented frozen layer, which is stiffer and stronger than the core.[196] The spherulitic core and oriented non-spherulitic skin (frozen layer) can be observed in the OM images, and very fine spherulites can be seen in the core region. The highly oriented, non-spherulitic skin of the thin-wall injection moulded PP nanocomposites increases significantly with decreasing injection speed. Due to the low thickness, the values of skin fraction are very high (up to 75 %) in the thin wall injection moulded parts. DSC and XRD results show that moulding conditions have very limited influence on the crystallinity of the injection moulded parts and the intercalation of clay particles, and they are unlikely to make any distinctive changes to the tensile properties. Strong orientation of clay particles in the flow direction can be observed in the TEM images for all samples, which is in good agreement with the greatly

enhanced peak intensity of XRD patterns. Therefore, it is proposed that the great enhancement in tensile properties with decreasing injection moulding is mainly attributed to a thicker skin, which is simultaneously more oriented and crystalline according to the reported studies.[27,202] In comparison to injection speed, mould temperature has very limited effect on the properties of thin wall injection moulded PPCNs, indicating that injection speed is most influential within the selected processing window of this study.

Additionally, the injection moulded PPCN parts show improvement in tensile properties, in comparison to the virgin PP parts. The enhancement is up to about 14 % for tensile modulus and 8 % for yield strength. Besides, the thin-wall injection moulded PPCN parts are much stronger and stiffer parallel to the flow direction in which the molecular chains and particles are oriented. From the flow direction to transverse direction, the tensile modulus of PPCNC samples decreases by 36.4 % and yield strength decreases by 13.6 %. Therefore, the particle and molecular orientation has a great effect on the tensile properties of thin-wall injection moulded PPCNs. The FWIT results that the impact toughness of the thin-wall injection moulded PPCNs is very stable, and is not distinctly affected by the changes in moulding conditions.

Although the optimum formulation of PPCNs has been found previously using DoE approach (section 5.3), it is still worthwhile to cast a glance at the effects of clay on injection moulded PPCN parts. The effects of clay concentration on the properties of injection moulded parts will be discussed next.

5.6 Effects of Clay Concentration on The Properties of Injection Moulded Parts

The properties of injection moulded parts with different clay concentrations were examined by differential scanning calorimetry (DSC), dynamic mechanical analysis (DMA), X-ray diffraction (XRD), falling weight impact tests (FWIT), optical microscopy (OM), transmission electron microscopy (TEM) and scanning electron microscopy (SEM). The resulting data is analysed in this section to reveal the effects of clay concentration on the properties of injection moulded parts.

5.6.1 Effects on Impact Properties

As mentioned previously, PP copolymers (PP-C) have the great potential to be used as automotive exterior parts for their excellent toughness compared to PP homopolymers, which are stiffer and have a higher yield strength. Environment temperature varies throughout the year, and drops below zero in many climates, in winter. Thus, low temperature toughness is of great importance for materials intended for automotive exterior parts.

The original DMA traces are shown in Appendix F. The results indicate that the glass transition temperatures (Tg) of PPC-C0 and PPCNC-C4 are 7.4 °C and 7.8 °C respectively. Therefore, it appears that the clay concentration shows no distinctive effects on the Tg of injection moulded PPCNs. As the Tg of moulded parts was found to be around 7 °C. Hence, -20 °C and 20 °C, which were below and above 7 °C, were selected as the comparative test temperatures.

Failure energy obtained in the tests indicates the energy that was absorbed by the specimen during the failure process. Thus, it was selected to represent the toughness of the material studied. Table 5.6-1 summaries the resulting data of FWIT analysis and the original raw data are shown in Appendix F.

Table 5.6-1 Summary of FWIT tests

Sample code	Failure energy at (J) at -20 °C	Stv.	Failure energy (J) at 20 °C	Stv.
PPC-C0	8.32	0.19	18.8	1.17
PPCNC-C1	7.99	0.42	18.3	0.34
PPCNC-C2	8.41	0.22	17.6	1.68
PPCNC-C3	8.23	0.14	18.6	0.26
PPCNC-C4	7.70	0.34	18.5	0.24
PPCNC-C5	7.88	0.24	18.0	0.75

Based on the data in Table 5.6-1, a graph of failure energy against clay concentration can be plotted as shown in Figure 5.6-1.

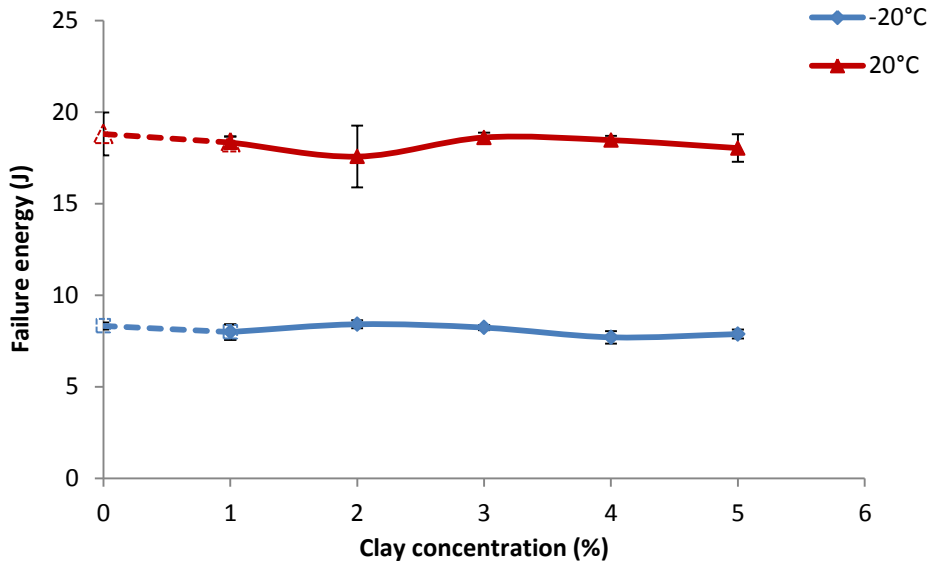

Figure 5.6-1 Failure energy vs. clay concentration

It should be noted that the control material PPC-C0 is pure virgin PP-C, and there was no nanoclay, PPgMA and erucamide in it. Therefore, its data is only shown as dotted line. The failure energy of the virgin PP-C was 8.4 J and 18.8 J at -20 °C and 20 °C respectively.

Clearly, the PP/clay nanocomposite specimens were much tougher at 20 °C than at -20 °C. It is well known that for a semi-crystalline polymer, the amorphous regions change from rigid glassy state to soft rubbery state at Tg, because the segmental motions of polymer chains are restricted below Tg but relaxation occurs when above Tg. Hence, higher failure energy was observed at 20 °C, as more energy was absorbed and dissipated by the irreversible segmental motions of PP chains. The big difference in failure energy and thus toughness below and above Tg was thus

expected. The picture of impacted samples showing different failure modes is in Appendix F. Ductile failure and brittle failure were observed for the samples tested at -20 °C and 20 °C respectively

In terms of the change in failure energy caused by clay concentration, the figure implies that there was actually no clear trend for the resulting failure energy obtained at either 20 °C or -20 °C, considering the experimental errors. This suggests that the effect of clay concentration on toughness was not evident at either 20 °C or -20 °C in the selected variation range for clay concentration.

In actual fact, the effect of clay concentration on the toughness or impact strength of PP/clay nanocomposites is quite controversial, according to the studies that have been reported in literature. In theory, the addition of clay particles promotes the brittle characteristics of nanocomposites, which is opposite to the ductility of pure PP matrix. Therefore, it has been reported in some studies that with increasing clay concentration, the impact strength of PPCNs decreases[136,141]. However, it has also been reported that the impact strength remains constant with increasing clay concentration[106,125], which is similar to the result of this study. Interestingly, other research shows that impact strength increases with clay concentration first and decreases after a threshold point, which is known as the optimum clay concentration [14,104]. Considering there was no difference in the toughness of the virgin PP-C and the PPCNs, the possible reason for the unaffected toughness with increasing clay content in this study, may be that the interactions between the clay particles and PP matrix was not strong enough to effectively restrict the segmental mobility of PP chains. Pukanszky *et al.*[235] point out that the long chain surfactants used for the coating of montmorillonite orientate more or less parallel to the surface and usually cover the platelets in a single layer, which lowers surface energy and facilitate exfoliation of clay. However, polymer/silicate interaction also decreases as an effect of decreasing surface tension. DK4 clay is coated with long chain alkyl ammonium salts, and it is very likely that the surfactant lead to weak filler matrix interaction, resulting in unchanged toughness.

The SEM images in Figure 5.6-2 show the fracture surface of sample PPCNC-C1 and PPCNC-C3.

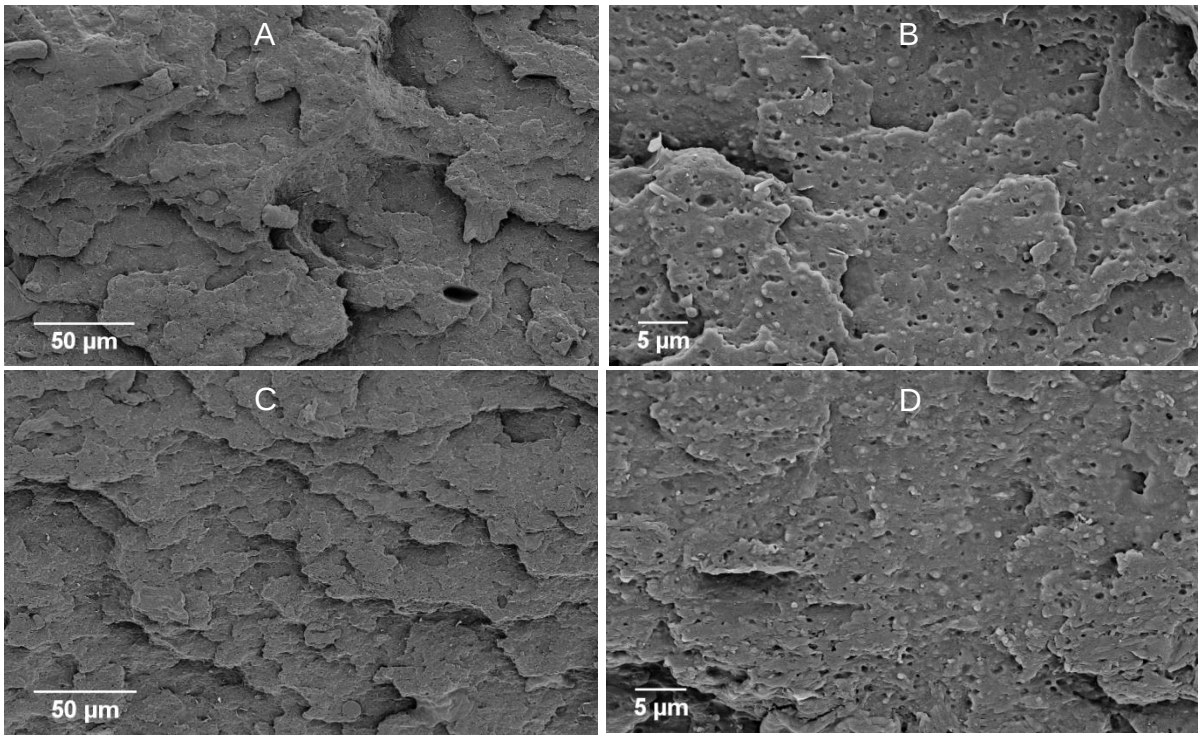

Figure 5.6-2 SEM images for fracture surfaces: (A) PPCNC-C1, magnification=1000x; (B) PPCNC-C1, magnification= 5000x; (C) PPCNC-C3, magnification=1000x, (D) PPCNC-C3, magnification=5000x.

Clearly, the holes due to the pull-out of clay particles can be seen in the SEM graphs at higher magnification, implying that the interactions between the clay particles and continuous PP are not very strong. Comparing the images of the two nanocomposites with different clay concentrations, it seems that the difference in clay concentration cause no big difference to the fracture surfaces. The pull-out of the tactoids at the filler levels studied may well be an energy dissipation mechanism, the increase in modulus and yield stress with increasing clay content, however, may cancel out the toughening effect, thereby leading to no net effect on impact energy as clay level is increased. This may partially explain the limited effects of clay concentration on impact toughness of thin wall injection moulded parts (see Figure 5.6-1).

As section 5.5 shows that the tensile modulus has been evidently improved, it is thus considered to be acceptable that the improvement in tensile modulus is not at the expense of toughness.

5.6.2 Effects on Crystallinity

The crystallinity of each sample was calculated according to the equation below that has been cited previously as Equation 5.5-13:

$$X_{cr}(\%) = \frac{\Delta H_f}{\omega_{PP} \cdot \Delta H_{100}} \quad (5.5\text{-}13)$$

In the study regarding effect of clay concentration, the weight fraction of PP (ω_{PP}) changed with clay concentration so the calculated crystallinities are summarised in Table 5.6-2.

Table 5.6-2 Summary of DSC results

Sample Code	Enthalpy of fusion (J/g)	ω_{PP} (%)	Crystallinity (%)	Melting point (°C)
PPCNC-C1	63.4	93.5	32.4	167.5
PPCNC-C2	63.5	92.5	32.8	167.1
PPCNC-C3	62.7	91.5	32.8	167.0
PPCNC-C4	64.2	90.5	33.9	166.7
PPCNC-C5	60.6	89.5	32.4	167.3

According to the resulting data, it is clear that the degree of crystallinity of the samples with different clay content remained almost constant (33 ± 1 %). Also, there is no clear trend that can reveal the relationship between crystallinity and clay concentration. Hence, the effect of crystallinity on the mechanical properties of PPCNs was considered to be negligible in this study. Similar results have been reported in many other studies [13,106,170,245]. The minor effect of clay concentration on crystallinity might be due to the competing effects of clay particles in the PP matrix. The clay particles affected the nucleation process increasing the crystallinity of PP, but it is also suggested that they also restricted the motion of PP chains decreasing the degree of crystallisation.[245]

5.6.3 Effects on Clay Dispersion

Interlayer spacing of clay (d_{001}) was calculated from XRD analysis using Bragg's law ($n\lambda = 2d sin\theta$). The calculated values of d_{001} are summarised in Appendix F. It should be noted that for sample PPCNC-C4 and PPCNC-C5, their d_{001} values were

deduced from d_{002}, as their (001) peaks have dropped below $2\theta = 1.8°$ and were completely masked by background scattering.

The XRD patterns for all samples are shown in Figure 5.6-3.

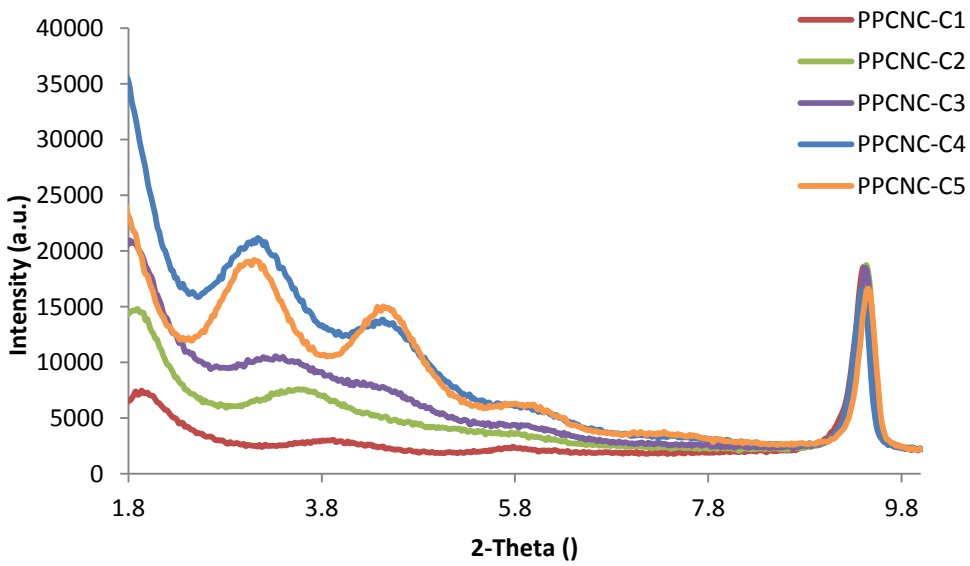

Figure 5.6-3 XRD patterns for sample PPCNC-C2 and pure clay (DK4)

The XRD patterns show a clear trend that exfoliation level decreases, but interlayer spacing and stacking uniformity increases, when the clay level increases. Figure 5.6-4 illustrates the trend of d_{001} values with increasing clay concentrations.

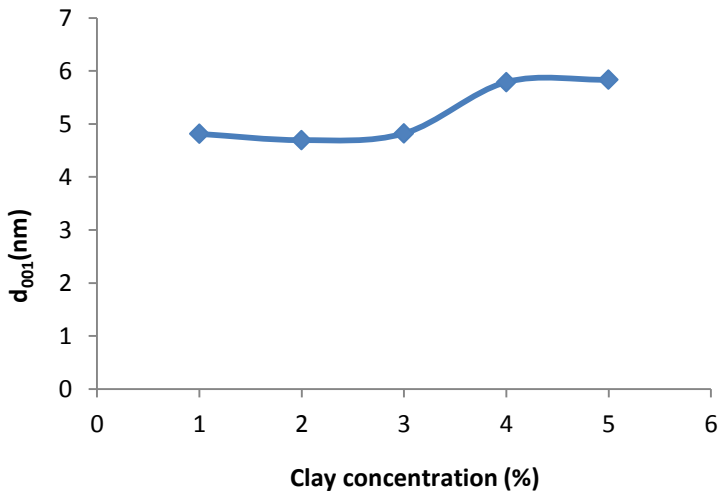

Figure 5.6-4 Interlayer spacing vs. clay concentration

Clearly, the graph shows that greater interlayer spacing was achieved at higher clay concentrations and 4 % was a threshold point. Below 4 % clay concentration, the d_{001} value stayed around 4.8 nm, but when the clay concentration was increased to 4 % or above, the d_{001} value increased to around 5.8 nm.

It appears that the intercalation of clay was improved with increasing clay content, based on the discussion above. However, the TEM images obtained for sample PPCNC-C1 and PPCNC-C4 show an additional trend. As an example Figure 5.6-5 illustrates the TEM images with magnification of 100,000 times for both samples, and the other TEM images can be found in Appendix F.

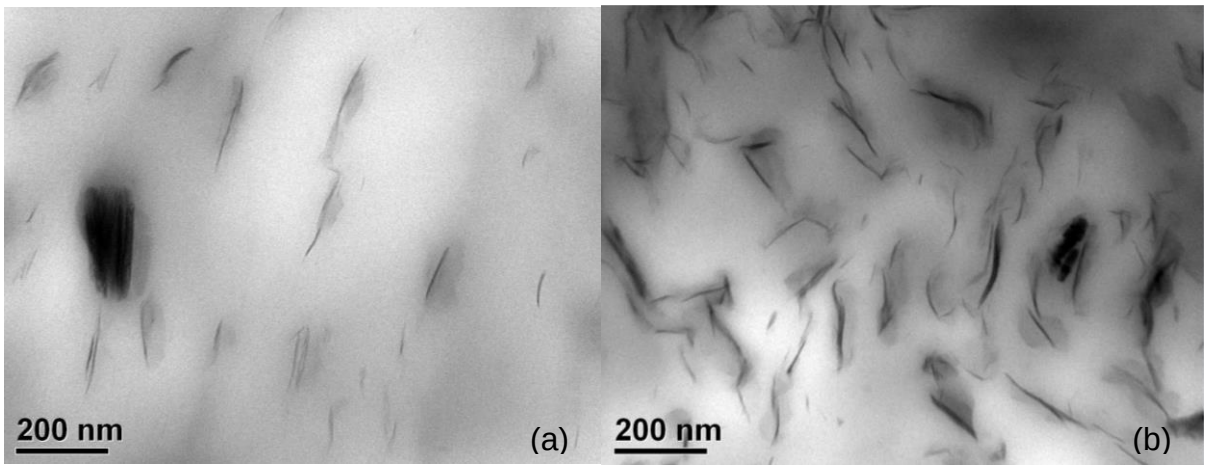

Figure 5.6-5 TEM images for (a) PPCNC-C1 and (b) PPCNC-C4

Firstly, the images confirm that the clay particles are in a partially exfoliated state, as both individual clay platelets and layered stacks can be found. As clay concentrations were different in the two samples, it is reasonable to see more clay particles in sample PPCNC-C4 (Figure 5.6-5b), and grater evidence of clay overall, in the field of view.

Figure 5.6-5(a) implies that in sample PPCNC-C1, a high proportion of the clay particles were exfoliated well and existed in the PP matrix as thin platelets. Those single clay sheets cannot diffract X-rays, and hence, they are not observed by XRD. The peaks in the XRD pattern and thus interlayer spacing measured for PPCNC-C1 were due to the layered clay stacks, although there were very few of them according to the TEM image.

On the other hand, although a few individual clay platelets can be found in PPCNC-C4 (Figure 5.6-5b), most of the clay particles were small clay stacks which consisted of a few layers, and they contributed to the peaks in the XRD pattern and the resulting interlay spacing d_{001}. Thickness of a typical clay plate in Figure 5.6-5 (a) is about 12 nm, while that in Figure 5.6-5 (b) is about 30 nm. It is known that the d-values for PPCNC-C1 is 4.8 nm, while that for PPCNC-C4 is 5.8 nm, according to

the XRD results. The number of layers (n) in a clay tactoids can be estimated by the equation:

$$Tactoid\ thickness = nd_{001} + 0.95 \tag{5.6-1}$$

Thus, there are about 2 layers in a typical clay plate for PPCNC-C1, while 5 layers in a typical plate for PPCNC-C4.

Combining the TEM and XRD results, it is clear that PPCNC-C1 has lower intercalation but higher exfoliation, in comparison to PPCNC-C4. This is because in PPCNC-C1 most clay particles have intercalated well and then exfoliated, the rest have maintained a low d-value. In PPCNC-C4, the clay stacks are intercalated, but far fewer have further delaminated to cause exfoliation.

The peak at $2\theta = 9.4°$ is very likely due to the nucleating agent in the original PP-C material. Talc is widely used as a nucleating agent for polypropylene. It is known that it has a characteristic (001) peak around at $2\theta = 9.45°$, therefore, talc may be the nucleating agent contained in the PPC used for this research.

5.6.4 Effects on Morphology

The thin sections of the injection moulded parts with different clay concentrations were examined by optical microscopy (OM). The OM images for PPCNC-C1 and PPCNC-C5 are shown in Figure 5.6-6 and 5.6-7 as examples. The OM images for the other samples can be found in Appendix F.

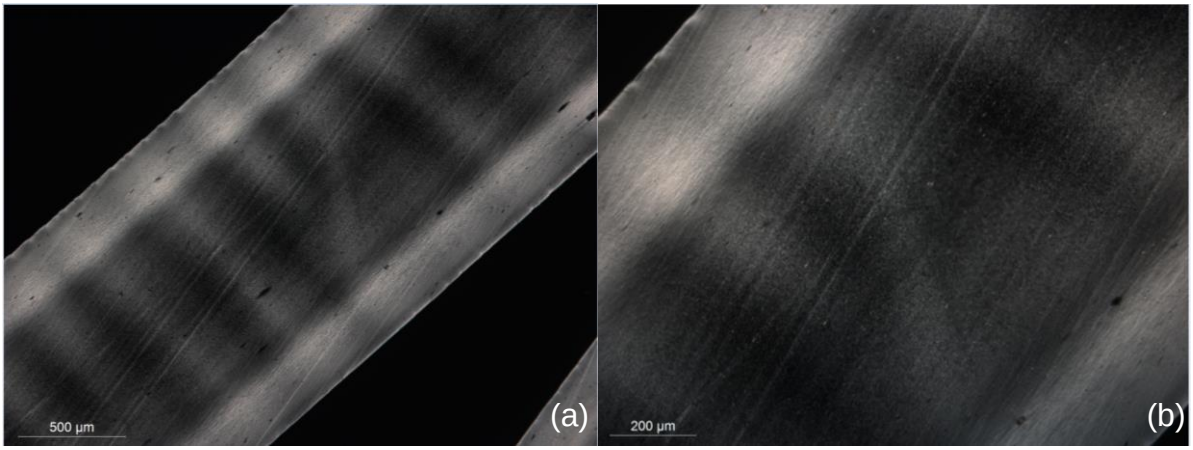

Figure 5.6-6 OM images for PPCNC-C1 at magnification of (a) 50x and (b) 100x

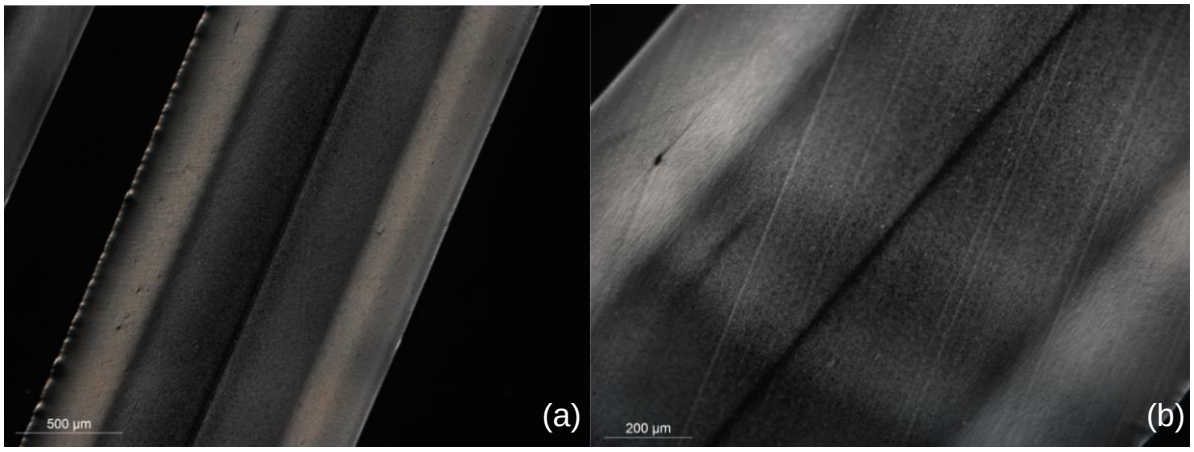

Figure 5.6-7 OM images for PPCNC-C1 at magnification of (a) 50x and (b) 100x

The morphology of injection moulded parts (skin-core structures) has been presented previously in the literature review and also in section 5.5.9. A frozen layer or skin is a highly oriented crystalline texture, which is stiffer and stronger than the core.[196] A thicker skin is simultaneously more oriented and crystalline.[27,202] The morphology of moulded parts is strongly affected by the moulding conditions, and has great influence on the resulting tensile properties of moulded parts, as discussed previously.

The section puts emphasis on the effect of clay concentration. The part thickness, frozen layer thickness and frozen layer fraction have been measured and summarised in Appendix F, according to the OM images obtained. Figure 5.6-8 shows the plot of frozen layer fraction vs. clay concentration.

PPCNC-C1 had the lowest frozen layer fraction (37.1 %) among those PPCN samples, but the difference was still very small, in comparison to the data in section 5.5 which focuses the effects of processing conditions. This implies that the effect of clay content on frozen layer fraction was very small compared to that of processing conditions.

Although the effect of clay concentration was found to be insignificant, the trend of frozen layer faction against clay content can still be identified. Basically, it increases with increasing clay concentration, which is in agreement with the study reported by Costantino *et al*.[26]

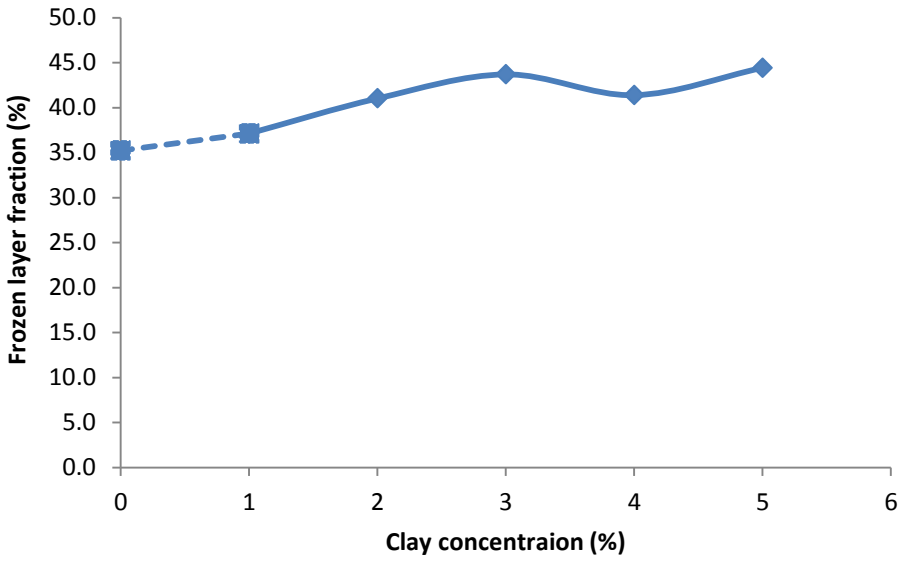

Figure 5.6-8 Frozen layer fraction against clay concentration

It has been reported in literature that thermal conductivity of pure PP is improved by the incorporation of clay and it is increased with increasing clay concentration[246,247]. When thermal conductivity is increased, simultaneous heat transfer from the hot melt to the cold mould wall surface will be faster during mould filling stage. As a result of the increased cooling rate, more molecular and particle orientation will be frozen-in resulting in a thicker frozen layer.

5.6.5 Summary

The effect of clay concentration on the properties of injection moulded parts was investigated in this section.

The preliminary results imply that clay concentration had very limited effects on the crystallinity and impact toughness of injection moulded PPCNs. The crystallinity of PPCN samples remained constant at around 33 %. The negligible effect of clay concentration on crystallinity is very likely due to cancellation of two competing factors; the clay particles affected the nucleation process increasing the crystallinity of PP, but they also restricted the motion of PP chains decreasing the degree of crystallisation. The failure energy measured in falling weight impact tests was about 8 J at -20 °C and 18 J at 20 °C. Ductile failure was observed for PPCN samples impacted at 20 °C while brittle failure mode was observed at -20 °C. The SEM

images show that there is no big difference between the fracture surfaces of PPCNs with different clay content.

Higher intercalation, but lower exfoliation was observed for PPCN samples with more clay content in the range of 1-5 %. On the contrary, lower intercalation, higher exfoliation was observed for PPCNs with less clay content. Increasing clay concentration led to a slight increase in frozen layer fraction of thin-wall injection moulded PPCN parts, this may be, due to the increased thermal conductivity. Increased thermal conductivity led to a faster heat transfer from the hot melt to the cold mould wall surface, as a result, more particle and molecular orientation was frozen-in forming a thicker frozen layer.

So far, the effects of moulding conditions and clay concentrations have been studied. In the next section, the effects of wall thickness will be discussed based upon the comparison made between the properties of thin and thick sections of the moulded PPCNs.

5.7 Effects of Wall Thickness on the Properties of Injection Moulded Parts

The properties of the thick sections of injection moulded parts were examined by tensile tests, differential scanning calorimetry (DSC), X-ray diffraction (XRD) optical microscopy (OM) and by transmission electron microscopy (TEM). In this section, the effects of wall thickness on the properties of injection moulded parts are analysed by comparing the resulting experimental data of the thick sections with those of the thin sections which have been obtained previously.

5.7.1 Effects on Tensile Properties

The original experimental data of tensile tests is shown in Appendix G, and Table 5.7-1 below summarises the results for both thin and thick sections of the injection moulded parts.

Table 5.7-1 Tensile modulus and yield strength of thin and thick sections

Sample code	Tensile modulus (MPa)	Std.	Yield strength (MPa)	Std.
PPCNH-t	752	88.7	39.0	0.99
PPCNH-T	562	86.3	35.2	1.49
PPCNC-t	361	46.2	22.8	0.45
PPCNC-T	307	24.2	21.1	0.58

As presented previously in section 4.7, ‘t’ and ‘T’ in the sample codes refers to thin and thick sections respectively, while ‘H’ and ‘C’ in the sample codes refers to their base polymers, PP-H and PP-C respectively.

The thermomechanical environment applied to the material during injection moulding affects the morphological development of an injection moulded part, is thus closely related to the mechanical properties of the components[27]. In this experiment, the thermomechanical environment was very different in the thin and thick sections during the moulding filling stage. When the PPCN melt was forced to enter the thin sections from the thick sections, cooling rate and shear rate level were significantly changed. Thus, difference in the mechanical properties was expected between the thin and thick sections. Figure 5.7-1 and 5.7-2 show the column charts of tensile

modulus and yield strength for the dumbbell samples cut from the sections with different thickness.

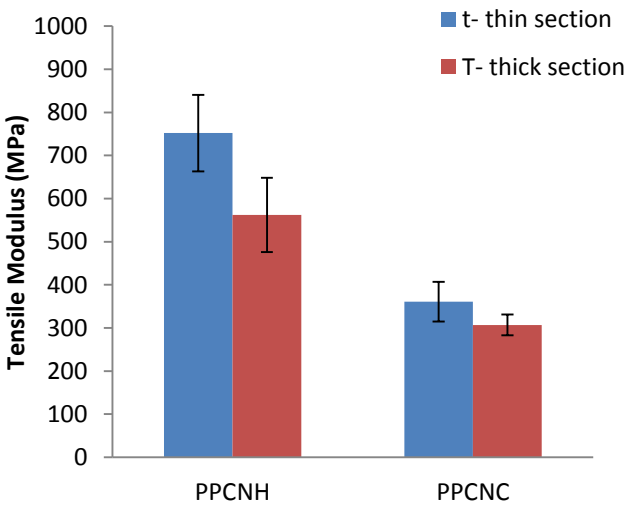

Figure 5.7-1 Tensile modulus of the samples from thin and thick sections

Clearly, PPCNH samples had much greater tensile modulus than the PPCNC samples, according to Figure 5.7-1. PPCNH samples were nanocomposites based on the PP homopolymer (PP-H), and it was thus validated to be stiffer and stronger than the PPCNC samples that were based on the PP copolymer (PP-C) (as discussed previously in section 5.5). Also, Figure 5.7-1 illustrates that the tensile modulus of the thin sections was significantly higher than that of the thick sections. For PPCNH samples, the modulus of the thin section was about 33.8 % higher than that of the thick section. It seems that the wall thickness has less effect on the tensile modulus of the PPCNC samples. However, the thin section still has a tensile modulus that was 17.6% higher than that of the thick section.

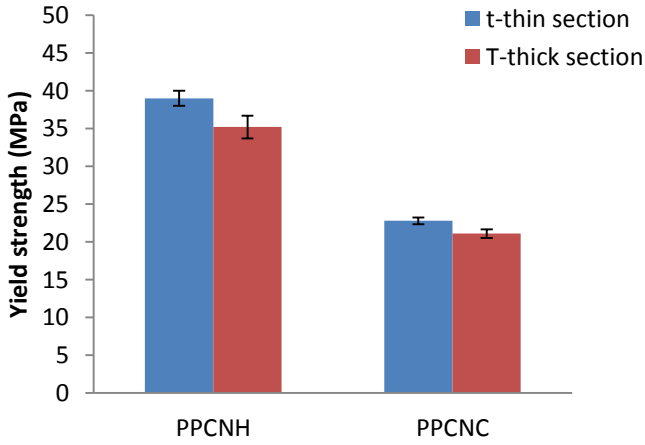

Figure 5.7-2 Yield strength of the samples from thin and thick sections

Similar results can be observed for the yield strength shown in Figure 5.7-2. PPCNH samples were stronger than PPCNC samples as expected. The thin section of the PPCNH sample could take 10.8 % more stress before yielding, in comparison to the thick section. For PPCNC samples, the yield strength of the thin section was found to be 8.1 % higher than that of the thick section.

Clearly, the preliminary result of tensile tests shows that the thin sections were significantly stiffer and stronger than the thick sections, especially for the PPCNH samples. The difference in the tensile properties of thick and thin sections was very likely due to the different internal morphologies developed under different thermomechanical environments imposed during injection moulding. This would be confirmed by the results from the other tests.

5.7.2 Effects on Crystallinity

Figure 5.7-3 illustrates the DSC traces of the samples cut from the thick sections of the injection moulded parts. The positions where the DSC samples were cut from the injection moulded parts has been demonstrated clearly in section 4.7.

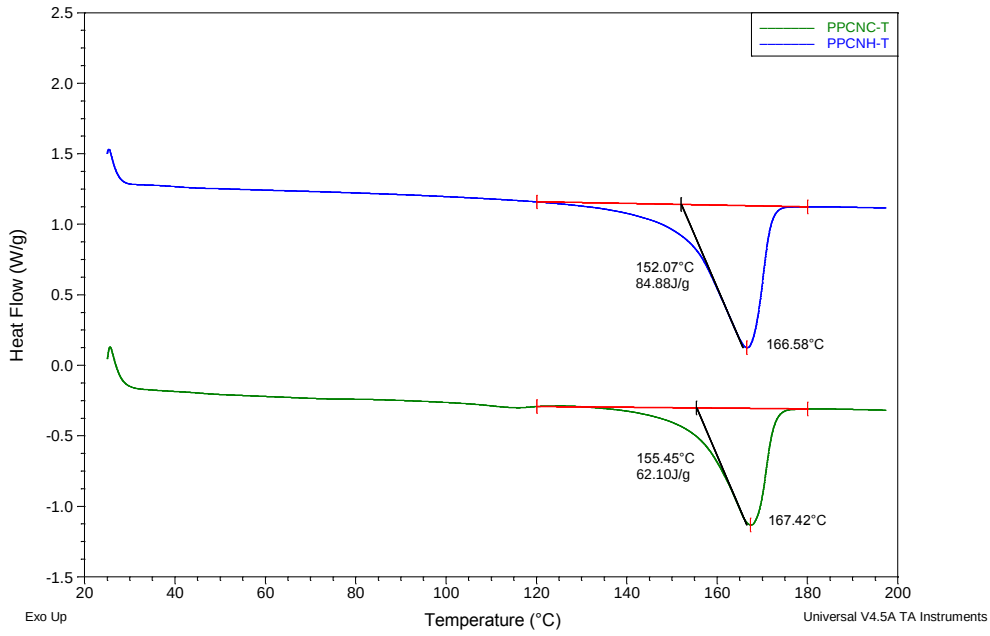

Figure 5.7-3 DSC curves for sample PPCNH-T and PPCNC-T

Table 5.7-1 summarises the DSC results for the thick sections, and the thin sections whose data have been obtained previously in section 5.5.

Table 5.7-2 DSC results for injection moulded PPCNs

Sample Code	Enthalpy of fusion (J g^{-1})	Crystallinity (%)	Melting point(°C)
PPCNH-t	85.7	45.3	166.2
PPCNH-T	84.9	44.9	166.6
PPCNC-t	64.0	33.7	166.7
PPCNC-T	62.1	33.1	167.4

The data in Table 5.7-2 shows that the nanocomposites based on PP-C have lower crystallinity than those based on PP-H, due to the comonomer content. It appears that the thick sections had slightly lower degree of crystallinity than the thin sections for both PPCNH and PPCNC samples. It is apparent that the cooling rate and shear rate level was significantly increased when the polymer melt was forced to enter the thin sections of the cavity from the thick sections. However, the increases in cooling rate and shear rate level are known to have opposite effects on the crystallinity of PP. A higher cooling rate would lead to a lower degree of crystallinity for polymers [248], while the increasing injection speed would increase the degree of crystallinity [210]. In this experiment, the increase in the shear rate level due to the change in channel depth should be more or less equivalent to the increase in injection speed. The overall effect of the decreased wall thickness was a slight increased crystallinity.

The difference in crystallinity between the thick and thin sections was at a negligible level ($\leq 0.6\ \%$), which indicates that the crystallinity was not evidently influenced by the wall thickness in this experiment. Furthermore, the slight difference in crystallinity was unlikely to cause the significant difference in mechanical properties. However, the OM should confirm that the morphology of the thin section is different: the crystallites will be ‘chain extended’ (i.e. oriented), even though the degree of crystallinity is similar.

5.7.3 Effects on Morphology

The images obtained from optical microscopy (OM) were used to analyse the microstructure and to measure the skin layer thickness, using the image processing programme, ImageJ.

The OM images for the thick sections are shown in Figure 5.7-4 below. Clearly, there were two skin layers and an interior core for sample PPCNH-T (Figure 5.7-4a). Two skin layers, two intermediate layers and an inner core can be observed for sample PPCNC-T (Figure 5.7-4b). Generally, the basic skin-core microstructures of the thick sections were consistent with those of the thin sections shown in section 5.5 and Appendix E.

As mentioned previously in section 5.5, the development of the microstructure of the moulding is controlled by the thermomechanical environment imposed to the polymer during processing[27,205]. Hence, the difference observed in the internal morphology between the two samples was due to the different thermomechanical environments induced by the difference in intrinsic materials properties and the presence of nucleating agent in the PP-C material.[207]

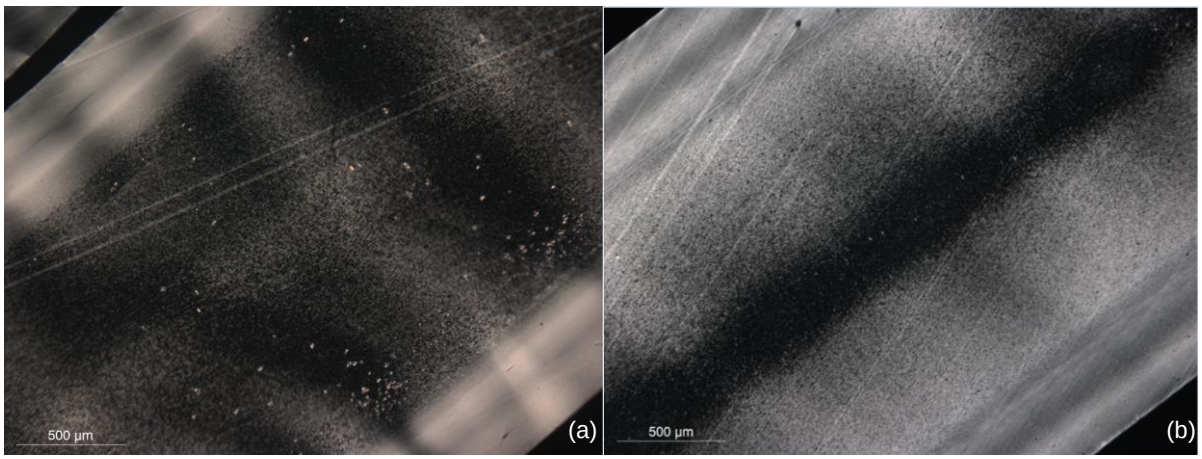

Figure 5.7-4 OM images for (a) PPCNH-T and (b) PPCNC-T (magnification=50x)

The spherulitic core and oriented non-spherulitic skin can be observed in the OM images, and the development of the skin-core structure in injection moulded parts has been considered in detail in sections 2.2.3 and 5.5.9. The measured skin thickness and calculated skin fraction are summarised in Table 5.7-3 below.

Table 5.7-3 Frozen layer thickness

Sample code	Part thickness (µm)	Total frozen layer thickness (µm)	Frozen layer fraction (%)
PPCNH-t	1380	636	46.1
PPCNH-T	2793	467	16.7
PPCNC-t	1556	644	41.4
PPCNC-T	2850	483	16.9

It is very clear that for both PPCNH and PPCNC samples, the thin sections had a much thicker skin layer than the thick sections, as shown in Figure 5.7-5. The big difference in the frozen layer thickness, hence oriented structure, was due to that the thermomechanical environment imposed to the PPCN melt being very different in the thin and thick sections. More specifically, when the material entered the thin section from the thick section during filling stage, the cooling rate and shear rate level were significantly changed. The estimated shear rate in actual moulding and predicted shear rate by simulation will be compared and discussed in a later section (section 5.8).

As introduced in section 5.5, the formulation of frozen layer is the result of crystallisation under high cooling rate and stress fields, where the flow induced orientation cannot relax completely before reaching the crystallisation temperature T_c. The development of frozen layer are related to two time variables [202]: time allowed for relaxation of the flow induced particle/molecular orientation until crystallisation temperature is achieved, t_r, and the relaxation time of the material, λ. A highly oriented skin layer is formed when $t_r < \lambda$.[202]

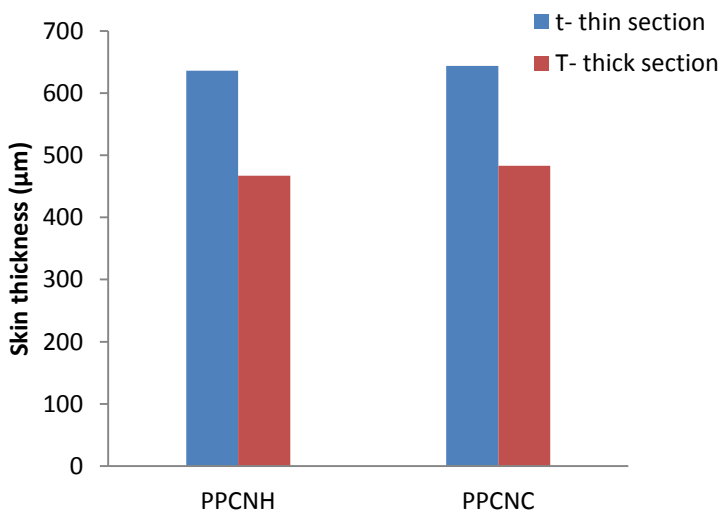

Figure 5.7-5 Skin thickness of the samples

In this experiment, the cavity section depth was greatly reduced to 1.2 mm from 2.7 mm when the material is forced to enter the thin sections from the thick sections, resulting in a significantly increased cooling rate. The increased cooling rate reduces the time (t_r) to reach crystallisation temperature T_c, leading to thicker skins, although T_c is slightly reduced with increased cooling rate.[205]

On the other hand, local difference in shear rate/stress was considerably increased when the material entered the thin sections, as the channel depth was greatly reduced when the injection flow rate remained constant. The increased shear rate might decrease both the time (t_r) to reach T_c and the relaxation time of material (λ) [205]. The overall effect on frozen layer thickness depends on the magnitude of these competing effects. According to the discussion regarding the effects of injection speed on skin thickness in section 5.5, the final balance seems to be the reduction of skin layers with increased shear rate or injection speed.

Moreover, it should be noted that the actual melt temperature was anticipated to be lower in the thin section because the melt flowed through the thick sections first and lost some heat before entering the thin sections. The reduction in the melt temperature led to a decrease in the time (t_r) to reach crystallisation temperature, resulting in thicker skins. The predicted bulk temperature data (Moldflow® simulation) for thin and thick sections under different moulding conditions will be shown and discussed in section 5.9.

The difference in the thermomechanical environment resulted in the different skin-core microstructures for the thin and thick sections. The overall effect of the three aspects discussed above, allowed the thin sections to have much thicker frozen layers. Furthermore, the skin layer fraction of the thin sections was very high (>40 %) and much greater than in the thick sections. Oriented skins have been reported to be much stiffer and stronger than the core for injection moulded PP parts[196], and a thicker skin is simultaneously more oriented and crystalline[27,202], indicating more shear-induced orientation effects.

5.7.4 Clay Dispersion

Interlayer spacing of clay (d_{001}) was calculated from XRD analysis using Bragg's law ($n\lambda = 2dsin\theta$). The XRD patterns of PPCNH-T and PPCNH-t are shown in Figure 5.7-6 as an example, while the XRD patterns of PPCNC-T and PPCNC-t are in Appendix G.

It is well known that the penetration depth of X-ray can reach only a few microns in polymer samples at most, thus, the XRD results actually reveal the dispersion of clay

particles predominantly in the skin layers as they were a few hundred microns thick (Table 5.7-3).

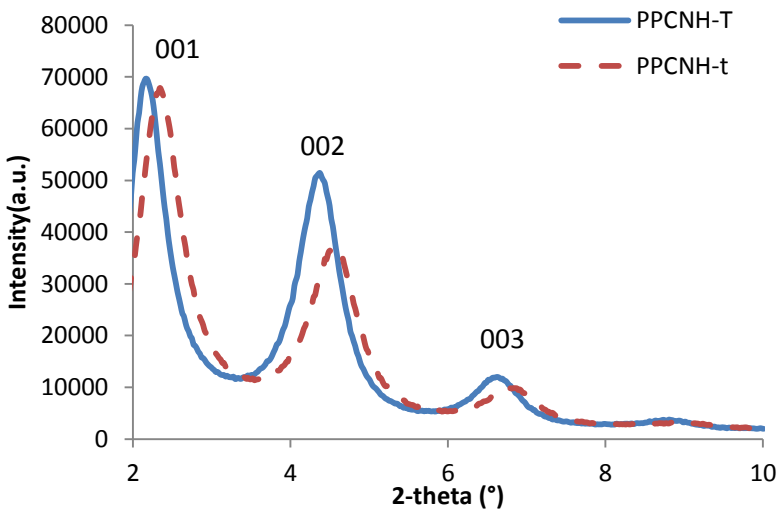

Figure 5.7-6 XRD patterns for PPCNH-T and PPCNH-t

Clearly, the (001) peak was observed at lower two-theta angle for the thick section (PPCNH-T), which indicates greater interlayer spacing, d_{001}. Figure 5.7-7 displays the calculated interlayer spacing for the thin and thick sections. For sample PPCNC-T and PPCNC-t, their d_{001} values were deduced from d_{002}, as their (001) peaks have dropped below $2\theta = 1.6°$ and were completely masked by the background scattering.

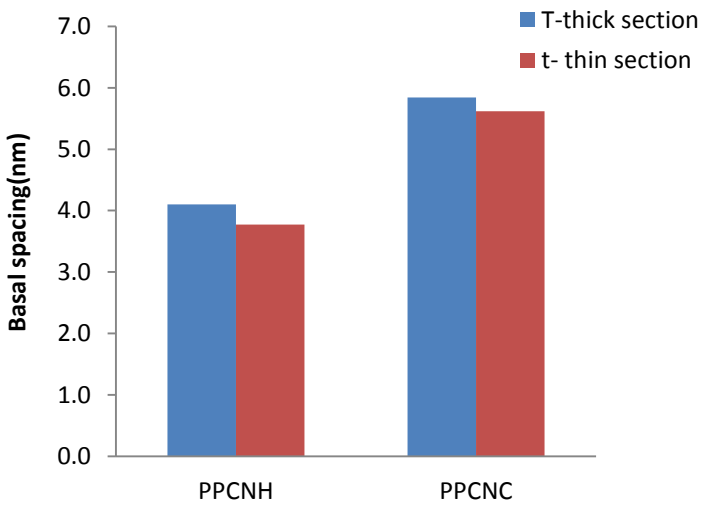

Figure 5.7-7 Interlayer spacing (d_{001}) of the samples tested

Firstly, the PPCNC samples had higher interlayer spacing than the PPCNH samples, which has been discussed previously in section 5.5.6. The resulting data of interlayer spacing suggests that the thick sections had higher clay intercalation than the thin sections. So far, this phenomenon has been scarcely reported and studied in the

literature. Thus, a possible reason is proposed below to explain the reduced interlayer spacing in the thin sections.

The channel depth is greatly reduced 2.7 mm to 1.2 mm, when the material is forced to enter the thin sections from the thick sections. According to the equation cited previously as Equation 5.5-14, when channel depth, H, is reduced to 1.2 mm from 2.7 mm, the apparent shear rate in the thin section is 5.1 times of that in the thick sections.

$$\dot{\gamma}_A = \frac{6Q}{WH^2} \tag{5.5-14}$$

Cooling rate was significantly increased in the thin sections, thus, the viscosity of the melt increased more rapidly due to faster heat loss. Due to the simultaneous increases in shear rate and cooling rate, the increase in shear stress was thus much more extreme. Higher degree of molecular and particle orientation was induced in the thin sections (see Figure 5.7-9), as a result of the intensive shear rate/stress level. Very likely, the polymer chains existing in the clay galleries were also significantly affected by the increased shear rate/stress level, and they were also stretched and oriented to a higher level in the flow direction. Figure 5.7-8 shows a simple sketch of this process.

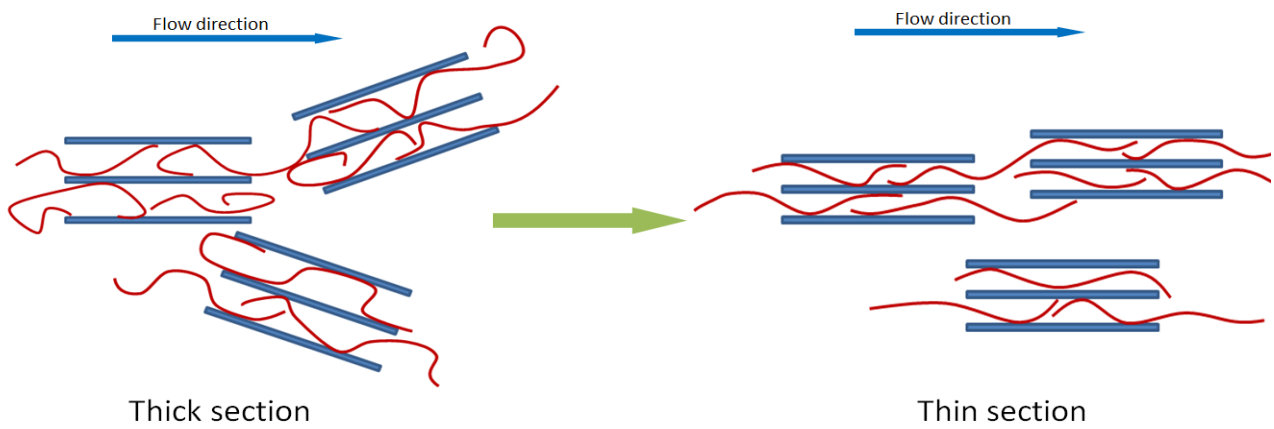

Figure 5.7-8 Stretch and orientation of PP chains in the clay galleries due to high shear rate/stress level

As the PP chains existing between the clay sheets were significantly stretched and oriented in the thin sections, thus, less inter layer space was needed to accommodate those chains. As a result, the compaction of clay stacks happened, leading to decreased interlayer spacing. Due to the extremely high cooling rates, skin layers form very rapidly, and within the skin layer no time was allowed for the

stretched and oriented molecular chains to relax and expand the interlayer spacing again. As mentioned previously, the XRD results actually reveal the intercalation of clay particles in the skin layer. Thus, decreased interlayer spacing was observed for the samples taken from the thin section. Probably, the mechanical properties were not affected evidently by the decreased d-spacing, as the compatibility and interaction between the PP and clay particles were not affected.

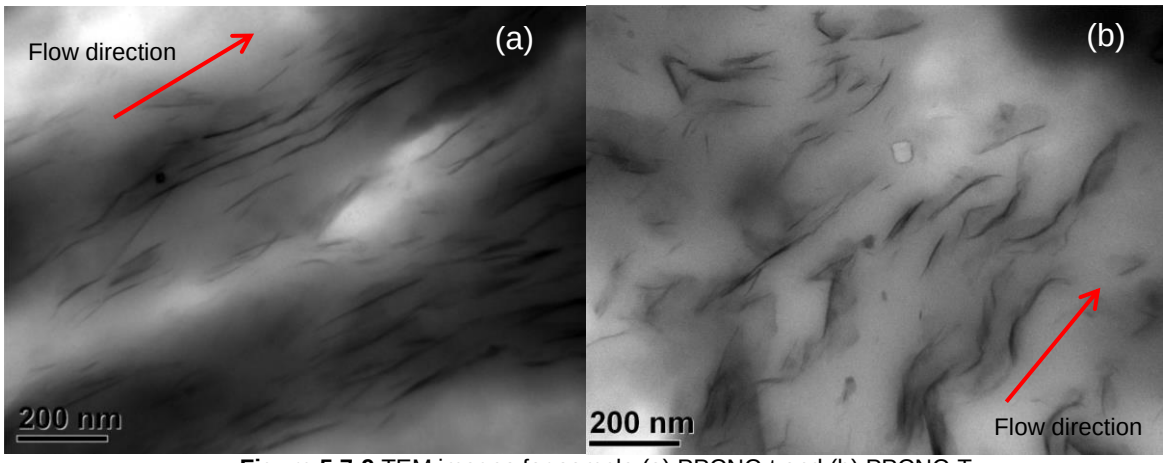

Figure 5.7-9 TEM images for sample (a) PPCNC-t and (b) PPCNC-T

The TEM images in Figure 5.7-9 shows clearly that the level of clay orientation in the thin section is much higher than in the thicker section, indicating much stronger shear induced orientation. As discussed previously in section 5.5.4, the shear induced particle/molecular orientation can significantly enhance the tensile properties. Therefore, the big difference between the tensile properties of the thin and thick sections is very likely due to the significant difference in the shear induced effects, which leads to different skin layer fraction and level of clay orientation.

5.7.1 Summary

The effects of wall thickness on the properties of thin-wall injection moulded parts were investigated by comparing the thin and thick sections of the moulded parts. To this end, tensile tests, DSC analysis, OM, TEM and XRD analysis were performed on the moulded parts.

The preliminary experimental results suggest that the thin sections at the end of flow had higher tensile modulus and strength compared to the thick sections for both PPCNH and PPCNC samples. Significantly higher frozen layer fractions and higher

level of clay orientation were found for the thin sections according to the OM and TEM images. The strong shear induced effects (a thicker skin and higher level of clay orientation) in the thin sections is thus believed to contribute to the enhanced tensile properties.

There was only a negligible difference in the degree of crystallinity between the thin and thick sections, thus the crystallinity was unlikely to make any observable change to the tensile properties. Reduced interlayer spacing of clay was observed in the thin sections, and a possible reason has been proposed: the PP chains in the clay galleries were stretched and oriented to a higher level in the thin sections, due to the more intensive shear conditions. Compaction of clay stacks occurred, as less inter layer space is needed to accommodate those stretched chains, resulting in reduced interlayer spacing. Rapid cooling of the skin layer allowed no time for the chains to relax and expand the galleries back again.

So far, all the results from the actual injection moulding of the stepped plaques have been thoroughly presented and discussed. In the next section, the data obtained from Moldflow® simulation will be compared with that obtained during the actual injection moulding process.

5.8 Injection Moulding Analysis: Actual moulding vs. Real-time simulation

In this section, the resulting data obtained from the actual injection moulding and the real-time simulations are compared. The emphasis of section 5.8 is put on the in-cavity pressure, frozen layer fraction, bulk shear rate and bulk temperature data. The resulting data are discussed and related to the results obtained in the previous studies of actual injection moulding.

The coding system used in this section has been introduced in section 4.8, and it is consistent with the previous studies of actual moulding. 'S' has been added to the sample code, indicating the data obtained from the simulation experiments. All the measured and calculated data are summarised in Appendix H.

5.8.1 In-cavity pressure

a) Example of Actual – Simulation Comparisons

In actual injection moulding, the in-cavity pressure was measured by a pressure transducer that was placed next to the gate of one of the four cavities (section 4.8). Thus, the pressure at the same position was measured for the real-time simulation (shown in Figure 4.8-2). The resulting pressure data was used to plot the in-cavity pressure data obtained in the simulations. Figure 5.8-1 shows the plots of in-cavity pressure against time for sample PPC-30-25 and PPC-30-25-S as an example.

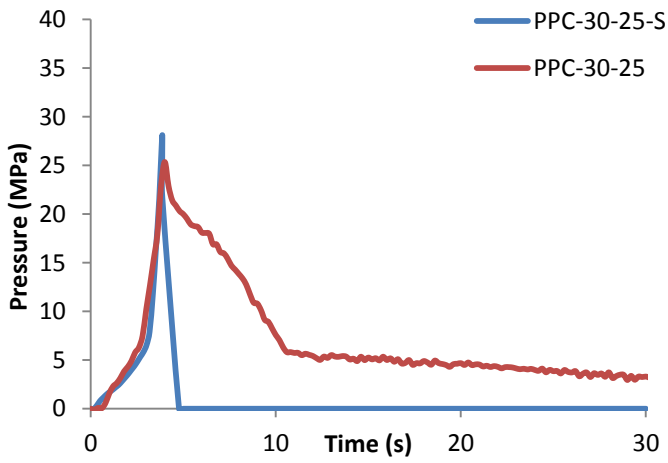

Figure 5.8-1 Plots of in-cavity pressure vs. time

The measured pressure profile has been discussed and correlated to the corresponding phases during an injection moulding cycle earlier in section 5.5.3, so it will not be repeated in this section.

Clearly, the pressure plots obtained from actual injection moulding and simulation show a very good consistency in the mould filling stage (from 0 to about 3.9 s). In the graph, it is clear that sample PPC-30-25-S has a higher predicted maximum in-cavity pressure or injection pressure than PPC-30-25. This is very likely to be due to the fact that during the actual injection moulding, the required clamp force exceeded the capability of the machine, opening the mould very slightly when the injection pressure was high enough. This has been discussed and confirmed in section 5.5. It is thus reasonable to see a lower injection pressure for the actual moulding operation, as the channel depth was increased by opening the mould, and the pressure failed to build up further. So far, it seems that the simulation process was reasonably accurate, in terms of the pressure build-up during mould filling stage.

Figure 5.8-2 shows the clamp force profile for PPC-30-25-S estimated by Moldflow® Insight. Clearly, the clamp force required for the moulding process is approximately 60 tonnes, according to Figure 5.8-2. However, the injection moulding machine, NB62, has a maximum clamp force of 62 tonnes. This strongly implies that during the actual injection moulding cycle, the clamp force provided by the machine may not be enough to lock the mould tight all the time, if the force being set is not transmitted fully to the mould tool faces.

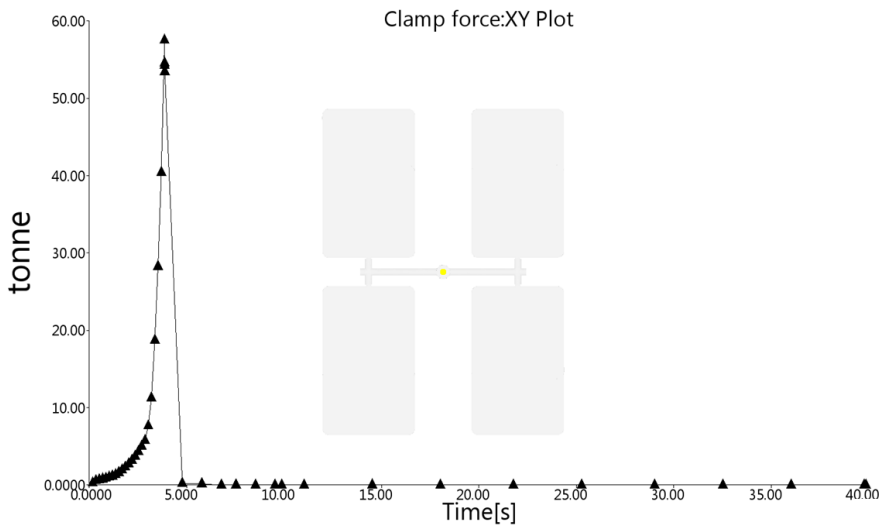

Figure 5.8-2 Plot of clamp force generated by Moldflow® Synergy for PPC-30-25-S

During the actual injection moulding process, the opened mould also affected the packing and cooling phases. The increased channel depth or part thickness may have slowed down the cooling process. Also, the pressure transducer was always under pressure for the moulded was thicker than the cavity depth (see Figure 5.5-8). As a result, the measured in-cavity pressure cannot drop to zero at the end of a moulding cycle. Therefore, it is not unexpected to observe such as a significant difference between the pressure plots for actual moulding and the simulation during the packing and cooling phases (from 3.9 to 30 s). The predicted pressure drops to zero rapidly during the packing stage, most probably, due to the packing pressure (7.7 MPa) being too low leading to rapid gate freeze off.

It can generally be concluded that the injection moulding simulation was fairly accurate within the mould filling phase. Higher simulation accuracy would be expected if the mould had not opened during the filling stage of the actual injection moulding cycle.

b) Comparison of actual versus simulation: effect of injection speed

Figure 5.8-3 shows the in-cavity pressure plots at different injection speeds, for both actual moulding and simulation experiments.

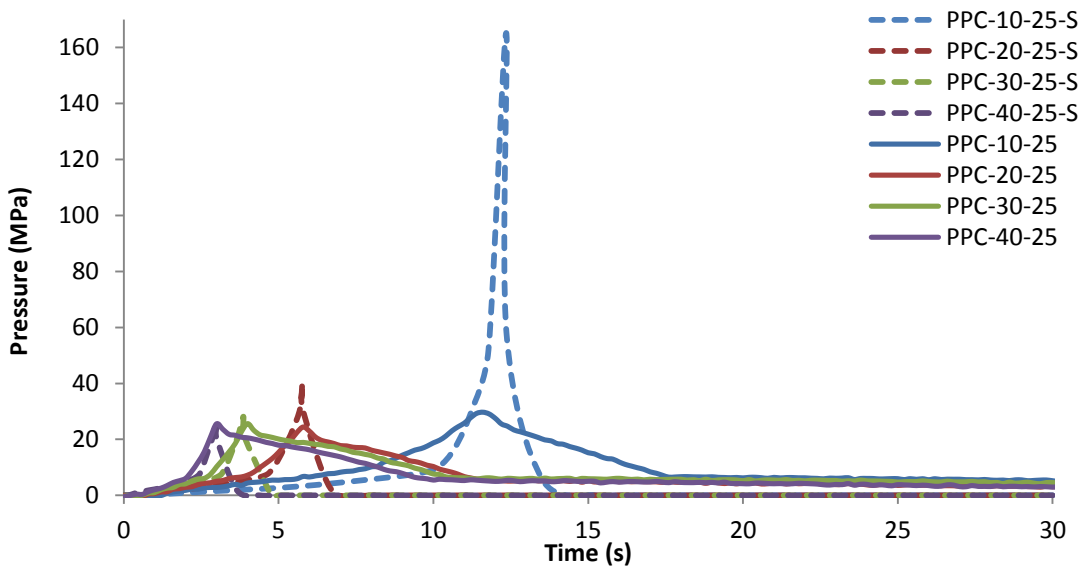

Figure 5.8-3 Pressure plots at different injection speeds

PPC-10-25-S shows an extraordinarily high injection pressure in the graph, because a short shot was actually reported during the simulation run. On the contrary, the

actual injection moulding under the same conditions (PPC-10-25), give rise to much lower injection pressure, moulding was also successful at 10 % injection speed. Again, this difference is likely to be due to the fact that the machine failed to lock the mould tightly under such high pressure. The predicted clamp force required for PPC-10-25-S (based on the pressure prediction) is approximately 360 tonnes according to the simulation, which is far beyond the capability of the machine.

Figure 5.8-4 shows the effect of injection speed on injection pressure or maximum in-cavity pressure. It is very clear that the simulation result becomes more accurate with increasing injection speed, with very good prediction at greater than 30% injection speed. The pressure plot obtained from simulation experiments simply implies that higher pressure was needed to fill the mould at a lower injection speed. At a very low speed (10 %), massive pressure was required for mould filling, due to the increased frozen layer thickness and the significantly reduced channel depth. The relationship between injection speed and injection pressure has been discussed in section 5.5. For actual injection moulding, due to the lack of clamp force, the pressure failed to build up further during the mould filling stage, when it reached a level that was enough to force the mould open. Therefore, Figure 5.8-4 shows that for the actual moulding operation, the injection speed has very limited effect on the injection pressure, in comparison to the simulation experiments.

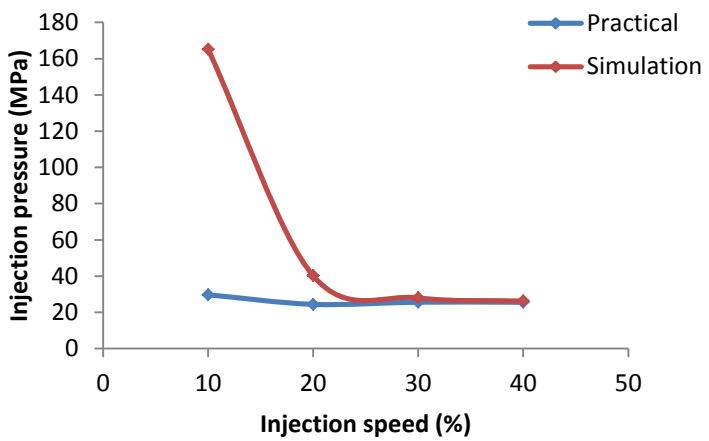

Figure 5.8-4 Injection pressure vs. injection speed

For a stable injection moulding process, the variation in the injection pressure is very small from one cycle to another. Therefore, the error bars for the measured data from actual moulding are too small to be seen on the graph.

c) Comparison of actual versus simulation: effect of mould temperature

The plots of in-cavity pressure at different mould temperatures for both actual moulding and simulation experiments are in Appendix H. The plots of injection pressure or maximum in-cavity pressure against mould temperature are shown in Figure 5.8-5.

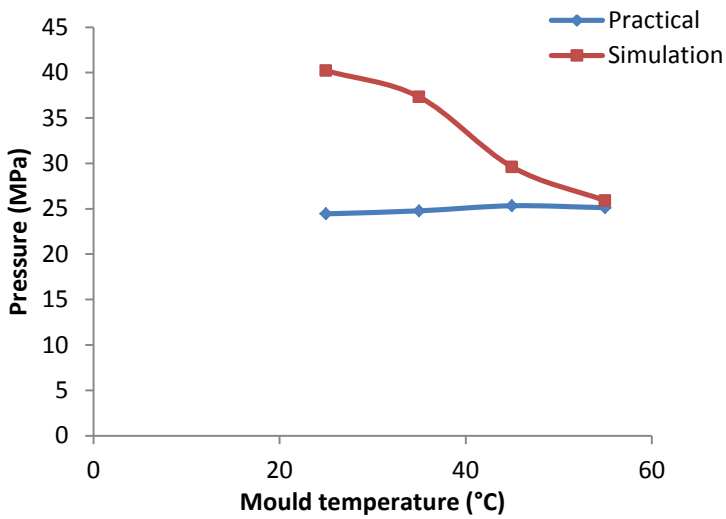

Figure 5.8-5 Plots of injection pressure vs. mould temperature

Clearly, the pressure plot obtained from the simulation experiments shows that the injection pressure reduces with increasing mould temperature. This is in good agreement with the theory. When mould temperature is increased while the other injection parameters remain unchanged, cooling rate is reduced and thus thinner frozen layer will be formed during moulding filling. Thinner frozen layer means more channel depth and thus less pressure is needed to fill the mould. However, the pressure plot obtained from actual moulding is almost a horizontal line and shows no clear trend. Undoubtedly, the effect of mould temperature was completely masked, because the mould opened slightly during packing at all mould temperatures investigated.

From another point of view, the discrepancies between the data from simulation and actual moulding emphasise the importance of mould tool design. Any error made during the design process can be very expensive and unforgiving. Changing process conditions makes this process more complex, since (without accurate simulation) it is difficult to predict the effects on pressure, hence mould clamp force.

5.8.1 Frozen layer fraction

As mentioned in the previous studies of the actual moulding process, there is a highly oriented layer frozen immediately below the part surface due to a combination of high shear stress and high cooling rate adjacent to the mould wall. This frozen layer, or skin, is an indication of the flow induced effects, which have significant effects on the mechanical properties of injection moulded parts.[249–251] The frozen layer fraction is very high in the case of the thin wall injection moulded PPCN parts in this research project, and are critical to the tensile properties of moulded PPCNs, according to the previous studies (sections 5.5 – 5.7).

During mould filling, in the areas with continuous flow, the frozen layer may maintain a constant thickness because the heat loss to the mould wall is balanced by the entry of hot melt, but when the flow stops, the heat loss becomes dominant. PP is known as a good thermal insulator, which means the material in the core part has sufficient time to relax and crystallise under quiescent conditions during packing and cooling stages. In other words, the packing and cooling stages make little contribution to the skin layer fraction. Therefore, it is believed that the skin layer that can be observed clearly under polarised light by an optical microscope is mainly formed during the mould filling stage. For the simulation experiments, the 'frozen layer fraction prediction at the end of fill' was thus used as the frozen layer fraction.

The frozen layer fraction was measured for both the thin and thick sections, during the simulation experiments. The original data is summarised in Appendix H. The plots of frozen layer fraction against processing conditions are shown in Figure 5.8-6 and 5.8-7.

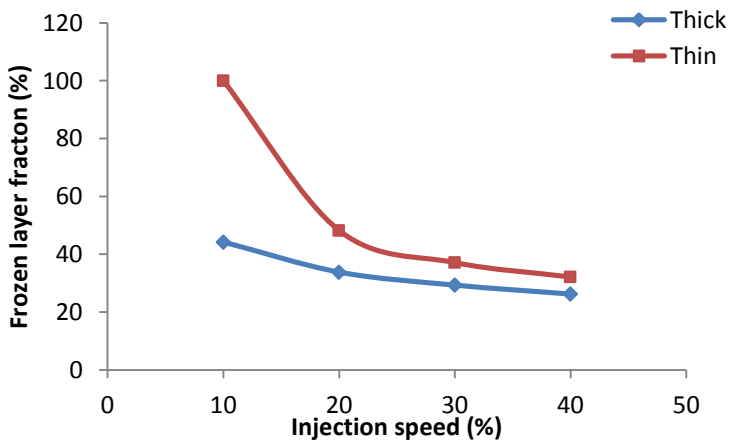

Figure 5.8-6 Predicted frozen layer fraction vs. injection speed for PP-C

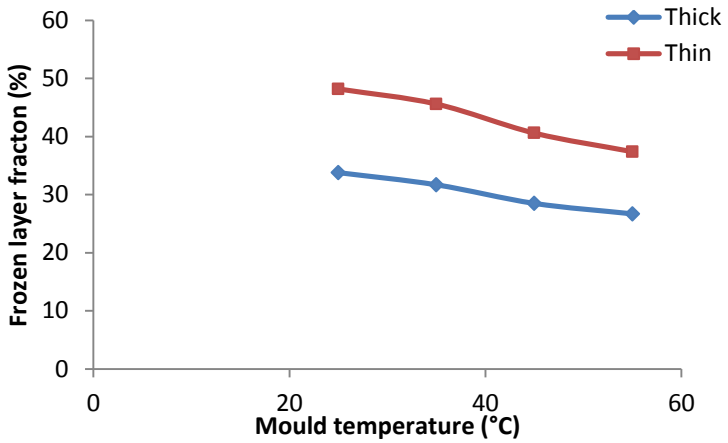

Figure 5.8-7 Frozen layer fraction vs. mould temperature for PP-C

Clearly, the plots above show that the frozen layer fraction decreases with increasing injection speed or mould temperature. At 10 % injection speed, a short shot was reported during the simulation run, thus frozen layer fraction of 100 % was observed for the thin sections. In comparison to mould temperature, injection speed shows more influence on the frozen layer fraction, in the selected experiment ranges. In other words, the simulation results and the results obtained in the previous studies of the moulding operation (section 5.5) show a good consistency, although the frozen layer data obtained for the actual moulding operations were based on PP/clay nanocomposites.

In terms of the effects of processing conditions on frozen layer fraction, the data obtained from the simulation experiments and actual injection moulding, as well as the studies reported in the literature, are in good agreement [196,205]. The effects of processing conditions on frozen layer fraction has been thoroughly discussed and explained previously in section 5.5, thus, it is not repeated here. There is some difference between the frozen layer fraction obtained from the simulation and the actual moulding process, although they almost display the same qualitative trends. Figure 5.8-9 shows the difference between the thin section results from simulation and actual moulding.

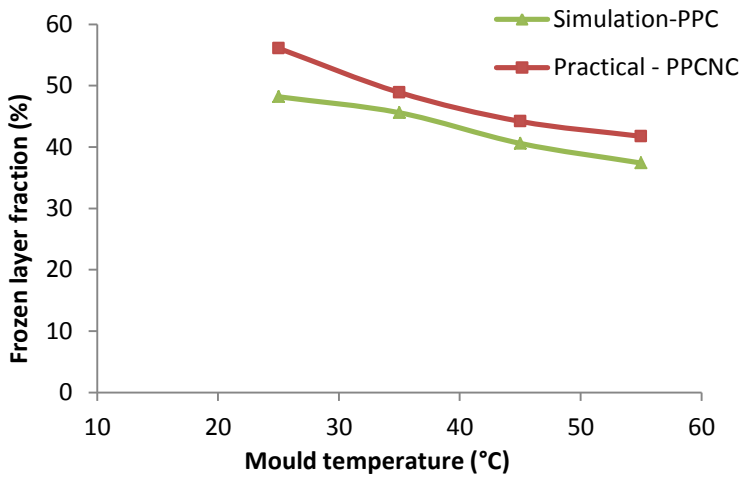

Figure 5.8-8 Frozen layer fraction vs. mould temperature (thin sections)

The simulation process was performed with pure PPC, while the data obtained from the actual moulding operation was based on the PPC nanocomposites. According to the study reported in section 5.6, frozen layer thickness increases with increasing clay concentration, due to the increased thermal conductivity. Therefore, the actual injection mouldings show a higher frozen layer fraction, due to the presence of clay particles. In other words, the simulation is still considered to be relatively reliable.

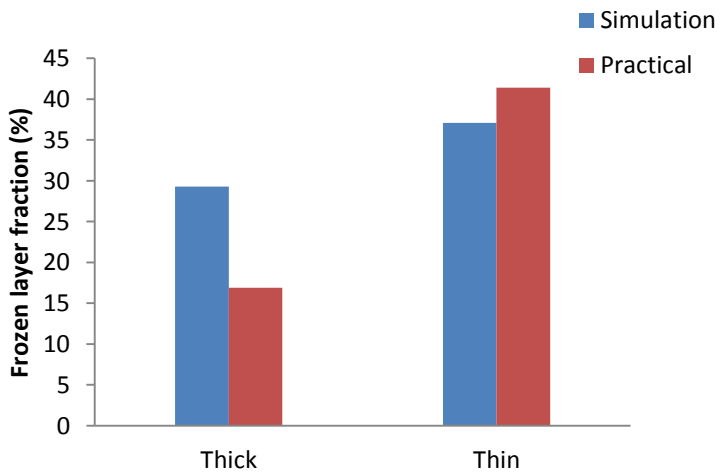

Figure 5.8-9 Frozen layer fraction vs. wall thickness

Figure 5.8-9 shows the effects of wall thickness on skin fraction, based on PPC-30-25-S and PPC-30-25. Clearly, both simulation and actual injection moulding indicate that the thick section possesses a lower frozen layer fraction compared to the thin section. The effects of wall thickness suggested by the simulation and actual moulding are very consistent. In comparison, the actual injection mouldings show more difference between the thick and thin sections. For the thin section, the slight

difference between simulation and actual moulding is due to the presence of clay. For the thick section, the big difference might be due to a problem related to the mesh type used in the simulation. Dual domain meshing, which is suitable for thin-wall structures, was selected in the study. However, the thick section (2.7 mm in thickness) is not thin enough to be considered as a thin wall structure to some extent. As result, there is discrepancy in the simulation result.

5.8.2 Bulk Shear Rate

The bulk shear rate data obtained from the simulation experiments indicate the magnitude of the shear rate through a cross-section, and it gives an overview of the shear rate distribution at the filling stage[216]. According to the explanation given by Moldflow® Insight 2017[216], bulk shear rate is derived from the wall-shear stress and the fluidity of the polymer. From the fluidity and part thickness, representative viscosity is calculated first, and then the bulk shear rate is calculated according to the presentative viscosity and wall-shear stress. For the simulation experiments performed under different processing conditions, the bulk shear rates at the centre points of the thick and thin sections during mould filling stage were measured.

For the actual injection moulding process, shear rate in a rectangular channel can be roughly estimated by Equation (5.8-1), assuming the process is isothermal. The power law index, n, is 0.37 according to the flow curve obtained at 200°C (see Table 5.1-3).

$$\dot{\gamma} = \frac{6Q}{WH^2}\left(\frac{3n+1}{4n}\right) \tag{5.8-1}$$

The width (W) of channel is 66 mm, and the height (H) is 2.7 mm and 1.2 mm for the thick and thin sections, respectively. Therefore, the shear rate in the thin and thick sections during actual injection moulding can be roughly estimated. Figure 5.8-10 and 5.8-11 show the plots of shear rate against processing conditions.

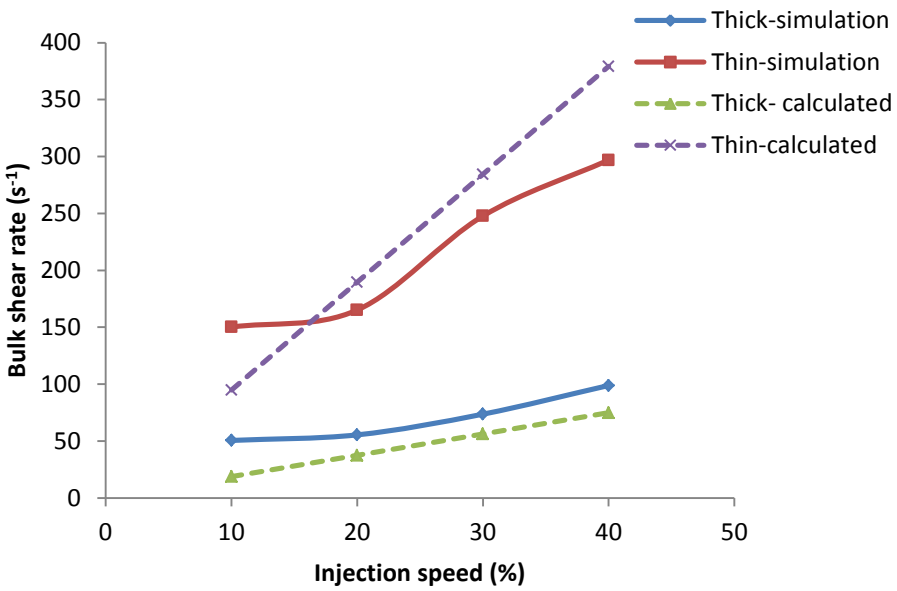

Figure 5.8-10 Bulk shear rate vs. injection speed

Clearly, Figure 5.8-9 shows that increasing injection speed increases the shear rate for both actual moulding and simulation experiments. Apparently, volumetric flow rate (Q) is linearly proportional to the set injection speed, and thus the calculated shear rate ($\dot{\gamma}$) shown in Figure 5.8-10 increases linearly with increasing injection speed. However, injection moulding is a non-isothermal process, and the temperature varies across part thickness and the frozen layer forms simultaneously. As the bulk shear rate data generated in the simulation experiments have taken the non-isothermal conditions into consideration, thus, as shown in Figure 5.8-9, there is clear difference between the bulk shear rate from simulation and the calculated value, and the trend of predicted bulk shear rate is not simply linear in a non-isothermal process. Another reason for the discrepancy between the predicted bulk shear rate and calculated shear rate is that the Moldflow® simulation is based on Cross/WLF equation (see Equation 2.2-8, in literature review), in which pressure sensitivity and temperature sensitivity are also considered in addition to the shear sensitivity.

Figure 5.8-6 shows that the frozen layer thickness decreases with increasing injection speed, and as a result, the effective channel depth increases with injection speed. The increased channel depth, in turn, reduces the shear rate. However, the plots of bulk shear rate indicate clearly that the effect of volumetric flow rate is predominating, whilst the effect of effective channel depth is masked completely.

In section 5.5, it was found that the tensile modulus and yield strength of injection moulded parts decreased with increasing injection speed (Figures 5.5-16 and 5.5-17). According to Figure 5.8-6 and 5.8-10, it is very likely that the formation and thickness of the frozen layer, has significant effects on the tensile properties of injection moulded parts, which is in good consistency with the literature [196].

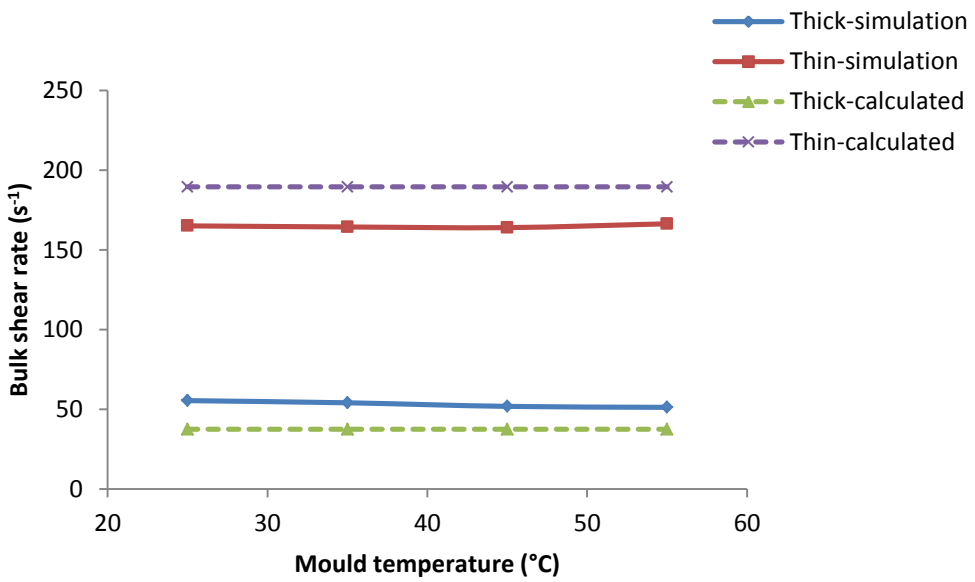

Figure 5.8-11 Bulk shear rate vs. mould temperature

Figure 5.8-11 shows plots of shear rate against mould temperature. The calculated shear rate remains constant as Equation (5.8-1) is for an isothermal process. There is also no clear trend for the plots of bulk shear rate against mould temperature, although the frozen layer decreases with increasing mould temperature (Figure 5.8-6).

It appears that the mould temperature (over the range studied) has very limited effects on the bulk shear rate. According to previous discussion regarding the effect of injection speed on shear rate, it is clear that the change in volumetric flow rate is the dominating factor, whilst the effect of reduced frozen layer thickness, or increased effective channel depth, is masked completely. The injection speed or volumetric flow rate is constant when changing mould temperature, and thus the bulk shear rate relies on the change in the frozen layer thickness or effective channel depth. Figure 5.8-7 shows that the frozen layer fraction decreases from 33.8 % to 26.7 % when the mould temperature is increased from 25 °C to 55 °C. According to Equation (5.8-1), the following equation can be obtained:

$$\frac{\dot{\gamma}_{25°C}}{\dot{\gamma}_{45°C}} = \frac{H_{55°C}^2}{H_{25°C}^2} = \frac{(1-0.267)^2}{(1-0.338)^2} = 1.2 \quad (5.8\text{-}1)$$

where $H_{55°C}$ and $H_{25°C}$ are the effective channel depths at the mould temperature of 55 °C and 25 °C respectively. The bulk shear rate for a mould temperature of 25 °C should be 1.2 times that at the mould temperature at 55 °C; however, this is not observed in Figure 5.8-11. As mentioned previously, the bulk shear rate is calculated from wall-shear stress and fluidity, whilst the wall-shear stress is the shear force at the solid-liquid interface, per unit shear area [216]. After the formation of the frozen layer, the solid-liquid interface is actually the one between the frozen (static) layer and the polymer melt undergoing dynamic flow. Increasing mould temperature decreases the frozen layer thickness, resulting in increased effective channel depth. The increased channel depth, in turn, reduces the wall-shear stress as the volumetric flow rate is constant at a fixed injection speed. The increasing mould temperature also reduces cooling rate and gives lower viscosity to the polymer melt. Thus, increasing mould temperature decreases the viscosity and wall-shear stress at the same time. If the reductions in viscosity and wall-shear stress are similar, little change will be observed in the bulk shear rate derived from the wall-shear stress and viscosity.

5.8.3 Bulk Temperature

It is common knowledge that during the entire injection moulding cycle, the melt temperature changes with time and location and also across the part thickness. The bulk temperature data given by Moldflow® Insight indicates the local velocity-weighted average temperature across the part thickness. Areas with continuous flow typically have a higher bulk temperature.[216]

It is well known that the frozen layer thickness depends basically on the local thermal conditions for a given material, and the bulk temperature is a good estimation for the local thermal level. Therefore, the bulk temperature at the end of fill was predicted for the centre points of both thick and thin sections, during the simulation experiments. The resulting data would be compared to the frozen layer data obtained previously. Figure 5.8-12 shows the plots of bulk temperature against injection speed.

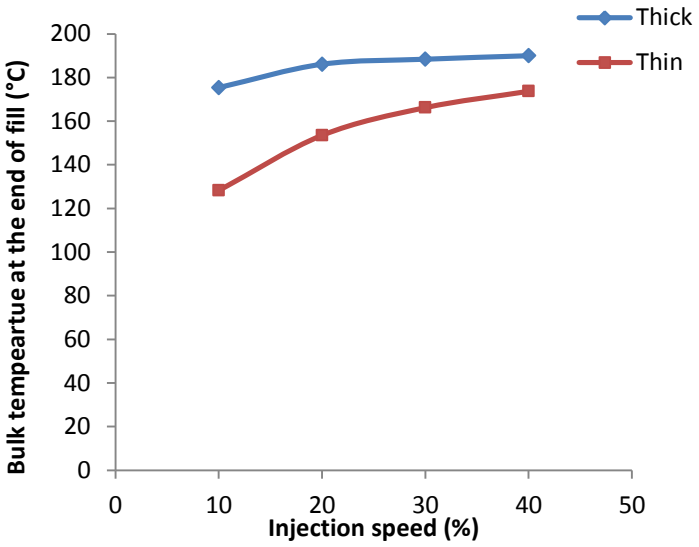

Figure 5.8-12 Bulk temperature at the end of fill vs. injection speed

Clearly, Figure 5.8-11 shows that the bulk temperature increases with increasing injection speed. During the simulation experiments, a short shot was reported for 10 % injection speed, thus the bulk temperature at the end of fill actually means the temperature when the flow stopped. In the plots, the maximum change in bulk temperature occurs when the injection speed is increased from 10 % to 20 %. For 10 % injection speed, the bulk temperature of the centre point of thin section is 128.2 °C, which is below 134 °C, the onset temperature of crystallisation measured by DSC in section 5.1 (Table 5.1-4). In other words, the thin section is actually frozen off, which is the reason for the short shot observation.

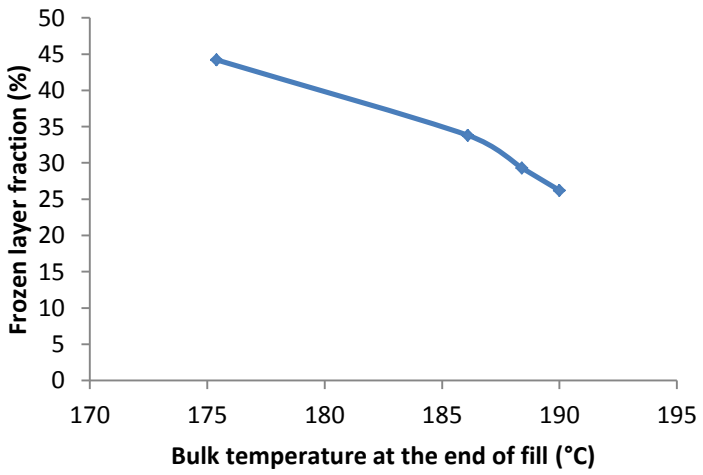

Figure 5.8-13 Frozen layer fraction vs. bulk temperature at the end of fill (thick section)

According to the simulation results shown in Figure 5.8-7 and Figure 5.8-12, the bulk temperature and frozen layer fraction are in good agreement with each other. Higher bulk temperature at the end of fill leads to lower frozen layer fraction in the moulded parts, and the maximum change appears between the injection speeds of 10 % and 20 %. Figure 5.8-13 shows the relationship between the bulk temperature and the frozen layer fraction, on the basis of the thick section of injection moulded parts.

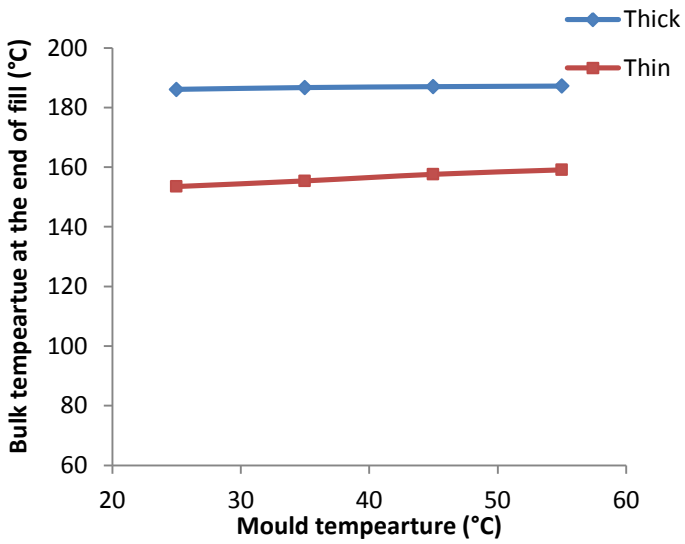

Figure 5.8-14 Bulk temperature at the end of fill vs. mould temperature

Figure 5.8-14 shows the plots of predicted bulk temperature against the set mould temperature. It seems that the bulk temperature of the thin section increases slightly with increasing mould temperature, while bulk temperature of the thick section almost remains constant.

The bulk temperature of the thick section is around 187 °C, which is very close to 190 °C, the melt temperature set for the moulding process. In comparison, the bulk temperature of the thin section is much lower, which is around 160 °C. The higher bulk temperature in the thick section is due to the fact that there is continuous flow in the thick section before the whole cavity system is completed filled. Due to the very high bulk temperature, the change in mould temperature shows very limited effects. Due to the high heat loss and cooling rate, the thin section is more likely to be affected by the change in mould temperature. Overall, the effect of mould temperature on the bulk temperature at the end of fill is very limited compared to that of injection speed, although mould temperature shows certain effects on the frozen

layer fraction. Therefore, in the selected experimental ranges, injection speed is more influential than mould temperature.

5.8.4 Summary

In this section, comparisons were made between the data obtained from actual moulding and equivalent simulation experiments. The resulting data obtained from the simulations were also related to the studies of the actual injection moulding process reported in the previous sections. The discussion mainly focuses on the outputs of in-cavity pressure, frozen layer fraction, bulk shear rate and bulk temperature.

In terms of the in-cavity pressure data, the real-time simulation and actual moulding show very good consistency for the mould filling stage, but large differences are apparent for the rest of the injection moulding cycle. The discrepancy is mainly due to the mould opening slightly during moulding filling, as the clamp force needed was beyond the capability of the injection moulding machine. Because of the parting of the mould faces, the actual moulding operation failed to reveal the effects of processing conditions, as the in-cavity pressure was not able to build up further once the mould was opened. On the other hand, the data from simulation experiments is in agreement with the theory. From another point of view, this discrepancy highlights the importance of mould tool design. Any mistake made during the design process can be expensive and unforgiving.

Good consistency was obtained for the frozen layer fraction data. Data from both simulation experiments and actual moulding suggest that frozen layer fraction decreases with increasing injection speed and mould temperature. The slight difference between the two types of data is most probably due to the presence of clay in the actual injection moulded parts. Bulk shear rate from real-time simulation and the estimated shear rate data for actual moulding show very similar trends whereby shear rate increases with injection speed, and remains almost constant with mould temperature. The difference between the bulk shear rate and estimated shear rate is due to the non-isothermal conditions utilised by the algorithms in the real-time simulation. Furthermore, the simulation calculations were based on the Cross/WLF

equation, where pressure and temperature sensitivity are also considered. Bulk temperature at the end of fill and the frozen layer fraction are in good agreement with each other, as bulk temperature estimates the thermal level, on which the frozen layer thickness depends.

Overall, after combing the results of the previous studies, it is quite clear that injection speed is of utmost importance to the moulding process and thus the properties of the moulded parts, in the selected experimental ranges of this research. In comparison, the effects of mould temperature are relatively negligible.

The DoE approach has played a significant role in this research project, when optimising the PPCN formulation and compounding conditions. Therefore, some thoughts and comments on the DoE approach are discussed in the next section.

5.9 Discussion on DoE Approach

Design of Experiments (DoE) is a well-known statistical method used for 'quality control and improvement'. This approach can maximise information gained with the minimum resources when investigating experimental systems or processes, and it is a very powerful statistical technique when dealing with multi-factor systems. Therefore, it has been widely used as a tool in scientific research across different disciplines, which have been presented in the literature review.

Montgomery [32] points out that the objective of every DoE is a quantitative statistical model of the process. In this research project, DoE approach has been applied when studying single screw extrusion of recycled PP blends (section 5.2), the optimum formulation of PPCNs (section 5.3) and the optimum compounding conditions (section 5.4). In the three DoE studies, the relationships between the selected input factors and the responses of interest were quantified by the regression models developed using DoE software, which allowed the optimisation of the processes or systems. In this section, some thoughts and comments on the DoE approach are discussed, on the basis of the three DoE studies conducted in this project.

5.9.1 Checking Assumptions

In the DoE studies, analysis of variance (ANOVA) was performed using the DoE software (Design Expert®) to determine the model significance. F-ratios and p-values were calculated and compared, and the calculation method has been introduced previously in section 4.2. The initial full second order regression models were simplified by removing the negligible terms with p-values greater than 0.10. The terms with p-values lower than 0.05 were considered as significant and were kept in the models.

In actual fact, when ANOVA is applied to a model, it has been assumed that the observations are normally and independently distributed with the same variance in each factor level, according to Montgomery.[32] Therefore, these assumptions need to be checked. Residuals, the difference between observations and the corresponding factor-level mean, can be used to check the assumptions.

a) Normality assumption

To check the normality assumption, a convenient way is to construct a normal probability of the residuals [32]. In the DoE studies, the plots of normal probability against residuals were generated by the Design Expert® software automatically. Figure 5.9-1 and 5.9-2 are two of the normal probability plots generated in the DoE study of single screw extrusion of recycled PP blends. All the other normal probability plots obtained in the DoE studies are shown in Appendix I.

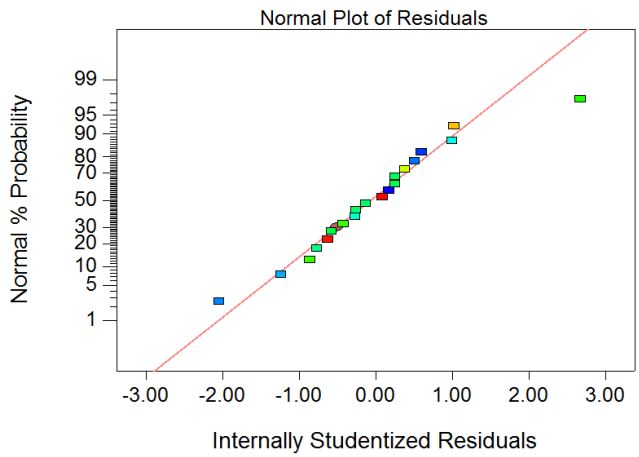

Figure 5.9-1 Normal probability plot for the response of melt pressure (single screw extrusion experiment)

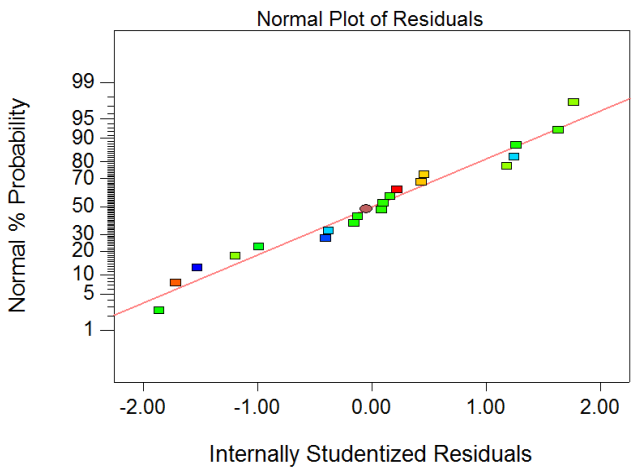

Figure 5.9-2 Normal probability plot for the response of mass output (single screw extrusion experiment)

According to the graphs above, it is clear that the observations lie along the straight lines, which indicates that there was no problem with the normality assumption for the DoE experiments in this project.

b) Independence assumption

To check the independence assumption, plots of residuals against the run order in which the experiment was performed can be used. According to statistics[32], if a pattern exists in the plots (*e.g.* sequences of positive and negative residuals), it may indicate that the observations are not independent. A typical plot of residuals versus run order from the single screw extrusion experiment is shown in Figure 5.9-3 as an example, and the other plots are in Appendix I.

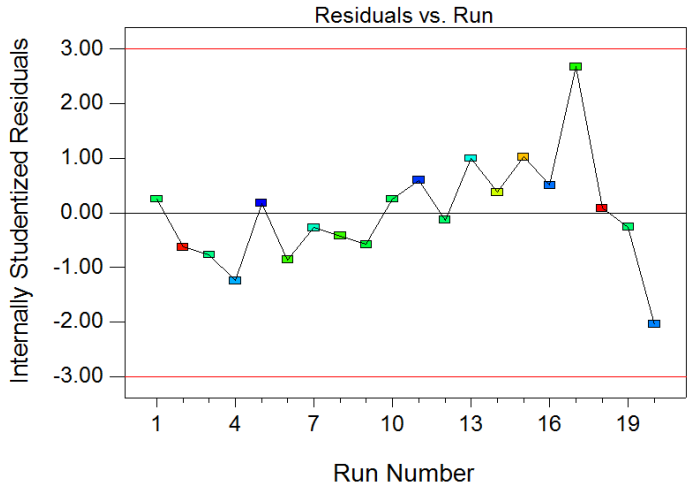

Figure 5.9-3 Plot of residuals versus run order for the response of melt pressure (single screw extrusion experiment)

Clearly, the plot of residuals versus run order shows no clear pattern, indicating that the independence assumption for the observations in the single screw extrusion experiment was also acceptable.

c) Equal variance assumption

The assumption of equal variance at each factor level can be checked by plotting residuals against the factor levels and comparing the spread in the residuals. The variability in the residuals should not depend in any way on the factor levels.[252] If a pattern appears in the plots, it usually suggests data transformation so that the data need to be analysed in a different metric. Figure 5.9-4 shows a typical plot of residuals versus factor levels in the single screw extrusion experiment, and the other plots are shown in Appendix I.

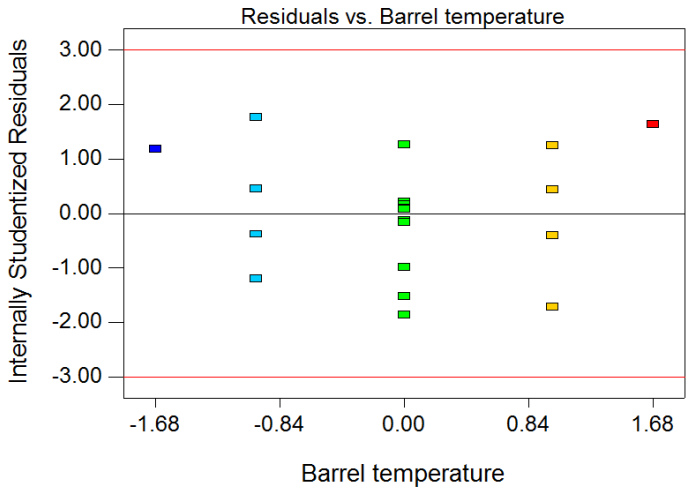

Figure 5.9-4 Plot of residuals versus barrel temperature level for the response of mass output (single screw extrusion experiment)

For a central composite design (CCD), it is known that the factors are varied in five levels: ± alpha (axial points), ± 1 (factorial points) and the centre point (0,0). Therefore, five factor levels for screw speed can be found clearly in Figure 5.9-4, and there 2 points at ± $\sqrt{3}$ (alpha) levels, 8 points at ± 1 levels and 10 points at 0 level. Each point in the graph represents an experimental run. As there is only one point at –alpha level and +alpha level, the variance in residuals at the ± alpha levels cannot be compared to that at the other levels. Comparing the variance of the residuals at ±1 and 0 levels, it is very clear that the spread of residuals at the three different levels are very similar, which strongly suggests equal variance at each factor level. The plots of residuals against factor levels have checked for the other responses and factors of the single screw extrusion study. The resulting plots suggest that there was no problem with the assumption of equal variance.

The assumptions of normality, independence and equal variance have been checked for all the three DoE studies to confirm that the ANOVA was valid when used to calculate F-ratios or p-values and simplify the predictive models. The relevant plots of residuals are shown in Appendix I.

5.9.2 Thoughts on Experimental Errors and Uncertainties

a) Experimental errors

In a typical central composite design (CCD), a single replicate or observation is performed for each experiment run. For instance, in a typical CCD with 2 factors as shown in Figure 5.9-5, there are four axial points, four factorial points and 1 centre point. When constructing the design matrix, there will be four axial runs, four factorial runs but several centre runs (at least 1). As only a single replicate is required for the CCD, only one resulting data can be typed back into the design matrix for each experimental run. Thus, the variance in observations can only be estimated by the several centre runs. In other words, the variance in observations is not evaluated for each factor level at all. To a greater or lesser extent, this may cause some experimental errors, although it has been assumed that the observations are normally and independently distributed with the same variance in each factor level when applying ANOVA.

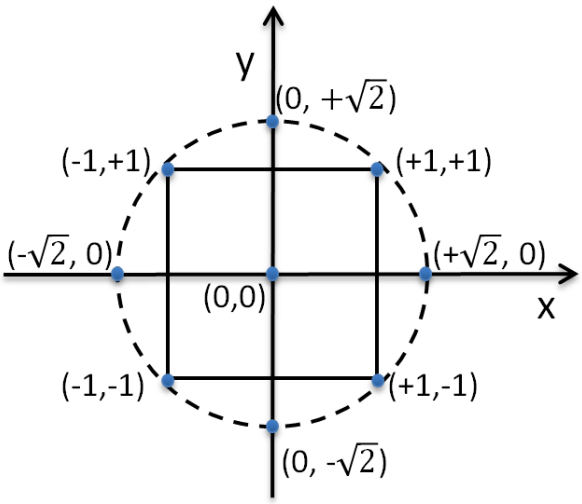

Figure 5.9-5 Central composite design with 2 factors

For techniques that are fairly accurate and precise, such X-ray diffraction (XRD), differential scanning calorimetry (DSC) *etc.*, a single observation is usually performed and there is thus only one resulting data generated for each experimental run. Hence, the resultant data from those tests can be conveniently entered into the design matrix for each experimental run, as only a single replicate is required by CCD. Its variability is evaluated by a few centre-point runs. On the other hand, mechanical testing, such as tensile and impact tests, possesses relatively large

inherent levels of variability. A single observation is obviously not suitable for such tests. To overcome high variability, quite a few observations are performed in order to get the average values first. Then the average data are entered into the design matrix for each experimental run. Again, the variance is estimated by several centre-point runs, but it should be noted that the data for each centre run is also the average of the observations. In other words, the variance might be underestimated as it is based on the averages. Therefore, it is very likely that the difference in the number of observations for different responses might be another source of experimental error, and tests with high variability might not be suitable for CCD.

Good examples are the DoE studies of optimum formulation and processing conditions (sections 5.3 and 5.4), in which interlayer spacing d_{001} derived from XRD patterns and tensile properties were the responses. A single observation is performed for the XRD test, while at least 8 replicates were carried out for each experimental run to get the average data during tensile tests. As mentioned above, the variance in tensile tests might be underestimated, and it is likely that this resulted in overestimates of the effects of factors on the tensile properties. Furthermore, the response, interlayer spacing, d_{001}, was also related to the other responses, tensile properties. The variance in the d_{001} values was estimated normally while that of the tensile properties was not. Therefore, it is very likely the accuracy of the final predictive models were affected to some extent.

The type of data might be another source of experimental errors. In the DoE experiment of single screw extrusion, melt pressure at the end of the metering zone (ΔP), screw torque (M), mass output ($\dot{m}$) and the temperature difference between the die and the melt (ΔT) were the responses. Melt pressure (ΔP) and screw torque (M) were monitored continuously on the extruder. The nearest whole numbers were taken as the resulting values for experimental runs, as some slight fluctuations were evident. Some errors could be introduced during this process and might have some negative influence on the accuracy of DoE analysis. Mass output rate ($\dot{m}$) was measured by weighing the collected extrudates (for 1-minute time increments), while the temperature difference between the die and the melt (ΔT) was measured by an infrared thermometer. Three observations were performed for both ($\dot{m}$) and (ΔT), and the average data were typed into the design matrix. Therefore, the data for previous

two responses were approximations, whilst for the latter two responses were averaged numbers. The difference in data type implies that errors could be generated especially when comparing the effects of those factors on the different responses.

b) Uncertainties

The significance level (α) is of great importance, as it determines if a factor is significant or not by comparing the calculated p-values with the selected significance level (α). Normally, the significance level is set as 0.05, which was used throughout the DoE experiments in this project. In these DoE studies, the full second order regression model for each response was simplified by removing the negligible terms with p-values greater than 0.10. On the other hand, the terms with p-values lower than 0.05 were considered as important and kept in the models. However, some uncertainties are generated when the terms had p-values between 0.05 and 0.10, as these terms could be either significant or insignificant. In other words, the decisions on whether the terms with p-values between 0.05 and 0.01 should be kept or removed are quite arbitrary. Apparently, these decisions made by the experimenters have direct effects on the final predictive models and the thus results of experiments.

The DoE experiment on optimum compounding conditions is a good example (section 5.4.1). When investigating the effect on the response of interlayer spacing of clay in the PPCNs prepared by APV twin screw extrusion, there seemed to be no significant terms at first. However, after removing the other insignificant terms, the p-value of term B dropped from 0.1398 to 0.0671, which was considered as barely significant (between 0.05 and 0.1) and kept in the model. Therefore, the final predictive equation becomes:

$$d_{001}(APV) = 4.02 + 0.15B \tag{5.4-1}$$

Clearly, the above equation suggests that factor B is significant and the interlayer spacing d_{001} changes as term B changes. However, if term B was considered as barely insignificant and removed from the model, then the model would show a constant value of interlayer spacing d_{001}. If so, the experiment result might be

changed a little bit. Therefore, the presence of uncertainty as such, has direct effects on the accuracy of predictive model and the final result of the DoE experiment.

5.9.3 Summary

Design of Experiments (DoE) is a powerful statistical tool especially when dealing with multi-factor systems. In this section, Design of Experiments (DoE) approach has been discussed on the basis of the three DoE-structured experiments in this research project. The assumptions of normality, independence and equal variance that are required by ANOVA have been checked for the DoE studies, in order to make sure that the use of ANOVA was valid for those experiments.

Some thoughts regarding the experimental errors and uncertainties of the DoE approach have been discussed. Due to the fact that a single replicate is required for a central composite design (CCD), the variance in observations can only be evaluated by the few centre runs. A single observation may be very suitable for those tests that are very precise and have very limited variability, such as XRD or DSC. For the tensile tests which have greater variability, the variance is very likely to be underestimated with the centre runs. For instance, in the DoE experiments in this project, the averaged tensile properties of 8 observations were input to the design matrix for each experimental run. As the centre runs had averaged values, the actual variance was very likely to be underestimated. As a result, the effects of factors might be overestimated, in turn. Uncertainties can be generated when the terms in the predictive model have p-values between 0.05 and 0.10, because they can be either significant or insignificant. This depends on arbitrary decisions taken by the experimental team, and has large effects on the resulting predictive models and experiment results.

CHAPTER 6: CONCLUSIONS AND FUTURE WORK

In this research project, optimum formulations for PP/clay nanocomposites (PPCNs) and compounding conditions were investigated with the aid of a powerful statistical tool, Design of Experiments (DoE). The outcomes from the DoE were then applied to investigate thin-wall injection moulding of PPCNs, where the emphasis was placed on the effects of moulding conditions, clay concentration and wall thickness on the injection moulded parts. To perform the thin-wall injection moulding, a four-cavity injection moulding system was designed using CAD software and a new moulding tool was constructed based upon this design, accommodating cooling channels, ejection systems and facilities for in-cavity pressure measurement. Real-time simulation of the injection moulding process was also carried out using Autodesk Moldflow® software package, to compare the predicted performance with that obtained in practice by the in-cavity pressure sensor.

Tensile tests and falling weight impact tests (FWIT) were performed to study the mechanical properties of the PPCN samples. The crystallinity was examined using differential scanning calorimetry (DSC), and the intercalation behaviour of clay particles was analysed using X-ray diffraction (XRD) and transmission electron microscopy (TEM). The fracture surfaces of moulded PPCN parts were examined using scanning electron microscopy (SEM). Optical microscopy (OM) was employed to investigate the internal morphological skin-core structure of the thin-wall injection moulded PPCNs. All the pre-set objectives for this research programme have been completed successfully, and the main conclusions can be drawn as in the following sections.

6.1 Conclusions

a) Single screw extrusion of PP blends

To develop a good understanding of DoE and the underlying statistical principles in a polymer processing context, single screw extrusion dynamics were investigated first using a DoE approach. The variables (factors) studied were barrel temperature, rotational screw speed and the concentration of a low viscosity recycled component

in a PP blend system. The measured responses for the steady-state process operation included melt pressure, mass output, screw torque and the temperature rise at the die.

It was found that within the experimental ranges of the three chosen factors, the content of recycled PP (hence shear viscosity of the blends) had the highest effect on melt pressure and screw torque. Consistent with the trends that can be derived from extrusion theory, screw speed was found to be a predominant factor for the extruder output rate. Overall, the respective effects of the variables examined on mass output were made more complex by two-factor interactions, which were proved to be statistically significant. The simple linear regression model obtained for die temperature rise implies that screw speed and recycled PP content are the most significant factors, having quantitatively similar but opposite effects.

This study of single screw extrusion demonstrated that the DoE is a powerful tool, making it possible to make accurately predict the process dynamics of single screw extrusion. A similar approach was therefore deemed to be feasible for the studies of optimising PPCN formulation and compounding conditions of PPCNs.

b) Optimum formulation of PPCNs

To optimise the formulation of PPCNs, levels of: organoclay (DK4), a functional compatibiliser (PPgMA) and co-intercalant (erucamide) were selected as the formulation variables in the DoE experiments. The responses were the basal spacing of clay platelets (d_{001}) from XRD and subsequent mechanical properties (tensile modulus and yield strength).

According to the resulting data and predictive regression models generated by the DoE approach, the initial optimum formulation was determined to be: 4 wt% DK4, 4 wt% PPgMA and 1 wt% erucamide. As the maximum interlayer spacing was set as the main criterion to assess the degree of intercalation, the optimum formulation was then slightly adjusted to 4 wt% DK4, 4 wt% PPgMA and 1.5 wt% erucamide. The PPCNs used in all subsequent studies of compounding and thin-wall injection moulding were on the basis of this experimentally determined optimum formulation.

c) Optimum compounding conditions for PPCNs

Both large scale mixing (twin-screw extrusion) and small scale mixing (twin rotor batch-mixing) were investigated using a DoE approach. Feed rate and screw speed were selected as the factors for the continuous twin screw extrusion process, whilst mixing time and rotor speed were selected for the twin rotor batch-mixing. The compounded PPCNs were then compression moulded into flat sheets to cut samples for XRD analysis and tensile testing. Interlayer spacing of clay, d_{001}, tensile modulus and yield strength were selected as the responses for both processing methods.

The important results are briefly summarised and the two mixing processes are compared in Table 6.1-1.

Table 6.1-1 Summaries and comparison of the two compounding methods

	Twin screw extrusion	Twin rotor batch-mixing
Shear rate	• Extreme • Controlled by screw speed and feed rate for a given screw design	• Medium • Controlled by rotor speed
Residence time	• Controlled by screw speed and feed rate • Less important than shear rate to the dispersion of clay	• Controlled by mixing time • Showed no effect on clay dispersion and tensile properties
Intercalation	• Lower • Increased with increasing screw speed	• Higher • Decreased with increasing rotor speed
Exfoliation	• Higher • Due to the extreme shear conditions	• Lower • Due to the medium shear conditions
Aspect ratio	• Lower • Fragmented by extreme shear rate	• Higher • Less loss under medium shear rate
Tensile modulus	• Lower • Due to reduced aspect ratio and chain scission • Decrease with increasing screw speed	• Higher • Due to higher aspect ratio • Constant
Yield strength	• Higher • Due to higher level of exfoliation • Increase with increasing feed rate	• Lower • Due to lower level of exfoliation • Constant

Optimisation was only considered for the twin screw extruder, as it would then be used to produce a large amount of PPCN compounds for the subsequent study of

thin-wall injection moulding. The results suggest that the lowest screw speed (159 rpm) and highest feed rate (5.4 kg h^{-1}) are the optimum compounding conditions to prepare PPCN compounds by melt-state mixing, although the maximum basal spacing (d_{001}) for clay is not achieved under such conditions. However, the optimised conditions are only for the twin screw extruder with existing screw design, used to manufacture the PPCN pellets.

d) Effects of processing conditions on moulded PPCN parts

Melt temperature was not considered as a variable for thin-wall injection moulding of PPCNs, considering the possible degradation of organoclay at a high temperature. The effects of injection speed and mould temperature were therefore investigated as primary variables.

Within the selected processing window, tensile modulus and yield strength of thin wall injection moulded PPCN parts increase significantly with decreasing injection speed, which is in good agreement with the reported studies on injection moulding of PP or filled PP.[27,196,208] This is highly likely to be due to the significant increase in the highly oriented frozen layer fraction, which is stiffer and stronger in the flow direction than the core.[196] The spherulitic core and oriented non-spherulitic skin (frozen layer) can be observed in the OM images, and very fine spherulites can be seen in the core region. The thickness of the highly oriented, non-spherulitic skin of the thin-wall injection moulded PP nanocomposites increases significantly with decreasing injection speed. Due to the low thickness, the values of skin fraction are very high (up to 75 %) in the thin wall injection moulded parts. DSC and XRD results show that moulding conditions have a very limited influence on the crystallinity of the injection moulded parts and the intercalation of clay particles, and they are unlikely to make any distinctive changes to the tensile properties. Strong orientation of clay particles in the flow direction can be observed in the TEM images for all samples, which is in good agreement with the greatly enhanced peak intensity of XRD patterns. Therefore, it is proposed that the great enhancement in tensile properties with decreasing injection moulding is mainly attributed to a thicker skin, which is simultaneously more oriented and crystalline according to the reported studies.[27,202] In comparison to injection speed, mould temperature has very limited effect on the

properties of thin wall injection moulded PPCNs, indicating that injection speed is most influential in the selected processing window of this study.

Additionally, the injection moulded PPCN parts show improvement in tensile properties, in comparison to the virgin PP parts. The enhancement is up to about 14 % for tensile modulus and 8 % for yield strength. Besides, the thin-wall injection moulded PPCN parts are much stronger and stiffer parallel to the flow direction in which the molecular chains and particles are oriented. From the flow direction to transverse direction, the tensile modulus of PPCNC samples decreases by 36.4 % and yield strength decreases by 13.6 %. Therefore, the particle and molecular orientation has a great effect on the tensile properties of thin-wall injection moulded PPCNs.

The FWIT results show that the impact toughness of the thin-wall injection moulded PPCNs is very consistent, and is not distinctly affected by the changes in moulding conditions.

e) Effects of clay concentration on moulded PPCN parts

The properties of thin wall injection moulded PPCN parts with different clay concentrations were investigated. The FWIT and DSC results imply that the clay concentration has a very limited effect on both impact toughness and crystallinity, in the selected range of 1-5 wt% of clay. The SEM images confirm that there is no clear difference between the fracture surfaces of PPCN samples with different clay concentrations. The TEM images and XRD patterns suggest that higher intercalation but lower exfoliation is achieved in PPCN parts with higher clay content and vice versa. The OM images show a slightly thicker skin with increasing clay concentration, due to the increased thermal conductivity of the composites promoting more rapid cooling.

Overall, it is clear that the improvement in tensile modulus and strength by the addition of nanoclay, is not at the expense of toughness, which implies an improved balance of mechanical properties in the PPCN parts.

f) Effects of wall thickness on moulded PPCN parts

The properties of the thin and thicker sections of injection moulded PPCN parts were also explored and compared. The experimental results suggest that the thin sections (at the end of flow) have significantly higher tensile modulus and yield strength compared to the thick sections. According to the TEM and OM images, this is most likely attributed to the enhanced orientation of clay particles and more highly oriented skin in the thin section.

According to the DSC results, a negligible difference in crystallinity was observed between the thin and thick sections, which is unlikely to make any observable change to the tensile properties. Interestingly, reduction in interlayer spacing of clay was observed in the thin sections, and a possible reason is now proposed: the PP chains in the clay galleries were stretched and oriented to a higher level in the thin sections, due to the more intensive shear conditions. Compaction of clay stacks occurred, as less interspace is needed to accommodate those stretched chains, resulting in reduced interlayer spacing. Rapid cooling of the skin layer then allows less time for the chains to relax and expand the galleries back again.

g) Actual injection moulding vs. real-time simulation

Comparisons were made between the data obtained from real-time actual injection moulding and flow simulation, and specific emphasis was placed on in-cavity pressure, frozen layer fraction, bulk shear rate and bulk temperature.

The comparative data for in-cavity pressure show good consistency for the mould filling stage, however significant deviations are apparent over the remainder of the injection moulding cycle. The discrepancy is attributed to the mould opening slightly during mould filling, as the required clamp force exceeded the capacity of the machine. Good consistency was also obtained for the frozen layer fraction data, confirming that frozen layer fraction decreases with increasing injection speed and mould temperature. Bulk shear rate from the simulation process and the estimated shear rate data for the actual moulding process show very similar trends whereby shear rate increases with injection speed and remains almost constant with changes

in mould temperature. Bulk temperature, which estimates the local thermal level that the frozen layer depends on, is in good agreement with frozen layer fraction.

Overall, after combing the results from the actual injection moulding and simulations, it is very clear that injection speed is of utmost importance to the thin-wall injection moulding process and thus the properties of the moulded PPCN parts, in the selected experimental ranges of this research. In comparison, the effects of mould temperature are much less significant.

h) Summary

On the basis of the results obtained in this research project, some recommendations for formulation, mixing and moulding of PP/clay nanocomposites can be given.

The optimum formulation obtained in this study is 4 wt% DK4 nanoclay, 4 wt% PPgMA compatibiliser and 1.5 wt% erucamide, based on the PP-H (Sabic571P) material. When the base PP is changed, the optimum formulation may also change. For example, it is found that the PP nanocomposites based on PP-C (Sabic PHC26) with the same formulation always have much higher basal spacing (d_{001}) than those nanocomposites based on PP-H, which implies that the optimum formulation may be different with PP-C (copolymer) material. Thus, it should be borne in mind that any change to the materials may lead to a different optimum formulation of the PPCNs. Also, it may be necessary to keep PPgMA and erucamide at a low concentration level, as they can potentially plasticise the PP matrix reducing stiffness and strength, and erucamide may induce wall slip during processing.[11]

Mixing is a critical stage to achieve intercalation/exfoliation of clay. The results indicate that there are different requirements to achieve the optimum intercalation/exfoliation and thus resulting tensile modulus and yield strength. Extremely high shear rate in the twin screw extruder gives higher exfoliation and lower intercalation, but the moderate shear rate in the twin rotor mixer leads to higher intercalation and lower exfoliation. The PPCNs prepared by the twin screw extruder are stronger, while those prepared by the twin rotor mixer are stiffer but weaker. Therefore, this implies that the selection of mixing conditions (extreme or

moderate shear conditions) can be made according to the requirements for the target properties of moulded parts.

So far, very little research has reported on thin wall injection mould of PPCNs. The preliminary results in this study suggest that the orientation of clay particles and skin fraction have significant effects on the tensile properties of thin wall injection moulded PPCN parts, while their impact toughness are stable and not compromised. Therefore, either enhancing the orientation of clay particles in the specific direction or increasing the skin fraction is an effective way to improve the tensile properties, and this can be achieved by simply lowering injection speed or increasing injection time.

6.2 Future Work

The research reported in this thesis has investigated compounding and thin-wall injection moulding of PP/clay nanocomposites, a promising class of materials that have great potential to be widely used in many industry sectors. Although this thesis has highlighted a number of topics, on which further research would be beneficial, opportunities for expanding the scope of this research still remain. Thus, some suggestions for future work are made in this section.

a) Different materials

There are many types of nanoclay with different surface modification, and it is well known that the surface treatment of clay can significantly affect its dispersion in the PP matrix and thus the properties of PPCNs obtained. As only one organoclay was involved in this thesis, it seems worth investigating some other types of nanoclay. DK4 clay used in this study which is modified with dimethyl dehydrogenated tallow ammonium chloride. According to the literature review, clay modified with long chain amine such as 1,12 diaminoduodecane can also achieve highly exfoliated/intercalated nanocomposites.[108] Similarly, it may also be useful to formulate with some other types of compatibilisers and co-intercalants, which are also important factors for clay dispersion. For example, glycidyl methacrylate grafted

PP (PP-g-GMA) is another effective compatibiliser for PP/clay system.[121] In addition to AM, dibenzoyl peroxide (BPO) and N-imidazol-O-(bicyclo pentaerythritol phosphate)-O-(ethyl methacrylate) phosphate (PEBI) have been used as co-intercalants. [107,125]

Both the PP-H and PP-C materials used in this research are injection moulding grades. Other grades of PP materials, for example high viscosity extrusion grade PP, have different rheological properties and will show differences during compounding and processes.

It is highly likely that use of different materials will cause changes to the dispersion of clay in the continuous PP, the optimum PPCN formulation as well as the optimum processing conditions. It is thus considered to be helpful to investigate different materials, to further expand this work.

b) Thin-wall injection moulding under more extreme conditions

The effects of wall-thickness have been discussed in section 5.7. Clearly, the extreme shear conditions and rapid cooling in the thin sections lead to significantly improved tensile modulus and yield strength. The current wall thicknesses of moulded parts are 1.2 mm and 2.7 mm, for thin and thick sections respectively. There is a possibility to make even thinner injection moulded parts, to investigate thin-wall injection moulding under more extreme conditions, as relevant to packaging etc.

On the basis of the existing mould tool, wall thickness can be further reduced to create more extreme shear and cooling conditions, by fitting suitable steel shim into the cavities. Furthermore, different wall thicknesses can be achieved by using shim with different thickness, which can thus generate more useful data to further expand the study on the effects of wall thickness on moulded PPCN parts.

c) Micro injection moulding (MIM)

In recent years, there is an increasing trend towards product miniaturisation, as components and products in micro scale are of increasing importance in many fields like communication, IT, automotive, medical sectors *etc.* Micro injection moulding (MIM) is one of the key technologies for micro manufacturing for its capability of mass production and relatively low production cost. A wide range of micro components, such as micro pumps, micro gears and micro filters, can be produced by MIM in large quantities. Normally, a product manufactured by MIM is only few milligrams in weight and exhibits dimensions with tolerances in the micrometric range. For examples, the injection moulded plastic hinges have a thickness 0.3 to 0.5 mm only. Very likely, the shear and cooling conditions in MIM are even much more extreme than those in the thin-wall injection moulding studied in this thesis.

PPCNs are a promising class of materials, and it is very likely that there will be huge demands for micro PPCN components in the future. Therefore, MIM of PPCNs is worth studying in the future.

d) Other important properties

The thesis puts the emphasis on the mechanical properties of PPCNs, specifically tensile modulus, yield strength and impact toughness. The reason is that the targeted applications of the selected PP materials and their resulting PPCNs are interior and exterior automotive components.

According to the literature review, not only the mechanical properties but also other physical properties will be enhanced or influenced by the addition of nanoclay to form PPCNs. For applications other than automotive components, such as packaging, it is very likely that barrier properties to gas and water are more important than mechanical properties. Therefore, if other important properties of PPCNs are considered and used as criteria, the optimum formulation and compounding conditions may be very different from those obtained in the thesis. This would be very helpful to expand the scope of the research.

e) Other melt-processing techniques

It has been about 20 years since the pioneering work on fabrication of PP/clay nanocomposites was first reported.[66] PPCNs have been widely studied for their enormous potential to be used in many industrial sectors such as the automotive and packaging industries, for their excellent processibility, low cost and potential enhance to physical and chemical properties relative to the conventional unfilled PP materials.

Generally, PPCNs can be fabricated by in-situ polymerisation, solvent methods and by melt compounding. Among the three methods, melt compounding is significantly more economic and simpler than in-situ polymerisation, and more environmentally friendly and less expensive than solvent methods, as no solvents are required. Therefore, melt processing is most suitable for manufacturing PPCNs in industry. So far, limited research work has been reported on the melt processing of PPCNs even with the most common industry scale equipment such as twin screw extruders and injection moulding machines. That might be the one of the reasons that PPCNs have not been widely used in industry to date.

To lead a step-change in the use of PPCNs in industry, it would be worth expanding the research on melt-processing of PPCNs. Therefore, in addition to extrusion and injection moulding, the other melt-processing techniques commonly used for thermoplastics, such as blow moulding, thermo-forming etc., can be thoroughly studied for PPCNs.

References

1. Fu, T., Haworth, B. & Mascia, L. Analysis of process parameters related to the single-screw extrusion of recycled polypropylene blends by using design of experiments. *J. Plast. Film Sheeting* (2016). doi:10.1177/8756087916649006

2. Plastics Eruope. Plastics - the Facts 2016. (2016). Available at: http://www.plasticseurope.org/.

3. Hindle, C. Polypropylene. *British Plastics Federation* (2016). Available at: http://www.bpf.co.uk/plastipedia/polymers/PP.aspx.

4. ReportsWeb. *Global Polypropylene Industry 2015 Market Research Report*. (2015).

5. Reichert, P., Klinke, S., Brandsch, R., Thomann, R. & Mu, R. Poly (propylene)/ organoclay nanocomposite formation : Influence of compatibilizer functionality and organoclay modification. *Macromol. Mater. Eng.* **17,** 8–17 (2000).

6. Dias, M. L., Fernandes, R. M., Cunha, R. H., Jaconis, S. & Silvino, A. C. Highly filled clay polypropylene nanocomposites prepared by in situ polymerization with clay-supported magnesium/titanium catalysts. *Appl. Catal. A Gen.* **403,** 48–57 (2011).

7. Bagheri-Kazemabad, Sedigheh., Fox, Daniel., Chen, Yanhui., Geever, Luke M., Khavandi, Alireza., Bagheri, Reza., Higginbotham, Clement L., Zhang, Hongzhou. & Chen, B. Morphology, rheology and mechanical properties of polypropylene/ethylene–octene copolymer/clay nanocomposites: Effects of the compatibilizer. *Compos. Sci. Technol.* **72,** 1697–1704 (2012).

8. Shroff Rama, M., Neppalli, R., Chellaswamy, R. & Swaminathan, S. Exfoliation of clay layers in polypropylene matrix using potassium succinate-g-polypropylene as compatibilizer. *Compos. Sci. Technol.* **70,** 1550–1556 (2010).

9. Seyidoglu, T. & Yilmazer, U. Modification and characterization of bentonite with quaternary ammonium and phosphonium salts and its use in polypropylene nanocomposites. *J. Thermoplast. Compos. Mater.* **28,** 86–110

(2015).

10. Peng, P., Yang, Z., Wu, M., Zhang, Q. & Chen, G. Effect of montmorillonoite modification and maleic anhydride-grafted polypropylene on the microstructure and mechanical properties of polypropylene/montmorillonoite nanocomposites. *J. Appl. Polym. Sci.* n/a-n/a (2013). doi:10.1002/app.39653

11. Ratnayake, U. N., Haworth, B. & Hourston, D. J. Preparation of polypropylene-clay nanocomposites by the co-intercalation of modified polypropylene and short-chain amide molecules. *J. Appl. Polym. Sci.* **112,** 320–334 (2009).

12. Ratnayake, U. N. & Haworth, B. Polypropylene–clay nanocomposites: Influence of low molecular weight polar additives on intercalation and exfoliation behavior. *Polym. Eng. Sci.* **46,** 1008–1015 (2006).

13. Dong, Y. & Bhattacharyya, D. Investigation on the competing effects of clay dispersion and matrix plasticisation for polypropylene/clay nanocomposites. Part II: crystalline structure and thermo-mechanical behaviour. *J. Mater. Sci.* **47,** 4127–4137 (2012).

14. Dong, Y. & Bhattacharyya, D. Investigation on the competing effects of clay dispersion and matrix plasticisation for polypropylene/clay nanocomposites. Part I: morphology and mechanical properties. *J. Mater. Sci.* **47,** 3900–3912 (2012).

15. Furlan, L.G., Ferreira, C.I., Dal Castel, C., Santos, K.S., Mello, A.C.E., Liberman, S.a., Oviedo, M.a.S. & Mauler, R. S. Effect of processing conditions on the mechanical and thermal properties of high-impact polypropylene nanocomposites. *Mater. Sci. Eng. A* **528,** 6715–6718 (2011).

16. Jiang, G. & Huang, H. Melt-compounding of PP/clay nanocomposite and relationship between its microstructure and shear strain in the flow field based on rheological analysis. *Polym. Eng. Sci.* **51,** 2345–2352 (2011).

17. Barbas, J. M., Machado, A. V. & Covas, J. a. Processing Conditions Effect on Dispersion Evolution in a Twin-Screw Extruder: Polypropylene-Clay Nanocomposites. *Chem. Eng. Technol.* **37,** 257–266 (2014).

18. Rousseaux, D. D. J., Sclavons, M., Godard, P. & Marchand-Brynaert, J. Polypropylene/clay nanocomposites: An innovative one-pot process. *Polym. Compos.* **36,** 644–650 (2015).

19. Heynderickx, I. & Paridaans, F. Influence of processing conditions on the anisotropy in injection-moulded thermotropic LCPs. *Polymer (Guildf).* **34,** 4068–4074 (1993).

20. Mendoza, R., Régnier, G., Seiler, W. & Lebrun, J. L. Spatial distribution of molecular orientation in injection molded iPP: influence of processing conditions. *Polymer (Guildf).* **44,** 3363–3373 (2003).

21. Hsiung, C. M. A structure oriented model to simulate the shear induced crystallization in injection moulded polymers : a Lagrangian approach. *Polymer (Guildf).* **37,** 4555–4571 (1996).

22. Friesenbichler, W., Langecker, G. R. & Duretek, I. Polymer melt rheology at high shear rates using a new micro-rheology technique. in *Proceedings of the Polymer Processing Society 21st Annual Meeting* 87 (2005).

23. Kelly, A. L., Gough, T., Whiteside, B. R. & Coates, P. D. High shear strain rate rheometry of polymer melts. *J. Appl. Polym. Sci.* **114,** 864–873 (2009).

24. Moon, J.-S., Lee, J.-M., Lee, S.-H. & Choi, B.-H. Effect of process conditions on the dart impact properties of thin-wall injection-molded polycarbonate plates. *J. Appl. Polym. Sci.* **127,** 1466–1474 (2013).

25. Mnekbi, C., Vincent, M. & Agassant, J. F. Polymer behavior and mold filling of thin wall cavities. in *Proceedings of the Polymer Processing Society 29th Annual Meeting* 4–7 (2013).

26. Costantino, a., Pettarin, V., Viana, J., Pontes, A., Pouzada, A. & Frontini, P. Microstructure of PP/clay Nanocomposites Produced by Shear Induced Injection Moulding. *Procedia Mater. Sci.* **1,** 34–43 (2012).

27. Barbosa, C. N., Simoes, R., Franzen, M. & Viana, J. C. Thermomechanical environment characterisation in injection moulding and its relation to the mechanical properties of talc-filled polypropylene. *J. Mater. Sci.* **48,** 2597–

2607 (2013).

28. Barbosa, C. N., Carvalho, F., Viana, J. C., Franzen, M. & Simoes, R. Impact performance prediction of injection-molded talc-filled polypropylene through thermomechanical environment assessment. *Int. J. Adv. Manuf. Technol.* **77,** 873–883 (2014).

29. Costantino, Alejandra., Pettarin, Valeria., Viana, Júlio., Pontes, António., Pouzada, António. & Frontini, P. Morphology−performance relationship of polypropylene−nanoclay composites processed by shear controlled injection moulding. *Polym. Int.* **62,** 1589–1599 (2013).

30. Chaudhary, A. K. & Jayaraman, K. Extrusion of linear polypropylene-clay nanocomposite foams. *Polym. Eng. Sci.* **51,** 1749–1756 (2011).

31. Oh, K., Seo, Y. P. & Seo, Y. Study of PP/clay nanocomposites prepared by supercritical fluid foaming. in *18th International Conference on Composite Materials* (2011).

32. Montgomery, D. *Introduction to Statistical Quality Control*. (John Wiley & Sons, Inc, 2009).

33. Cui, Y., Kumar, S., Rao Kona, B. & van Houcke, D. Gas barrier properties of polymer/clay nanocomposites. *RSC Adv.* **5,** 63669–63690 (2015).

34. Liu, X., Zheng, Y. & Wang, X. Controllable Preparation of Polyaniline-Graphene Nanocomposites using Functionalized Graphene for Supercapacitor Electrodes. *Chemistry* **21,** 10408–15 (2015).

35. Wei, J., Vo, T. & Inam, F. Epoxy/graphene nanocomposites – processing and properties: a review. *RSC Adv.* **5,** 73510–73524 (2015).

36. Chee, W. K., Lim, H. N., Huang, N. M. & Harrison, I. Nanocomposites of graphene/polymers: a review. *RSC Adv.* **5,** 68014–68051 (2015).

37. Khalaj, M.-J., Ahmadi, H., Lesankhosh, R. & Khalaj, G. Study of physical and mechanical properties of polypropylene nanocomposites for food packaging application: Nano-clay modified with iron nanoparticles. *Trends Food Sci. Technol.* **51,** 41–48 (2016).

38. Tamayo, L., Azócar, M., Kogan, M., Riveros, A. & Páez, M. Copper-polymer nanocomposites: An excellent and cost-effective biocide for use on antibacterial surfaces. *Mater. Sci. Eng. C. Mater. Biol. Appl.* **69,** 1391–409 (2016).

39. Marouf, B. T., Mai, Y.-W., Bagheri, R. & Pearson, R. a. Toughening of Epoxy Nanocomposites: Nano and Hybrid Effects. *Polym. Rev.* **56,** 70–112 (2016).

40. de Leon, Al C., Chen, Qiyi., Palaganas, Napolabel B., Palaganas, Jerome O., Manapat, Jill. & Advincula, R. C. High performance polymer nanocomposites for additive manufacturing applications. *React. Funct. Polym.* **103,** 141–155 (2016).

41. Park, S., He, S., Wang, J., Stein, A. & Macosko, C. W. Graphene-polyethylene nanocomposites: Effect of graphene functionalization. *Polymer (Guildf).* **104,** 1–9 (2016).

42. Kojima, Yoshitsugu., Usuki, Arimitsu., Kawasumi, Masaya., Okada, Akane. & Fukushima, Y. Mechanical properties of nylon 6-clay hybrid. *J. Mater. Res.* **8,** 1185–1189 (1993).

43. Usuki, Arimitsu., Kojima, Yoshitsugu., Kawasumi, Masaya., Okada, Akane., Fukushima, Yoshiaki., Kurauchi, T. & & Kamigaito, O. Synthesis of nylon 6-clay hybrid. *J. Mater. Res.* **8,** 1179–1184 (1993).

44. Nunes, Mário a.B.S., Galvão, Luciana S., Ferreira, Thiago P.M., Luiz, Emerson J.F.T., Bastos, Y. L. M. & & Santos, A. S. F. Reprocessability of high impact polystyrene/clay nanocomposites in extrusion. *Polym. Degrad. Stab.* **125,** 87–96 (2016).

45. Gajjela, S., Ramachandran, V. & Somasekharan, J. Influence of interphase material and clay particle shape on the effective properties of epoxy-clay nanocomposites. *Compos. Part B Eng.* **88,** 11–18 (2016).

46. Wang, M., Fan, X., Thitsartarn, W. & He, C. Rheological and mechanical properties of epoxy/clay nanocomposites with enhanced tensile and fracture toughnesses. *Polymer (Guildf).* **58,** 43–52 (2015).

47. Peng, S. & Iroh, J. O. Synthesis and characterization of crosslinked polyurethane/clay nanocomposites. *J. Appl. Polym. Sci.* **133,** (2016).

48. George, S. C., Rajan, R., Aprem, A. S., Thomas, S. & Kim, S. S. The fabrication and properties of natural rubber-clay nanocomposites. *Polym. Test.* **51,** 165–173 (2016).

49. Luduena, L., Stocchi, A. & Alvarez, V. Fracture behavior of polycaprolactone/clay nanocomposites. *J. Compos. Mater.* **50,** 3863–3872 (2016).

50. Mistretta, M. C., Morreale, M. & La Mantia, F. P. Thermomechanical degradation of polyethylene/polyamide 6 blend-clay nanocomposites. *Polym. Degrad. Stab.* **99,** 61–67 (2014).

51. Filippone, G., Carroccio, S.C., Curcuruto, G., Passaglia, E., Gambarotti, C. & Dintcheva, N. T. Time-resolved rheology as a tool to monitor the progress of polymer degradation in the melt state – Part II: Thermal and thermo-oxidative degradation of polyamide 11/organo-clay nanocomposites. *Polymer (Guildf).* **73,** 102–110 (2015).

52. Ebrahimi Jahromi, Ali., Ebrahimi Jahromi, Hamid Reza., Hemmati, F., Saeb, Mohammad Reza., Goodarzi, V. & & Formela, K. Morphology and mechanical properties of polyamide/clay nanocomposites toughened with NBR/NBR-g-GMA: A comparative study. *Compos. Part B Eng.* **90,** 478–484 (2016).

53. Vorsina, I. a., Grigor'eva, T. F., Udalova, T. a., Vosmerikov, S. V. & Lyakhov, N. Z. Mechanochemical preparation of polymeric composites consisting of polyamide and clay materials. *Russ. J. Appl. Chem.* **88,** 488–493 (2015).

54. Follain, N., Alexandre, B., Chappey, C., Colasse, L., Médéric, P. & Marais, S. Barrier properties of polyamide 12/montmorillonite nanocomposites: Effect of clay structure and mixing conditions. *Compos. Sci. Technol.* **136,** 18–28 (2016).

55. Arunachalam, S., Battisti, M. G., Vijayakumar, C. T. & Friesenbichler, W. An Investigation of Mechanical and Thermal Properties of Polypropylene Clay Nanocomposites Containing Different Nanoclays. *Macromol. Mater. Eng.* **300,** 966–976 (2015).

56. Zaman, H. U., Hun, P. D., Khan, R. a. & Yoon, K.-B. Polypropylene/clay nanocomposites: Effect of compatibilizers on the morphology, mechanical properties and crystallization behaviors. *J. Thermoplast. Compos. Mater.* **27,** 338–349 (2012).

57. Rodríguez-Llamazares, Saddys., Rivas, Bernabé L., Pérez, Mónica., Perrin-Sarazin, Florence., Maldonado, Alvaro. & Venegas, C. The effect of clay type and of clay-masterbatch product in the preparation of polypropylene/clay nanocomposites. *J. Appl. Polym. Sci.* **122,** 2013–2025 (2011).

58. Smartech Global Solutions Ltd. Growth momentum expected to continue in global Polypropylene industry with CAGR of 3.7% uptil 2017. (2013). Available at: www.plastemart.com.

59. Radhakrishna, S. & Arof, A. K. *Polymeric Materials*. (Narosa Publishing House, 1998).

60. Karger-Kocsis, J. *Polypropylene: structure, blends and composites/ Vol.1 Structure and morphology*. (Chapman & Hall, 1994).

61. Chen, X. Study on crystallisation of isotactic PP: effect of stereotacticity defects and nanofillers. (Rensselaer Polytechnic Institute, 2007).

62. Tripathi, D. *Practical Guide to Polypropylene*. (Ismithers Rapra Publishing, 2002).

63. Wang, L. & Huang, B. Structure and properties of propylene-ethylene block copolymers and the corresponding blends. *J. Polym. Sci. Part B Polym. Phys.* **28,** 937–949 (1990).

64. Guo, C., Zhou, L. & Lv, J. Effects of expandable graphite and modified ammonium polyphosphate on the flame-retardant and mechanical properties of wood flour-polypropylene composites. *Polym. Polym. Compos.* **21,** 449–456 (2013).

65. Pavlidou, S. & Papaspyrides, C. D. A review on polymer–layered silicate nanocomposites. *Prog. Polym. Sci.* **33,** 1119–1198 (2008).

66. Kawasumi, M., Hasegawa, N. & Kato, M. Preparation and mechanical

properties of polypropylene-clay hybrids. *Macromolecules* **9297,** 6333–6338 (1997).

67. Alexandre, M. & Dubois, P. Polymer-layered silicate nanocomposites : preparation , properties and uses of a new class of materials. *Mater. Sci. Eng.* **28,** 1–63 (2000).

68. Odom, I. E. Smectite clay Minerals: Properties and Uses. *Philos. Trans. R. Soc. A Math. Phys. Eng. Sci.* **311,** 391–409 (1984).

69. Giannees, B. E. P. Polymer Layered Silicate Nanocomposites. *Adv. Mater.* 29–35 (1996).

70. Dennis, H.R., Hunter, D.L., Chang, D., Kim, S., White, J.L., Cho, J.W. & Paul, D. R. Effect of melt processing conditions on the extent of exfoliation in organoclay-based nanocomposites. *Polymer (Guildf).* **42,** 9513–9522 (2001).

71. Hoffmann, B., Kressler, J. & Sto, G. Influence of nano fillers on the deformation process in layered silicate / polyamide-12 nanocomposites. *Polymer (Guildf).* **42,** 1095–1100 (2001).

72. Chin, I. J., Thurn-Albrecht, T., Kim, H. C., Russell, T. P. & Wang, J. On exfoliation of montmorillonite in epoxy. *Polymer (Guildf).* **42,** 5947–5952 (2001).

73. Beyer, G. Nanocomposites: a new class of flame retardants for polymers. *Plast. Addit. Compd.* **4,** 22–28 (2002).

74. Varlot, K., Reynaud, E., Kloppfer, M H., Vigier, G. & Varlet, J. Clay-reinforced polyamide: Preferential orientation of the montmorillonite sheets and the polyamide crystalline lamellae. *J. Polym. Sci. Part B Polym. Phys.* **39,** 1360–1370 (2001).

75. Crosby, A. J. & Lee, J. Polymer Nanocomposites: The ‘Nano’ Effect on Mechanical Properties. *Polym. Rev.* **47,** 217–229 (2007).

76. Vaia, R. A. & Wagner, H. D. Framework for nanocomposites. *Materials Today* **7,** 32–37 (2004).

77. Zanetti, M., Lomakin, S. & Camino, G. Polymer layered silicate

nanocomposites. *Macromol. Mater. Eng.* **279,** 1–9 (2000).

78. Liu, Xiaohui., Wu, Qiuju., Berglund, Lars A., Lindberg, H., Fan, Jiaqi. & Qi, Z. Polyamide 6/clay nanocomposites using a cointercalation organophilic clay via melt compounding. *J. Appl. Polym. Sci.* **88,** 953–958 (2003).

79. Mohd Ishak, Z. a., Chow, W. S. & Takeichi, T. Compatibilizing effect of SEBS-g-MA on the mechanical properties of different types of OMMT filled polyamide 6/polypropylene nanocomposites. *Compos. Part A Appl. Sci. Manuf.* **39,** 1802–1814 (2008).

80. Ataeefard, M. & Moradian, S. Polypropylene/Organoclay Nanocomposites: Effects of Clay Content on Properties. *Polym. Plast. Technol. Eng.* **50,** 732–739 (2011).

81. Phua, Y. J., Lau, N.-S., Sudesh, K., Chow, W. S. & Ishak, Z. M. A study on the effects of organoclay content and compatibilizer addition on the properties of biodegradable poly(butylene succinate) nanocomposites under natural weathering. *J. Compos. Mater.* **49,** 891–902 (2014).

82. Omar, M. F., Akil, H. M., Rasyid, M. F. a. & Sharif, J. M. Thermal properties of polypropylene/muscovite layered silicate composites: effects of organic modifications and compatibilisers. *J. Compos. Mater.* **49,** 1195–1209 (2014).

83. Sinha Ray, S. & Okamoto, M. Polymer/layered silicate nanocomposites: a review from preparation to processing. *Prog. Polym. Sci.* **28,** 1539–1641 (2003).

84. Mahesh, K. R. Vishnu., Murthy, H. N. Narasimha., Kumaraswamy, B. E., Raghavendra, N., Sridhar, R., Krishna, M., Pattar, Niranjan., Pal, Ratna. & Sherigara, B. S. Synthesis and characterization of organomodified Na-MMT using cation and anion surfactants. *Front. Chem. China* **6,** 153–158 (2011).

85. Vaia, R. A. & Giannelis, E. P. Polymer Melt Intercalation in Organically-Modified Layered Silicates: Model Predictions and Experiment. *Macromolecules* **30,** 8000–8009 (1997).

86. Vaia, R. A. & Liu, W. X-ray powder diffraction of polymer/layered silicate

nanocomposites: Model and practice. *J. Polym. Sci. Part B Polym. Phys.* **40,** 1590–1600 (2002).

87. Ma, J., Xu, J., Ren, J.-H., Yu, Z.-Z. & Mai, Y.-W. A new approach to polymer/montmorillonite nanocomposites. *Polymer (Guildf).* **44,** 4619–4624 (2003).

88. Morgan, A. B. & Gilman, J. W. Characterization of polymer-layered silicate (Clay) nanocomposites by transmission electron microscopy and x-Ray diffraction : A comparative study. *App.Polym.sci* **87,** 1329–1338 (2003).

89. Banerjee, S., Joshi, M. & Ghosh, A. K. Investigations on clay dispersion in polypropylene/clay nanocomposites using rheological and microscopic analysis. *J. Appl. Polym. Sci.* **130,** 4464–4473 (2013).

90. Basu, S. K., Fasulo, P. D. & Rodgers, W. R. Stereology-based quantitative characterization of dispersion from TEM micrographs of polymer-clay nanocomposites. *J. Appl. Polym. Sci.* **119,** 396–411 (2011).

91. Lei, S., Hoa, S. & Tonthat, M. Effect of clay types on the processing and properties of polypropylene nanocomposites. *Compos. Sci. Technol.* **66,** 1274–1279 (2006).

92. Wu, H.-D., Tseng, C.-R. & Chang, F.-C. Chain Conformation and Crystallization Behavior of the Syndiotactic Polystyrene Nanocomposites Studied Using Fourier Transform Infrared Analysis. *Macromolecules* **34,** 2992–2999 (2001).

93. Loo, L. & Gleason, K. Fourier transform infrared investigation of the deformation behavior of montmorillonite in nylon-6/nanoclay nanocomposite. *Macromolecules* **36,** 2587–2590 (2003).

94. Porter, D., Metcalfe, E. & Thomas, M. J. K. Nanocomposite Fire Retardants - A Review. *Fire Mater* **24,** 45–52 (2000).

95. Allen, Norman S., Edge, Michele., Sandoval, Gonzalo., Ortega, Amaya., Liauw, Christopher M., Stratton, John. & McIntyre, R. B. Interrelationship of spectroscopic properties with the thermal and photochemical behaviour of

titanium dioxide pigments in metallocene polyethylene and alkyd based paint films: Micron versus nanoparticles. *Polym. Degrad. Stab.* **76,** 305–319 (2002).

96. VanderHart, D. L., Asano, a. & Gilman, J. W. NMR Measurements Related to Clay-Dispersion Quality and Organic-Modifier Stability in Nylon-6/Clay Nanocomposites. *Macromolecules* **34,** 3819–3822 (2001).

97. VanderHart, D. L., Asano, A. & Gilman, J. W. Solid-state NMR investigation of paramagnetic nylon-6 clay nanocomposites. 1. Crystallinity, morphology, and the direct influence of Fe3+ on nuclear spins. *Chem. Mater.* **13,** 3781–3795 (2001).

98. VanderHart, D. L., Asano, a. & Gilman, J. W. Solid-State NMR Investigation of Paramagnetic Nylon-6 Clay Nanocomposites. 2. Measurement of Clay Dispersion, Crystal Stratification, and Stability of Organic Modifiers. *Chem. Mater.* **13,** 3796–3809 (2001).

99. Fornes, T. D., Yoon, P. J., Keskkula, H. & Paul, D. R. Nylon 6 nanocomposites: the effect of matrix molecular weight. *Polymer (Guildf).* **42,** 09929–09940 (2001).

100. Kim, S. W., Jo, W. H., Lee, M. S., Ko, M. B. & Jho, J. Y. Preparation of clay-dispersed poly(styrene-co-acrylonitrile) nanocomposites using poly(ϵ-caprolactone) as a compatibilizer. *Polymer (Guildf).* **42,** 9837–9842 (2001).

101. Lagaly, G. Introduction : from clay mineral – polymer interactions to clay mineral – polymer nanocomposites. *Appl. Clay Sci.* 1–9 (1999).

102. Solomon, M. J., Almusallam, A. S., Seefeldt, K. F., Somwangthanaroj, A. & Varadan, P. Rheology of Polypropylene/Clay Hybrid Materials. *Macromolecules* **34,** 1864–1872 (2001).

103. Hasegawa, N., Kawasumi, M., Kato, M., Usuki, A. & Okada, A. Preparation and Mechanical Properties of Polypropylene – Clay Hybrids Using a Maleic Anhydride-Modified Polypropylene Oligomer. *J. Appl. Polym. Sci.* **67,** 87–92 (1998).

104. Mingliang, G. & Demin, J. Preparation and properties of polypropylene/clay

nanocomposites using an organoclay modified through solid state method. *J. Reinf. Plast. Compos.* **28,** 5–16 (2008).

105. Palza, H., Vergara, R., Yazdani-Pedram, M. & Quijada, R. Polypropylene/clay nanocomposites: Effect of different clays and compatibilizers on their morphology. *J. Appl. Polym. Sci.* **112,** 1278–1286 (2009).

106. Tarapow, J. A., Bernal, C. R. & Alvarez, V. A. Mechanical properties of polypropylene/clay nanocomposites: Effect of clay content, polymer/clay compatibility, and processing conditions. *J. Appl. Polym. Sci.* **111,** 768–778 (2008).

107. Song, P., Tong, L. & Fang, Z. Polypropylene / Clay Nanocomposites Prepared by In Situ Grafting-Melt Intercalation with a Novel Cointercalating Monomer. (2008). doi:10.1002/app

108. Sánchez-Valdes, S., Mendez-Nonell, J. & Ramos de valle, L. . Effect of different amine modified clays on the compatibility and clay dispersion of polypropylene nanocomposites. *e-Polymers* 1–16 (2009).

109. Seyidoglu, T. & Yilmazer, U. Production of modified clays and their use in polypropylene-based nanocomposites. *J. Appl. Polym. Sci.* **127,** 1257–1267 (2013).

110. Usuki, a., Kato, M., Okada, a. & Kurauchi, T. Synthesis of polypropylene-clay hybrid. *J. Appl. Polym. Sci.* **63,** 137–138 (1997).

111. Hasegawa, N., Okamoto, H., Kato, M. & Usuki, A. Preparation and mechanical properties of polypropylene-clay hybrids based on modified polypropylene and organophilic clay. *J. Appl. Polym. Sci.* **78,** 1918–1922 (2000).

112. Sun, T. & Garcés, J. M. High-Performance Polypropylene-Clay Nanocomposites by In-situ Polymerization with Metallocene/Clay Catalysts. *Adv. Mater.* **14,** 128–130 (2002).

113. Hwu, J.-M. & Jiang, G.-J. Preparation and characterization of polypropylene-montmorillonite nanocomposites generated byin situ metallocene catalyst polymerization. *J. Appl. Polym. Sci.* **95,** 1228–1236 (2005).

114. Reddy, C. S. & kumar Das, C. Synthesis and Characterization of in situ Polyethylene and Polypropylene Nanocomposites: Gas Phase Polymerization by Nanosilica Supported bis (Cyclopentadienyl) Zirconium (IV) Dichloride Catalyst System. *J. Polym. Res.* **14,** 129–139 (2006).

115. He, A., Wang, L., Li, J., Dong, J. & Han, C. C. Preparation of exfoliated isotactic polypropylene/alkyl-triphenylphosphonium-modified montmorillonite nanocomposites via in situ intercalative polymerization. *Polymer (Guildf).* **47,** 1767–1771 (2006).

116. Yang, Feng., Zhang, Xuequan., Zhao, Haichao., Chen, Bin., Huang, Baotong. & Feng, Z. Preparation and properties of polyethylene/montmorillonite nanocomposites byin situ polymerization. *J. Appl. Polym. Sci.* **89,** 3680–3684 (2003).

117. Lee, Dong-ho., Kim, Hyuk-soo., Yoon, Keun-byoung., Min, Kyung Eun., Seo, Kwan Ho. & Noh, S. K. Polyethylene/MMT nanocomposites prepared by in situ polymerization using supported catalyst systems. *Sci. Technol. Adv. Mater.* **6,** 457–462 (2005).

118. Cornelius, Baltus., Galdino, Rafael., Clelia, Ana., Ferreira, B., Universitário, Centro., Humberto, Av. & Bernardo, S. Synergistic Effect of Compatibilizer in Flame-Retardant Polypropylene Compounds. in *32nd International Conference of the POLYMER PROCESSING SOCIETY* (2016).

119. Wang, Y., Chen, F.-B., Li, Y.-C. & Wu, K.-C. Melt processing of polypropylene/clay nanocomposites modified with maleated polypropylene compatibilizers. *Compos. Part B Eng.* **35,** 111–124 (2004).

120. Zhang, Y.-Q., Lee, J.-H., Jang, H.-J. & Nah, C.-W. Preparing PP/clay nanocomposites using a swelling agent. *Compos. Part B Eng.* **35,** 133–138 (2004).

121. López-Quintanilla, M. L., Sánchez-Valdés, S., Ramos de Valle, L. F. & Medellín-Rodríguez, F. J. Effect of some compatibilizing agents on clay dispersion of polypropylene-clay nanocomposites. *J. Appl. Polym. Sci.* **100,** 4748–4756 (2006).

122. Zhong, W., Qiao, X., Sun, K., Zhang, G. & Chen, X. Polypropylene-clay blends compatibilized with MAH-g-POE. *J. Appl. Polym. Sci.* **99,** 2558–2564 (2006).

123. Liaw, W., Huang, P., Chen, C., Lo, C. & Chang, J. PPgMA/APTS compound coupling compatabilizer in PP/clay hybrid nanocomposite. *J. Appl. Polym. Sci.* **109,** 1871–1880 (2008).

124. Kato, M., Usuki, A. & Okada, A. Synthesis of Polypropylene Oligomer – Clay Intercalation. *J. Appl. Polym. Sci.* 1781–1785 (1997).

125. Liu, X. & Wu, Q. PP/clay nanocomposites prepared by grafting-melt intercalation. *Polymer (Guildf).* **42,** 10013–10019 (2001).

126. Zhang, Y.-Q., Lee, J.-H., Rhee, J. M. & Rhee, K. Y. Polypropylene–clay nanocomposites prepared by in situ grafting-intercalating in melt. *Compos. Sci. Technol.* **64,** 1383–1389 (2004).

127. Dolgovskij, Michail K., Fasulo, Paula D., Lortie, Frédéric., Macosko, Christopher W. & Robert, A. Effect of mixer type on exfoliation of polypropylene nanocomposites. in *Annual Technical Conference - ANTEC* 2255–2259 (2003).

128. Lertwimolnun, W. & Vergnes, B. Effect of processing conditions on the formation of polypropylene/organoclay nanocomposites in a twin screw extruder. *Polym. Eng. Sci.* **46,** 314–323 (2006).

129. Modesti, M., Lorenzetti, a., Bon, D. & Besco, S. Thermal behaviour of compatibilised polypropylene nanocomposite: Effect of processing conditions. *Polym. Degrad. Stab.* **91,** 672–680 (2006).

130. Li, J., Ton-That, M.-T., Leelapornpisit, W. & Utracki, L. A. Melt compounding of polypropylene-based clay nanocomposites. *Polym. Eng. Sci.* **47,** 1447–1458 (2007).

131. Xie, Wei., Gao, Zongming., Pan, Wei-Ping., Hunter, Doug., Singh, Anant. & Vaia, R. Thermal Degradation Chemistry of Alkyl Quaternary Ammonium Montmorillonite. *Chem. Mater.* **13,** 2979–2990 (2001).

132. Rezaiean, N., Ebadi-Dehaghani, H., Khonakdar, H. a., Jafary, P. & Jafari, S. M.

a. & Ghorbani, R. Microstructure and Properties of Polypropylene/Clay Nanocomposites. *J. Macromol. Sci. Part B* **55,** 1022–1038 (2016).

133. Dong, Y. & Bhattacharyya, D. Effects of clay type, clay/compatibiliser content and matrix viscosity on the mechanical properties of polypropylene/organoclay nanocomposites. *Compos. Part A Appl. Sci. Manuf.* **39,** 1177–1191 (2008).

134. Lee, E. C., Mielewski, D. F. & Baird, R. J. Exfoliation and dispersion enhancement in polypropylene nanocomposites by in-situ melt phase ultrasonication. *Polym. Eng. Sci.* **44,** 1773–1782 (2004).

135. Chow, W. S., Mohd Ishak, Z. a., Karger-Kocsis, J., Apostolov, a. a. & Ishiaku, U. S. Compatibilizing effect of maleated polypropylene on the mechanical properties and morphology of injection molded polyamide 6/polypropylene/organoclay nanocomposites. *Polymer (Guildf).* **44,** 7427–7440 (2003).

136. Dong, Y., Bhattacharyya, D. & Hunter, P. Experimental characterisation and object-oriented finite element modelling of polypropylene/organoclay nanocomposites. *Compos. Sci. Technol.* **68,** 2864–2875 (2008).

137. Xu, Weibing., Liang, Guodong., Wang, Wei., Tang, Shupei., He, Pingsheng. & Pan, W. P. PP-PP-g-MAH-Org-MMT nanocomposites. I. Intercalation behavior and microstructure. *J. Appl. Polym. Sci.* **88,** 3225–3231 (2003).

138. Osman, M. a. & Rupp, J. E. P. Interfacial Interactions and Properties of Polyethylene-Layered Silicate Nanocomposites. *Macromol. Rapid Commun.* **26,** 880–884 (2005).

139. Mittal, V. Polypropylene-Layered Silicate Nanocomposites: Filler Matrix Interactions and Mechanical Properties. *J. Thermoplast. Compos. Mater.* **20,** 575–599 (2007).

140. Sathe, Sachin N., Devi, Surekha., Srinivasa Rao, G. S. & Rao, K. V. Relationship between morphology and mechanical properties of binary and compatibilized ternary blends of polypropylene and nylon 6. *J. Appl. Polym. Sci.* **61,** 97–107 (1996).

141. Kim, D. H., Fasulo, P. D., Rodgers, W. R. & Paul, D. R. Structure and properties of polypropylene-based nanocomposites: Effect of PP-g-MA to organoclay ratio. *Polymer (Guildf).* **48,** 5308–5323 (2007).

142. Sathe, S. N., Rao, G. S. S. & Ra, K. V. The Effect of Composition on Morphological, Thermal, and Mechanical Properties of Polypropylene/Nylon-6/Polypropylene-g-Butyl Acrylate Blends. *Polym. Eng. Sci.* **36,** (1996).

143. Flory, P. J. On the Morphology of the Crystalline State in Polymers. *J. Am. Chem. Soc.* **84,** 2857–2867 (1962).

144. Graham, R. S. Molecular modelling of flow-induced crystallisation in polymers. *J. Eng. Math.* **71,** 237–251 (2011).

145. Somani, R. H., Yang, L., Zhu, L. & Hsiao, B. S. Flow-induced shish-kebab precursor structures in entangled polymer melts. *Polymer (Guildf).* **46,** 8587–8623 (2005).

146. Karger-Kocsis, J. *Polypropylene: Structure Blends and Composites: Structure and Morphology Copolymers and Blends Composites*. (Chapman&Hall, 1995).

147. Bruckner, S., Meille, S. V & Petraccone, I. V. Polymorphism in isotactic polypropylene. *Prog. Polym. Sci.* **16,** 361–404 (1991).

148. Zheng, W., Lu, X., Ling Toh, C., Hua Zheng, T. & He, C. Effects of clay on polymorphism of polypropylene in polypropylene/clay nanocomposites. *J. Polym. Sci. Part B Polym. Phys.* **42,** 1810–1816 (2004).

149. Yuan, Q., Deshmane, C., Pesacreta, T. C. & Misra, R. D. K. Nanoparticle effects on spherulitic structure and phase formation in polypropylene crystallized at moderately elevated pressures: The influence on fracture resistance. *Mater. Sci. Eng. A* **480,** 181–188 (2008).

150. Nam, Pham Hoai., Maiti, Pralay., Okamoto, Masami., Kotaka, Tadao., Hasegawa, N. & & Usuki, A. A hierarchical structure and properties of intercalated polypropylene/clay nanocomposites. *Polymer (Guildf).* **42,** 9633–9640 (2001).

151. Perrin-Sarazin, F., Ton-That, M.-T., Bureau, M. N. & Denault, J. Micro- and

nano-structure in polypropylene/clay nanocomposites. *Polymer (Guildf).* **46,** 11624–11634 (2005).

152. Hegde, R. R., Spruiell, J. E. & Bhat, G. S. Different crystallization mechanisms in polypropylene–nanoclay nanocomposite with different weight percentage of nanoclay additives. *J. Mater. Res.* **27,** 1360–1371 (2012).

153. Karger-kocsis, J. & Varga, J. Transformation on the Static and Dynamic Tensile Behavior of Isotactic Polypropylene. *J. Appl. Polym. Sci.* **62,** 291–300 (1996).

154. Rabek, J. *Photostabilization of Polymers:Principles and Application*. (ELSEVIER SCIENCE PUBLISHER LTD, 1990).

155. Botta, L., Dintcheva, N. T. & La Mantia, F. P. The role of organoclay and matrix type in photo-oxidation of polyolefin/clay nanocomposite films. *Polym. Degrad. Stab.* **94,** 712–718 (2009).

156. Dintcheva, N. T., Al-Malaika, S. & La Mantia, F. P. Effect of extrusion and photo-oxidation on polyethylene/clay nanocomposites. *Polym. Degrad. Stab.* **94,** 1571–1588 (2009).

157. La Mantia, F. P., Dintcheva, N. T., Malatesta, V. & Pagani, F. Improvement of photo-stability of LLDPE-based nanocomposites. *Polym. Degrad. Stab.* **91,** 3208–3213 (2006).

158. Leroux, F., Meddar, L., Mailhot, B., Morlat-Thérias, S. & Gardette, J.-L. Characterization and photooxidative behaviour of nanocomposites formed with polystyrene and LDHs organo-modified by monomer surfactant. *Polymer (Guildf).* **46,** 3571–3578 (2005).

159. Mailhot, Bénédicte., Morlat, Sandrine., Gardette, Jean-Luc., Boucard, Sylvain., Duchet, Jannick. & Gérard, J.-F. Photodegradation of polypropylene nanocomposites. *Polym. Degrad. Stab.* **82,** 163–167 (2003).

160. Morlat-Therias, Sandrine., Fanton, Elisabeth., Gardette, Jean-Luc., Dintcheva, Nadka Tzankova., La Mantia, Francesco P. & Malatesta, V. Photochemical stabilization of linear low-density polyethylene/clay nanocomposites: Towards

durable nanocomposites. *Polym. Degrad. Stab.* **93,** 1776–1780 (2008).

161. Qin, H., Zhao, C., Zhang, S., Chen, G. & Yang, M. Photo-oxidative degradation of polyethylene/montmorillonite nanocomposite. *Polym. Degrad. Stab.* **81,** 497–500 (2003).

162. Shah, R. K. & Paul, D. R. Organoclay degradation in melt processed polyethylene nanocomposites. *Polymer (Guildf).* **47,** 4075–4084 (2006).

163. Morreale, M., Dintcheva, N. T. & La Mantia, F. P. The role of filler type in the photo-oxidation behaviour of micro- and nano-filled polypropylene. *Polym. Int.* **60,** 1107–1116 (2011).

164. Singala, K. J., Mungray, A. A. & Mungray, A. K. Degradation Behavior of Polypropylene–Organically Modified Clay Nanocomposites. *Ind. Eng. Chem. Res.* **51,** 10557–10564 (2012).

165. Hoàng, E. M., Liauw, C. M., Allen, N. S., Fontán, E. & Lafuente, P. Effect of metal stearate antacid on the melt stabilization performance of phenolic/phosphite antioxidants in metallocene LLDPE. Part 1: Melt processing stability. *J. Vinyl Addit. Technol.* **10,** 137–143 (2004).

166. Morlat-Therias, S., Mailhot, B., Gonzalez, D. & Gardette, J. L. Photooxidation of polypropylene/montmorillonite nanocomposites. 2. Interactions with antioxidants. *Chem. Mater.* **17,** 1072–1078 (2005).

167. Morreale, M. Accelerated weathering of PP based nanocomposites: Effect of the presence of maleic anhydryde grafted polypropylene. *Express Polym. Lett.* **7,** 703–715 (2013).

168. Ben Hadj Salah, H., Ben Daly, H., Denault, J. & Perrin, F. UV degradation of clay-reinforced polypropylene nanocomposites. *Polym. Eng. Sci.* **56,** 469–478 (2016).

169. Papageorgiou, Dimitrios G., Filippousi, Maria., Pavlidou, Eleni., Chrissafis, Konstantinos., Van Tendeloo, Gustaaf. & Bikiaris, D. Effect of clay modification on structure–property relationships and thermal degradation kinetics of β-polypropylene/clay composite materials. *J. Therm. Anal. Calorim.* **122,** 393–

406 (2015).

170. Fitaroni, L. B., de Lima, J. a., Cruz, S. a. & Waldman, W. R. Thermal stability of polypropylene–montmorillonite clay nanocomposites: Limitation of the thermogravimetric analysis. *Polym. Degrad. Stab.* **111,** 102–108 (2015).

171. Koo, C. M., Kim, S. O. & Chung, I. J. Study on Morphology Evolution, Orientational Behavior, and Anisotropic Phase Formation of Highly Filled Polymer-Layered Silicate Nanocomposites. *Macromolecules* **36,** 2748–2757 (2003).

172. Chen, L., Wong, S. & Pisharath, S. Fracture Properties of Nanoclay-Filled Polypropylene. *J. Appl. Polym. Sci.* **88,** 3298–3305 (2002).

173. Zhu, L. & Xanthos, M. Effects of process conditions and mixing protocols on structure of extruded polypropylene nanocomposites. *J. Appl. Polym. Sci.* **93,** 1891–1899 (2004).

174. Birley, A., Haworth, B. & Batchelor, J. in *Physics of Plastics* (Hanser, 1992).

175. Osswald, T. & Rudolph, N. *Polymer Rheology*. (Carl Hanser Verlag GmbH & Co. KG, 2014). doi:10.3139/9781569905234

176. Rajsekaran. Extrusion of Plastics/Extrusion Molding/Extrusion Process. *Mechanical Engineer's World* (2015). Available at: http://www.mechscience.com/extrusion/.

177. Rauwendaal, C. *Polymer extrusion*. (Hanser Gardner Publications, 1994).

178. White, J. L. & Potente, H. *Screw extrusion*. (Hanser Gardner Publications, 2003).

179. Acur, E. E. & Vlachopoulos, J. Numerical simulation of a single-screw plasticating extruder. *Polym. Eng. Sci.* **22,** 1084–1094 (1982).

180. Wilczyński, K., Nastaj, A. & Wilczyński, K. J. Melting Model for Starve Fed Single Screw Extrusion of Thermoplastics. *Int. Polym. Process.* **28,** 34–42 (2013).

181. Wilczyński, K. J., Nastaj, A., Lewandowski, A. & Wilczyński, K. A composite

model for starve fed single screw extrusion of thermoplastics. *Polym. Eng. Sci.* **54,** 2362–2374 (2014).

182. Wilczyński, K. J., Lewandowski, A., Nastaj, A. & Wilczyński, K. A Global Model for Starve-Fed Nonconventional Single-Screw Extrusion of Thermoplastics. *Adv. Polym. Technol.* **36,** 23–35 (2017).

183. Wilczyński, K. J., Lewandowski, A., Nastaj, A. & Wilczyński, K. Modeling for Starve Fed/Flood Fed Mixing Single-Screw Extruders. *Int. Polym. Process.* **31,** 82–91 (2016).

184. Längauer, Manuel., Liu, Keyan., Kneidinger, Christian., Schaffler, Gernot., Purgleitner, Bianca. & Zitzenbacher, G. Experimental analysis of the influence of pellet shape on single screw extrusion. *J. Appl. Polym. Sci.* **132,** (2015).

185. Abeykoon, C., Kelly, A. L., Brown, E. C. & Coates, P. D. The effect of materials, process settings and screw geometry on energy consumption and melt temperature in single screw extrusion. *Appl. Energy* **180,** 880–894 (2016).

186. Twin-screw Schematic. Available at: http://www.suggest-keywords.com/dHdpbi1zY3JldyBzY2hlbWF0aWM/.

187. Gasner, G. E., Bigio, D., Marks, C., Magnus, F. & Kiehl, C. A New Approach to Analyzing Residence Time and Mixing in a Co-Rotating Twin Screw Extruder. *Polym. Eng. Sci.* **39,** 286–298 (1999).

188. Padmanabhan, B. & Jayanth, C. C. Shear uniformity in co-rotating twin screw extruder - a geometrical study of shear rates in a fully filled zone. in *67th Annual Techniqual Conference of the Society of Plastics Engineers* 182 (2009).

189. Teixeira, C., Gaspar-Cunha, A. & Covas, J. a. Flow and Heat Transfer Along the Length of a Co-rotating Twin Screw Extruder. *Polym. Plast. Technol. Eng.* **51,** 1567–1577 (2012).

190. Tang, H., Wrobel, L. & Fan, Z. Fluid flow aspects of twin-screw extruder process: numerical simulations of TSE rheomixing. *Model. Simul. Mater. Sci. Eng.* **11,** 771–790 (2003).

191. Andersen, P. G. & Corporation, C. Simulation of Co-Rotating Fully

Intermeshing Twin-Screw Compounding Extruders: Alternatives for Process Design. in *SPE ANTEC* 915–920 (2016).

192. Sinotech, I. Injection Molded Parts. (2016). Available at: https://www.sinotech.com/resources/tutorials/injection-molded-parts/.

193. Crawford, R. J. *Plastics Engineering*. (Butterworth-Heinemann, 1998).

194. Kistler Inc. Increased cost efficiency with cavity pressure-based systems. *documentation* (2014).

195. Lenk, R. S. *Polymer Rheology*. (Applied Science Publishers, 1978).

196. Hnatkova, E. & Dvorak, Z. Effect of the skin-core morphology on the mechanical properties of injection-moulded parts. *Mater. Tehnol.* **50,** 195–198 (2016).

197. Jaruga, T. & Bociaga, E. Structure of polypropylene parts from multicavity injection mould. *Arch. Mater. Sci. Eng.* **28,** 429–432 (2007).

198. Lednicky, F. *Microscopy and Morphology of Polymers*. (Technical university of Liberec, 2009).

199. Saiu, M., Brucato, V., Piccarolo, S. & Titomanlio, G. Injection Molding of iPP. *Int. Polym. Process.* **7,** 267–273 (1992).

200. Viana, J., Cunha, A. & Billon, N. The effect of the skin thickness and spherulite size on the mechanical properties of injection mouldings. *J. Mater. Sci.* **6,** 4411–4418 (2001).

201. Phillips, R., Herbert, G., News, J. & Wolkowicz, M. High Modulus Polypropylene: Effect of Polymer and Processing Variables on Morphology and Properties. *Polym. Eng. Sci.* **34,** 1731–1743 (1994).

202. Viana, J., Cunha, A. & Billon, N. The thermomechanical environment and the microstructure of an injection moulded polypropylene copolymer. *Polymer (Guildf).* **43,** 4185–4196 (2002).

203. Viana, J. & Cunha, A. Prediction of the Tensile Impact Behavior of Injection Molded Samples From Quasi-Static Data. *Polym. Eng. Sci.* **39,** 1463–1472

(1999).

204. Brito, A. M., Cunha, A. M., Pouzada, A. S. & Crawford, R. J. Predicting the Skin-Core Boundary Location in Injection Moldings. *Int. Polym. Process.* **6,** 370–377 (1991).

205. Viana, J. C. Development of the skin layer in injection moulding: phenomenological model. *Polymer (Guildf).* **45,** 993–1005 (2004).

206. Jerschow, P. & Janeschitz-Kriegl, H. The Role of Long Molecules and Nucleating Agents in Shear Induced Crystallization of Isotactic Polypropylenes. *Int. Polym. Process.* **12,** 72–77 (1997).

207. Gahleitner, Markus., Wolfschwenger, Johannes., Bachner, Claudia., Bernreitner, Klaus. & Neibl, W. Crystallinity and mechanical properties of PP-homopolymers as influenced by molecular structure and nucleation. *J. Appl. Polym. Sci.* **61,** 649–657 (1996).

208. Viana, J., Billon, N. & Cunha, A. The thermomechanical environment and the mechanical properties of injection moldings. *Polym. Eng. Sci.* **44,** 1522–1533 (2004).

209. Feldmann, M. The effects of the injection moulding temperature on the mechanical properties and morphology of polypropylene man-made cellulose fibre composites. *Compos. Part A Appl. Sci. Manuf.* **87,** 146–152 (2016).

210. Zhang, X. X., Wang, L. & Liao, Q. H. Experimental Study on the Crystallinity and Mechanical Properties of the Injection Molded Polypropylene. *Adv. Mater. Res.* **239–242,** 2809–2812 (2011).

211. Chen, S., Peng, H., Huang, L. & M, C. Investigations of the Tensile Properties on Polycarbonate Thin-Wall Injection Molded Parts. *J. Reinf. Plast. Compos.* **22,** 479 (2003).

212. Friesenbichler, W., Langecker, G. R., Duretek, I. & Schuschnigg, S. Polymer melt rheology at high shear rates using a new micro-rheology technique. *7th Austrian Polym. Meet.*

213. Liao, S. J., Chang, D. Y., Chen, H. J., Tsou, L. S., Ho, J. R., Yau, H. T., Hsieh,

W. H., Wang, James T. & Su, Y. C. Optimal process conditions of shrinkage and warpage of thin-wall parts. *Polym. Eng. Sci.* **44,** 917–928 (2004).

214. Mullath, A., Haworth, B., Carao, J. & Fenn, C. R. PROCESS SIMULATION AND IN-CAVITY PRESSURE MEASUREMENT FOR THIN-WALL INJECTION MOULDINGS. *Proc. Polym. Process. Soc. 29th Annu. Meet.* (2013).

215. Wang, T.-H. & Young, W.-B. Study on residual stresses of thin-walled injection molding. *Eur. Polym. J.* **41,** 2511–2517 (2005).

216. Autodesk Moldflow. Moldflow Insight 2017. (2017).

217. Montgomery, Douglas, C. *Introduction to statistical quality control*. (John Wiley & Sons, Inc, 2005).

218. Tahboub, K. K. & Rawabdeh, I. a. A design of experiments approach for optimizing an extrusion blow molding process. *J. Qual. Maint. Eng.* **10,** 47–54 (2004).

219. Coles, Stuart R., Jacobs, Daniel K., Meredith, James O., Barker, Guy., Clark, Andrew J., Kirwan, Kerry., Stanger, Jon. & Tucker, N. A design of experiments (DoE) approach to material properties optimization of electrospun nanofibers. *J. Appl. Polym. Sci.* **117,** 2251–2257 (2010).

220. Tsimpliaraki, A., Svinterikos, S., Zuburtikudis, I., Marras, S. I. & Panayiotou, C. Nanofibrous Structure of Nonwoven Mats of Electrospun Biodegradable Polymer Nanocomposites - A Design of Experiments (DoE) Study. *Ind. Eng. Chem. Res.* **48,** 4365–4374 (2009).

221. Ramos, V. D., Costa, H. M. Da, Rocha, M. C. G. & Gomes, A. D. S. Study of different peroxide types on the modification of LLDPE. Part 1. Factorial experimental design and thermal properties. *Polym. Test.* **25,** 306–312 (2006).

222. Teixeira, Sylvia C.S., Moreira, Maria Margareth., Lima, Aline P., Santos, Luciene S., da Rocha, Bianca M., de Lima, Edson S., da Costa, Raphael a.a.F., da Silva, Ana Lúcia N., Rocha, Marisa C.G. & Coutinho, F. M. B. Study of blends of HDPE and different grades of CaCO3. Part I. Factorial experimental design. *Polym. Test.* **24,** 983–987 (2005).

223. Rocha, M. C. G., Silva, A. H. M. F. T., Coutinho, F. M. B. & Silva, A. L. N. Study of composites based on polypropylene and calcium carbonate by experimental design. *Polym. Test.* **24,** 1049–1053 (2005).

224. Costa, Thais H.S., Carvalho, Daisy L., Souza, Denise C.S., Coutinho, Fernanda M.B., Pinto, José Carlos. & Kokta, B. V. Statistical experimental design and modeling of polypropylene–wood fiber composites. *Polym. Test.* **19,** 419–428 (2000).

225. Jang, J. & Lim, B. Investigation of a fiber-reinforced plastic/rubber adhesive system using statistical experimental design. *Polym. Test.* **20,** 117–123 (2001).

226. Désiré, A., Paillard, B., Bougaret, J., Baron, M. & Couarraze, G. Extruder scale-up assessment in the process of extrusion-spheronization: comparison of radial and axial systems by a design of experiments approach. *Drug Dev. Ind. Pharm.* **39,** 176–85 (2013).

227. Kim, H. K., Kim, J. G. & Hong, J. W. Determination of key variables affecting surface properties of UV curable coatings using experimental design. *Polym. Test.* **21,** 417–424 (2002).

228. Raghukandan, K. & Senthilvelan, T. Analysis of P/M hollow extrusion using design of experiments. *J. Mater. Process. Technol.* **153–154,** 416–419 (2004).

229. Pye, R. G. W. *Injection mould design : a design manual for the thermoplastics industry*. (Godwin, in association with the Plastics and Rubber Institute, 1983).

230. Cracknell, P. S. & Dyson, R. W. *Handbook of thermoplastics injection mould design*. (Blackie Academic & Professional, 1993).

231. Zhang, H. L., Ong, N. S. & Lam, Y. C. Experimental investigation of key parameters on the effects of cavity surface roughness in microinjection molding. *Polym. Eng. Sci.* **48,** 490–495 (2008).

232. Zhang, H. L., Ong, N. S. & Lam, Y. C. Mold surface roughness effects on cavity filling of polymer melt in micro injection molding. *Int. J. Adv. Manuf. Technol.* **37,** 1105–1112 (2008).

233. Zeng, Q. H., Yu, A. B., Lu, G. Q. (Max) & Paul, D. R. Clay-Based Polymer

Nanocomposites: Research and Commercial Development. *J. Nanosci. Nanotechnol.* **5,** 1574–1592 (2005).

234. Nakas, G. I. & Kaynak, C. Use of different alkylammonium salts in clay surface modification for epoxy-based nanocomposites. *Polym. Compos.* **30,** 357–363 (2009).

235. Kádár, F., Százdi, L., Fekete, E. & Pukánszky, B. Surface Characteristics of Layered Silicates: Influence on the Properties of Clay/Polymer Nanocomposites. *Langmuir* **22,** 7848–7854 (2006).

236. Cogswell, F. N. *Polymer Melt Rheology: A Guide for Industry Practice*. (G. Godwin in association with Plastics and Rubber Institute, 1981).

237. Gee, D. & Melia, T. Thermal properties of melt and solution crystallized isotactic polypropylene. *Die Makromol. Chemie* **132,** 195–201 (1970).

238. Borgaonkar, H. & Ramani, K. Stability analysis in single screw extrusion of thermoplastic elastomers using simple design of experiments. *Adv. Polym. Technol.* **17,** 115–126 (1998).

239. Tadmor, Z. & Gogos, G. *Principles of polymer processing*. (John Wiley, 2006).

240. Stevens, M. J. & Covas, J. A. *Extruder Principles and Operation*. (Chapman & Hall, 1995).

241. Li, Q., Yang, Q., Huang, Y., Chen, G. & Lv, Y. Effect of Compatibilizer Content on the Shear and Extensional Rheology of Polypropylene/Clay Nanocomposites. *J. Macromol. Sci. Part B* **51,** 1776–1793 (2012).

242. Al-Malaika, S., Sheena, H., Fischer, D. & Masarati, E. Influence of processing and clay type on nanostructure and stability of polypropylene–clay nanocomposites. *Polym. Degrad. Stab.* **98,** 2400–2410 (2013).

243. Lertwimolnun, W. & Vergnes, B. Influence of screw profile and extrusion conditions on the microstructure of polypropylene/organoclay nanocomposites. *Polym. Eng. Sci.* **47,** 2100–2109 (2007).

244. Liu, Q., Sun, X., Li, H. & Yan, S. Orientation-induced crystallization of isotactic

polypropylene. *Polymer (Guildf).* **54,** 4404–4421 (2013).

245. Perez, C. J. & Alvarez, V. A. Overall crystallization behavior of polypropylene-clay nanocomposites; Effect of clay content and polymer/clay compatibility on the bulk crystallization and spherulitic growth. *J. Appl. Polym. Sci.* **114,** 3248–3260 (2009).

246. Nejad, S. J. & Golzary, A. Investigation and modeling of the thermal conductivity of PP/clay nanocomposites and PP/MWCNT nanocomposites. *e-Polymers* **10,** (2010).

247. Mohaddespour, A., Abolghasemi, H., Mostaedi, M. T. & Habibzadeh, S. A new model for estimation of the thermal conductivity of polymer/clay nanocomposites. *J. Appl. Polym. Sci.* **118,** 1042–1050 (2010).

248. Wasiak, A., Sajkiewicz, P. & Woz, A. Effects of Cooling Rate on Crystallinity of i-Polypropylene and Polyethylene Terephthalate Crystallized in. *J. Polym. Sci. Part B Polym. Phys.* **37,** 2821–2827 (1999).

249. Kim, K. H., Isayev, A. I. & Kwon, K. Flow-induced crystallization in the injection molding of polymers: A thermodynamic approach. *J. Appl. Polym. Sci.* **95,** 502–523 (2005).

250. Isayev, A. I., Chan, T. W., Gmerek, M. & Shimojo, K. Injection molding of semicrystalline polymers. II. Modeling and experiments. *J. Appl. Polym. Sci.* **55,** 821–838 (1995).

251. Guo, X., Isayev, A. I. & Demiray, M. Crystallinity and microstructure in injection moldings of isotactic polypropylenes. Part II: Simulation and experiment. *Polym. Eng. Sci.* **39,** 2132–2149 (1999).

252. Allen, T. T. *Introduction to engineering statistics and six sigma : statistical quality control and design of experiments and systems*. (Springer, 2005).

Appendices

Appendix A

Section 1

SABIC® PP 571P

PP homopolymer for Injection moulding

Description:
This grade is characterized by excellent gloss and good surface hardness. Typical applications are sanitary, closures with and without integral hinges.

Health, Safety and Food Contact regulations:
Material Safety Data Sheets (MSDS) and Product Safety declarations are available on our Internet site http://www.SABIC-europe.com

The product mentioned herein is in particular not tested and therefore not validated for use in pharmaceutical / medical applications.

This grade material is UL registered under File E111275 (www.ul.com)

IMDS 7172624

Typical values Revision

Properties		Unit (Si)	Values	Test methods
Polymer properties				
Melt flow rate (MFR)				ISO 1133
at 230 °C and 2.16 kg		dg/min	**5.7**	
Density		kg/m³	**905**	ISO 1183
Formulation				
Anti static agent		-	**No**	-
Nucleating agent		-	**No**	-
Mechanical properties				
Tensile test				ISO 527-2 1A
stress at yield	1)	MPa	**37**	
strain at yield	1)	%	**8**	
tensile modulus	2)	MPa	**1700**	
Izod impact notched				ISO 180/1A
at 23 °C		kJ/m²	**3.0**	
Charpy impact notched				ISO 179/1eA
at 23 °C		kJ/m²	**4.0**	
Hardness Shore D		-	**69**	ISO 868
Thermal properties				
Heat deflection temperature	3)			ISO 75
at 1.80 MPa (HDT/A)		°C	**55**	
at 0.45 MPa (HDT/B)		°C	**85**	
Vicat softening temperature	4)			ISO 306
at 10 N (VST/A)		°C	**154**	
at 50 N (VST/B)		°C	**95**	

1) Speed of testing: 50 mm/min
2) Speed of testing: 1 mm/min
3) Flat wise (testbar 80*10*4mm)
4) Temperature rate: 120°C/h

internet www.sabic-europe.com
email pp.info@sabic-europe.com

SABIC® PP PHC26

PP block copolymer for Injection moulding

Description: This grade combines very high impact resistance, also at low temperatures, with high stiffness and offers good flow properties. Due to its narrow molecular weight distribution, the very low tendency to warp and the excellent surface quality, SABIC® PP PHC26 is typically used in injection moulding of suitcase shells, crates & boxes and automotive parts.

Health, Safety and Food Contact regulations:
Material Safety Data Sheets (MSDS) and Product Safety declarations are available on our Internet site http://www.SABIC-europe.com

The product mentioned herein is in particular not tested and therefore not validated for use in pharmaceutical/ medical applications.

IMDS 80775790

Typical values Revision 20121121

Properties		Unit (Si)	Values	Test methods
Polymer properties				
Melt flow rate (MFR)				ISO 1133
at 230 °C and 2.16 kg		dg/min	**8.0**	
Density		kg/m³	**905**	ISO 1183
Formulation				
UV stabilized		-	**No**	-
Anti static agent		-	**No**	-
Nucleating agent		-	**Yes**	-
Mechanical properties				
Tensile test				ISO 527-2 1A
stress at yield	1)	MPa	**23**	
strain at yield	1)	%	**5**	
tensile modulus	2)	MPa	**1250**	
Izod impact notched				ISO 180/1A
at 23 °C		kJ/m²	**No Break**	
at 0 °C		kJ/m²	**20**	
at -20 °C		kJ/m²	**10**	
Charpy impact notched				ISO 179/1eA
at 23 °C		kJ/m²	**60**	
at 0 °C		kJ/m²	**15**	
at -20 °C		kJ/m²	**9**	
Charpy impact unnotched				ISO 179/1eU
at 23 °C		kJ/m²	**No Break**	
Hardness Shore D		-	**60**	ISO 868
Thermal properties				
Heat deflection temperature	3)			ISO 75
at 1.80 MPa (HDT/A)		°C	**50**	
at 0.45 MPa (HDT/B)		°C	**85**	
Vicat softening temperature	4)			ISO 306
at 10 N (VST/A)		°C	**147**	
at 50 N (VST/B)		°C	**68**	

1) Speed of testing: 50 mm/min
2) Speed of testing: 1 mm/min
3) Flat wise (testbar 80*10*4mm)
4) Temperature rate: 120°C/h

internet www.sabic-europe.com
email pp.info@sabic-europe.com

Cloisite® 15A

Typical Physical Properties Bulletin

Description:
Cloisite® 15A is a natural montmorillonite modified with a quaternary ammonium salt.

Designed Used:
Cloisite® 15A is an additive for plastics to improve various plastic physical properties, such as reinforcement, HDT, CLTE and barrier.

Typical Properties:

Treatment/Properties:	Organic Modifier (1)	Modifier Concentration	% Moisture	% Weight Loss on Ignition
Cloisite® 15A	2M2HT	125 meq/100g clay	< 2%	43%

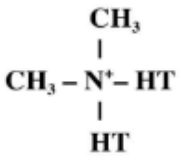

Where HT is Hydrogenated Tallow (~65% C18; ~30% C16; ~5% C14)

Anion: Chloride

(1) 2M2HT: dimethyl, dehydrogenated tallow, quaternary ammonium

Typical Dry Particle Sizes: (microns, by volume)

10% less than:	50% less than:	90% less than:
2µm	6µm	13µm

Color: Off White

Density:

Loose Bulk, lbs/ft^3	Packed Bulk, lbs/ft^3	Density, g/cc
10.79	18.64	1.66

X Ray Results: d_{001} = 31.5Å

SIGMA-ALDRICH®

sigma-aldrich.com

3050 Spruce Street, Saint Louis, MO 63103, USA
Website: www.sigmaaldrich.com
Email USA: techserv@sial.com
Outside USA: eurtechserv@sial.com

Product Specification

Product Name:
Nanoclay, surface modified - contains 35-45 wt. % dimethyl dialkyl (C14-C18) amine

Product Number: 682624

TEST	Specification
Appearance (Color)	Beige
Appearance (Form)	Powder
Loss on Drying	≤ 3 %
Bulk Density	200 - 500 kg/m3
Size	≤ 20 micron
Average Particle Size	

Specification: PRD.0.ZQ5.10000023456

ZHEJIANG FENGHONG NEW MATERIAL CO. ,LTD.
Http://www.zjfenghong.com E-mail: Bentonite@zjfenghong.com
Tel: +86-571-63806068/63711876 Fax:+86-571-63751569/63806098
Add: No.441,Lintian Road ,Lin'an city ,Zhejiang province,China. PC:311300

ZHEJIANG FENGHONG NEW MATERIAL CO., LTD.

www.zjfenghong.com

DK®4
Polymer Grade Organic Clay

DK®4 polymer grade organic clay is one kind of high purity long-chain alkyl ammonium modified montmorillonite. It is mainly used as modifier in polyolefin and twin screw melt extrusion of thermoplastic polymers such as EVA, TPO. It improves the tensile strength, flexural strength, modulus and other mechanical properties, as well as to improve the heat distortion temperature (HDT), dimensional stability, gas barrier properties, flame retardant properties of the polymer. Its application performance is similar to Nanomer 1.44P and Cloisite 15A, 20A.

Typical physical and chemical properties:

Appearance	**White Powder**
Montmorillonite Content %	**≥98**
Crystalline Silica %	**≤1**
Loss on Ignition（900℃）%	**≥44.0**
Moisture Content%	**<3.0**
Powder Fineness-20μ%	**90**
Bulk Density g/cm3	**0.25**
Specific Gravity g/cm3	**1.7**
XRD d001 nm	**3.6**

Chemtura

Technical Information
www.chemtura.com
Effective: 03.31.2009

Polybond 3200

Polymer Modifier

Polybond 3200 is a chemically modified polyolefin.

Chemical Structure

Composition: Maleic anhydride modified homopolymer polypropylene

Features

- Chemical coupling agent for glass, mica, talc, wood and natural fiber reinforced polypropylene giving enhanced physical and thermal properties.
- Compatibilizer for blends such as polypropylene/polyamide and polypropylene/EVOH to improve processing and mechanical properties.
- Physical properties comparable to other Polybond products can be obtained using lower addition levels.

Typical Physical Properties

Appearance	Pellets
Melt Flow Rate (190/2.16)	115 g/10 min. (ASTM D-1238)
Density @ 23°C	0.91 g/cc (ASTM D-792)
Melting Point	157°C (DSC)
Maleic Anhydride Level	1.0 weight %

Properties in 30% Glass-filled Polypropylene

Increase in Properties due to addition of Polybond 3200

PROPERTY	0.25% PB 3200	0.5% PB 3200	1% PB 3200	2% PB 3200
Tensile Strength	17%	19%	22%	27%
Flexural Strength	15%	20%	26%	27%
Izod Impact				
Unnotched	42%	45%	66%	75%
Notched	36%	80%	104%	120%

Generation of above data was via twin-screw extrusion. Polybond addition level was based on total weight of composite. Glass type was PPG 3242 1/8".

Storage and Handling Precautions

Keep Polybond 3200 dry prior to processing. Loss of anhydride functionality may occur due to conversion to acid groups by reaction with atmospheric moisture. Tie liners of open gaylords, when not in use to prevent exposure to moisture. If exposure occurs, Polybond 3200 can be dried in a hopper dryer or oven for three hours at 105°C to remove moisture.
A slight pungent odor is normal during processing of Polybond 3200. Purge equipment with polypropylene before and after running Polybond 3200.

For additional handling information, please see the Material Safety Data Sheet.

SIGMA-ALDRICH®
sigma-aldrich.com

3050 Spruce Street,Saint Louis,MO 63103,USA
Website: www.sigmaaldrich.com
Email USA: techserv@sial.com
Outside USA: eurtechserv@sial.com

Product Specification

Product Name:
cis-13-Docosenoamide

Product Number:	**280577**
CAS Number:	112-84-5
MDL:	MFCD00882379
Formula:	C22H43NO
Formula Weight:	337.58 g/mol

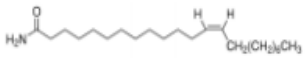

TEST	Specification
Appearance (Color)	White to Brown
Appearance (Form)	Beads
Infrared spectrum	Conforms to Structure
Carbon	66.5 - 90.0 %
Nitrogen	3.5 - 4.8 %
Purity (GC)	≥ 85.0 %

Section 2

Calculations and results for RH7 Rheometry

An example is given here for PP-H at 200°C. For the first stage of piston speed, pressure measured at the die entrance is P_L=2.02 MPa for the long die (L=20mm, R=0.5mm), and P_S=0.11 MPa for the zero die.

Due to the pressure drop at die entrance and Bagley end correction is required. Therefore, true pressure drop $\Delta P = P_L - P_S$

The true shear stress can be calculated using the following equation:

$$\tau_{true} = \frac{\Delta P \cdot R}{2L}$$

$$= \frac{(P_L - P_S)R}{2L}$$

$$= \frac{(2.02 - 0.11) \times 0.5}{2 \times 20}$$

$$= 23.9kPa$$

The apparent shear rate at the first stage of piston speed ($\dot{\gamma}_{app}$) is given as 20 s^{-1} and the resultant power law coefficient (n) is 0.52. Thus the true shear rate is:

$$\dot{\gamma}_{true} = \frac{3n+1}{4n}\dot{\gamma}_{app}$$

$$= \frac{3 \times 0.52 + 1}{4 \times 0.52} \times 20$$

$$= 24.6\ s^{-1}$$

Thus the true viscosity (η_{true}) is:

$$\eta_{true} = \frac{\tau_{true}}{\dot{\gamma}_{true}}$$

$$= \frac{23.9kPa}{24.6\ s^{-1}}$$

$$= 971\ Pa \cdot s$$

Table 1 Data of PP-H (571P) at 200°C

	16x1						
	Stage	Corrected shear stress (kPa)	Shear rate (s^{-1})	Shear viscosity (Pa.s)	n	Corrected shear rate (s^{-1}) (Rabinowitsch)	Corrected shear viscosity (Pa.s)
	1	26.76	20	1337.96	0.49	25.2	1062
	2	36.45	43.09	845.85	0.45	56.3	648
	3	50.87	92.83	548.01	0.41	126.2	403
	4	68.1	199.78	340.86	0.37	284.8	239
	5	87.01	429.83	202.44	0.33	648.0	134
	6	111.05	927.93	119.67	0.28	1524.5	73
	7	136.64	1999.4	68.34	0.24	3582.3	38
	8	109.27	928.71	117.66	0.28	1525.7	72
	9	85.89	431.38	199.09	0.33	650.3	132
	10	66.65	200.17	332.98	0.37	285.4	234
200°C	11	49.66	92.83	534.91	0.41	126.2	393
	12	35.11	43.09	814.76	0.45	56.3	624
	13	23.23	20	1161.54	0.49	25.2	922
		20x1					
	1	23.89	20	1194.42	0.52	24.6	971
	2	36.07	43.09	837.12	0.47	55.2	653
	3	50.58	92.83	544.89	0.42	124.9	405
	4	66.51	200.56	331.64	0.38	282.4	236
	5	86.33	432.16	199.77	0.33	651.5	133
	6	109.23	927.93	117.72	0.28	1524.5	72
	7	138.43	1999.4	69.24	0.24	3582.3	39
	8	111.1	928.71	119.63	0.28	1525.7	73
	9	86.61	430.6	201.13	0.33	649.2	133
	10	66.43	199.78	332.52	0.38	281.3	236
	11	49.13	92.83	529.2	0.42	124.9	393
	12	34.71	43.09	805.54	0.47	55.2	628
	13	23.23	20	1161.27	0.52	24.6	944

Table 2 Data of PP-H (571P) at 220°C

	16x1						
	Stage	Corrected shear stress (kPa)	Shear rate (s^{-1})	Shear viscosity (Pa.s)	n	Corrected shear rate (s^{-1}) (Rabinowitsch)	Corrected shear viscosity (Pa.s)
	1	18.46	20	922.79	0.55	24.1	766
	2	27.88	43.09	647.01	0.5	53.9	518
	3	39.27	92.83	423.07	0.45	121.2	324
	4	53.69	199.78	268.72	0.4	274.7	195
	5	72.95	431.38	169.11	0.35	631.7	115
	6	94.53	928.71	101.79	0.3	1470.5	64
	7	119.15	2000.17	59.57	0.26	3423.4	35
	8	92.71	927.93	99.91	0.3	1469.2	63
	9	73.06	431.38	169.36	0.35	631.7	116
	10	55.2	199.78	276.32	0.4	274.7	201
220°C	11	40.47	92.83	435.99	0.45	121.2	334
	12	27.72	43.09	643.22	0.5	53.9	515
	13	17.66	20	882.86	0.55	24.1	733
	20x1						
	1	19.9	20	994.99	0.54	24.3	820
	2	29.23	43.09	678.48	0.49	54.3	538
	3	41.43	92.83	446.27	0.44	122.4	339
	4	56.95	199.78	285.07	0.4	274.7	207
	5	74.98	430.6	174.13	0.35	630.5	119
	6	96.54	928.71	103.95	0.3	1470.5	66
	7	121.48	2000.17	60.73	0.26	3423.4	35
	8	95.58	928.71	102.91	0.3	1470.5	65
	9	74.74	430.6	173.56	0.35	630.5	119
	10	56.56	199.78	283.13	0.4	274.7	206
	11	40.94	92.83	441	0.44	122.4	335
	12	28.17	43.09	653.66	0.49	54.3	519
	13	18.48	20	923.88	0.54	24.3	762

Table 3 Data of PP-H (571P) at 240°C

	16x1						
	Stage	Corrected shear stress (kPa)	Shear rate (s^{-1})	Shear viscosity (Pa.s)	n	Corrected shear rate (s^{-1}) (Rabinowitsch)	Corrected shear viscosity (Pa.s)
	1	15.44	20	772.08	0.61	23.2	666
	2	21.87	43.09	507.5	0.55	51.9	421
	3	33.06	92.83	356.08	0.48	118.0	280
	4	46.78	200.17	233.71	0.42	269.3	174
	5	63.14	431.38	146.37	0.36	623.1	101
	6	81.14	928.71	87.37	0.3	1470.5	55
	7	99.5	2000.17	49.75	0.24	3583.6	28
	8	80.49	927.93	86.75	0.30	1469.2	55
	9	62.8	431.38	145.57	0.36	623.1	101
	10	46.85	199.78	234.5	0.42	268.8	174
240°C	11	33.19	92.83	357.48	0.48	118.0	281
	12	21.78	43.09	505.41	0.55	51.9	420
	13	13.24	20	662.15	0.61	23.2	571
		20x1					
	1	14.72	20	735.95	0.63	22.9	642
	2	23.31	43.09	540.93	0.56	51.6	452
	3	36.07	92.83	388.58	0.49	117.0	308
	4	49.17	199.78	246.1	0.42	268.8	183
	5	66.12	431.38	153.27	0.35	631.7	105
	6	83.67	927.93	90.17	0.28	1524.5	55
	7	103.54	1999.4	51.79	0.21	3879.8	27
	8	84.56	928.71	91.05	0.28	1525.7	55
	9	64.97	431.38	150.61	0.35	631.7	103
	10	48.73	200.17	243.46	0.42	269.3	181
	11	34.4	92.83	370.59	0.49	117.0	294
	12	22.85	43.09	530.33	0.56	51.6	443
	13	14.22	20	710.82	0.63	22.9	620

Table 4 Data of PP-C (PHC26) at 200°C

200°C	**16x1**						
	Stage	Corrected shear stress (kPa)	Shear rate (s^{-1})	Shear viscosity (Pa.s)	n	Corrected shear rate (s^{-1})	Corrected shear viscosity (Pa.s)
	1	17.79	20	889.55	0.69	22	800
	2	28.04	43.09	650.67	0.6	50	558
	3	43.6	92.83	469.69	0.52	114	382
	4	62.05	200.17	309.97	0.43	267	233
	5	82.16	430.6	190.81	0.35	631	130
	6	104.55	928.71	112.57	0.27	1556	67
	7	128.26	2000.17	64.12	0.18	4278	30
	8	104.26	927.93	112.36	0.27	1555	67
	9	82.38	431.38	190.97	0.35	632	130
	10	61.67	199.78	308.7	0.43	266	232
	11	43.28	92.83	466.23	0.52	114	379
	12	27.99	43.09	649.58	0.6	50	557
	13	15.96	20	797.99	0.69	22	717
		20x1					
	1	20.14	20	1006.75	0.63	23	878
	2	29.52	43.09	685	0.56	52	573
	3	45.15	92.83	486.32	0.49	117	386
	4	64.08	200.17	320.13	0.42	269	238
	5	84.66	430.6	196.62	0.35	631	134
	6	107.06	929.48	115.18	0.27	1558	69
	7	131.27	1999.4	65.65	0.2	3999	33
	8	106.81	928.71	115.01	0.27	1556	69
	9	84.66	430.6	196.6	0.35	631	134
	10	63.84	200.56	318.3	0.42	270	237
	11	45.46	92.83	489.69	0.49	117	389
	12	29.69	43.09	689.03	0.56	52	576
	13	17.91	20	895.28	0.63	23	781

Table 5 Data of PP-C (PHC26) at 220°C

220°C	**16x1**						
	Stage	Corrected shear stress (kPa)	Shear rate (s^{-1})	Shear viscosity (Pa.s)	n	Corrected shear rate (s^{-1})	Corrected shear viscosity (Pa.s)
	1	14.14	20	707.08	0.7	22	639
	2	22.96	43.09	532.94	0.62	50	462
	3	36.01	92.83	387.9	0.54	113	320
	4	53.2	199.78	266.28	0.46	258	206
	5	72.53	430.6	168.43	0.38	606	120
	6	93.84	928.71	101.04	0.3	1470	64
	7	115.95	1999.4	57.99	0.21	3880	30
	8	92.96	929.48	100.01	0.3	1472	63
	9	72.34	430.6	168	0.38	606	119
	10	52.89	200.17	264.24	0.46	259	204
	11	36.06	92.83	388.44	0.54	113	320
	12	23.1	43.09	536.12	0.62	50	465
	13	13.42	20	670.99	0.7	22	606
		20x1					
	1	14.4	20	719.91	0.71	22	653
	2	23.05	43.09	534.98	0.63	49	466
	3	36.35	92.83	391.55	0.54	113	323
	4	53.55	199.78	268.04	0.46	258	207
	5	73.25	431.38	169.79	0.38	607	121
	6	94.57	927.93	101.91	0.29	1496	63
	7	117.34	1999.4	58.69	0.21	3880	30
	8	96.35	928.71	103.75	0.29	1497	64
	9	74.8	432.16	173.08	0.38	608	123
	10	54.96	199.78	275.11	0.46	258	213
	11	37.36	92.83	402.47	0.54	113	332
	12	23.28	43.09	540.25	0.63	49	471
	13	13.76	20	688.1	0.71	22	624

Table 6 Data of PP-C (PHC26) at 240°C

	16x1						
	Stage	Corrected shear stress (kPa)	Shear rate (s^{-1})	Shear viscosity (Pa.s)	n	Corrected shear rate (s^{-1})	Corrected shear viscosity (Pa.s)
240°C	1	11.69	20	584.45	0.73	22	535
	2	17.89	43.09	415.29	0.66	49	368
	3	29.31	92.83	315.73	0.58	110	267
	4	44.59	200.17	222.76	0.5	250	178
	5	62.89	430.6	146.06	0.42	579	109
	6	83.46	928.71	89.87	0.34	1379	61
	7	104.96	2000.17	52.47	0.27	3352	31
	8	83.21	928.71	89.59	0.34	1379	60
	9	62.49	430.6	145.13	0.42	579	108
	10	43.6	200.17	217.82	0.5	250	174
	11	28.37	92.83	305.61	0.58	110	259
	12	17.38	43.09	403.35	0.66	49	357
	13	9.81	20	490.55	0.73	22	449
		20x1					
	1	10.68	20	533.99	0.77	21	497
	2	18.12	43.09	420.45	0.68	48	376
	3	29.73	92.83	320.22	0.59	109	273
	4	45.23	199.78	226.42	0.5	250	181
	5	63.88	431.38	148.09	0.42	580	110
	6	84.61	928.71	91.1	0.33	1400	60
	7	106.69	2000.17	53.34	0.24	3584	30
	8	83.19	928.71	89.58	0.33	1400	59
	9	62.55	430.6	145.27	0.42	579	108
	10	44.43	199.78	222.39	0.5	250	178
	11	28.94	92.83	311.79	0.59	109	266
	12	17.88	43.09	414.87	0.68	48	371
	13	9.95	20	497.64	0.77	21	463

Estimation of power law constants

Power law is known as: $\eta = k(\dot{\gamma})^{n-1}$

After changing into logarithmic form, it is:

$$\log \eta = \log k + (\mathrm{n} - 1)\log \dot{\gamma}$$

By plotting $\log \eta$ vs. $\log \dot{\gamma}$, a straight line will be obtained, and the intercept is $\log k$ while gradient is (n-1).

An example is given for PP-H at 200°C with 20x1 mm die.

Table 7 Calculated $\log \eta$ and $\log \dot{\gamma}$

Shear rate (s^{-1})	$\log \eta$	Viscosity (Pa.s)	$\log \dot{\gamma}$
24.6	1.39	957.3	3.0
55.2	1.74	640.5	2.8
124.9	2.10	399.0	2.6
282.4	2.45	235.8	2.4
651.5	2.81	132.8	2.1
1524.5	3.18	72.3	1.9
3582.3	3.55	38.8	1.6

A graph can be plotted as below according to data in Table 7.

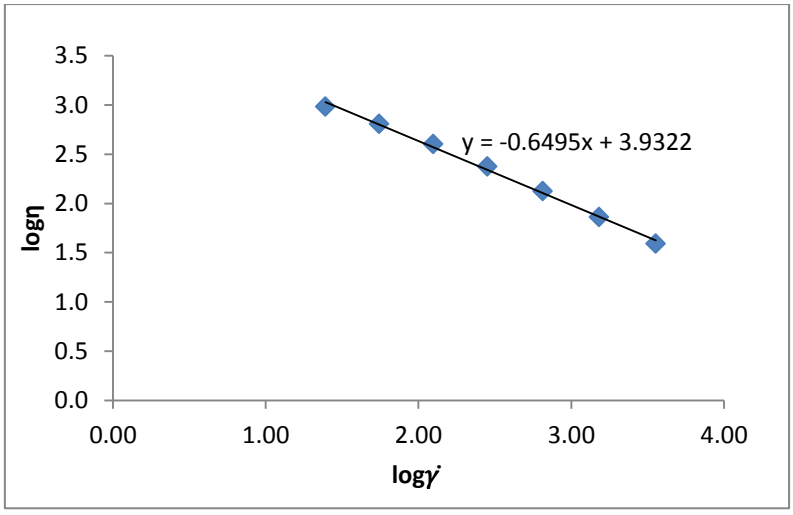

Figure 1 Plot of $\log \eta$ vs. $\log \dot{\gamma}$

Therefore, $\log k = 3.9322$ and $(n - 1) = -0.6495$. After calculation, $k = 8555$ and $n = 0.35$.

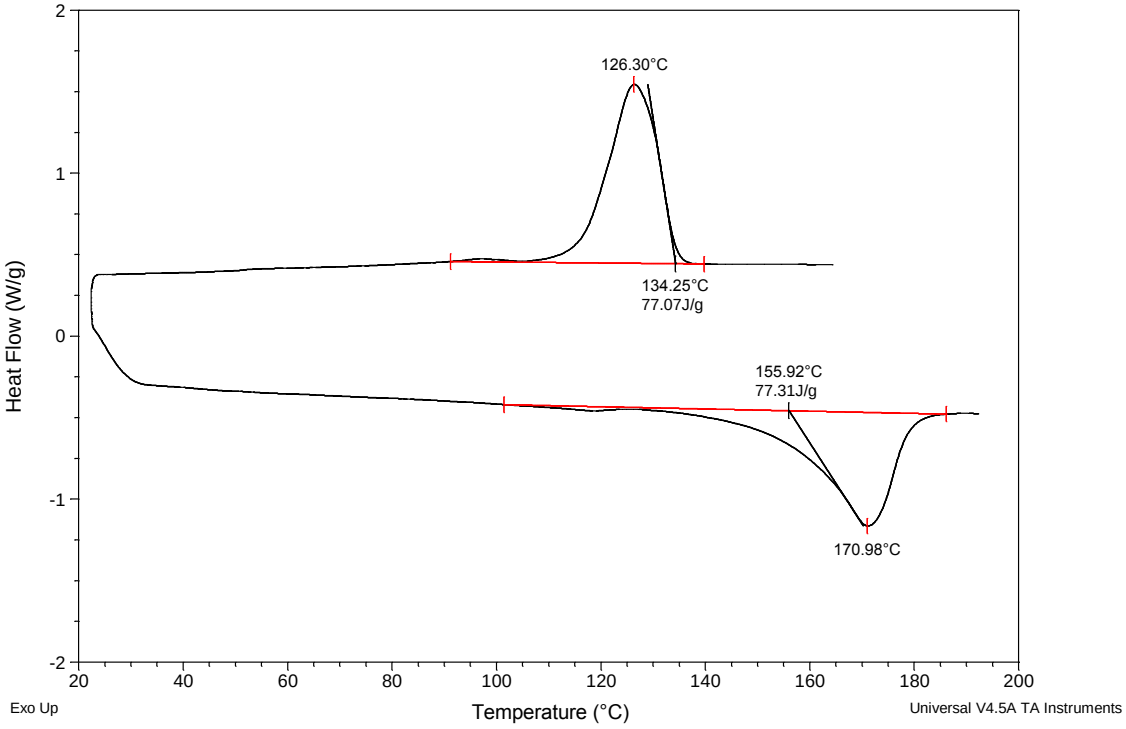

Figure 2 DSC curve of PP-C

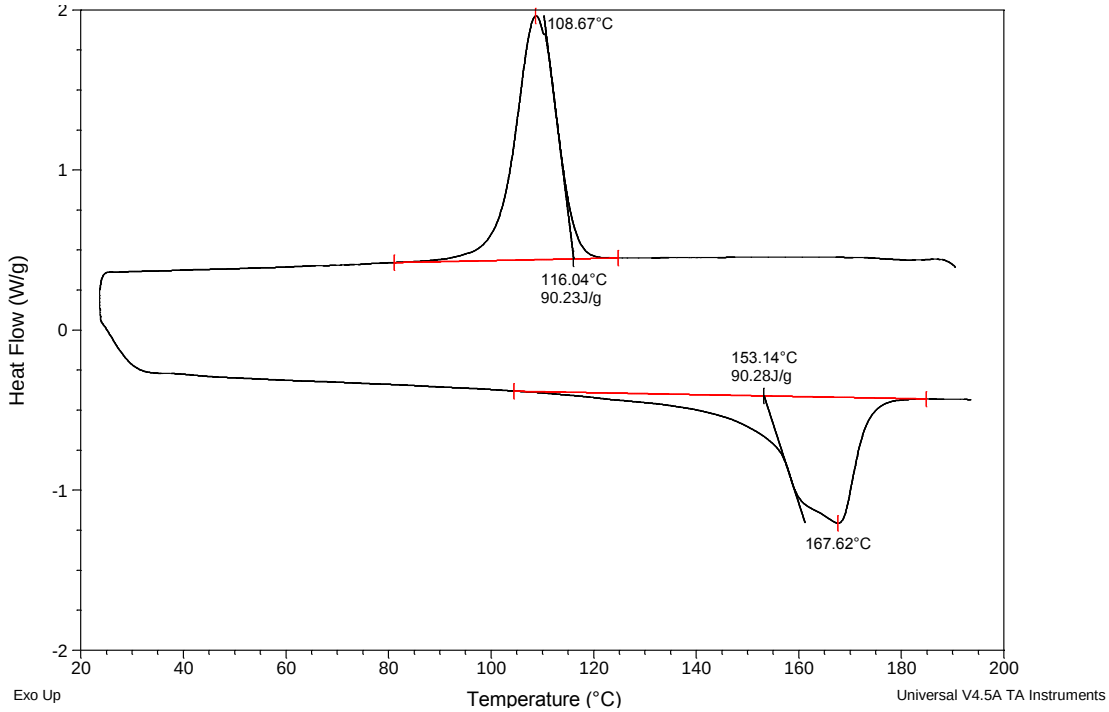

Figure 3 DSC curve of PPgMA

Appendix B

Table 1 ANOVA Table for mass output (A = barrel temperature, B = screw speed, C = blend concentration of A850 recycled PP)

Source	Sum of Squares	Df	Mean Square	F-Value	p-value
Model	3838.45	9	426.49	40.13	< 0.0001
A	39.66	1	39.66	3.73	0.0822
B	3150.8	1	3150.8	296.49	< 0.0001
C	85.59	1	85.59	8.05	0.0176
AB	290.89	1	290.89	27.37	0.0004
AC	119.2	1	119.2	11.22	0.0074
BC	108.63	1	108.63	10.22	0.0095
A^2	34.22	1	34.22	3.22	0.103
B^2	5.03	1	5.03	0.47	0.507
C^2	0.72	1	0.72	0.068	0.8001
Residual	106.27	10	10.63		

Table 2 ANOVA Table for mass output (A = barrel temperature, B = screw speed, C = blend concentration of A850 recycled PP)

Source	Sum of Squares	Df	Mean Square	F-Value	p-value
Model	3084.36	9	342.71	18.09	< 0.0001
A	584.74	1	584.74	30.87	0.0002
B	163	1	163	8.6	0.015
C	1980.31	1	1980.31	104.54	< 0.0001
AB	3.13	1	3.13	0.16	0.6932
AC	21.13	1	21.13	1.12	0.3158
BC	3.13	1	3.13	0.16	0.6932
A^2	47.35	1	47.35	2.5	0.145
B^2	14.87	1	14.87	0.79	0.3964
C^2	264.91	1	264.91	13.98	0.0038
Residual	189.44	10	18.94		

Table 3 ANOVA Table for temperature increase at the die (A = barrel temperature, B = screw speed, C = blend concentration of A850 recycled PP)

Source	Sum of Squares	Df	Mean Square	F-Value	p-value
Model	284.66	9	31.63	7.48	0.0021
A	0.39	1	0.39	0.093	0.7666
B	128.33	1	128.33	30.34	0.0003
C	155.55	1	155.55	36.78	0.0001
AB	0	1	0	0	1
AC	0	1	0	0	1
BC	0	1	0	0	1
A^2	6.45E-03	1	0.006452	0.001526	0.9696
B^2	6.45E-03	1	0.006452	0.001526	0.9696
C^2	0.35	1	0.35	0.083	0.7798
Residual	42.29	10	4.23		

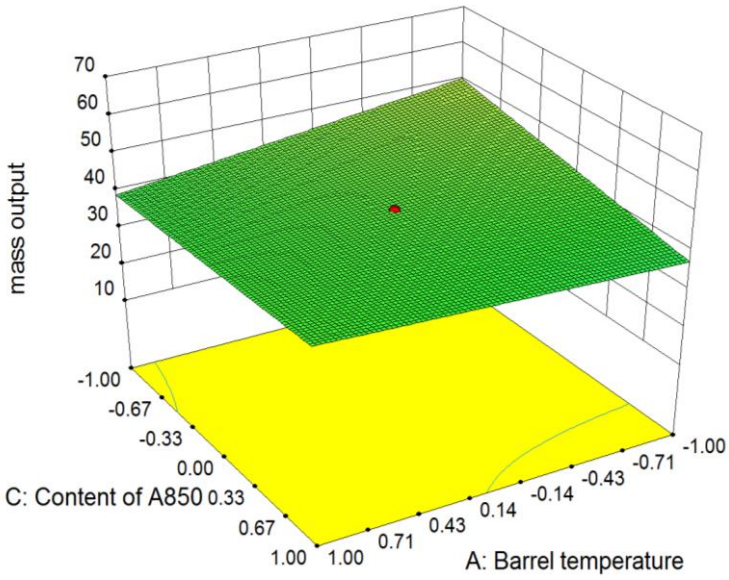

Figure 1 Response surface of mass output as a function of barrel temperature (factor A) and composition ratio (content of A850, factor C). A is set at the neutral point, i.e. zero-level).

Appendix C

Table 1 ANOVA Table for yield strength (A = concentration of AM, B = concentration of PPgMA, C = concentration of organoclay)

Source	Sum of Squares	Df	Mean Square	F-Value	p-value
Model	109.29	9	12.14	0.68	0.7131
A	1.71	1	1.71	0.096	0.7636
B	0.64	1	0.64	0.036	0.8537
C	44.05	1	44.05	2.47	0.1473
AB	10.58	1	10.58	0.59	0.4592
AC	3.92	1	3.92	0.22	0.6494
BC	22.44	1	22.44	1.26	0.2884
A^2	14.99	1	14.99	0.84	0.3811
B^2	2.66	1	2.66	0.15	0.7075
C^2	7.83	1	7.83	0.44	0.5228
Residual	178.53	10	17.85		

Table 2 ANOVA Table for tensile modulus (A = concentration of AM, B = concentration of PPgMA, C = concentration of organoclay)

Source	Sum of Squares	Df	Mean Square	F-Value	p-value
Model	8790.99	9	976.78	2.77	0.0644
A	5067.16	1	5067.16	14.35	0.0036
B	24.19	1	24.19	0.069	0.7988
C	923.8	1	923.8	2.62	0.1368
AB	347.16	1	347.16	0.98	0.3448
AC	1232.56	1	1232.56	3.49	0.0913
BC	20.16	1	20.16	0.057	0.816
A^2	19.6	1	19.6	0.056	0.8185
B^2	97.35	1	97.35	0.28	0.611
C^2	998.96	1	998.96	2.83	0.1235
Residual	3531.07	10	353.11		

Table 3 Raw data of tensile tests (Run1 to Run 12).

Run 1	Yield strength (MPa)	Tensile modulus (MPa)	Run 2	Yield strength (MPa)	Tensile modulus (MPa)	Run 3	Yield strength (MPa)	Tensile modulus (MPa)
1-1	33.8	773.9	**2-1**	20.7	725.5	**3-1**	22.8	661.7
1-2	32.7	715.0	**2-2**	22.7	754.2	**3-2**	23.7	694.2
1-3	30.1	757.1	**2-3**	24.0	780.0	**3-3**	25.6	653.2
1-4	33.3	763.2	**2-4**	24.4	767.6	**3-4**	22.6	710.3
1-5	32.6	735.5	**2-5**	24.1	731.3	**3-5**	19.7	755.0
1-6	28.3	796.6	**2-6**	23.2	756.6	**3-6**	23.2	721.7
1-7	31.1	784.0	**2-7**	22.7	741.5	**3-7**	20.9	724.3
1-8	32.3	763.1	**2-8**	23.7	763.5	**3-8**	22.6	708.6
Ave.	31.8	761.1	**Ave.**	23.2	752.5	**Ave.**	22.6	703.6
Run 4			**Run 5**			**Run 6**		
4-1	22.9	662.2	**5-1**	23.6	725.9	**6-1**	31.0	767.1
4-2	25.6	702.8	**5-2**	31.8	704.3	**6-2**	34.5	704.9
4-3	29.4	686.2	**5-3**	35.3	752.8	**6-3**	30.4	698.0
4-4	23.9	732.7	**5-4**	31.3	732.5	**6-4**	25.0	708.7
4-5	20.6	671.5	**5-5**	23.8	752.2	**6-5**	21.0	755.4
4-6	30.9	665.7	**5-6**	33.1	664.6	**6-6**	27.4	693.7
4-7	24.7	748.6	**5-7**	32.9	752.7	**6-7**	26.1	642.0
4-8	25.5	710.5	**5-8**	30.4	702.4	**6-8**	30.5	721.5
Ave.	25.4	697.5	**Ave.**	30.3	723.4	**Ave.**	28.2	711.4
Run 7			**Run 8**			**Run 9**		
7-1	27.5	705.8	**8-1**	27.7	766.5	**9-1**	27.7	720.8
7-2	25.5	793.0	**8-2**	34.8	752.0	**9-2**	28.5	706.2
7-3	30.7	767.8	**8-3**	35.2	679.9	**9-3**	27.3	720.6
7-4	29.7	778.0	**8-4**	34.6	784.1	**9-4**	19.9	734.0
7-5	20.9	753.3	**8-5**	32.6	728.3	**9-5**	20.5	700.7
7-6	23.4	749.7	**8-6**	35.6	749.2	**9-6**	27.3	741.8
7-7	21.0	795.0	**8-7**	34.1	769.3	**9-7**	25.7	733.3
7-8	24.4	773.4	**8-8**	33.4	763.1	**9-8**	24.7	708.1
Ave.	25.4	764.5	**Ave.**	33.5	749.0	**Ave.**	25.2	720.7
Run 10			**Run 11**			**Run 12**		
10-1	32.3	730.4	**11-1**	26.4	719.3	**12-1**	28.6	754.8
10-2	28.7	712.7	**11-2**	30.0	753.5	**12-2**	29.7	612.7
10-3	26.8	728.7	**11-3**	24.3	696.2	**12-3**	20.2	686.8
10-4	23.4	673.2	**11-4**	28.3	779.0	**12-4**	27.9	745.0
10-5	25.3	659.4	**11-5**	25.7	682.6	**12-5**	24.2	726.3
10-6	25.3	739.1	**11-6**	28.3	754.5	**12-6**	25.9	627.1
10-7	25.0	623.4	**11-7**	24.9	701.8	**12-7**	26.4	699.4
10-8	26.2	683.4	**11-8**	28.1	732.5	**12-8**	25.2	678.6
Ave.	26.6	693.8	**Ave.**	27.0	727.4	**Ave.**	26.0	693.6

Table 4 Raw data of tensile tests (Run13 to Run 20).

Run 13	Yield strength (MPa)	Tensile modulus (MPa)	Run 14	Yield strength (MPa)	Tensile modulus (MPa)	Run 15	Yield strength (MPa)	Tensile modulus (MPa)
13-1	35.3	668.9	**14-1**	34.3	750.6	**15-1**	35.7	744.6
13-2	31.2	726.7	**14-2**	35.7	770.8	**15-2**	32.7	650.2
13-3	32.6	730.1	**14-3**	34.4	704.9	**15-3**	33.4	713.6
13-4	38.0	706.2	**14-4**	33.7	733.4	**15-4**	35.3	686.8
13-5	37.0	711.3	**14-5**	31.5	782.5	**15-5**	33.0	699.2
13-6	28.5	694.8	**14-6**	35.4	805.9	**15-6**	27.7	706.1
13-7	29.6	647.2	**14-7**	31.3	715.2	**15-7**	31.8	678.5
13-8	33.4	723.6	**14-8**	34.1	769.1	**15-8**	31.9	711.0
Ave.	33.2	701.1	**Ave.**	33.8	754.1	**Ave.**	32.7	698.7
Run 16			**Run 17**			**Run 18**		
16-1	17.7	723.3	**17-1**	37.0	716.2	**18-1**	29.5	668.1
16-2	30.9	662.8	**17-2**	28.0	701.0	**18-2**	33.3	714.1
16-3	26.4	621.9	**17-3**	28.7	735.9	**18-3**	33.8	707.7
16-4	24.2	664.6	**17-4**	34.6	714.3	**18-4**	35.2	754.6
16-5	31.2	704.7	**17-5**	27.7	701.1	**18-5**	31.3	635.0
16-6	31.9	664.4	**17-6**	20.7	675.2	**18-6**	33.1	719.9
16-7	28.0	691.1	**17-7**	38.5	780.8	**18-7**	32.3	705.3
16-8	27.9	680.1	**17-8**	32.3	720.0	**18-8**	32.1	731.2
Ave.	27.3	676.6	**Ave.**	30.9	718.1	**Ave.**	32.6	704.5
Run 19			**Run 20**					
19-1	37.7	804.1	**20-1**	33.9	699.4			
19-2	37.3	717.9	**20-2**	32.8	752.9			
19-3	35.4	664.5	**20-3**	24.4	692.9			
19-4	38.2	748.2	**20-4**	34.3	678.1			
19-5	35.4	681.6	**20-5**	28.7	686.9			
19-6	30.9	693.8	**20-6**	31.3	726.2			
19-7	36.0	710.3	**20-7**	24.8	687.3			
19-8	37.3	688.5	**20-8**	30.2	681.9			
Ave.	36.0	713.6	**Ave.**	30.0	700.7			

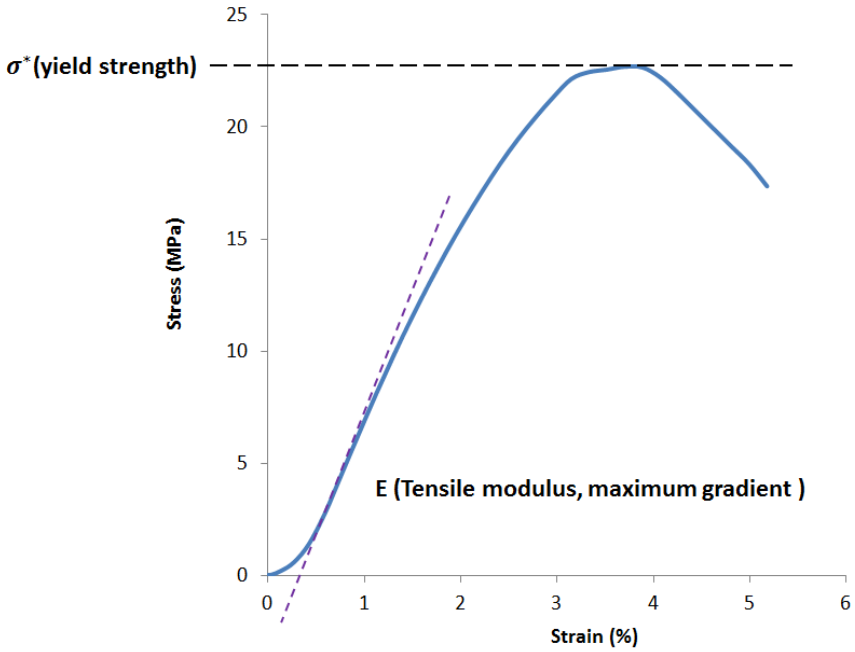

Figure 1 A typical stress-strain graph obtained from the PPCN samples

Appendix D

Table 1 Tensile test results (samples prepared by APV twin screw extruder)

Run 1	Tensile modulus (MPa)	Yield strength (MPa)	Run 2	Tensile modulus (MPa)	Yield strength (MPa)	Run 3	Tensile modulus (MPa)	Yield strength (MPa)
1-1	689.6	33.4	**2-1**	687.3	35.1	**3-1**	651.5	32.9
1-2	693.8	35.2	**2-2**	670.2	34.3	**3-2**	671.4	34.6
1-3	684.7	34.1	**2-3**	697.3	34.3	**3-3**	621.3	31.3
1-4	654.4	30.6	**2-4**	661.5	35.2	**3-4**	641.2	34.4
1-5	664.2	31.8	**2-5**	604.5	34.5	**3-5**	656.7	32.8
1-6	654.7	33.5	**2-6**	594.9	34.2	**3-6**	614.7	35.6
1-7	684.2	34.5	**2-7**	635.5	35.3	**3-7**	684.5	35.2
1-8	635.6	34.4	**2-8**	664.7	33.9	**3-8**	703.9	34.3
Ave.	670.1	33.4	**Ave.**	652.0	34.6	**Ave.**	655.7	33.9
Run 4			**Run 5**			**Run 6**		
4-1	686.2	35.1	**5-1**	689.5	37.3	**6-1**	610.3	34.7
4-2	649.7	34.1	**5-2**	651.6	36.0	**6-2**	711.2	38.2
4-3	673.3	33.6	**5-3**	634.3	35.8	**6-3**	643.3	36.0
4-4	659.6	32.9	**5-4**	695.2	37.6	**6-4**	655.6	36.2
4-5	669.2	32.7	**5-5**	738.3	38.4	**6-5**	636.3	34.4
4-6	657.3	34.0	**5-6**	689.8	36.5	**6-6**	647.8	33.5
4-7	589.2	32.9	**5-7**	670.7	36.2	**6-7**	622.3	32.3
4-8	636.5	30.1	**5-8**	700.2	38.0	**6-8**	621.5	34.7
Ave.	652.6	33.2	**Ave.**	683.7	37.0	**Ave.**	643.5	35.0
Run 7			**Run 8**			**Run 9**		
7-1	660.1	32.2	**8-1**	631.3	35.0	**9-1**	612.8	34.7
7-2	607.9	31.8	**8-2**	619.4	35.1	**9-2**	698.9	37.1
7-3	563.0	31.5	**8-3**	599.6	33.9	**9-3**	672.3	38.0
7-4	601.6	29.7	**8-4**	613.3	34.5	**9-4**	659.7	35.7
7-5	561.8	27.6	**8-5**	636.0	32.6	**9-5**	587.9	33.2
7-6	617.6	29.5	**8-6**	590.8	34.1	**9-6**	620.3	33.9
7-7	611.0	31.0	**8-7**	646.9	35.9	**9-7**	627.1	34.0
7-8	607.9	31.1	**8-8**	655.3	36.1	**9-8**	601.2	34.9
Ave.	603.9	30.5	**Ave.**	624.1	34.6	**Ave.**	635.0	35.2
Run 10			**Run 11**			**Run 12**		
10-1	634.6	36.9	**11-1**	717.5	36.5	**12-1**	608.8	34.0
10-2	615.9	35.2	**11-2**	683.2	36.6	**12-2**	641.2	35.1
10-3	651.1	34.3	**11-3**	652.2	35.5	**12-3**	618.0	36.4
10-4	614.3	34.8	**11-4**	666.6	34.6	**12-4**	636.3	36.6
10-5	667.5	35.0	**11-5**	621.0	34.8	**12-5**	727.7	37.9
10-6	664.8	35.0	**11-6**	569.3	31.9	**12-6**	660.2	38.7
10-7	670.5	35.3	**11-7**	640.4	35.0	**12-7**	614.1	37.7
10-8	585.2	34.7	**11-8**	644.9	34.8	**12-8**	557.0	34.6
Ave.	638.0	35.1	**Ave.**	649.4	35.0	**Ave.**	632.9	36.4
Run 13								
13-1	592.2	34.1						
13-2	624.7	34.2						
13-3	656.5	33.5						
13-4	646.4	32.1						
13-5	638.4	34.9						
13-6	695.1	35.7						
13-7	612.8	33.8						
13-8	560.8	35.0						
Ave.	628.4	34.2						

Table 2 Tensile test results (sample prepared by Haake twin rotor mixer)

Run 1	Tensile modulus (MPa)	Yield strength (MPa)	Run 2	Tensile modulus (MPa)	Yield strength (MPa)	Run3	Tensile modulus (MPa)	Yield strength (MPa)
1-1	692.2	33.1	**2-1**	720.5	29.1	**3-1**	700.0	27.9
1-2	710.5	31.1	**2-2**	707.1	29.7	**3-2**	656.9	31.5
1-3	612.7	27.5	**2-3**	685.8	29.5	**3-3**	661.9	23.2
1-4	701.3	23.2	**2-4**	710.5	30.1	**3-4**	704.8	29.5
1-5	628.9	29.9	**2-5**	693.3	28.9	**3-5**	682.1	21.7
1-6	674.3	30.1	**2-6**	715.8	30.7	**3-6**	653.5	26.7
1-7	680.6	28.5	**2-7**	695.4	28.7	**3-7**	705.4	28.1
1-8	652.3	29.0	**2-8**	707.8	28.7	**3-8**	684.6	26.1
Ave.	669.1	29.0	**Ave.**	704.5	29.4	**Ave.**	681.1	26.8
Run 4			**Run 5**			**Run6**		
4-1	702.3	32.1	**5-1**	665.7	31.3	**6-1**	662.9	30.4
4-2	707.5	29.5	**5-2**	661.8	22.1	**6-2**	640.6	19.8
4-3	627.3	30.2	**5-3**	702.9	24.8	**6-3**	713.8	20.9
4-4	679.5	26.4	**5-4**	699.3	25.1	**6-4**	664.3	23.9
4-5	643.9	30.6	**5-5**	708.9	27.6	**6-5**	682.2	24.4
4-6	664.1	31.1	**5-6**	652.3	26.8	**6-6**	692.3	23.1
4-7	683.2	28.2	**5-7**	659.4	25.1	**6-7**	653.1	22.9
4-8	669.1	30.2	**5-8**	664.2	26.4	**6-8**	670.8	24.3
Ave.	672.1	29.8	**Ave.**	676.8	26.1	**Ave.**	672.5	23.7
Run 7			**Run 8**			**Run9**		
7-1	748.7	27.5	**8-1**	666.6	32.5	**9-1**	704.8	32.4
7-2	682.0	24.7	**8-2**	713.6	32.5	**9-2**	699.3	32.8
7-3	682.3	25.8	**8-3**	731.2	33.5	**9-3**	715.0	32.8
7-4	651.7	29.3	**8-4**	677.2	31.6	**9-4**	657.3	32.1
7-5	710.5	28.8	**8-5**	701.9	30.9	**9-5**	706.7	32.6
7-6	701.2	27.7	**8-6**	650.7	32.5	**9-6**	709.7	32.3
7-7	678.3	26.9	**8-7**	711.9	32.9	**9-7**	697.1	33.7
7-8	705.9	27.5	**8-8**	667.3	33.3	**9-8**	682.8	32.4
Ave.	695.1	27.3	**Ave.**	690.1	32.5	**Ave.**	696.6	32.6
Run 10			**Run 11**					
10-1	712.2	24.3	**11-1**	657.0	28.4			
10-2	672.5	30.0	**11-2**	690.0	32.6			
10-3	688.3	33.0	**11-3**	642.5	31.6			
10-4	725.1	29.7	**11-4**	693.9	28.7			
10-5	621.1	33.2	**11-5**	705.1	32.4			
10-6	699.7	28.7	**11-6**	671.3	31.7			
10-7	679.3	29.1	**11-7**	701.2	29.4			
10-8	671.9	32.3	**11-8**	660.8	31.5			
Ave.	683.8	30.0	**Ave.**	677.7	30.8			

Table 3 ANOVA Table for interlayer spacing (Twin screw extruder, A = feed rate, B = screw speed)

Source	Sum of Squares	Df	Mean Square	F-Value	p-value
Model	0.200	5	0.040	0.630	0.682
A	0.016	1	0.016	0.260	0.627
B	0.170	1	0.170	2.770	0.140
AB	0.000	1	0.000	0.002	0.969
A2	0.008	1	0.008	0.130	0.730
B2	0.001	1	0.001	0.015	0.906
Residual	0.440	7	0.063		

Table 4 ANOVA Table for yield strength (Twin screw extruder, A = feed rate, B = screw speed)

Source	Sum of Squares	Df	Mean Square	F-Value	p-value
Model	16.810	5	3.360	1.710	0.250
A	7.970	1	7.970	4.060	0.084
B	2.420	1	2.420	1.230	0.304
AB	0.200	1	0.200	0.100	0.758
A2	0.330	1	0.330	0.170	0.696
B2	5.430	1	5.430	2.760	0.140
Residual	13.760	7	1.970		

Table 5 ANOVA Table for interlayer spacing (Twin rotor mixer, A = mixing time, B = rotor speed)

Source	Sum of Squares	Df	Mean Square	F-Value	p-value
Model	0.170	5	0.034	2.110	0.216
A	0.040	1	0.040	2.460	0.178
B	0.100	1	0.100	6.300	0.054
AB	0.000	1	0.000	0.000	0.995
A2	0.002	1	0.002	0.150	0.711
B2	0.029	1	0.029	1.800	0.238
Residual	0.081	5	0.016		

Table 6 ANOVA Table for yield strength (Twin rotor mixer, A = mixing time, B = rotor speed)

Source	Sum of Squares	Df	Mean Square	F-Value	p-value
Model	17.930	5	3.590	0.320	0.883
A	0.053	1	0.053	0.005	0.948
B	3.500	1	3.500	0.310	0.602
AB	14.060	1	14.060	1.250	0.315
A2	0.160	1	0.160	0.014	0.911
B2	0.066	1	0.066	0.006	0.942
Residual	56.460	5	11.290		

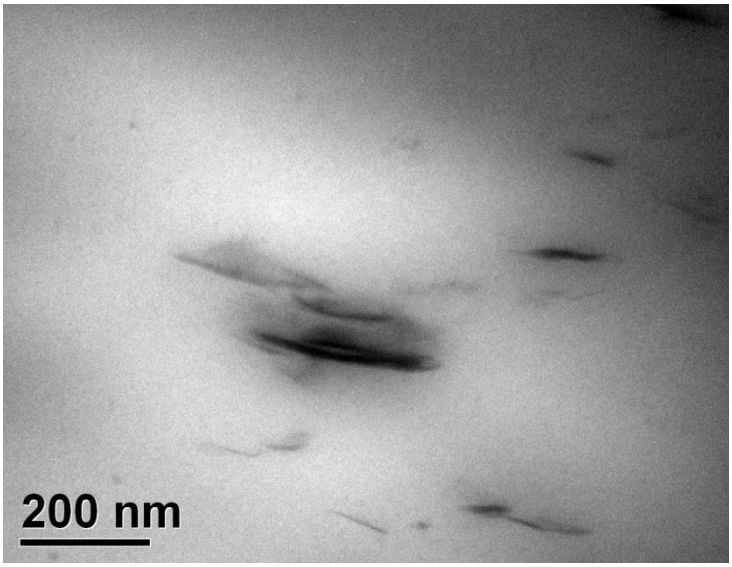

Figure 1 TEM image for PPCN prepared by APV twin screw extruder (300rpm, 4kg h^{-1})

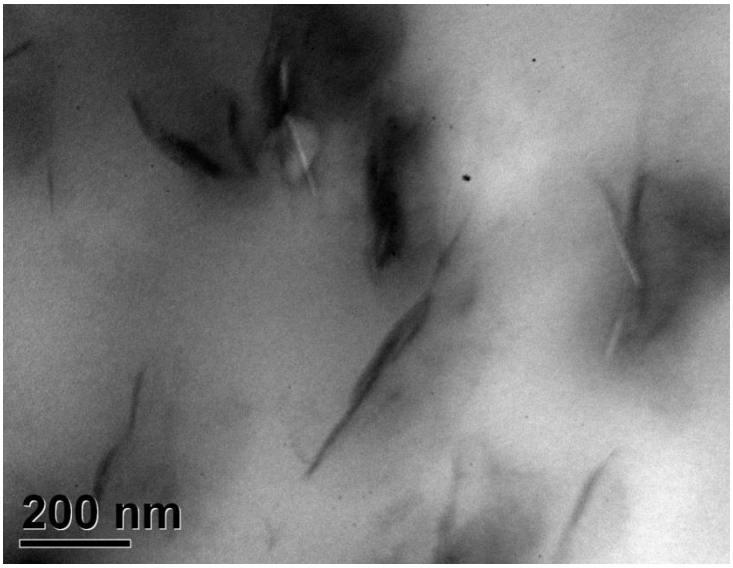

Figure 2 TEM image for PPCN prepared by Haake twin rotor mixer (70rpm, 7min)

Appendix E

Table 1 Weight of injection moulded part vs. hold-on time for PPCNH series (hold-on pressure: 10bar)

Hold-on time	Moulding 1	Moulding 2	Moulding 3	Average	Stdv
2	54.4	54.3	53.7	54.1	0.38
4	54.6	54.4	54.6	54.5	0.12
6	55	55.1	54.6	54.9	0.26
8	54.8	54.7	55.2	54.9	0.26
10	54.5	55.2	54.8	54.8	0.35

Table 2 Tensile test results for samples cut parallel and perpendicular to flow direction

	Modulus (MPa)		**Strength (MPa)**	
Angle to flow direction	0°	90°	0°	90°
PPC-20-25	338.4	296.0	22.9	21.0
Stv.	85.7	39.3	0.3	0.5
PPCNC-20-25	360.8	229.6	22.8	19.7
Stv.	46.2	44.5	0.4	0.3

Table 3 FWIT result for PPCNC parts produced under different conditions

Sample code	**Failure Energy**	**Stv.**
PPCNC-10-25	8.33	0.28
PPCNC-20-25	7.71	0.42
PPCNC-30-25	7.80	0.30
PPCNC-40-25	8.12	0.40
PPCNC-20-35	7.69	0.28
PPCNC-20-45	7.05	0.56
PPCNC-20-55	7.68	0.13

Table4 Thickness of the thick section of PPCNC samples

Sample code	**Thickness of thick section (mm)**
PPCNC-10-25	2.85
PPCNC-20-25	2.77
PPCNC-30-25	2.79
PPCNC-40-25	2.83
PPCNC-20-35	2.78
PPCNC-20-45	2.75
PPCNC-20-55	2.77

Table 5 Resulting data for tensile tests

Sample code	Modulus (MPa)	Stv.	Strength (MPa)	Stv.
PPH-10-25	771.6	52.8	39.4	1.1
PPH-20-25	693.8	50.5	40.3	1.3
PPH-30-25	626.0	42.6	38.5	0.7
PPH-40-25	615.0	64.1	38.3	0.8
PPH-20-35	715.4	28.8	38.2	0.3
PPH-20-45	739.0	40.3	39.0	0.5
PPH-20-55	731.3	78.3	37.3	1.0
PPCNH-10-25	815.4	34.8	42.4	1.3
PPCNH-20-25	772.1	45.7	38.4	1.1
PPCNH-30-25	704.3	65.9	38.5	0.6
PPCNH-40-25	699.0	66.0	37.6	0.8
PPCNH-20-35	752.3	44.3	39.0	1.0
PPCNH-20-45	767.5	66.1	38.5	0.7
PPCNH-20-55	756.1	55.5	37.9	0.5

Table 6 Result of tensile tests at 80°C

Sample	Modulus (MPa)	Stv.	Strength (MPa)	Stv.
PPH-30-25	147.6	12.6	16.5	1.3
PPCNH-30-25	163.0	14.8	16.6	0.5

Table 7 DSC result for PPCNH samples

Sample Code	Enthalpy of fusion (J g^{-1})	Crystallinity (%)	Melting point(°C)
PPCNH-10-25	84.10	44.46	166.38
PPCNH-20-25	84.92	44.90	166.81
PPCNH-30-25	85.68	45.30	166.17
PPCNH-40-25	87.18	46.09	166.02
PPCNH-20-35	85.20	45.04	166.53
PPCNH-20-45	85.47	45.19	166.87
PPCNH-20-55	86.40	45.68	166.34

Table 8 DSC results for PPCNC samples

Sample Code	Enthalpy of fusion (J/g)	Crystallinity (%)	Melting point(°C)
PPCNC-10-25	60.65	31.92	167.82
PPCNC-20-25	62.21	32.75	167.00
PPCNC-30-25	64.01	33.69	166.65
PPCNC-40-25	65.33	34.39	167.03
PPCNC-20-35	66.05	34.77	166.20
PPCNC-20-45	67.03	35.28	166.16
PPCNC-20-55	67.26	35.40	165.89

Table 9 d_{001} values of injection moulded parts

Sample code	d_{001}	Sample code	d_{001}
PPCNH-10-25	3.85	PPCNC-10-25	5.58
PPCNH-20-25	3.85	PPCNC-20-25	5.58
PPCNH-30-25	3.82	PPCNC-30-25	5.62
PPCNH-40-25	3.85	PPCNC-40-25	5.70
PPCNH-20-35	3.85	PPCNC-20-35	5.62
PPCNH-20-45	3.82	PPCNC-20-45	5.62
PPCNH-20-55	3.85	PPCNC-20-55	5.58

Table 10 Calculated frozen layer fraction

Sample code	Part thickness (um)	Frozen layer thickness (um)	Frozen layer fraction (%)
PPCNH-10-25	1354	1016	75.0
PPCNH-20-25	1218	742	60.9
PPCNH-30-25	1380	636	46.1
PPCNH-40-25	1421	579	40.7
PPCNH-20-35	1411	788	55.8
PPCNH-20-45	1331	624	46.9
PPCNH-20-55	1340	580	43.3
PPCNC-10-25	1360	1016	74.7
PPCNC-20-25	1433	804	56.1
PPCNC-30-25	1556	644	41.4
PPCNC-40-25	1534	348	22.7
PPCNC-20-35	1452	710	48.9
PPCNC-20-45	1394	616	44.2
PPCNC-20-55	1437	600	41.8

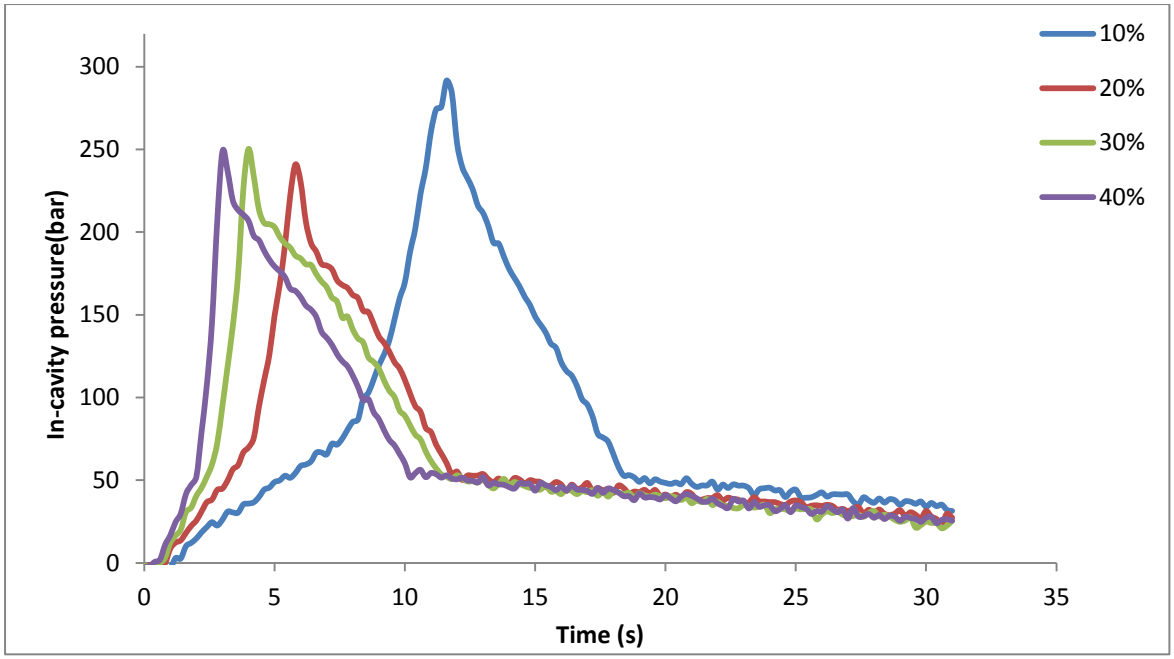

Figure 1 Effect of injection speed on the plots of in-cavity pressure vs. time for PPCNC samples.

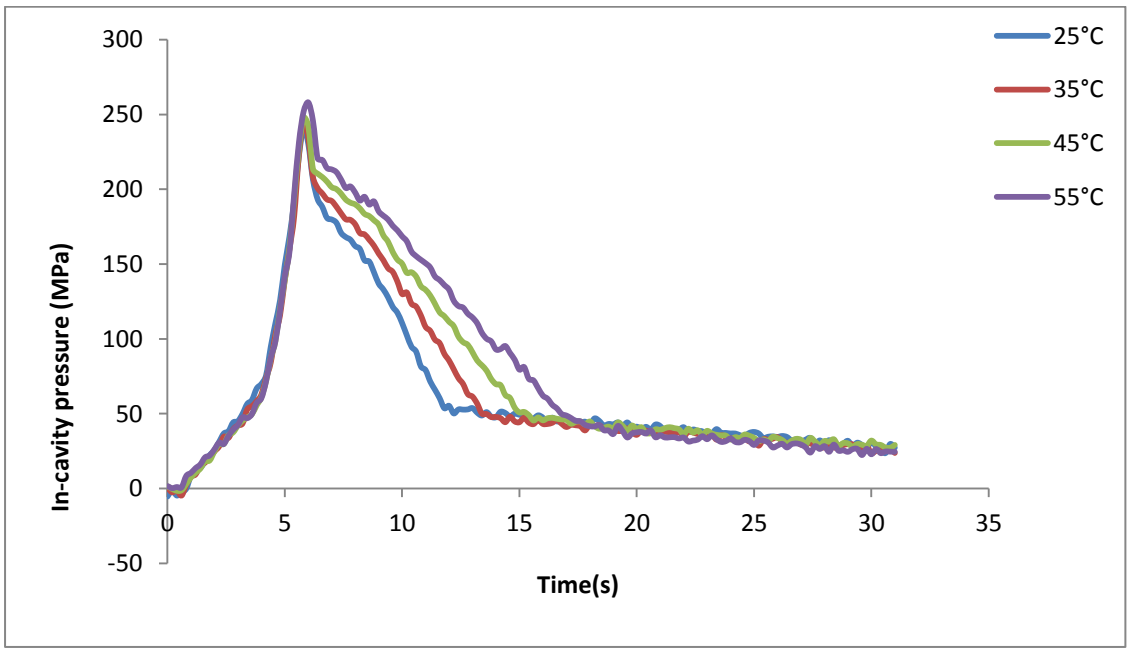

Figure 2 Effect of mould temperature on the plots of in-cavity pressure vs. time for PPCNC.

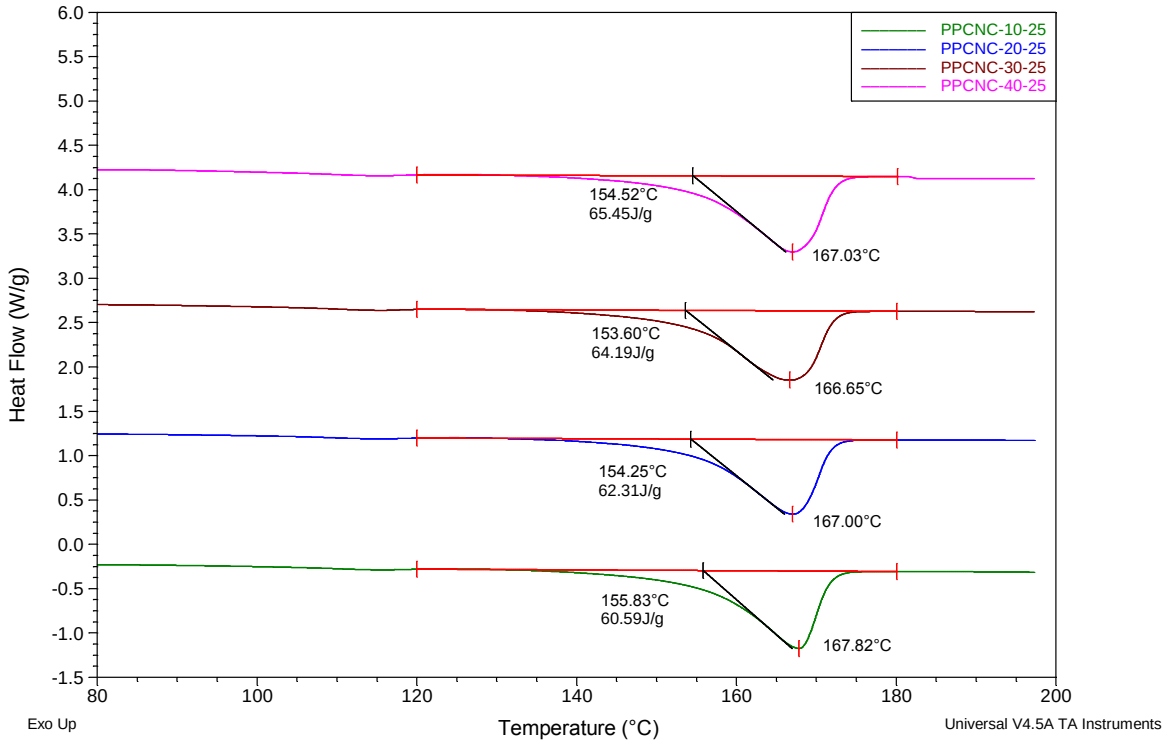

Figure 3 DSC curves for PPCNC samples produced under different injection

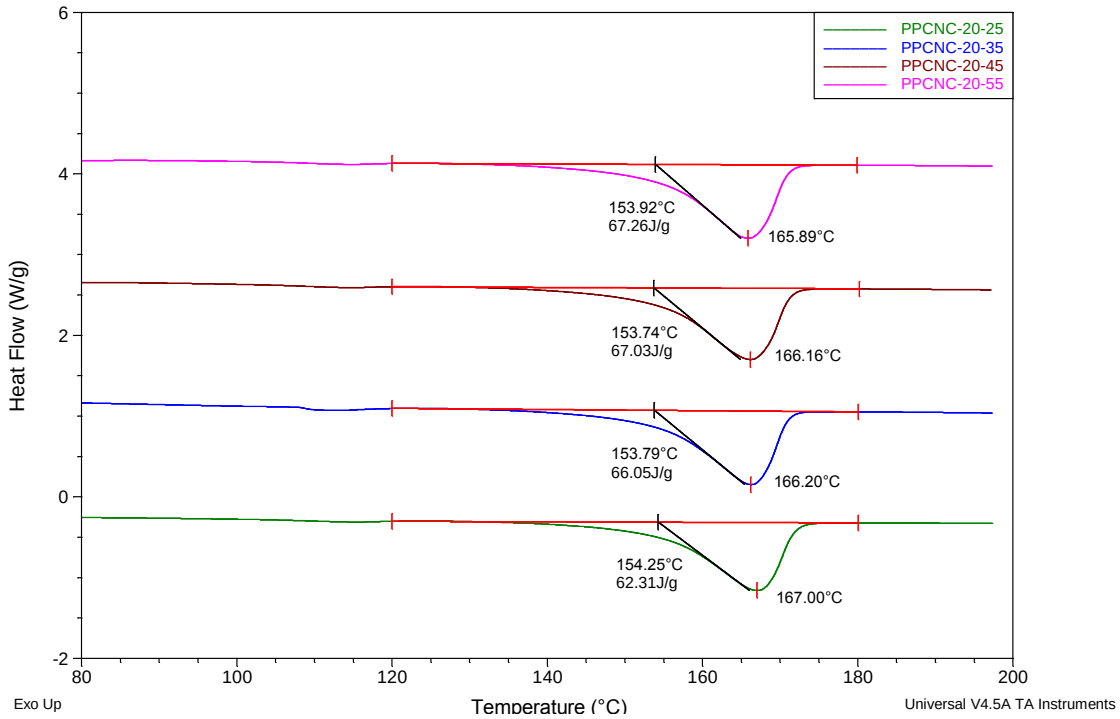

Figure 4 DSC curves for PPCNC samples produced under mould temperature

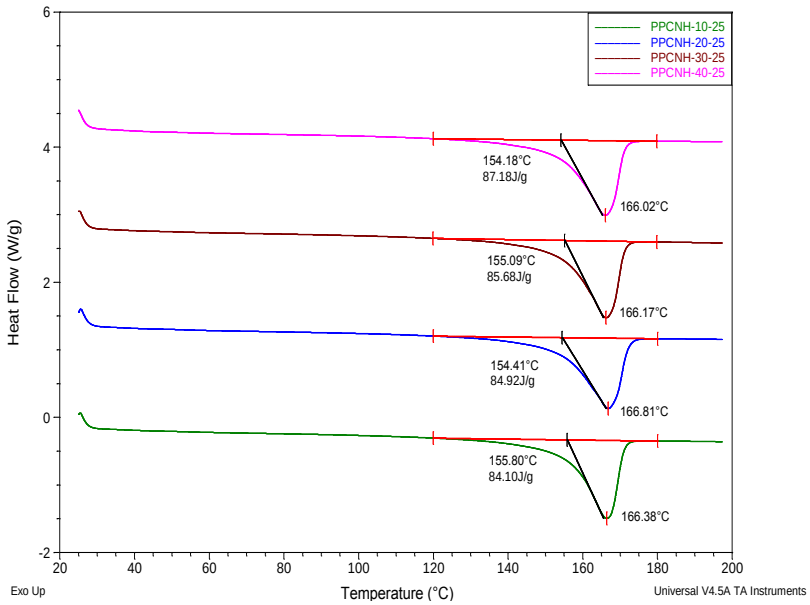

Figure 5 DSC curves of PPCNH samples produced under different injection speeds

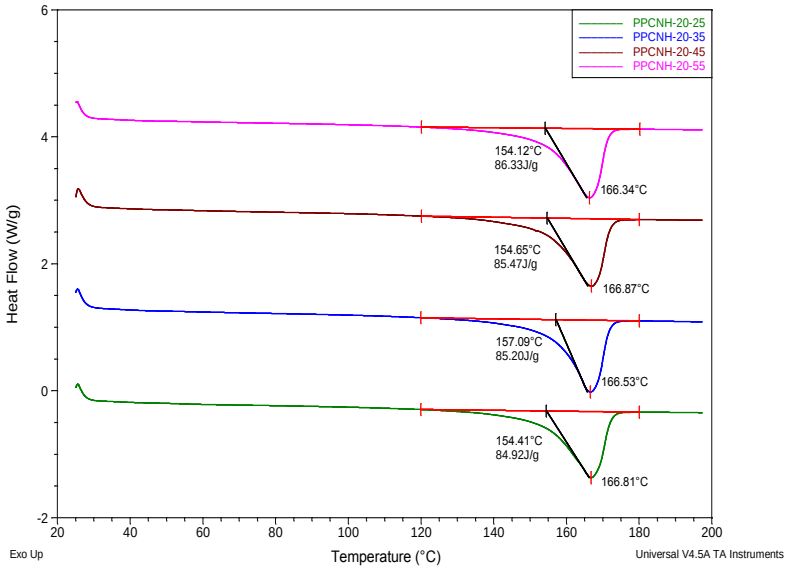

Figure 6 DSC curves of PPCNH samples produced under different mould temperatures

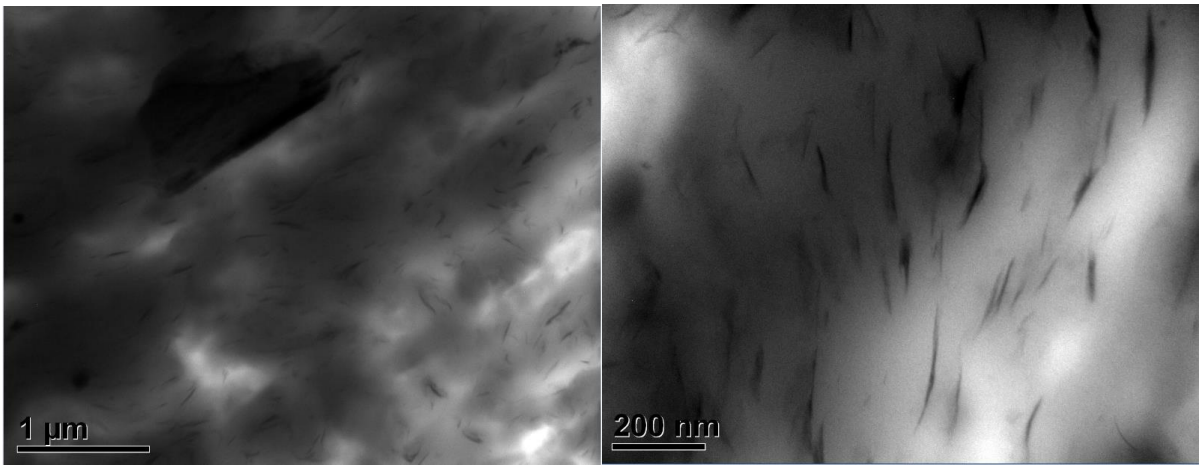

Figure 7 TEM images for PPCNC-20-25 at 30,000x magnification and (b) 100,000x magnification

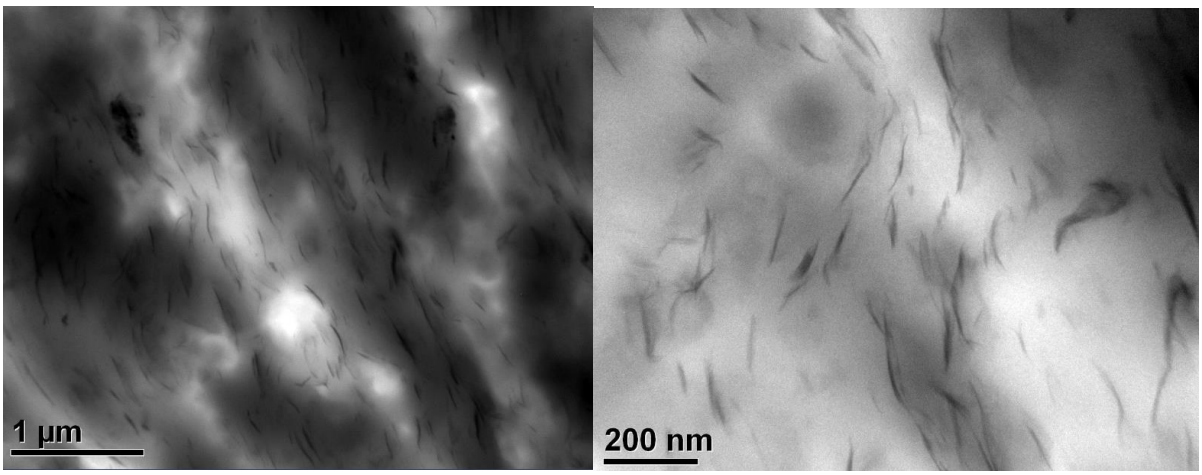

Figure 8 TEM images for PPCNC-30-25 at (a) 30,000x magnification and (b) 100,000x magnification8

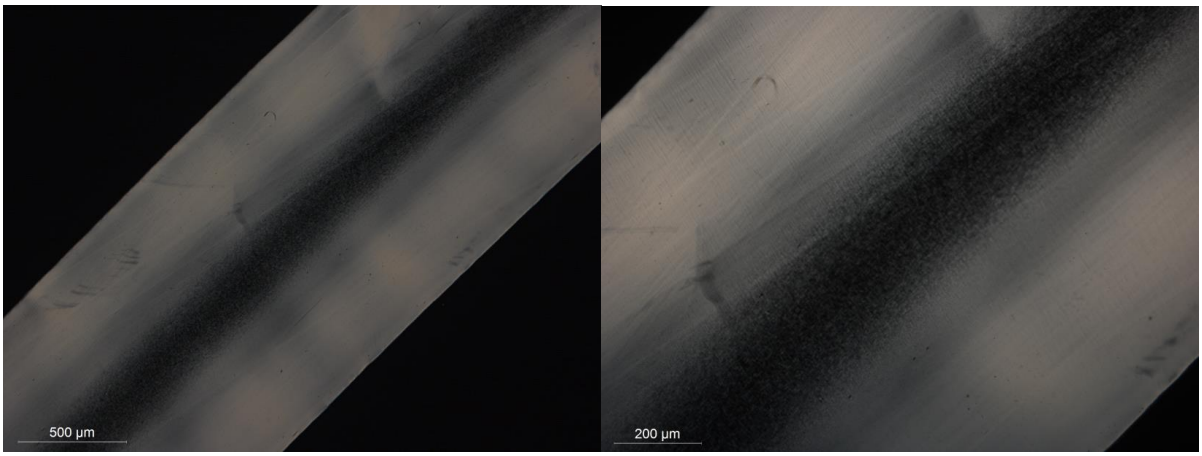

Figure 9 OM images for PPCNH-10-25

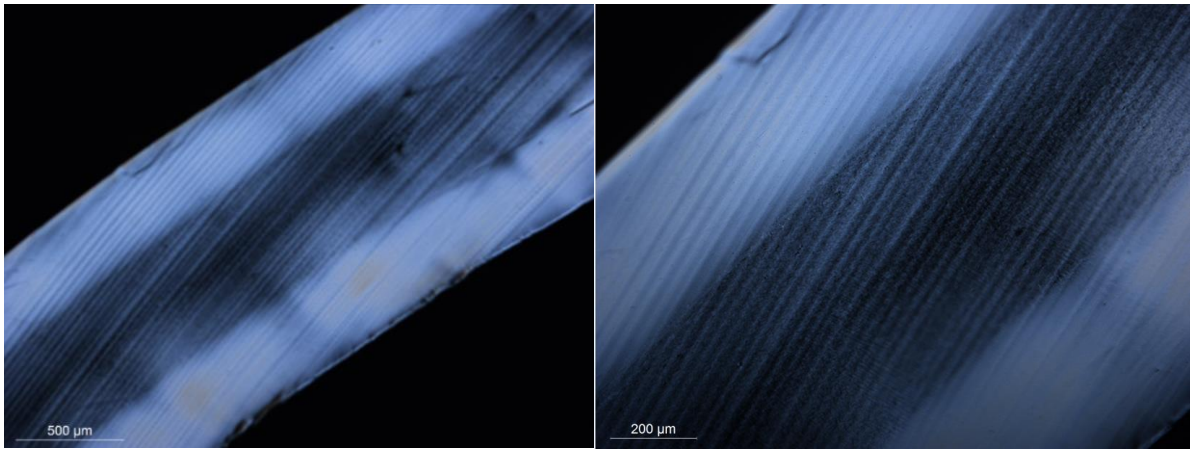

Figure 10 OM images for PPCNH-20-25

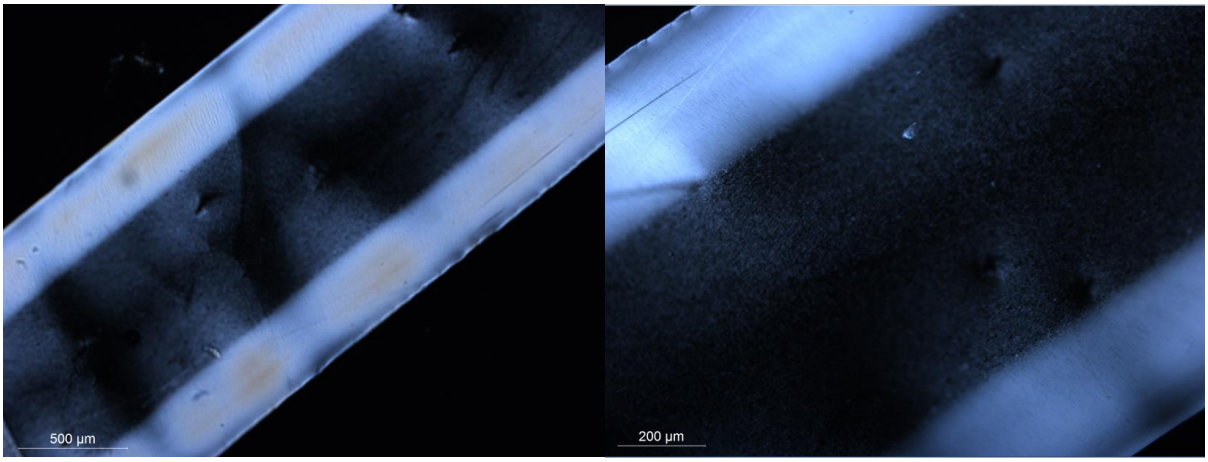

Figure 11 OM images for PPCNH-30-25

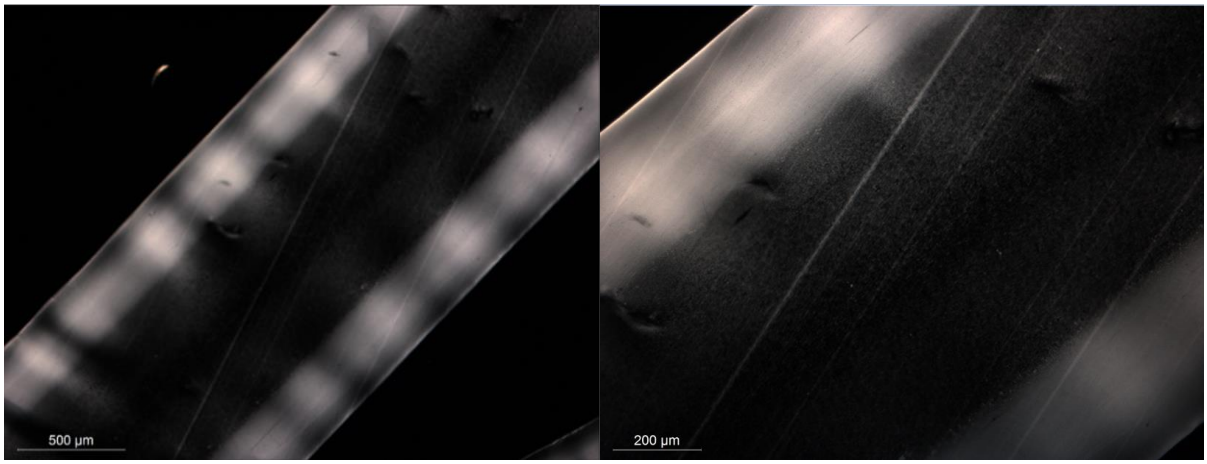

Figure 12 OM images for PPCNH-40-25

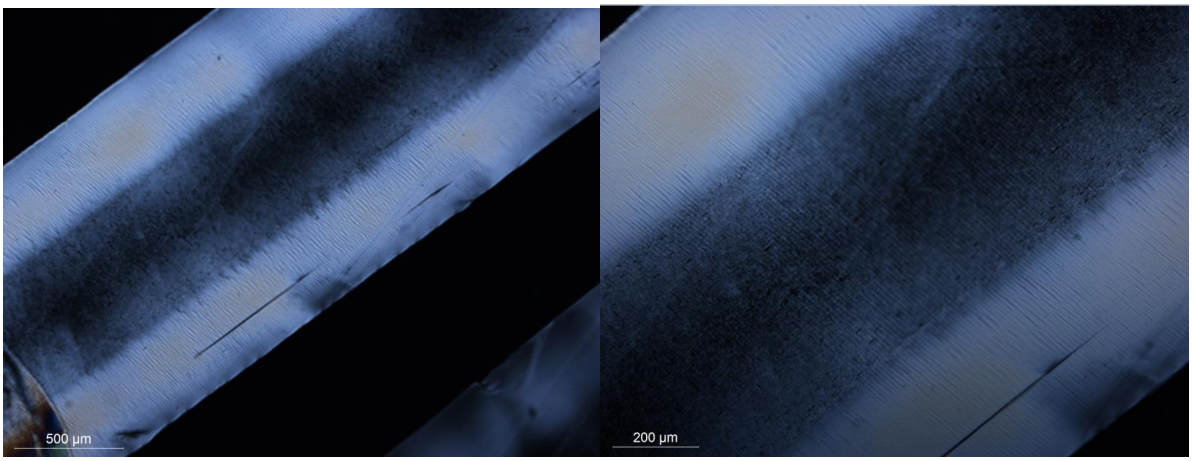

Figure 13 OM images for PPCNH-20-35

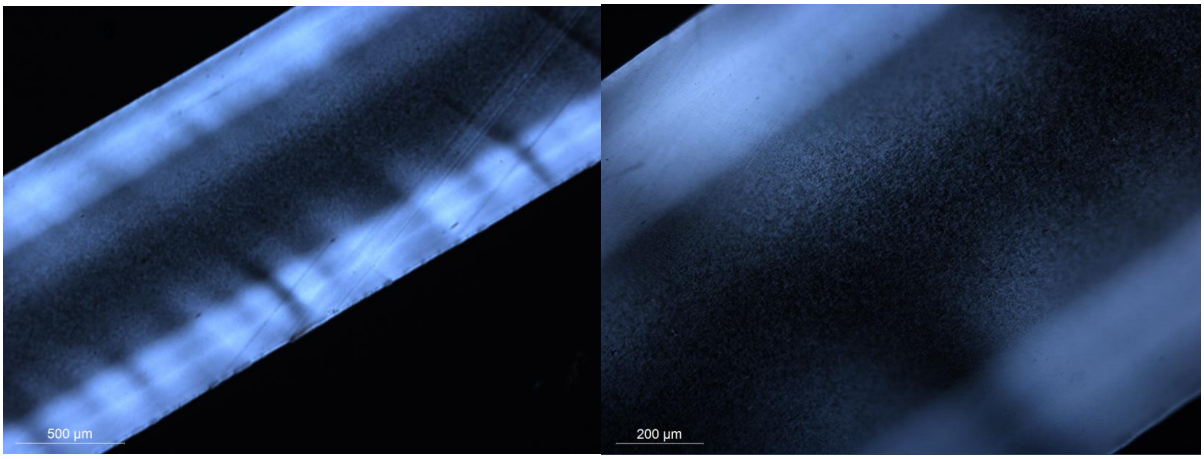

Figure 14 OM images for PPCNH-20-45

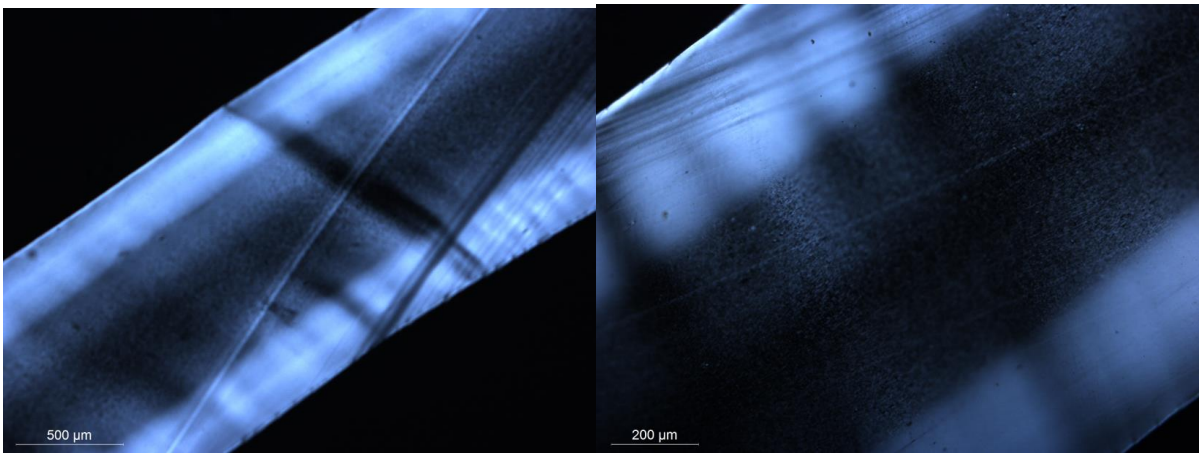

Figure 15 OM images for PPCNH-20-55

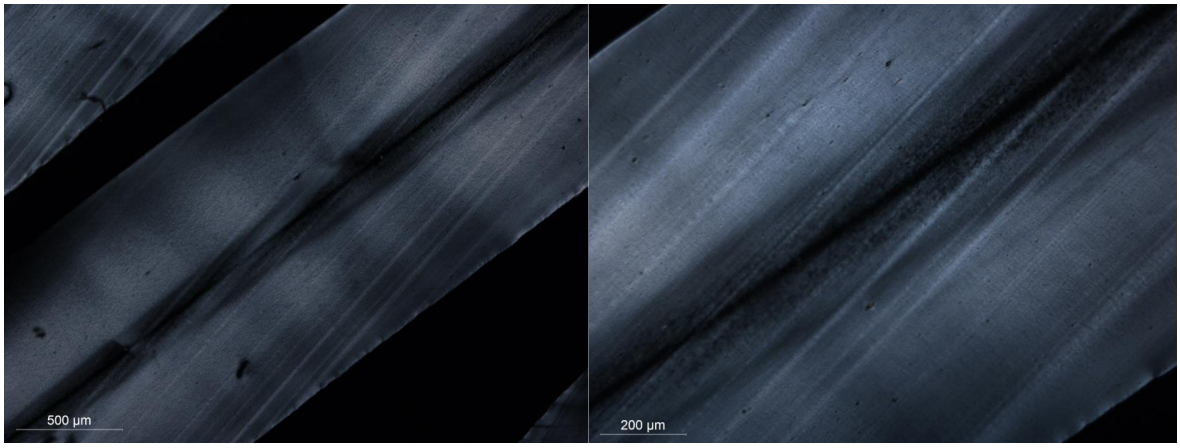

Figure 16 OM images for PPCNC-10-25

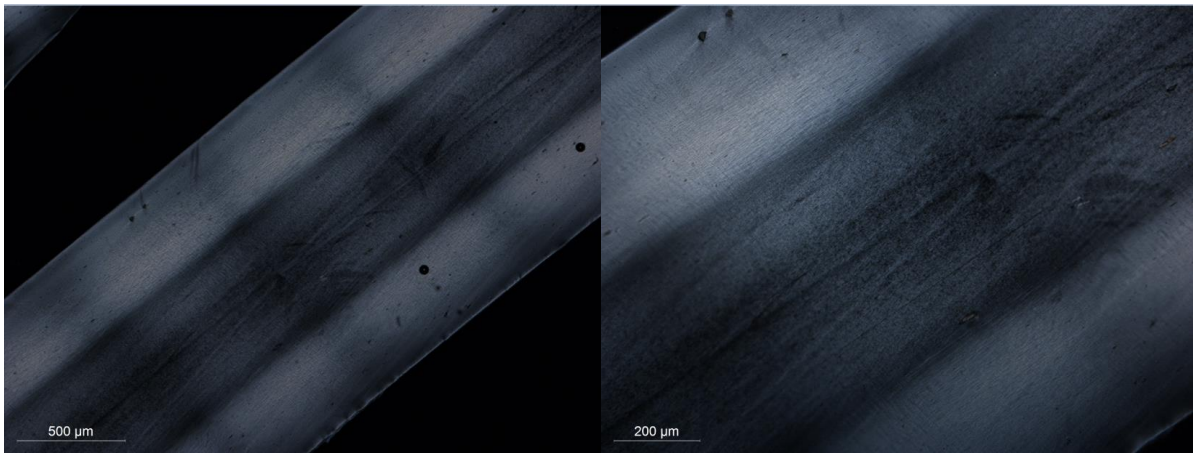

Figure 17 OM images for PPCNC-20-25

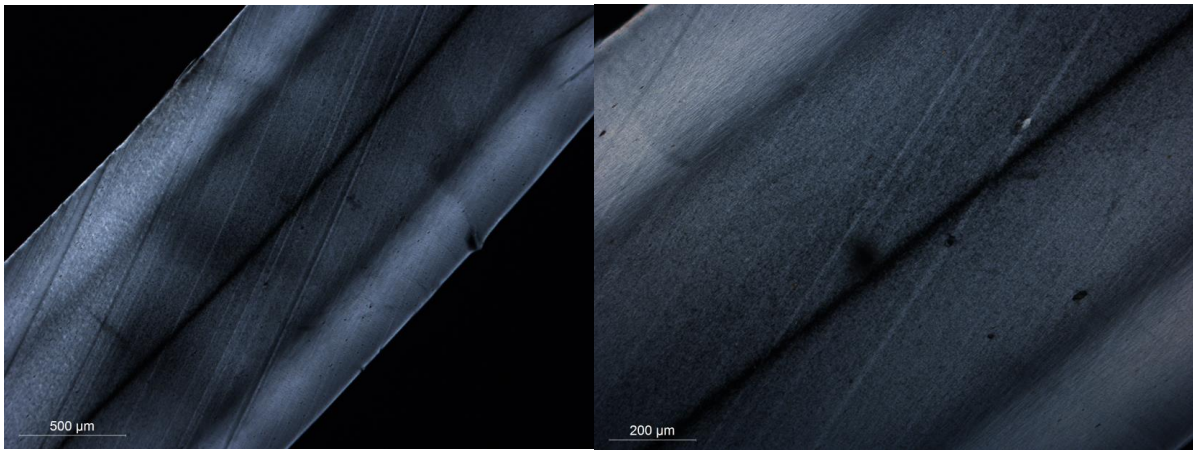

Figure 18 OM images for PPCNC-30-25

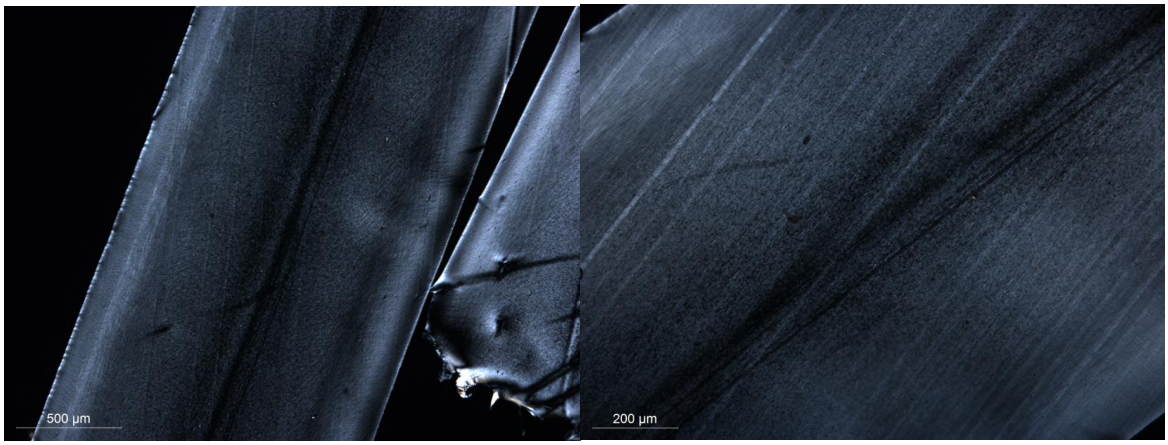

Figure 19 OM images for PPCNC-40-25

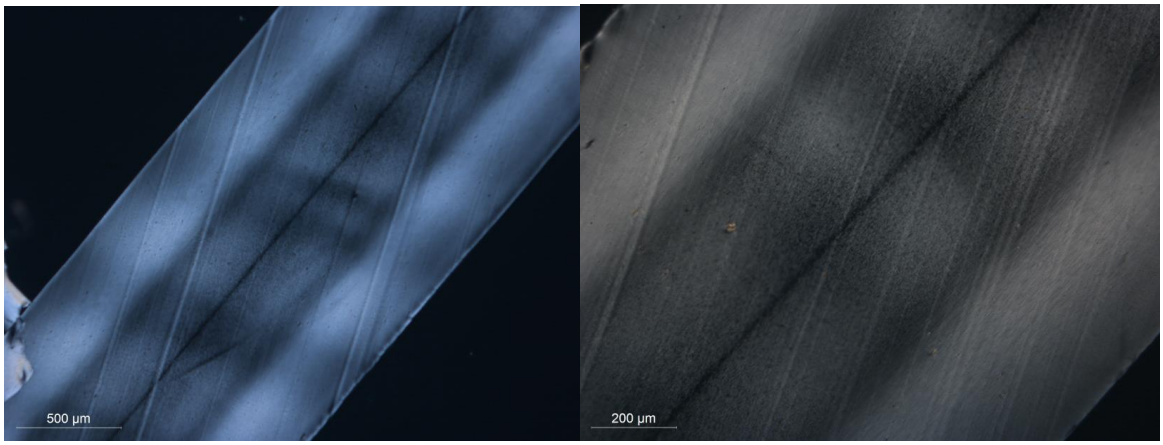

Figure 20 OM images for PPCNC-20-35

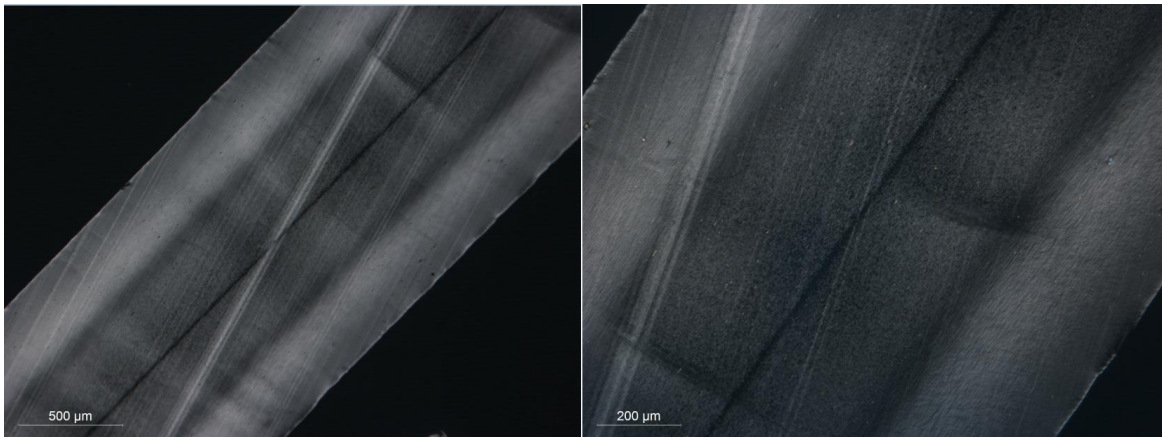

Figure 21 OM images for PPCNC-20-45

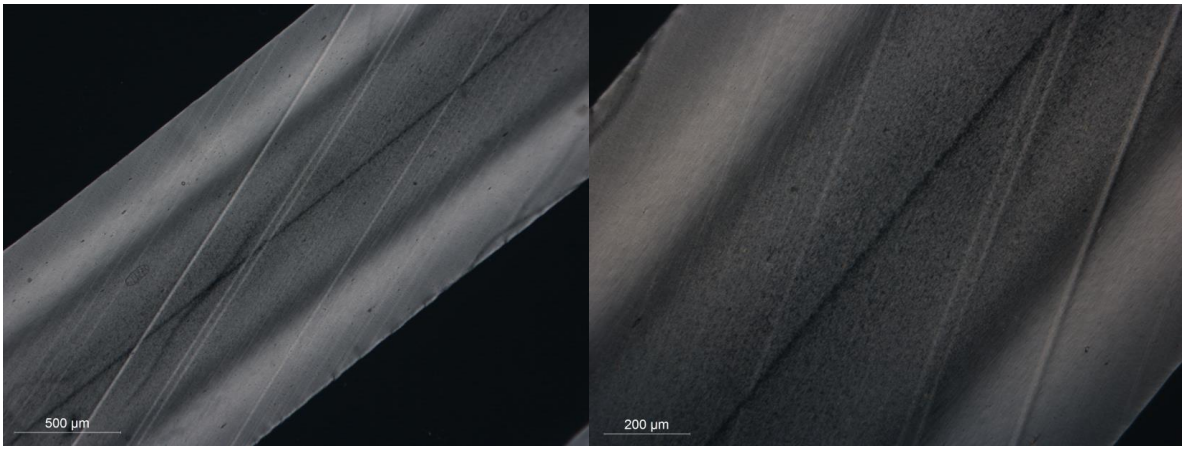

Figure 22 OM images for PPCNC-20-55

Appendix F

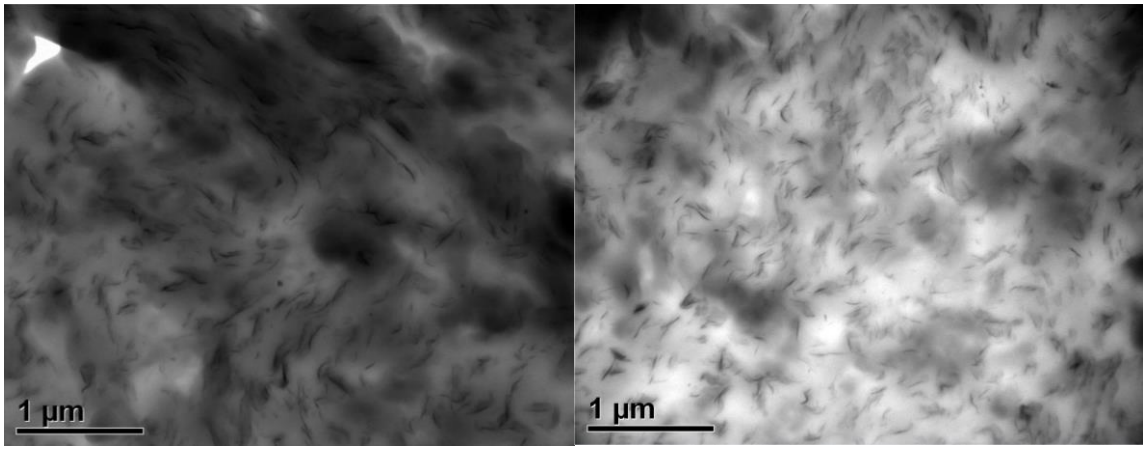

Figure 1 TEM images for (a) PPCNC-C1 and (b) PPCNC-C4

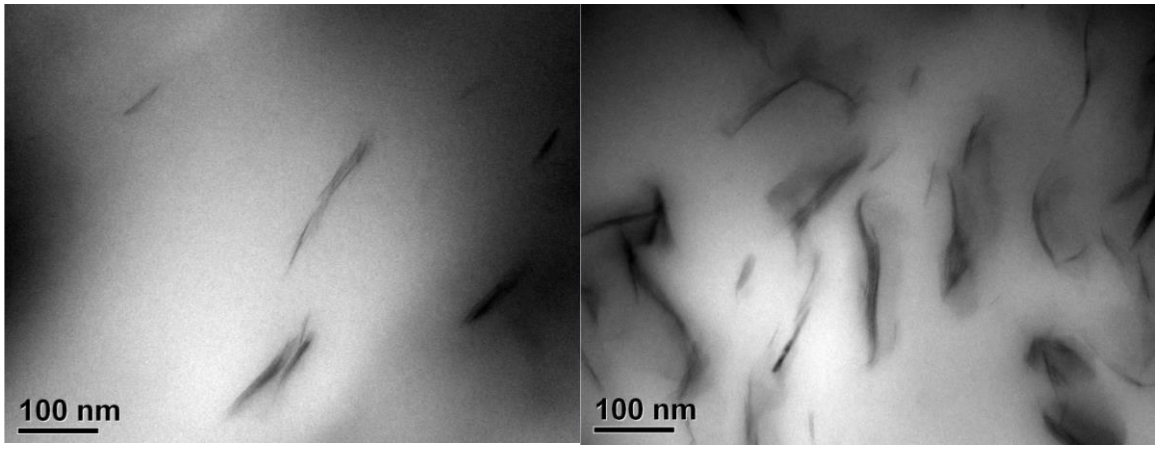

Figure 2 TEM images for (a) PPCNC-C1 and (b) PPCNC-C4

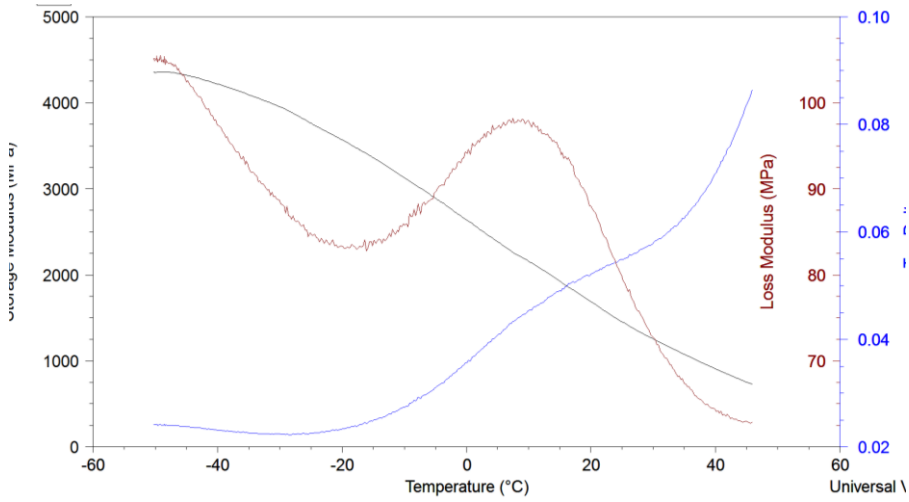

Figure 3 DMA pattern for PPC-C0

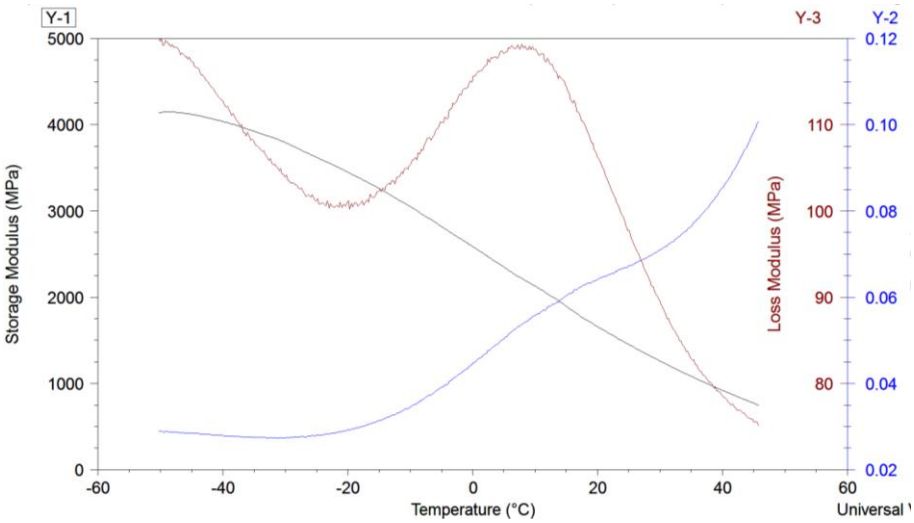

Figure 4 DMA pattern for PPCNC-C4

Figure 5 Impacted PPCN samples. PPCNC-C1 at 20°C(top left) and -20°C(bottom left); PPCNC-C3 at 20°C (top left) and -20°C (bottom right)

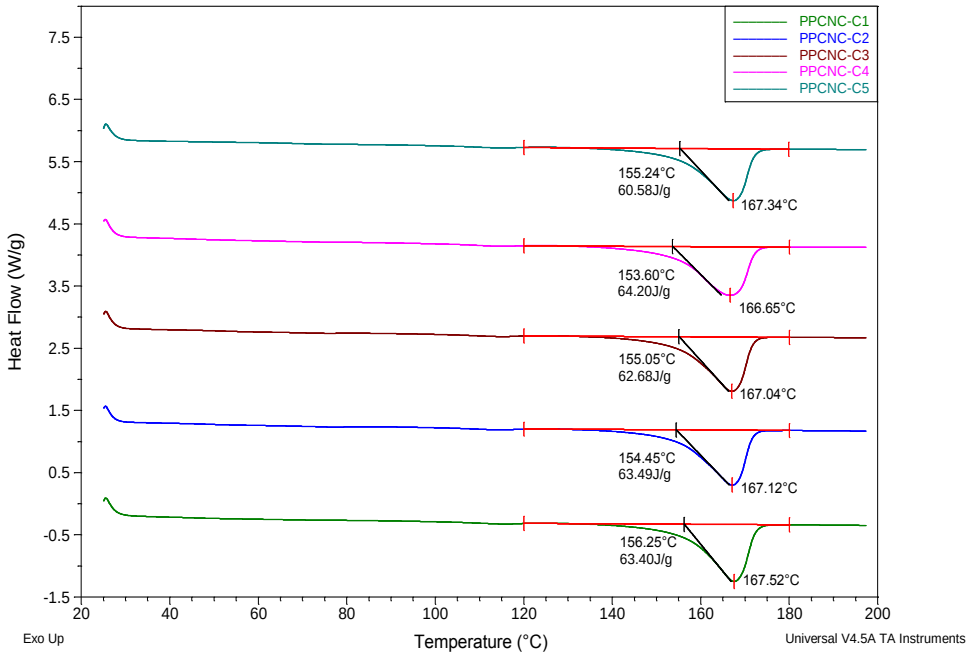

Figure 6 DSC curves of PPCNC samples with different clay content

Table 1 Results of falling weight impact tests at -20°C

Sample	Peak Force (kN)	Peak Deflation(mm)	Peak Energy (J)	Failure deflation (mm)	Failure Energy (J)
	1.99	5.45	5.69	7.16	8.32
	2.04	5.44	5.86	7.15	8.55
PPC-C0	2.01	5.39	5.61	7.16	8.37
	1.97	5.34	5.47	7.06	8.12
	2.07	5.38	5.85	7.08	8.58
Average	2.016	5.40	5.70	7.12	8.39
Stv	0.040	0.05	0.17	0.05	0.19
	1.98	5.11	5.15	6.85	7.86
	1.92	4.94	4.86	6.69	7.50
PPCNC-C1	2.01	5.33	5.55	7.05	8.27
	2.06	5.38	5.83	7.09	8.55
	1.92	5.14	5.13	6.92	7.77
Average	1.978	5.18	5.30	6.92	7.99
Stv		0.18	0.38	0.16	0.42
	1.97	5.22	5.34	7.00	8.09
PPCNC-C2	2.04	5.47	5.87	7.10	8.56
	2.02	5.56	5.86	7.27	8.57
	2.03	5.42	5.77	7.12	8.43
Average	2.015	5.42	5.71	7.12	8.41
Stv		0.14	0.25	0.11	0.22
	1.99	5.28	5.44	7.00	8.13
PPCNC-C3	2.01	5.48	5.69	7.23	8.44
	1.98	5.22	5.32	7.00	8.07
	1.97	5.48	5.64	7.21	8.28
Average	1.9875	5.37	5.52	7.11	8.23
Stv		0.12	0.15	0.11	0.14
	1.91	5.08	5.08	6.81	7.67
	1.88	4.80	4.66	6.60	7.29
PPCNC-C4	1.97	5.16	5.29	6.95	8.02
	1.97	5.19	5.36	6.96	8.07
	1.9	4.94	4.85	6.68	7.45
Average	1.926	5.03	5.05	6.80	7.70
Stv		0.17	0.29	0.16	0.34
	1.93	4.99	5.08	6.78	7.78
	1.99	5.27	5.58	6.99	8.20
PPCNC-C5	1.92	4.97	4.94	6.71	7.54
	1.98	5.14	5.30	6.86	7.96
	1.94	5.19	5.30	6.92	7.90
Average	1.952	5.11	5.24	6.85	7.88
Stv	0.031	0.13	0.24	0.11	0.24

Table 2 Results of falling weight impact tests at ambient temperature

Sample code	Peak Force (kN)	Peak Deflation(mm)	Peak Energy (J)	Failure deflation (mm)	Failure Energy (J)
	1.64	12.30	11.20	17.90	16.79
	1.72	12.10	11.00	16.80	19.30
PPC-C0	1.77	12.00	11.30	18.30	19.81
	1.83	11.90	10.90	17.60	18.93
	1.82	12.40	11.50	17.30	19.19
Average	1.76	12.14	11.18	17.58	18.80
Stv	0.08	0.21	0.24	0.57	1.17
	1.81	12.26	11.41	16.95	18.54
PPCNC-C1	1.77	12.14	11.08	16.76	18.01
	1.78	12.26	11.33	17.15	18.70
	1.75	12.21	11.02	16.92	18.09
Average	1.78	12.22	11.21	16.94	18.33
Stv	0.02	0.05	0.19	0.16	0.34
	1.75	12.34	10.97	17.55	18.64
	1.73	12.16	9.87	15.86	15.35
PPCNC-C2	1.69	11.43	9.48	16.12	16.16
	1.69	11.72	9.75	18.30	19.03
	1.70	12.52	10.97	17.91	18.65
Average	1.71	12.03	10.21	17.15	17.57
Stv	0.03	0.45	0.71	1.09	1.68
	1.72	12.16	10.79	17.50	18.60
	1.84	12.12	11.54	16.79	18.90
PPCNC-C3	1.79	12.32	11.41	16.83	18.24
	1.71	12.34	10.79	17.98	18.80
	1.68	12.35	10.63	17.91	18.51
Average	1.75	12.26	11.03	17.40	18.61
Stv	0.07	0.11	0.41	0.57	0.26
	1.66	12.58	10.90	18.12	18.63
	1.63	11.91	9.70	18.14	18.27
PPCNC-C4	1.62	12.30	10.35	18.20	18.33
	1.66	12.35	10.61	18.32	18.81
	1.61	11.98	9.49	18.66	18.29
Average	1.64	12.23	10.21	18.29	18.46
Stv	0.03	0.28	0.60	0.22	0.24
	1.64	12.30	10.37	18.30	18.53
	1.66	12.00	10.29	16.86	17.13
PPCNC-C5	1.65	12.18	10.32	18.01	18.27
	1.63	12.30	10.43	18.60	18.86
	1.65	12.00	10.21	17.20	17.36
Average	1.65	12.16	10.32	17.79	18.03
Stv	0.01	0.15	0.08	0.74	0.75

Table 3 Calculated interlayer spacing (d_{001})

Sample code	(001) 2-Theta (°)	(002) 2-theta (°)	d_{001}(nm)
PPCNC-C1	1.87	-	4.81
PPCNC-C2	1.89	-	4.70
PPCNC-C3	1.83	-	4.82
PPCNC-C4	-	3.05	5.79
PPCNC-C5	-	3.03	5.83

Table 4 Summary of OM results

Sample code	Part thickness (um)	Frozen layer thickness (um)	Frozen layer fraction (%)
PPC-C0	1411	497	35.2
PPCNC-C1	1460	542	37.1
PPCNC-C2	1414	580	41.0
PPCNC-C3	1396	610	43.7
PPCNC-C4	1556	644	41.4
PPCNC-C5	1337	594	44.4

Appendix G

Table 1 Summary of tensile test results for the thick sections of injection moulded parts

	Sample	Yield stress (MPa)	Tensile modulus (MPa)
PPCNH-T	1	35.2	597
	2	32.9	546
	3	36.4	523
	4	36.1	696
	5	35.0	448
	6	36.8	631
	7	36.3	603
	8	33.2	454
	Ave.	35.2	562
	Std.	1.49	86.3
PPCNC-T	Sample	Yield stress (MPa)	Tensile modulus (MPa)
	1	20.3	271
	2	21.6	332
	3	21.7	289
	4	21.2	344
	5	20.7	313
	6	20.3	279
	7	21.1	324
	8	21.9	300
	Ave.	21.1	307
	Std.	0.58	24.4

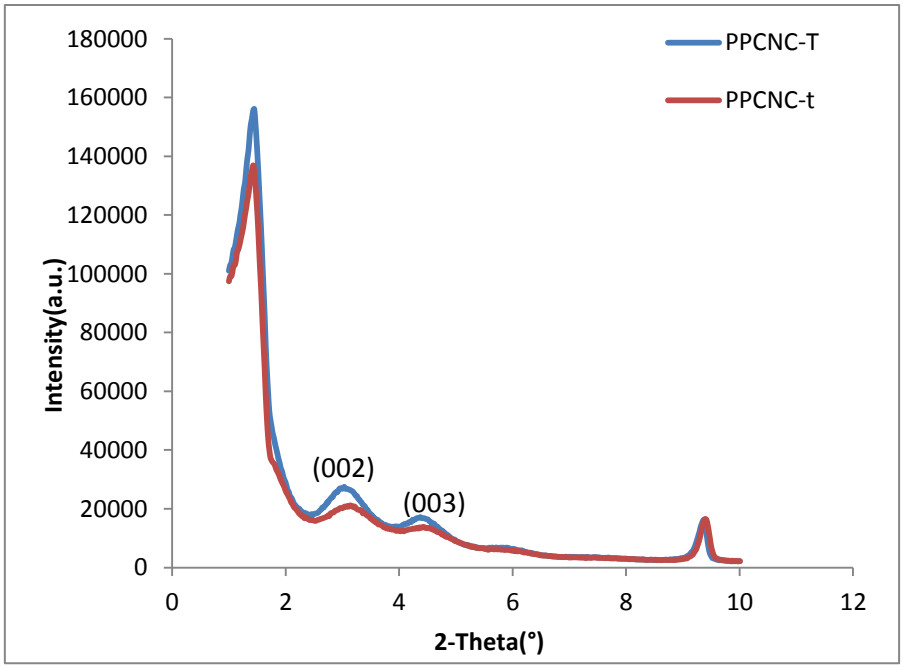

Figure 1 XRD patterns of PPCNC-T and PPCNC-t.

Appendix H

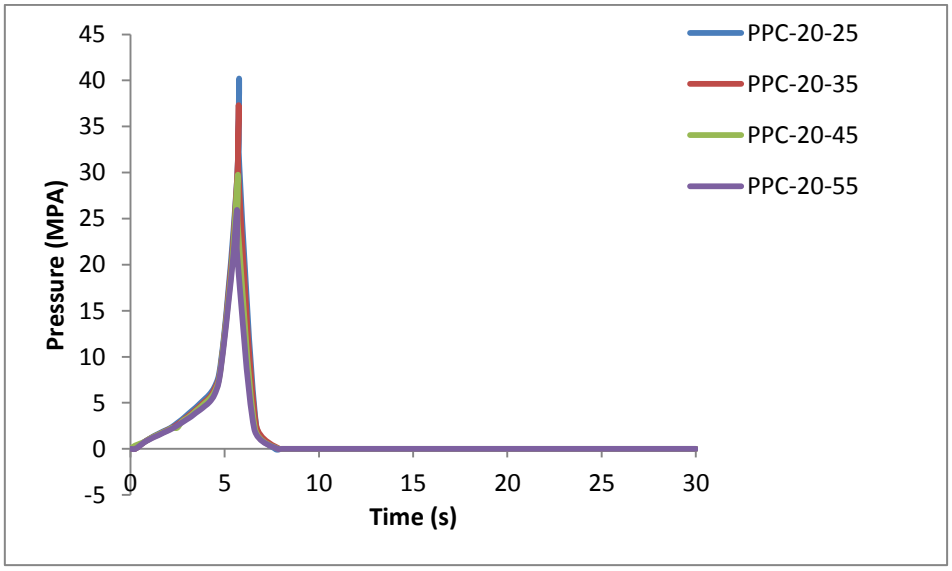

Figure 1 Plots of pressure against time obtained from simulation experiments

Table 1 Data from injection moulding simulation (P indicates data from actual moulding)

Injection speed (%)	Actual injection time *(s)	Injection pressure * (MPa)	Actual injection time (s)	Injection pressure (MPa)	Frozen layer fraction - thick (%)	Frozen layer fraction - thin (%)
10	11.9	29.71	11.9	165.2	44.2	100.0
20	5.8	24.44	5.8	40.21	33.8	48.2
30	3.9	25.63	3.9	28.01	29.3	37.1
40	3.0	25.58	3.0	26.22	26.2	32.1

Table 2 Data from injection moulding simulation (P indicates data from actual moulding)

Mould temp	Injection pressures (MPa)	Injection pressure * (MPa)	Frozen layer fraction - thick (%)	Frozen layer fraction - thin (%)
25	40.21	24.44	33.8	48.2
35	37.32	24.77	31.7	45.6
45	29.6	25.33	28.5	40.6
55	25.89	25.12	26.7	37.4

Table 3 Bulk shear rate obtained in simulation experiments

Sample code	Bulk shear rate (s^{-1})	
	Thick section	**Thin section**
PPC-10-25-S	50.5	150.1
PPC-20-25-S	55.4	165.1
PPC-30-25-S	73.6	247.7
PPC-40-25-S	98.8	296.9
PPC-20-35-S	54.04	164.4
PPC-20-45-S	51.8	164.0
PPC-20-55-S	51.2	166.4

Table 4 Bulk shear rate calculated by equation $\dot{\gamma} = \frac{6Q}{WH^2}(\frac{2n+1}{3n})$

Sample code	Bulk shear rate (s-1)	
	Thick section	Thin section
PPC-10-25	18.7	94.8
PPC-20-25	37.5	189.6
PPC-30-25	56.2	284.4
PPC-40-25	74.9	379.2
PPC-20-35	37.5	189.6
PPC-20-45	37.5	189.6
PPC-20-55	37.5	189.6

Table 5 Bulk temperature at the end of fill

Sample code	Bulk temperature at the end of fill (°C)	
	Thick section	**Thin section**
PPC-10-25-S	175.4	128.2
PPC-20-25-S	186.1	153.5
PPC-30-25-S	188.4	166.2
PPC-40-25-S	190.0	173.7
PPC-20-35-S	186.7	155.4
PPC-20-45-S	187.0	157.6
PPC-20-55-S	187.2	159.1

Appendix I

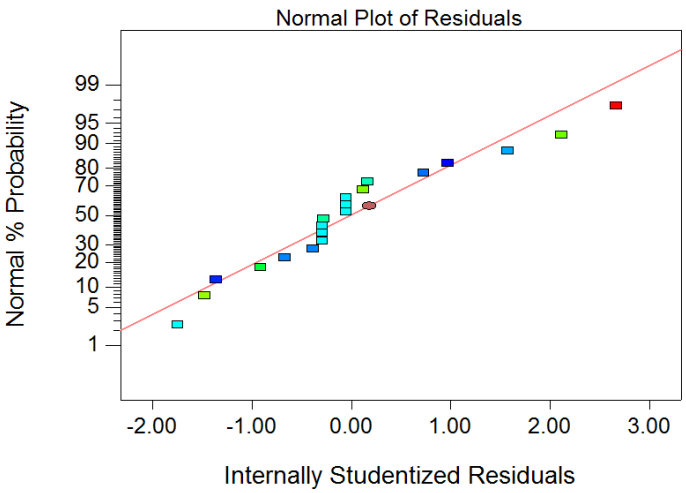

Figure 1 Normal probability plot for response, screw torque

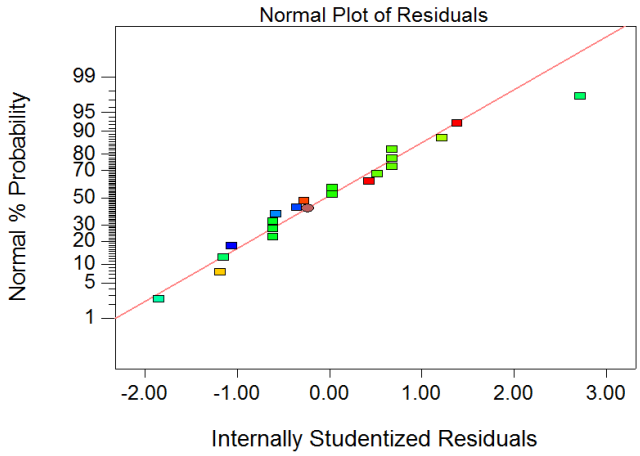

Figure 2 Normal probability plot for response, temperature difference between the die and melt

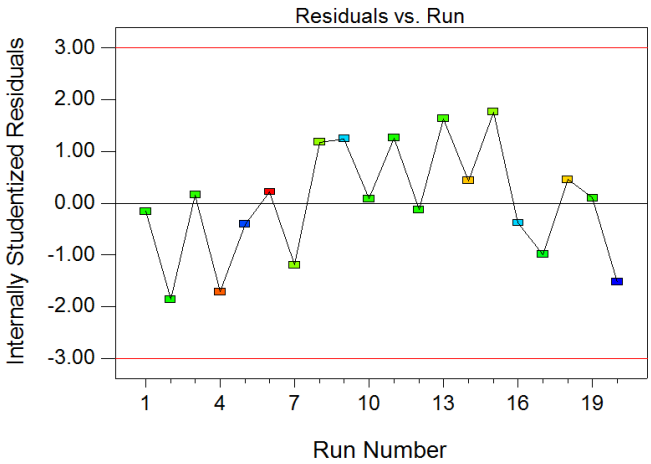

Figure 3 Plot of residuals vs. run order for response, mass output

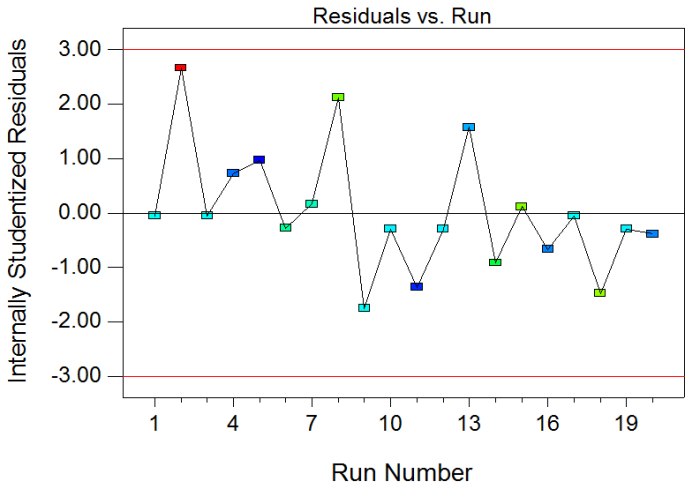

Figure 4 Plot of residuals vs. run order for response, screw torque

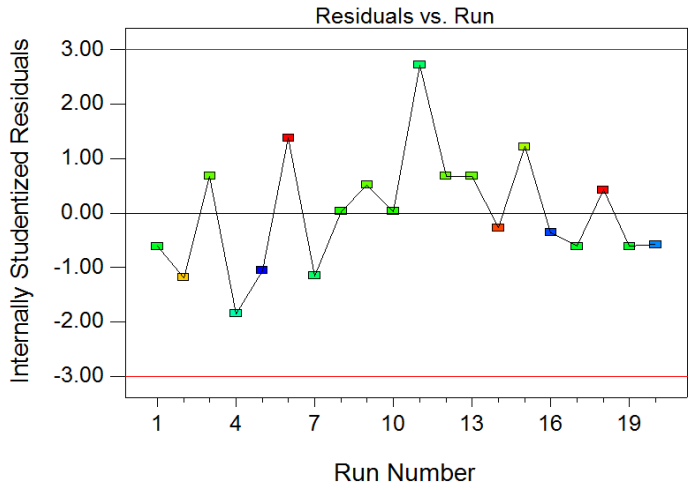

Figure 5 Plot of residuals vs. run order for response, temperature difference between the die and melt

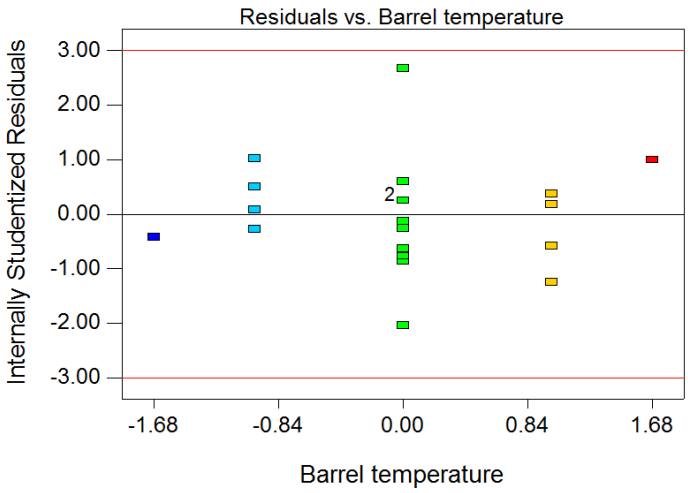

Figure 6 Plot of residuals vs. factor levels for response melt pressure

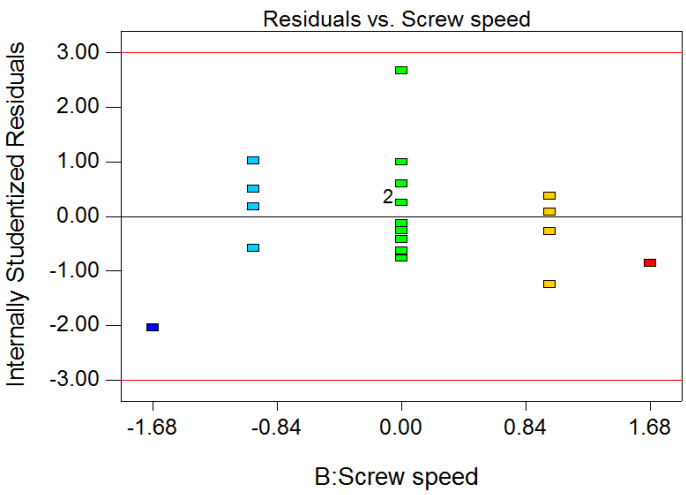

Figure 7 Plot of residuals vs. factor levels for response melt pressure

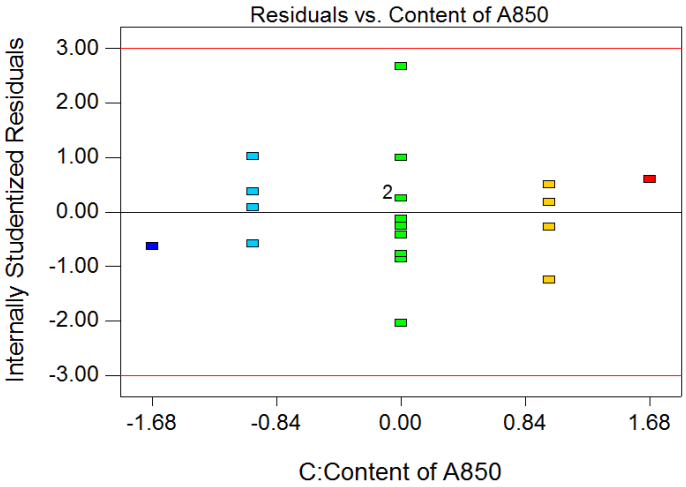

Figure 8 Plot of residuals vs. factor levels for response melt pressure

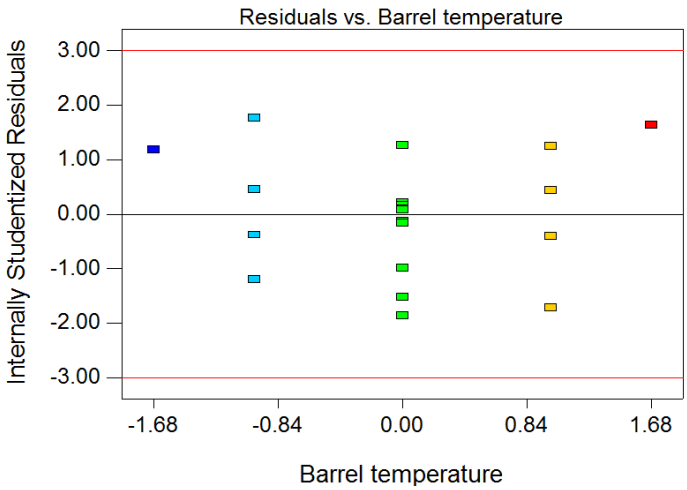

Figure 9 Plot of residuals vs. factor levels for response mass output

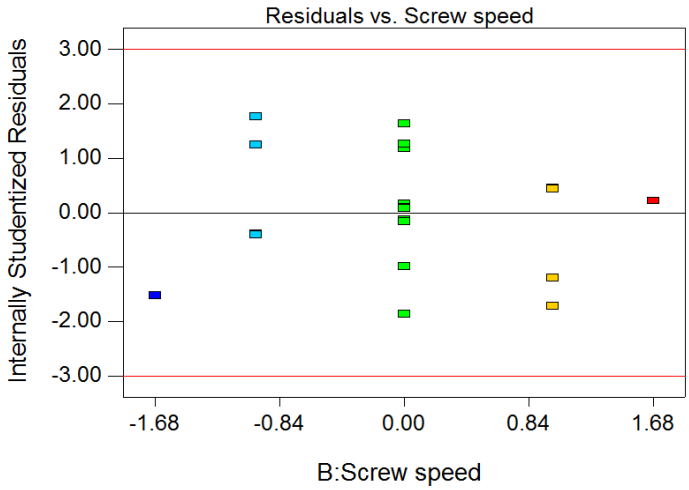

Figure 10 Plot of residuals vs. factor levels for response mass output

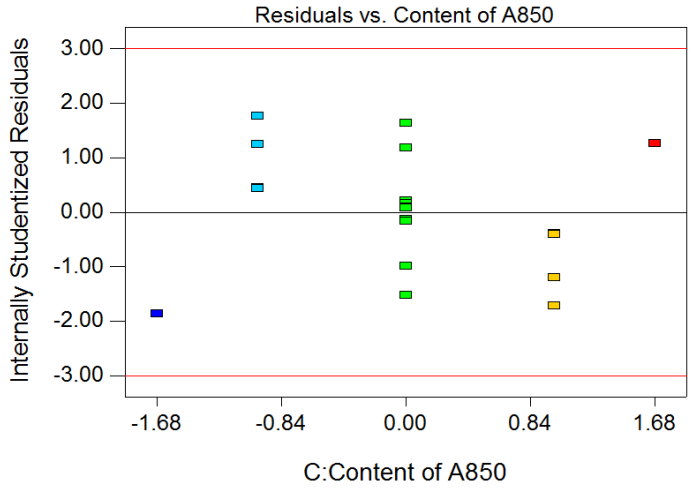

Figure 11 Plot of residuals vs. factor levels for response mass output

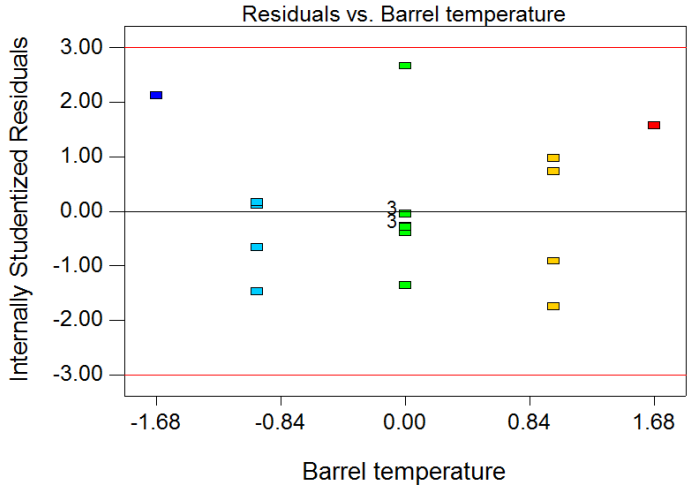

Figure 12 Plot of residuals vs. factor levels for response screw torque

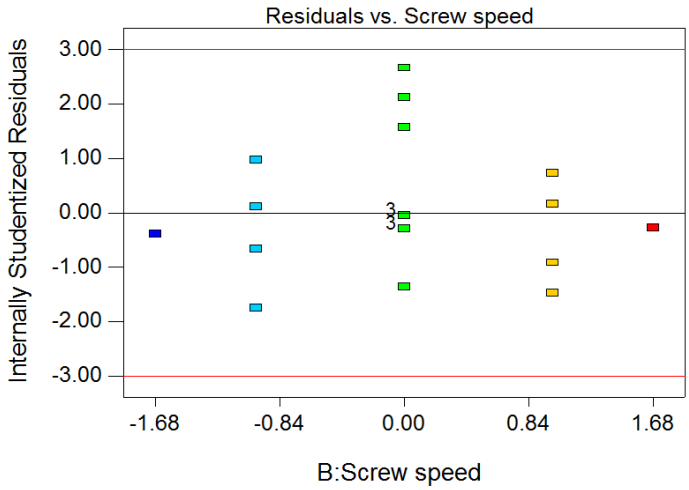

Figure 13 Plot of residuals vs. factor levels for response screw torque

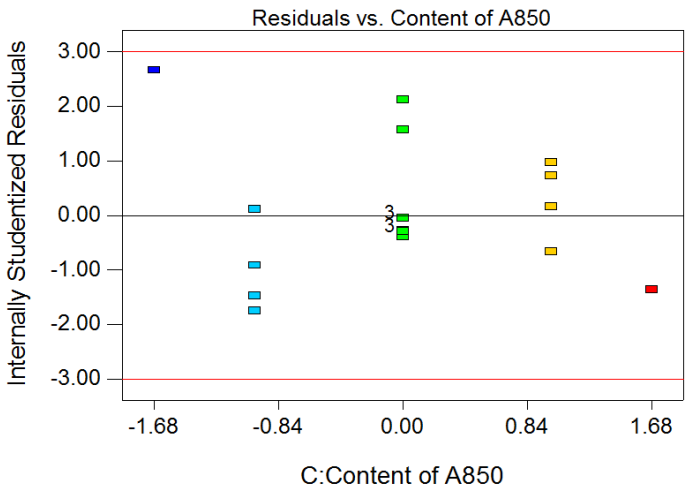

Figure 14 Plot of residuals vs. factor levels for response screw torque

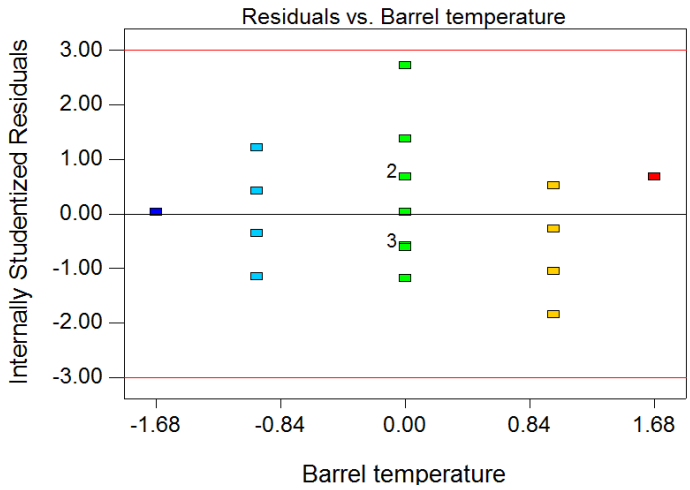

Figure 15 Plot of residuals vs. factor levels for response temperature difference

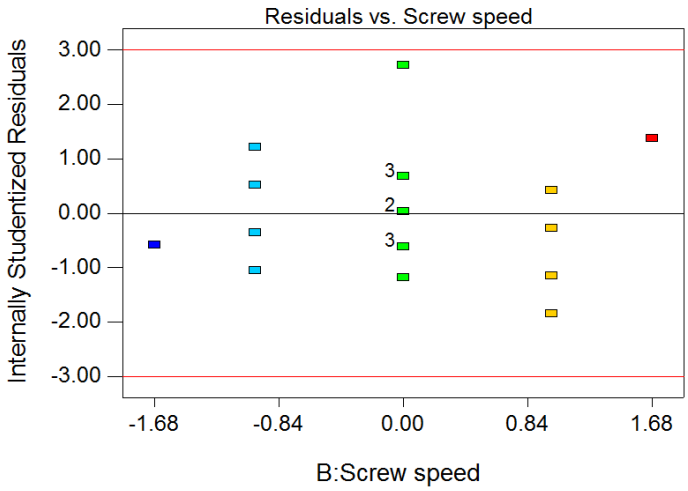

Figure 16 Plot of residuals vs. factor levels for response temperature difference

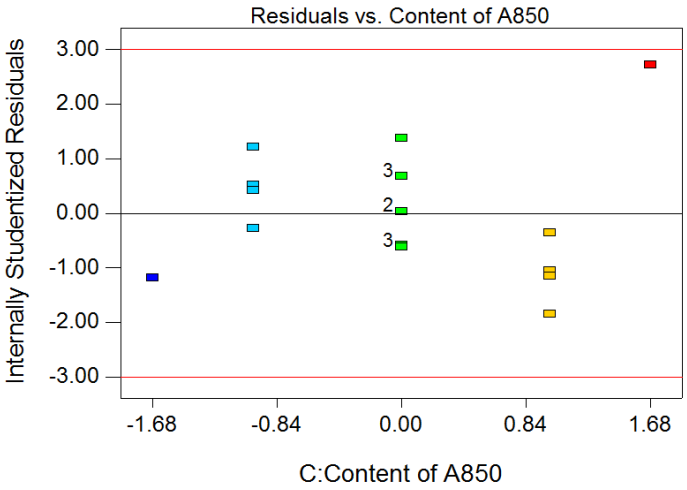

Figure 17 Plot of residuals vs. factor levels for response temperature difference